

INTERACTION OF IRON SPECIES AND SOOT PARTICLES IN AN ISOCTANE
DIFFUSION FLAME

By

KIBUM KIM

A DISSERTATION PRESENTED TO THE GRADUATE SCHOOL
OF THE UNIVERSITY OF FLORIDA IN PARTIAL FULFILLMENT
OF THE REQUIREMENTS FOR THE DEGREE OF
DOCTOR OF PHILOSOPHY

UNIVERSITY OF FLORIDA

2006

Copyright 2006

by

Kibum Kim

This work is dedicated to my family. Their support, encouragement and love made its completion possible.

ACKNOWLEDGMENTS

First and foremost, I am deeply grateful to Dr. David Hahn for his guidance and leadership during this study. Moreover, his encouragement always kept me looking at the bright side. His generosity and patience with my numerous mistakes in English and research allowed me to challenge myself without hesitation.

I would like to acknowledge the invaluable advice and suggestions of my committee members. I especially want to express my appreciation to Dr. Jill Peterson for her thoughtful concern about my school life.

I would also like to thank all of my lab mates (Leia Shanyfelt, Prasoon Diwakar, Cary Henry, Brett Windom, Philip Jackson, Soupy Alexander, Amy Twining, Chris Macarian, and Jeff Crosby) for their help and assistance while I was conducting my research. Their solidarity and friendship made lab life more enjoyable, and gave me a great opportunity to learn American culture including sports activities and insightful conversations. Special thanks also go to Kathryn Maseillo and Prasoon Diwakar for their valuable input and cooperation in my combustion research.

I would also like to thank my parents for their unconditional love and constant support. In addition, I sincerely thank my brother, Kee-Hoon for his concern and for stimulating me to even greater effort. Last but not least, words cannot express my gratitude to my lovely wife, Yong-Soon; and my adorable son, Daniel. At all times, Yong-Soon was a great support emotionally and mentally as I went through the ups and downs of private and professional life. My sweet little boy motivates me to work

constantly harder. I am really thankful that I could be with my family during the entire period of my study overseas.

TABLE OF CONTENTS

	<u>page</u>
ACKNOWLEDGMENTS	iv
LIST OF TABLES	ix
LIST OF FIGURES	xii
ABSTRACT	xvii
CHAPTERS	
1 INTRODUCTION	1
1.1 Soot Formation	3
1.1.1 Formation of Soot Precursor Molecules	4
1.1.2 Particle Coagulation and Growth	7
1.1.3 Particle Agglomeration	9
1.1.4 Soot Oxidation	10
1.2 Soot Suppression with Transition Metallic Additives	11
1.2.1 Manganese-Based Additives	13
1.2.2 Iron-Based Additives	14
1.2.2.1 Additives in premixed flames	14
1.2.2.2 Additives in diffusion flames	17
1.3 Studies of the Fractal Properties and the Structure of Soot Aggregates	19
1.4 Spectroscopic Method	22
1.5 Objectives of Present Research	25
2 FUNDAMENTAL SCIENCE AND BACKGROUND THEORY	27
2.1 Elastic Light Scattering Theory	27
2.1.1 Rayleigh Scattering Theory	29
2.1.2 Systems of Particles	31
2.1.3 Rayleigh-Debye-Gans (RDG) Scattering Theory	33
2.1.3.1 Rayleigh-Debye-Gans (RDG) scattering approximation	33
2.1.3.2 Evaluation of the extinction coefficient	35
2.1.4 Sampling and Analyzing Soot Aggregate	38
2.1.4.1 Thermophoretic sampling	38
2.1.4.2 Transmission electron microscopy	39
2.1.4.3 Energy dispersive x-ray spectroscopy (EDS)	41

2.2	Spontaneous Raman Scattering Theory	42
2.3	Laser Induced Fluorescence Theory	47
3	EXPERIMENTAL APPARATUS AND METHODS	51
3.1	Burner System	51
3.2	Fuel Vaporization and Delivery System	53
3.3	Flame	57
3.4	Optical Systems and Diagnostics.....	60
3.4.1	Light Scattering System	60
3.4.2	Light Scattering Calibration	67
3.4.3	Signal Processing.....	70
3.5	Laser Power Measurement	72
3.6	Transmission.....	73
3.7	Thermophoretic Sampling and Transmission Electron Microscopy	75
3.7.1	Thermophoretic Sampling	76
3.7.2	Transmission Electron Microscope	77
3.8	Spectroscopic Techniques	78
3.8.1	Preliminary CO Flame Study	79
3.8.2	Experimental Apparatus of Laser Induced Fluorescence Spectroscopy ..	81
3.8.3	Experimental Apparatus of <i>In Situ</i> Raman Spectroscopy	83
3.8.4	Isooctane Flame Study	86
4	INTEGRATED RESULTS AND DATA ANALYSIS	90
4.1	Smoke Point Study	90
4.2	Elastic Light Scattering Results.....	93
4.3	Transmission Results	97
4.4	Soot Characteristics Determined from RDG Theory.....	99
4.4.1	Transmission Electron Microscopy	99
4.4.2	Fractal Properties of Soot Aggregates.....	104
4.4.2	Primary Soot Particle Size.....	107
4.4.3	Number Density of Particles	109
4.4.4	Volume Fraction of Soot Particle.....	110
4.4.5	The Extinction Coefficient of Soot Particle	112
4.4.6	Discussion of Results	114
4.5	Spectroscopy.....	119
4.5.1	Laser Induced Fluorescence (LIF) Spectroscopy	122
4.5.2	<i>In Situ</i> Raman Spectroscopy.....	130
5	NUMERICAL ANALYSIS.....	136
5.1	Thermodynamic Equilibrium Calculations.....	136
5.1.1	Flame Temperature.....	136
5.1.2	O ₂ Flow Rates.....	142
5.1.3	Fe(CO) ₅ Concentrations	143

6	CONCLUSIONS AND FUTURE WORK.....	146
6.1	Summary and Conclusions.....	146
6.2	Future Work.....	152
APPENDICES		
A	ANALYSIS OF THE FLAME.....	153
B	RESULTS OF RDG CALCULATIONS.....	156
C	ERROR ANALYSIS.....	168
D	STRAY LIGHT CONSIDERATION.....	175
E	SOOT REDUCTION MECHANISM.....	178
F	PROPERTIES OF IRON PENTACARBONYL.....	182
	LIST OF REFERENCES.....	186
	BIOGRAPHICAL SKETCH.....	193

LIST OF TABLES

<u>Table</u>	<u>page</u>
1-1 Metallic additives in common.	12
1-2 Fractal dimension of various aggregates.	23
2-1 Raman shifts and the emission wavelengths of common species.	47
3-1 Data collection heights.	54
3-2 Summary of equipment for fuel vaporization and delivery system.	58
3-3 Summary of gases and fuel used in the study.	59
3-4 Description of the flame operating conditions.	60
3-5 Components of scattering system apparatus.	62
3-6 Real optical densities for various ND filters	65
3-7 The usage of the ND filters for individual height.	66
3-8 Average of the number densities, differential scattering cross sections, and scattering coefficient sets for methane and nitrogen calibration gases at 1 atm with standard deviation for 24 experimental.	69
3-9 Average results of calibration gas signal including stray light, a calibration ratio, stray light signal, the percentage of stray light, and the ideal reference ratio along with the standard deviation over all scattering experiments.	71
3-10 Summary of laser beam power properties for light scattering measurements.	73
3-11 Description of transmission apparatus.	74
3-12 Components of spectroscopic system apparatus.	87
3-13 Data collection heights for spectroscopy.	88
3-14 Components of the system apparatus for absorption spectroscopy.	89

4-1	Average of 4 oxygen flow rates with their standard deviation and relative standard deviation, the equivalence ratio, and oxygen to fuel ratio for 10 different concentrations.....	92
4-2	Average (N=10) K'_{VV} results of the unseeded and seeded flame and standard deviations. Flame heights are measured from the burner lip.	95
4-3	Average (N=6) transmission results of the unseeded and seeded flames and standard deviations. Flame heights are measured from the burner lip.....	98
4-4	The summary of the fractal dimension at all heights in the unseeded and seeded flames.	107
4-5	Diameters of primary soot particle at each height in the unseeded and seeded flames.	108
4-6	The summary of number densities for the unseeded and iron-seeded flames.....	110
4-7	The volume fraction as a function of flame height for the unseeded and iron-seeded flames.	112
4-8	The extinction coefficient of soot particle as function of flame height for the unseeded and iron seeded flames.	113
4-9	Complex refractive indices for soot from various sources. (2001).....	118
4-10	EDS result atomic ratio of iron oxide.....	121
4-11	Fe resonance transition wavelengths and corresponding fluorescence emission lines with their relative intensity.	122
4-12	Reference to iron oxides Raman shift (cm^{-1})	131
4-13	Fe atomic emission peaks.....	132
4-14	LIBS emission peaks.....	134
5-1	Mole of reactants used for input in the STANJAN code.	137
5-2	Products from STANJAN simulation.	137
B-1	Measured radius of the primary soot particle.....	156
B-2	The differential scattering cross section (cm^2/sr).....	157
B-3	Summary of calculated results for the unseeded flame.....	158
B-4	Summary of calculated results for the seeded flame.....	158

B-5	Uncorrected and corrected differential scattering coefficients ($\text{cm}^{-1}\text{sr}^{-1}$).....	159
B-6	Differential scattering cross section for a fractal aggregate (cm^2/sr).....	159
B-7	Number density of soot aggregates in the scattering volume ($\text{particles}/\text{cm}^3$).....	160
B-8	Total scattering cross section for a primary soot particle (cm^2).....	161
B-9	Total scattering cross section of an aggregate (cm^2).....	161
B-10	Absorption cross section of a primary particle (cm^2).....	162
B-11	Absorption cross section of an aggregate (cm^2).....	162
B-12	The extinction cross section of an aggregate (cm^2).....	163
B-13	The extinction coefficient (cm^{-1}).....	163
B-14	Number density of soot particles in the scattering volume ($\text{particles}/\text{cm}^3$).....	167
B-15	The volume fraction of soot particles in the scattering volume ($\text{cm}^3 \text{ soot}/\text{cm}^3$). ...	167
C-1	Summary of the calculated parameters with Equations C-6 through C-9 for the unseeded flame.....	169
C-2	Summary of the calculated parameters with Equations C-6 through C-9 for the seeded flame.....	170
C-3	Results of the calculation using Equation C-12 for the unseeded flame.....	171
C-5	Summary of calculated errors at each height for the particle size and number density.....	172
C-6	Summary of calculated parameters at each height for the unseeded flame.....	174
C-7	Summary of calculated parameters at each height for the seeded flame.....	174
F-1	Fe vapor pressure in Torr (mm Hg) as a function of the flame height.....	184

LIST OF FIGURES

<u>Figure</u>	<u>page</u>
1-1 Transmission electron microscope (TEM) images of soot aggregates from isooctane combustion. A) At 100 nm scale. B) At 0.2 μm scale.	4
1-2 Soot formation. Adapted with permission from a reference (Bockhorn 1994).....	5
1-3 The H-abstraction-C ₂ H ₂ -addition mechanism acting on a biphenyl molecule.....	8
1-4 Two processes of particle growth. A) Particle coagulation. B) Particle agglomeration.....	10
1-5 Soot formation regimes in a diffusion flame, the axial soot concentration profile at the center of the flame, and the radial soot concentration profile at an arbitrary flame height.....	12
2-1 Light scattering response to an incident light.....	28
2-2 Schematic of TEM	40
2-3 Energy level diagrams representing elastic scattering transitions and several inelastic Raman scattering transitions. A) Elastic scattering. B) Resonance Raman scattering. C) Stokes Raman scattering. D) Anti-Stokes Raman scattering.	43
2-4 Relationship between Rayleigh and Raman scattered lines in a scattering spectrum. Source: Ingle and Crouch 1998.	45
2-5 Energy level diagram of the fluorescence process for atoms or molecules.	48
3-1 Concentric diffusion burner schematic. A) Side view. B) Top view. Oxygen goes into the system through the annulus array of ports whereas isooctane and nitrogen flow through the tube in the center.	52
3-2 Concentric diffusion burner. A) Side view. B) Top view.	53
3-3 Data measurement heights.	55
3-4 Fuel vaporization system schematic.....	56
3-5 Fuel vaporization system.....	56

3-6	Alicat Scientific digital flow meters employed for regulating the flow rates of nitrogen coflow and oxygen.....	58
3-7	Chemical structure of isooctane.....	59
3-8	Photomultiplier tube. A series of dynodes between cathode and anode provide internal gain.....	64
3-9	Sample scattering signals from methane, nitrogen, and flame. Calibration gases are attenuated by a factor of $10^{0.3}$ and flame signal is attenuated by a factor of $10^{5.43}$ for signal linearity.....	70
3-10	Top view of the transmission system setup.....	73
3-11	A setup of thermophoretic sampling and grid. A) Side view. B) Formvar carbon-supported 150 mesh copper grid.....	76
3-12	Photograph of the TEM system.....	78
3-13	Vaporization system of iron pentacarbonyl and a CO flame burner.....	79
3-14	A photograph of the iron pentacarbonyl vaporization vessel and the heater.....	80
3-15	Photographs of CO flame. A) unseeded flame, B) iron seeded flame.....	81
3-16	The optical setup for laser-induced fluorescence spectroscopy.....	82
3-17	The optical set-up for <i>in situ</i> Raman spectroscopy.....	83
3-18	A photograph of an optical set-up inside OPO.....	84
3-19	The optical set-up for absorption spectroscopy.....	89
4-1	Plot of oxygen flow rate at the smoke point as function of time.....	91
4-2	Smoke point, as measured by the corresponding oxygen to fuel ratio and the equivalence ratio, as a function of iron pentacarbonyl concentration. Note that the equivalence ratio increases due to a reduction of the necessary oxygen quantity.....	93
4-3	Typical scattered signal response from photomultiplier tube measuring calibration gases and flames. Calibration gas signals are attenuated by a factor of $10^{0.3}$, and flame signals are attenuated by a factor of 10^5 to preserve signal linearity.....	94
4-4	Unseeded and seeded differential scattering coefficients in logarithmic scale. Error bars represent one standard deviation.....	96
4-5	Transmission through the unseeded and seeded flames.....	99

4-6	Transmission electron micrographs of soot particles at different axial positions. .100	100
4-7	A log-log plots of N versus R_g/d_p 25 soot aggregates were sampled at the height 7 in the unseeded flame.106	106
4-8	A log-log plots of N versus R_g/d_p 25 soot aggregates were sampled at the height 7 in the seeded flame.106	106
4-9	Diameters of the primary soot particle as a function of the flame height in the unseeded and seeded flames. A polynomial curve fit was used for extracting more accurate values of d_{par}109	109
4-10	The number of primary soot particle as a function of the flame height in the unseeded and iron-seeded flames. A logarithmic curve fit was used for extracting more accurate values of N_{par}111	111
4-11	Number density of the total soot particle for the unseeded and iron-seeded flames.111	111
4-12	The volume fraction as a function of flame height for the unseeded and iron-seeded flames. The error bar represents one standard deviation.113	113
4-13	The extinction coefficient of soot particle as a function of flame height for the unseeded and iron-seeded flames.114	114
4-14	Photographs of tips of the unseeded and seeded flames. Soot plume is seen in the unseeded flame while being not seen in seeded flame. A) the unseeded flame. B) the seeded flame.116	116
4-15	Photographs of the unseeded and seeded flames. A) the unseeded flame. B) the seeded flame.117	117
4-16	TEM images of samples collected in the Fe-seeded CO flame. A) sampled at the middle of the flame height. B) sampled at the flame tip.120	120
4-17	The typical signal window of EDS.120	120
4-18	Energy level diagram of Fe atom. Bold font indicates the best combination.123	123
4-19	Laser induced fluorescence peak for three excitation sources at the two third of normalized CO seeded flame height. Excitation lines are shown.124	124
4-20	Fe fluorescence corresponding to the excitation line of 296.69 nm as a function of the CO flame normalized four heights.124	124
4-21	Intensity of LIF measured in isoootane seeded flame at emission line of 373.49 nm corresponding to the excitation line of 296.69 nm. Flame tip is at height of 23.95 cm. Error bars represent one standard deviation.125	125

4-22	Transmission of Fe atomic light passing through the seeded flame at two different heights. Fe resonance transition line of 271.9 nm was chosen for this study. Flame tip is at the height of 23.95 cm.	127
4-23	Transmission of Fe atomic light from the lamp as a function of 5 different heights of the seeded flame. Fe resonance transition line of 271.9 nm was chosen for this study. Flame tip is at the height of 23.95 cm.	127
4-24	Spectra measured as function of the incident laser energy at flame tip using the 355 nm source in order to validate the LIBS effect on the LIF signal.	129
4-25	On-and-off resonant LIF signal induced by the excitation wavelength of 296.69 nm and 296.19 nm with the same pulse energy.	129
4-26	Energy level diagram of FeO molecule.	130
4-27	A spectrum obtained from <i>in situ</i> Raman experiment of CO flame using 532 nm as an excitation source.	132
4-28	Spectra obtained from <i>in situ</i> Raman experiment of CO flame using 355 nm as an excitation source at four different heights.	133
4-29	LIBS emission spectrum obtained from steel rod using 355 nm as an excitation source.	134
5-1	Relative mass fraction of products as a function of temperature.	138
5-2	Relative mass fraction of Fe species as a function of temperature.	139
5-3	Relative mass fraction of Fe as a function of temperature.	139
5-4	Flame temperature as a function of flame height.	140
5-5	Relative mass fraction of species as a function of temperature.	141
5-6	The decrease in relative mass fraction of the solid carbon as a function of the oxygen flow rate.	143
5-7	Relative mass fraction of the iron species as a function of the oxygen flow rate.	144
5-8	Mass fraction of carbon as a function of the Fe(CO) ₅ concentration.	145
6-1	Schematic of soot oxidation mechanism. A) Soot oxidation without Fe. B) Soot oxidation with Fe.	149
6-2	Schematic of surface reaction mechanism of hydrogen oxidation. Three steps of the mechanism are adsorption, surface reaction, and desorption.	150

B-1	The differential scattering coefficients measured along the radial positions at three different heights. Error bars represent one standard deviation.....	164
B-2	The extinction coefficients as a function of the unseeded flame height. The extinction coefficients determined using RDG scattering theory for two different refractive index were compared with that from transmission experiments.....	165
B-3	The extinction coefficients as a function of the seeded flame height. The extinction coefficients determined using RDG scattering theory for two different refractive index were compared with that from transmission experiments.....	166
D-1	Source of stray light in the light scattering optical setup.	176
F-1	Fe(CO) ₅ vapor pressure as a function of temperature (Gilbert and Sulzmann 1974, Trautz and Badstubner, 1929).	183
F-2	Fe vapor pressure as a function of the flame height. Over the flame height of 15 cm which is the oxidation regime, the vapor pressure is negligibly small.....	185

Abstract of Dissertation Presented to the Graduate School
of the University of Florida in Partial Fulfillment of the
Requirements for the Degree of Doctor of Philosophy

INTERACTION OF IRON SPECIES AND SOOT PARTICLES IN AN ISOCTANE
DIFFUSION FLAME

By

Kibum Kim

August 2006

Chair: David W. Hahn

Major Department: Mechanical and Aerospace Engineering

Metallic fuel additives have been considered for soot emission control over the last few decades. However, the exact mechanisms of soot reduction are poorly understood and remain controversial. In response to the need for elucidating the correct chemical processes, elastic light scattering, laser-induced fluorescence, and thermophoretic sampling followed by transmission electron microscopy analysis were carried out in a laboratory-scale isooctane diffusion laminar flame seeded with 4000 ppm iron pentacarbonyl as the metallic additive. These measurements yielded the size, number density, and volume fraction of soot particles throughout the flame, including formation and oxidation regimes. In comparison to the scattering parameters extracted from the unseeded flame, the soot suppression effects of iron pentacarbonyl can be determined to act primarily in the regime of soot burnout or oxidation. It is concluded that the additive has no direct effect on perturbation of soot in the soot growth zone of the flame, while

having a significant effect on soot in the burnout zone of the flame, namely enhanced oxidation, realizing an overall soot suppression effect.

In addition to the elastic scattering, laser-induced fluorescence and *in situ* Raman spectroscopy were performed to identify the state of the iron additive in the seeded flame. The results of the spectroscopic techniques reveal that the dominant iron species throughout the primary flame region was Fe, rather than any form of iron oxide. Moreover, elemental iron was observed to diminish through the soot oxidation region. The primary conclusion is that the catalytic effect of Fe atoms and possibly iron oxides enhanced soot oxidation in the burnout regime of the flame, thereby reducing the overall soot emissions. Consistent with this, the noted reduction in smoke point with the addition of iron was also observed.

CHAPTER 1 INTRODUCTION

Particulate matter (PM) is the term describing small particles found in the air such as dust, dirt, liquid droplets, smoke, and soot. These particles are emitted directly into the air from a variety of sources and are also formed in the air through chemical reactions. Sizewise, particles less than 2.5 μm in diameter are called PM_{2.5} (or fine particulate matter). Because such fine particles are linked to both human health concerns and environmental issues, various efforts have been made and many scientific studies have been done to find a way to decrease the production rates of fine particles. As a part of these efforts, the Environmental Protection Agency enacted [National Ambient Air Quality Standards](#) (NAAQS) for PM and declared that the annual average level of PM_{2.5} particles in the air should not exceed 15 micrograms per cubic meter (<http://www.epa.gov/region4/sesd/pm25/p2.htm>). Consequently, significant reductions have been achieved over the last two decades, however, more efforts are needed to ensure that the air is safe enough not to affect human health and the environment.

As far as human health is concerned, inhaling PM causes a broad range of illness such as asthma, acute or chronic bronchitis, shortness of breath, painful breathing, respiratory and heart illness, diminished lung function, and even premature mortality (<http://www.epa.gov/air/urbanair/pm/index.html>). Due to the small size of these particles, they are capable of penetrating and accumulating in the respiratory system. It is supported by a recent study that particulate pollutants increase the incidence of cardiopulmonary diseases and ischemic heart attack (Pope *et al.* 2004). A specific type

of PM is soot particles, which are rich in amorphous carbon and polycyclic aromatic hydrocarbons (PAHs), and are known to be mutagenic and carcinogenic (Katsouyanni and Pershagen 1997, Farmer *et al.* 2003).

In addition, PM has a harmful influence on the environment in many ways. For example, it leads to atmospheric haze resulting in reduction of visibility in many parts of the US. It also may play a role in acid rain, which may be responsible for a range of problems. When PM settles on soil and water, it changes the nutrient and chemical balance that are responsible for depleting ecosystems and ruining sensitive forests and farm crops. According to the latest studies, soot is twice as potent as carbon dioxide in contributing to global warming resulting from the green house effect because it can darken snow and ice that results in absorption of solar energy rather than reflection (<http://www.newscientist.com/article.ns?id=dn4508>). Such harmful impacts of PM can impact the broad areas because it can travel long distance from the sources (US EPA. 2003).

A major source of PM is soot, usually produced through incomplete combustion processes. Controlling these combustion processes is a key method to reduce soot production. There has been much interest in better understanding soot formation and methods of soot reduction. Soot reduction would benefit the health of those exposed to soot, for instance, ground crews working at the airport or on aircraft carriers. The moment a jet takes off, the engine thrust and fuel consumption rate are at maximum. As a result, soot emissions also are at maximum, and ground crews are exposed to high levels of soot in the exhaust gas from jet engines. Short- and long-term health effects of this exposure are serious concerns, and a means of reducing soot in turbine engines is of

great interest. While the performance of the engine is preserved at an optimum, suppression of malignant soot emissions is most desirable. One approach to achieve this is to increase the temperature of the combustion process, resulting in promotion of soot oxidation. Another way is to raise the local air-to-fuel ratio. However, these methods have shown the disadvantage of increasing the amount of NO_x formed. As a potential solution, soot suppression via fuel additives is an alternative area for exploration.

1.1 Soot Formation

Soot composed of carbonaceous particles is usually observed in flames and fires as orange luminescence during combustion of hydrocarbon fuels. Soot particles are mostly found as agglomerates of primary particles typically no larger than 500\AA . The hydrogen to carbon ratio in soot ranges between 1:8 and 1:10. Physical characteristics of soot are described in detail by Palmer and Cullis (1965:p265).

The carbon formed in flames generally contains at least 1% by weight of hydrogen. On an atomic basis this represents quite a considerable proportion of this element and corresponds approximately to an empirical formula of C_8H . When examined under an electron microscope, the deposited carbon appears to consist of a number of roughly spherical particles, strung together rather like pearls on a necklace. The diameters of these particles vary from 100 to 2000\AA and most commonly lie between 100 and 500\AA . The smallest particles are found in luminous but nonsooting flames, while the largest are obtained in heavily sooting flames.

A size distribution of individual soot particles is well modeled by a log-normal distribution (Haynes *et al.* 1981). The average diameter of soot particles corresponds to about one million carbon atoms. Figure 1-1 shows typical soot images taken as part of this study by transmission electron microscopy (TEM) at two magnifications.

Soot formation is a kinetically governed process consisting of fuel pyrolysis and oxidation reactions, formation of the first ring (benzene) and then polycyclic aromatic hydrocarbons (PAH), inception of the first particles, growth of soot particles due to

reactions with gas phase species, particle coalescence, agglomeration and finally oxidation. Figure 1-2 illustrates the soot formation process showing stages of formation on molecular and particulate scales (Bockhorn 1994). However, the process of soot formation has been more generally classified according to the four stages summarized below.

1. Formation of soot precursor molecules
2. Particle nucleation, coagulation and growth
3. Particle agglomeration
4. Soot oxidation.

Sooting characteristics of a flame are complex due to the possible multiple mechanisms of soot formation. Thus, an understanding of the process of soot formation is fundamental to the study of soot reduction in flames and practical combustion systems.

1.1.1 Formation of Soot Precursor Molecules

Soot precursor species, most likely polycyclic aromatic hydrocarbons (PAH), are formed in the first stage of soot formation. These species act as nucleation sites for the formation of soot. It is presumed that this stage is the rate-limiting step in the soot

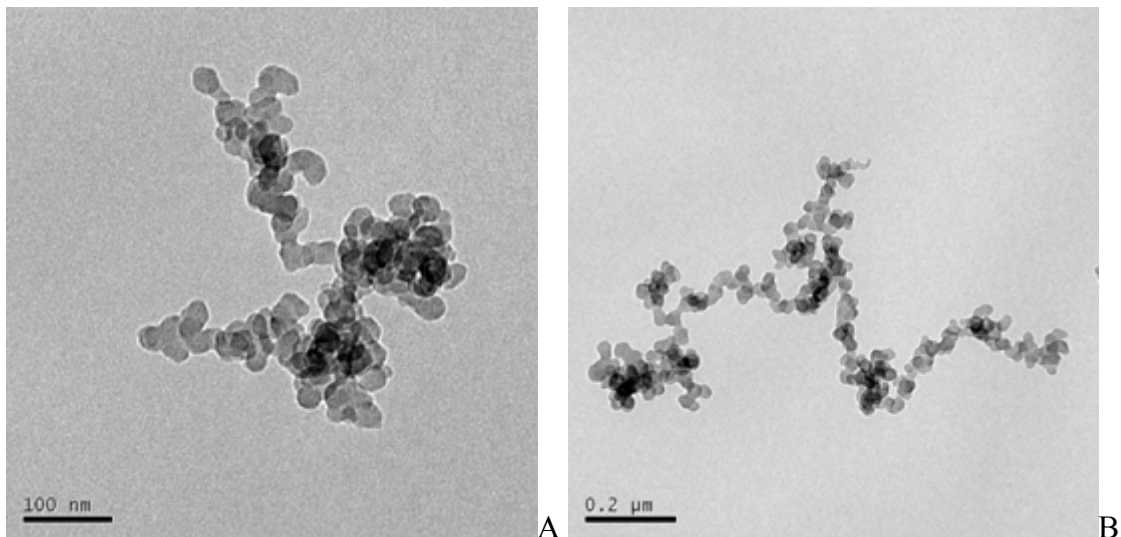


Figure 1-1. Transmission electron microscope (TEM) images of soot aggregates from isooctane combustion. A) At 100 nm scale. B) At 0.2 μm scale.

formation, and chemical kinetics play an important role in this stage. Numerous chemical mechanisms have been proposed to describe the formation of these nucleation sites. All of these mechanisms generally involve small aliphatic (open chained) compounds that form the first aromatic rings, typically benzene, C_6H_6 . Acetylene, C_2H_2 , is the most abundant aliphatic compound to initiate this process in the early stages of

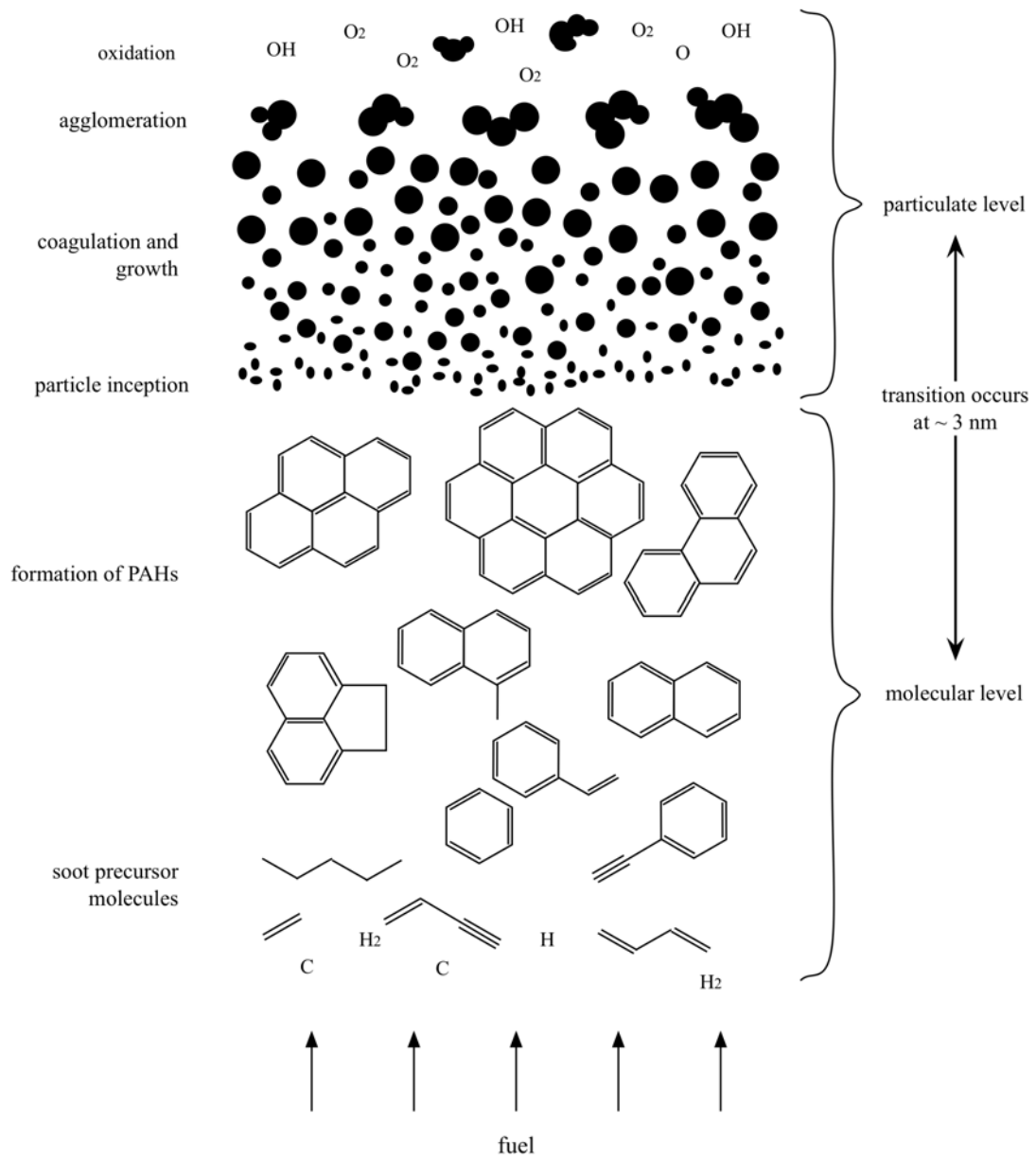


Figure 1-2. Soot formation. Adapted with permission from a reference (Bockhorn 1994).

combustion, and benzene leads to the production of more complex PAHs in the later stages (Frenklach 2002). One proposed mechanism is an even-carbon-atom pathway that involves the addition of acetylene to $n\text{-C}_4\text{H}_3$ and $n\text{-C}_4\text{H}_5$ (Equations 1-1 and 1-2).



It is proposed based on kinetic simulations of shock-tube acetylene pyrolysis that the reaction in Equation 1-1 plays an important role in forming the first aromatic ring (Frenklach *et al.* 1988). Moreover, the reaction in Equation 1-2 suggested by Bittner and Howard (1981) is an important pathway to aromatic ring formation at low temperatures. On the other hand, Miller and Melius (1992) suggested an odd-carbon-atom pathway via combination of stable hydrocarbon radicals like propargyl radicals,



They insisted that $n\text{-C}_4\text{H}_3$ and $n\text{-C}_4\text{H}_5$ are converted into their corresponding resonantly stabilized isomers very rapidly; thus, their concentrations would not be adequate so that it could significantly impact the formation of aromatic ring. However, recent Monte Carlo theoretical studies predicted the higher stability of $n\text{-C}_4\text{H}_3$ radical and $n\text{-C}_4\text{H}_5$, supporting rather the even-carbon-atom pathway described by the reactions in Equations 1-1 and 1-2 than the odd-carbon-atom pathway.

Another possible pathway for the initial ring formation is a combination of two reactant types, highly stable propargyl radical and the most abundant acetylene, to form a cyclopentadienyl radical by



The cyclopentadienyl radical is then rapidly converted benzene. By means of comparing reaction rates of Equation 1-4 with that of Equation 1-3, the reaction of Equation 1-4 is predicted to proceed faster than that of Equation 1-3 by a factor of 2 to 10^3 (Frenklach 2002). It implies that the reaction 1-4 plays a dominant role in forming the first aromatic ring. In addition to these pathways reviewed above, many others have been proposed to characterize the initial stage of soot formation, but have not been widely accepted. Soot inception is regarded as the most critical stage in soot formation, and is subject to perhaps the greatest debate.

1.1.2 Particle Coagulation and Growth

The transition from molecular to particle properties occurs in the second stage of soot formation, namely particle coagulation and growth. This transition occurs at a molecular weight of about 10^4 amu corresponding to an incipient soot particle diameter of about 3 nm. In this stage, soot particles collide with each other forming larger spherical particles. This is called the process of coagulation, which dominates the early soot particle growth. The size of particles increases while the particle number density decreases in the coagulating process. Coagulation is limited to very small particles, on the order of ~18 nm or less.

Aromatics play a role in growth toward soot particle, as gas phase species are attached to the surface of a particle and become incorporated into the particulate phase. Frenklach (2002) described this mechanism with a process of H-abstraction- C_2H_2 -addition (HACA), in which H atoms are abstracted from aromatic compounds, and gaseous acetylene is incorporated to bring on growth and cyclization of PAHs. The process of H-abstraction- C_2H_2 -addition is described by



where the notation A_i is an aromatic molecule with i peri-condensed rings, and A_{i-1} is its radical. The repetitive reaction sequence of two principal steps in Equations 1-5 and 1-6 implies abstraction of a hydrogen atom from the reacting hydrocarbon by a gaseous hydrogen atom, and the formation of the radical site by adding a gaseous acetylene molecule respectively. Figure 1-3 represents an example of the aromatics growth via the process of H-abstraction- C_2H_2 -addition that H abstraction from a biphenyl molecule and the subsequent addition of acetylene.

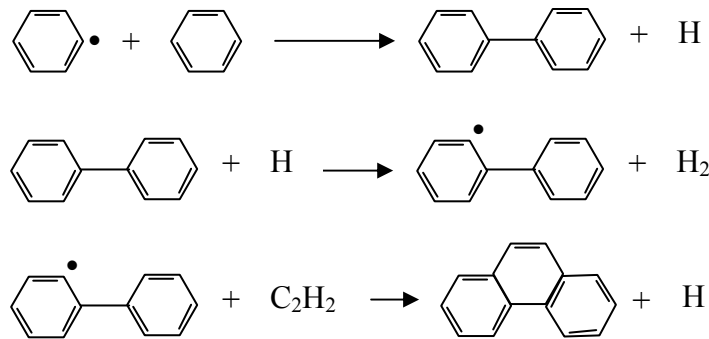


Figure 1-3. The H-abstraction- C_2H_2 -addition mechanism acting on a biphenyl molecule.

A biphenyl molecule is formed in the pyrolysis of benzene, a H atom is abstracted from a biphenyl molecule, and the subsequent addition of acetylene occurs. It is possible for the growth of aromatic compounds to occur via different mechanisms specific to the fuel and flame conditions; however, using numerical simulations Frenklach *et al.* (1988) showed that these alternate methods quickly relax to the acetylene-addition mechanism.

A process of HACA is sustained until the H atom concentration or the number of active sites on the soot particle surface reduces in this stage. Eventually, the surface

growth rate of soot particles declines and subsequently particle growth via these mechanisms ceases. Such phenomenon is termed soot surface aging. It was originally believed that the depletion of growth species was responsible for this phenomenon. Recently, it is now believed that a decrease in the surface reactivity of the soot is the main cause for the reduction of soot surface growth rate although it is not even fully understood how the soot particles lose surface reactivity (Harris *et al.* 1983). To support the theory, it is proposed that the decay of soot surface reactivity is strongly connected to increase in the ratio of C to H atoms in the soot (Harris *et al.* 1983, Haynes *et al.* 1979). By describing the proposal in a chemical sense, the surface reactions depend on a radical site formed by the abstraction of a H atom. Meanwhile, in physical sense, if it is assumed that the hydrogen in the particle is contained only at the edges of the aromatic ring, it can be seen that the C to H ratio will increase as the particle grows. As a result, the number of possible growth sites decreases. It is incomplete to fully characterize the decay of soot surface reactivity with this method. Both these chemical and physical effects would lead to a direct proportionality between the H to C ratio and surface reactivity with this model; however, the C to H ratio decays 2 to 3 times more slowly than the surface reactivity (Dasch 1985). The molecular details underlying the decay of the soot surface reactivity are under investigation to better understand this mechanism.

1.1.3 Particle Agglomeration

When the viscosity of the particles increases past a critical value due to dehydrogenation of the condensed phase, coagulation transitions into chain-forming collisions (Prado *et al.* 1981). This is the third stage of soot formation, that is, particle agglomeration. When individual soot particles collide, they stick to each other leading to fractal aggregates. Contrary to particle coagulation, the particles still preserve their

original identity in agglomeration. Soot aggregates have been analyzed in terms of fractal geometry. The fractal dimension, discussed in detail later, determined in numerous flames seems to be confined to a rather narrow range, namely 1.7-1.8. Individual aggregates of soot particles generally contain 30-1800 primary particles and are well characterized by a log-normal size distribution (Warnatz *et al.* 2001). Figure 1-4 elucidates the difference between coagulation and agglomeration.

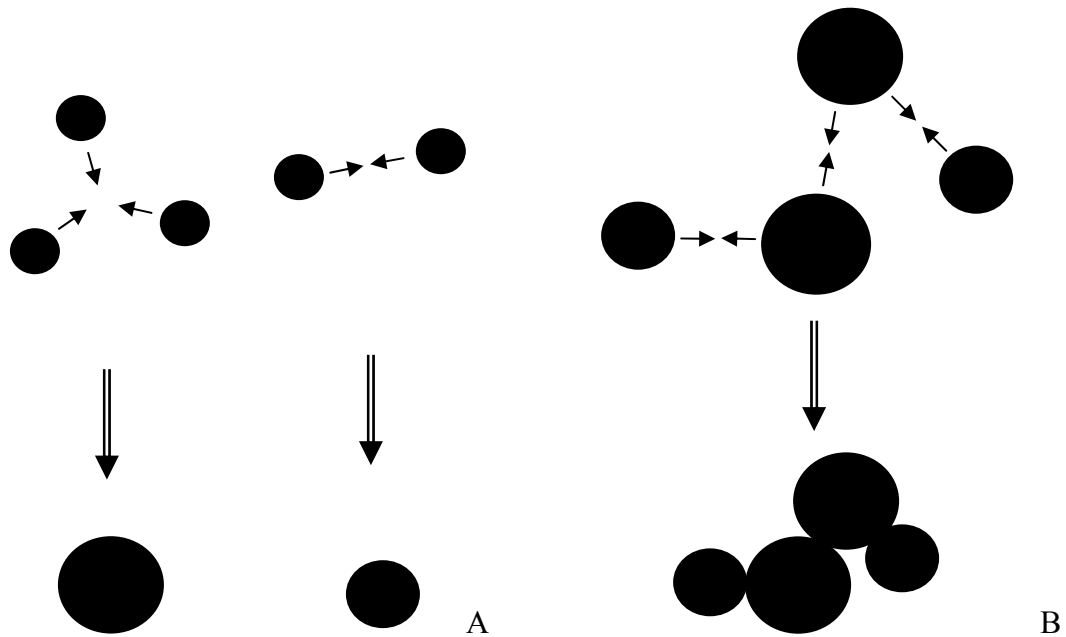


Figure 1-4. Two processes of particle growth. A) Particle coagulation. B) Particle agglomeration.

1.1.4 Soot Oxidation

Soot oxidation also called burnout, the final stage in soot formation, takes place at near the outer radii and the flame tip as oxygen diffuses into the combustion zone. In this stage, the soot particles are partially or completely broken down, which yields CO or CO₂ as a product. Oxidants in soot destruction are O atoms and OH radicals as well as O₂. According to studies by Warnatz *et al.* (2001), the concentration of O atoms is relatively low compared with that of other oxidants in sooting flames. Consequently, the

probability of reactions between O atoms and soot is also low. Therefore, it is assumed that OH radicals and O₂ are primarily responsible for the oxidation of soot particles (Warnatz *et al.* 2001).

A major source of soot is flames, which may be considered as either premixed or diffusion (or non-premixed) flames. In a premixed flame, fuels are premixed with oxidizers at the molecular level before any significant chemical reaction occurs. This type of flame is typically observed in Bunsen burner as well as the spark-ignition engine. This type of flame may have insignificant oxidation of soot because most of the oxidizers are consumed before soot particles are fully-grown. In a diffusion flame, the reactants are initially separated, and then they are mixed and react only at the interface between the fuel and oxidizer. A classic example of a diffusion flame is a candle. Soot oxidation in the diffusion flame is predominantly noticeable at higher flame heights as oxygen diffuses into the combustion regime and encounters mature soot particles. Therefore, the stages of soot formation can be divided more distinctly in the diffusion flame (Turns, 2000). Figure 1-5 shows soot formation regimes in a diffusion flame, the axial soot concentration profile at the center of the flame, and the radial soot concentration profile at an arbitrary flame height. It can be seen that small quantities of soot are present in the inception regime while peak formation occurs in the growth regime.

1.2 Soot Suppression with Transition Metallic Additives

A wide variety of metallic additives in fuels has been studied to determine their effects on soot formation in many practical and laboratory scale combustion systems. In common, the alkali, alkaline earth and main transition metals have been used as fuel additives to control soot emission. Common metallic additives are summarized in Table 1-1.

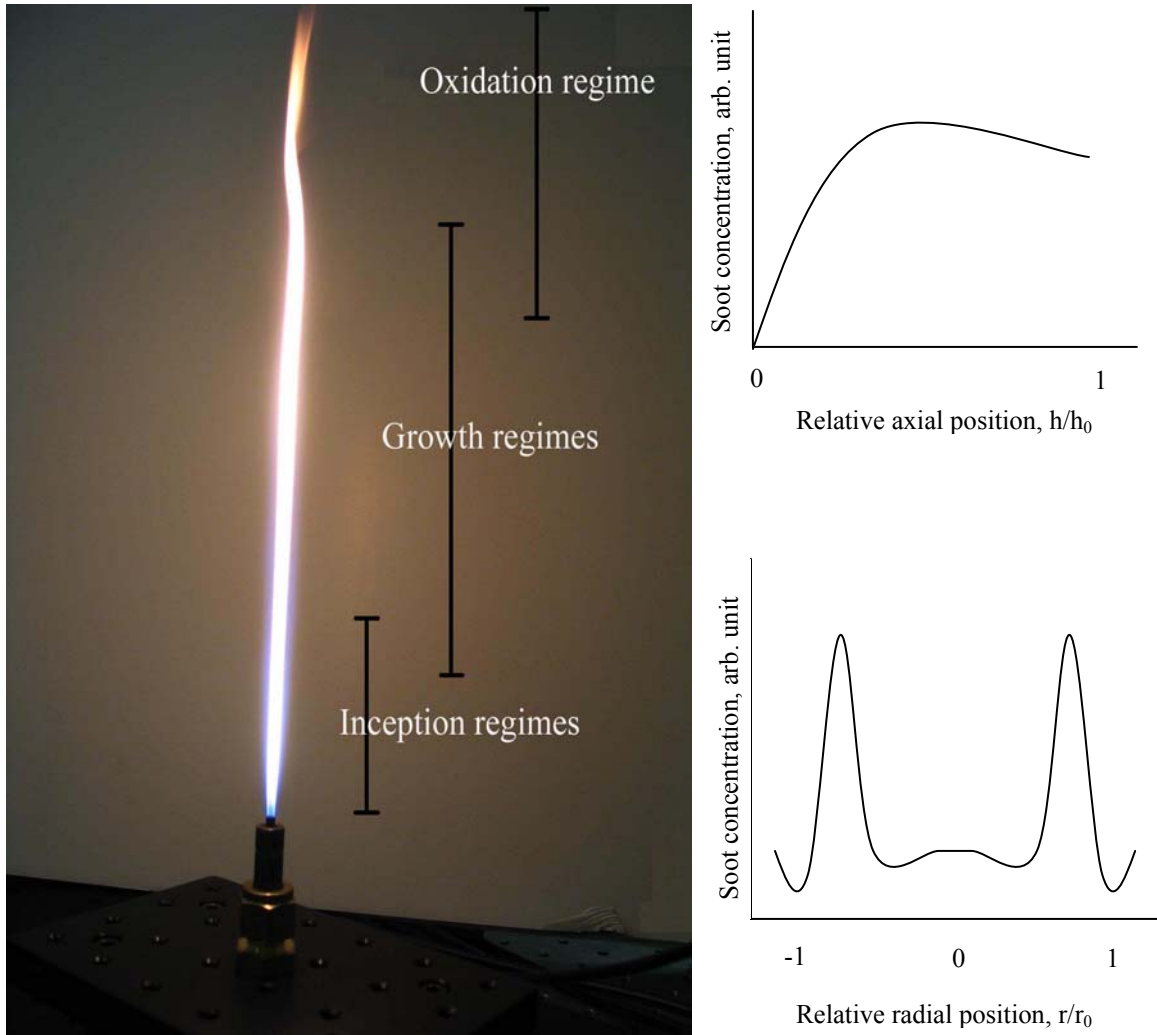


Figure 1-5. Soot formation regimes in a diffusion flame, the axial soot concentration profile at the center of the flame, and the radial soot concentration profile at an arbitrary flame height.

Table 1-1. Metallic additives in common.

Alkali	Li, Na, K, Rb, Cs
Alkaline earth	Mg, Ca, Sr, Ba
Transition	Fe, Mn, Cr, Ni

The mechanism of action of metallic fuel additives have been outlined in three different theories. Firstly, the fuel additive may affect nucleation mechanisms of soot formation in the early stage of soot particle inception. Secondly, the additive may enhance soot burnout as a result of rapid elimination of soot precursors attributed to

increase in hydroxyl radicals. Thirdly, the additive may accelerate the soot oxidation rate by occlusion within the soot phase. Obviously, all three mechanisms may be closely interrelated. The global and local effects of transition metallic additives were evaluated in many studies using a variety of techniques from simple visual observations to novel laser diagnostic measurements. The review conducted in this section will be limited to the key studies of transition metallic additives in premixed and diffusion flames. In spite of the same type of combustion conditions, many studies often have yielded different conclusions.

1.2.1 Manganese-Based Additives

Linteris *et al.* (2002) reported soot reduction effects of manganese and tin containing compounds by analyzing the burning velocity of methane/air flames. Greater than 50% reduction of the burning velocity was shown in the seeded flame. In comparisons of the reduction efficiency with other suppressants, manganese-based additives showed about a factor of two less than that of iron pentacarbonyl, but twice as effective as bromine-based additives.

This result is supported by a study of Wei and Lee (1999), who pyrolyzed polystyrene with manganese in a laboratory quartz reactor. Although results from several measurements varied slightly relying on the different conditions, overall 40% of reduction was obtained in the pyrolysis reaction with manganese. They concluded that the addition of manganese sulfate into the high temperature pyrolysis of PS inhibited the formation of PAHs in the reaction.

However, Feitelberg *et al.* (1993) found an adverse effect, namely that the additive increased soot volume fraction by approximately 50% in a study of a premixed ethylene flame seeded with manganese added in 140 ppm concentrations. They expected that

manganese would exist in the gaseous phase as free metal atoms at high temperatures and form solid MnO through precipitation at residence times.

Hayhurst and Jones (1989) also investigated the effects of metallic additives on ionization in premixed acetylene/oxygen/argon flames. It was found that manganese addition did not affect ion concentrations and soot particle size due to their relatively high ionization potentials that leads to the low rates of soot nucleation and particle growth. Consequently, they made a conclusion that manganese had no inhibition effect on soot production rates.

1.2.2 Iron-Based Additives

While manganese is a known neurotoxin, iron has relatively low toxicity; therefore, many combustion applications and laboratory studies have concentrated on the iron based additives such as ferrocene $[(C_5H_5)_2Fe]$ and iron pentacarbonyl $[Fe(CO)_5]$. In many studies, they have been shown to be highly effective soot suppressants (Bukewicz *et al.* 1974, Feitelberg *et al.* 1993). Iron pentacarbonyl was selected in this research to study the effects of the iron on a laminar prevaporized isooctane/oxygen diffusion flame. It is an organometallic solution that is soluble in liquid isooctane, allowing for a simple means of regulating and delivering the dopant to the combustion system before vaporization of the fuel. This factor makes iron pentacarbonyl an ideal additive for this study.

1.2.2.1 Additives in premixed flames

In a study of a laminar premixed ethylene flame seeded with 0.015-0.46% ferrocene by weight of the fuel, Ritrievi *et al.* (1987) studied the effects of the addition of ferrocene, $Fe(C_5H_5)_2$, on inception and growth of soot particles. As particles moved from inception to growth regime, an increase in the diameter of soot particles in both seeded and unseeded flames was observed, and the diameter of initial particles in the seeded

flames was smaller, whereas final particles had a larger diameter than those in the unseeded flames. Contrary to the size, the number density of particles in both flames was reduced with height. The same trend on number densities was observed in the previous work achieved by Haynes *et al.* (1980). As for the volume fraction of soot, indiscernible change was shown at early residence time for both flames, and the final volume fraction was greater in the seeded flame at all the times. In addition, the spatial profile of the elements iron and carbon in the soot particles was determined with Auger electron spectroscopy. They found that the soot particles consisted of dense iron at the core and a thick carbon-rich layer at the outer surface. Mossbauer spectroscopy was used to determine the chemical state of the iron in the particles, and iron oxide, FeO, was found to be the stable species on the given flame conditions. It is noted that all analysis was done with sampled (i.e. extracted) soot particles.

In order to account for the different behaviors of particle inception and growth shown for the seeded and unseeded flames at an early residence time, they proposed a hypothesis that FeO homogeneously nucleated early in the seeded flame, prior to soot particle inception. This was able to illustrate the behaviors and the stratification of the soot particle at an early residence time in the seeded flame very well. Additionally, they concluded that the carbon deposited on the particles was used for the direct reduction of FeO to metallic Fe. The consumption of carbon at the surface resulted in slower growth rates at the earlier growth region of the seeded flames and indicated that FeO is relatively less active in the later soot growth region. However, the catalytic effect of iron in the later residence time had an influence on growth of the particle surfaces.

Feitelberg *et al.* (1993) also found that the additives increased overall soot formation in studies of a laminar premixed ethylene flame seeded with ferrocene. Iron was added to the fuel in 200 ppm concentrations by a molar basis. Overall, the soot volume fraction in seeded flame increased three times at later residence time, and particle size also increased with increasing residence time. This agreed well with Ritrievi's conclusion (1987). However, they did not find any additive effect on the number density at an early soot inception region, while Ritrievi's group found a significant additive effect.

After analyzing the states of iron additive in the flame, Feitelberg concluded that the iron would initially exist in the gas phase as free metal atoms and precipitate out of the gas into metallic iron form at high temperatures of about 1760 K, or at residence times of around 4 ms. In addition, it was concluded that thermodynamically FeO was not formed in the fuel rich flame, whereas it existed in the seeded flame in the Ritrievi's work. To conclude, the role of the iron additives was not to affect soot particle inception but to increase the rate of gas-solid reactions leading to increase in the total mass of soot. As in Ritrievi's work, they also paid attention on the catalytic effects of iron in the flame with a catalyzed acetylene addition model, and concluded that the iron additive played a role as a catalyst to carbon deposition via acetylene which increased the final particle size.

Hahn (1992) assessed the role of iron pentacarbonyl, $\text{Fe}(\text{CO})_5$, in a premixed propane/oxygen flame with a fuel equivalence ratio of 2.4. Iron pentacarbonyl was added in concentrations of 0.32% by weight of iron to the fuel. The lower regions of the flames were not evaluated due to the limitation of *in situ* photocorrelation measurements.

Within all regions of the flame studied, the iron additive had an effect to increase the overall amount of soot in the flame. That is, the size, number density of soot particle and a volume fraction in the seeded flame were greater than those in the flame without the additive.

Even though *in situ* analysis was not carried out, the state of the iron in sampled particles was experimentally assessed using X-ray photoelectron spectroscopy rather than using prediction models. In this analysis, it was found that the form of iron oxide, Fe_2O_3 , was a dominant species in the extracted soot particles. Contrary to Ritrievi's conclusion or Feitelberg's analysis, significant quantities of elemental Fe or other iron oxide, FeO, were not identified in this study.

They hypothesized that the role of the metal additives on the reduction of soot emission is to accelerate soot oxidation rate in the burnout zone (Cotton *et al.* 1971, Hahn 1992). This region is not present in premixed flames; therefore, the full effect of the metal additive could not be seen. The foregoing studies of premixed flame have demonstrated that metallic additives made an increase in overall soot emission by either the catalytic effect of the metal in the later residence time, or acting as soot nucleation sites in the inception region. A complementary picture of the effect of additives can be investigated with the addition of the burnout regime in diffusion flames.

1.2.2.2 Additives in diffusion flames

In addition to premixed flame studies, there are a lot of soot suppression studies using iron based additives in diffusion flames. Bonczyk (1991) studied the effect of an additive on soot production with a pre-vaporized isooctane/air diffusion flame seeded with ferrocene added in 0.3% by weight of fuel. In this study, he observed an increase in the diameter, the number density of particles, and volume fraction in both seeded and

unseeded flames in the regime close to the burner lip. In the burnout regime of the flames, these parameters however, decayed rapidly in the seeded flame while those kept slightly increasing in the unseeded flame. This net effect of soot reduction was visually noted as well when the smoke plume existing in the unseeded flame completely disappeared in the seeded flame. Soot samples were collected post-flame and subjected to an Auger-type chemical analysis so that the species of iron present in the soot could be determined. From the Auger data, it was found that a condensate from the seeded flame with 0.3% ferrocene was determined to be Fe_2O_3 containing only negligible amounts of carbon. In contrast, the condensate was carbon retaining less than 2% of elemental iron when the percentage of ferrocene in the fuel was reduced to under 0.001%.

Bonczyk concluded that the metal additive contributed to not only soot enhancement in soot inception zone but also soot reduction in burnout zone. With respect to a qualitative illustration on the soot enhancement by additive in the early residence time, he supported conclusions of Cotton and Ritrievi that soot enhancement was a result of an increase in nucleation sites provided by solid Fe_xO_y particulates and an increase in the surface activity of particles resulting from a catalytic effect of iron on the carbon deposited on the surfaces of soot particles. The required Fe is produced by the reaction in Equation 1-7,



The presence of the metal additive enhances the soot reduction in the burnout zone as well. Iron oxide catalytically reinforces the removal of carbon by molecular oxygen, but this requires the iron metal to diffuse through the soot matrix to the surface and its subsequent oxidation by



In the combination of two reactions above, the net effect of carbon oxidation due to the metallic additive is expressed as



In short, the additive enhances carbon oxidation, and the result is a net reduction of soot in the burnout zone.

The similar tendency of soot reduction via addition of ferrocene into ethylene coflowing diffusion flame was found by Zhang and Megaridis (1996). Ferrocene seeding accelerated soot inception, but enhanced soot oxidation in the tip of the flame. The soot volume fraction of the seeded flame was about an order of magnitude less than that of the unseeded flame. Besides, ferrocene affected the primary particle size at the flame terminus so that 33% net reduction of soot was observed between the unseeded and seeded flames. Kasper *et al.* (1999) also reached the same conclusion in a study with ferrocene seeded methane/argon and acetylene/argon flames. The soot production rate of seeded flames was higher at the early residence time due to an increase in the surface of soot, but lower at the later residence time attributed to efficient soot oxidation by catalytic means of the additive.

1.3 Studies of the Fractal Properties and the Structure of Soot Aggregates

Numerous studies concerning the physical properties of soot aggregates have been reviewed by many researchers. A research group led by Faeth has performed numerous work on fractal and structure properties of soot aggregates using Rayleigh-Debye-Gans (RDG) scattering theory (Köylü *et al.* 1994&1995a&b, Farias *et al.* 1995, Wu *et al.* 1997,

Krishnan *et al* 2000&2001). They accomplished it with both gaseous (acetylene, ethylene, propylene, and butadiene) and liquid fuels (benzene, cyclohexane, toluene, and n-heptane) for a variety of flame conditions, for example, laminar and turbulent flames, as well as premixed and diffusion flames. Through their diverse works, it was concluded that fractal properties of soot aggregate are relatively independent of fuel type, flame condition, and position. They obtained a fractal dimension of 1.82 and a fractal prefactor of 8.5, with experimental uncertainties (95% confidence) of 0.08 and 0.5, respectively. Fractal theory is discussed in detail below. They also carried out numerical simulations to create soot aggregates based on cluster-cluster aggregation. They computationally evaluated RDG theory for the optical properties of soot using the Iskander-Chen-Penner (ICP) approach in small scattering angle regime and compared the results from the ICP approach with those from RDG theory. The results were in good agreement within numerical uncertainties. Fractal parameters used for the simulation in their study were D_f of 1.75 and K_f of 8.0 based on their proceeding information. In another study, they measured soot composition, density, structure, gravimetric volume fraction, and scattering and absorption properties for wavelengths between 350 and 800 nm in the fuel-lean region of buoyant turbulent diffusion flames fueled with acetylene, propylene, ethylene, and propane burning in still air. Then they analyzed these data to find soot fractal dimensions, refractive indices, refractive index functions, and dimensionless extinction coefficients using Rayleigh-Debye-Gans scattering for polydisperse mass fractal aggregates (RDG-PFA theory). They found both soot fractal dimensions of 1.77 in average and dimensionless extinction coefficients of 5.1 in average with a standard deviation of 0.04 and 0.5 respectively.

Kim and Choi *et al.* (1999&2003) measured the fractal properties of silica aggregates generated in hydrogen/oxygen coflow diffusion flame using light scattering, thermophoretic sampling and TEM observation. They also invented an *in situ* laser light scattering method for line measurement of aggregate size and shape, and applied it for the measurement of silica aggregates produced in a methane/air premixed flat flame. The mean radius of gyration and fractal dimension of 1.7 were obtained and examined based on the RDG scattering theory for fractal aggregates.

Wang and Sorensen (2002) compared scattering cross sections of fractal aggregates predicted by using RDG scattering theory with those that measured in an experiment and found a good agreement. For fractal aggregate aerosols of SiO₂ and TiO₂ formed fractal aggregates by diffusion-limited cluster aggregation, the fractal dimensions were roughly 1.75 and the number of primary particles per cluster was approximately 150.

Mountain and Mulholland (1988) simulated the growth of smoke agglomerates using the computer simulation technique of Langevin dynamics. In this study, 48 aggregates comprising between 10 and 687 primary particles per cluster were created to characterize soot agglomerates and calculate the light scattering from these agglomerates. The structural information and the results of the calculation were then used to obtain the fractal properties such as the primary particle size, the radius of gyration and the fractal dimension. In short, they discovered the fractal dimension of 1.9 and the fractal prefactor of 5.8.

Dobbines and Megaridis (1991) investigated the absorption, scattering, and differential scattering cross sections for polydisperse fractal aggregates with the prescribed fractal dimensions from 1.7 to 1.9 and uniform primary particle size.

Köylü and coworkers (1995a&b) determined the fractal properties for carbonaceous soot and Al_2O_3 (alumina) agglomerates created from various flame conditions using angular light scattering (ALS) and thermophoretic sampling followed by analyzing transmission electron micrographs. Both procedures yielded the fractal dimension of 1.7 with the standard deviation of 0.15 and the fractal prefactor of 2.4 with the standard deviation of 0.4.

Sorensen *et al.* (1995) sampled soot aggregates from a premixed methane/oxygen flame using thermophoretic sampling and analyzed them with transmission electron microscopy (TEM) method. They obtained the fractal dimension of 1.74.

An analysis with 36-aggregate samples of overfire soot from a laminar acetylene flame reported by Samson *et al.* (1987) yielded the fractal dimension of 1.4. However, it was regarded that the value was much skewed due to the lack of the number of samples.

Sorensen (2001) reviewed scattering and absorption of light by fractal aggregates and concluded that the aggregates typically have the fractal dimension of approximately 1.75. Fractal dimensions determined from various sources are summarized in Table 1-2. Even though the values of fractal dimension tabulated in Table 1-2 vary slightly depending on different measurement techniques and flame conditions, the main fractal properties of soot are generally considered to be independent of the fuel and the flame conditions.

1.4 Spectroscopic Method

For identifying the state of the metallic additive without perturbing the characteristics of the flame, the most effective method is to use an *in situ* spectroscopic method. Having an advantage of high sensitivity, Laser-induced fluorescence has been

Table 1-2. Fractal dimension of various aggregates.

Investigator	Fractal dimension	Condition	Method
Faeth et al.	1.82	soot from laminar and turbulent diffusion flames	TEM
	1.73~1.85	soot from various hydrocarbon fuels flame	scattering and extinction measurements
	1.75	general soot aggregate	computer simulation
Wang et al.	1.75	aerosols of SiO ₂ and TiO ₂	Light scattering
Choi and Kim	1.77	silica aggregates generated in hydrogen/oxygen coflow diffusion flame	Light scattering and TEM
	1.7	silica aggregates produced in a methane/air premixed flat flame	
Mountain et al.	1.9	smoke	computer simulation
Dobbines and Megaridis	1.62, 1.74	soot from laminar ethylene	TEM
Cai et al.	1.74	soot aggregates from a premixed methane/oxygen flame	TEM
Sorensen	1.75	general aggregate	Review
Samson et al.	1.4, 1.47	soot from laminar ethylene	TEM
Köylü et al.	1.75, 1.86	soot from various laminar and turbulent diffusion flames	Angular light scattering
	1.54~1.73		TEM

widely used for measuring the concentration and temperature of gaseous phase species in combustion flows.

Planar laser-induced fluorescence and Rayleigh/Mie imaging measurements were conducted to investigate the mechanisms of particle formation from gas phase species in a CH₄/O₂ premixed flame seeded with iron carbonyl (McMillin *et al.* 1996& Biswas *et al.* 1997). A XeCL excimer-pumped dye laser operating in 5 mJ pulse energy was used for FeO PLIF. While the excitation laser was being scanning from 558.5 nm to 561.0 nm, the fluorescence was monitored near 586 and 618 nm with PMT and boxcar averager. They found that the concentration of vapor phase FeO rapidly rises at the flame cone (i.e.

primary reaction zone) and FeO plays a role as precursors. To validate the experimental results, they developed a discrete sectional model which accounted for precursor vapor concentrations and particle growth process. The simulation was in good agreement with the experiment.

Son *et al.* (2000) conducted photolysis-probe experiment to generate the ground state FeO molecules which were detected by LIF method. By means of directing an unfocused weak UV laser beam into the mixture of Fe(CO)₅/(O₂ or N₂O)/(He or Ar), they created ground-state FeO molecule. The wavelength of the laser was in the range between 298 and 320 nm, and laser pulse energy of 0.5 ~ 1 mJ/pulse was used for photolysis. Then the fluorescence at 623.6 nm was detected when the FeO molecule was excited by a wavelength of 591.1 nm.

Telle *et al.* (2001) combined LIF with LIBS to detect elements in non-accessible environment. They performed a parametric study with the combination of LIF and LIBS to investigate analytical selectivity and sensitivity, and concluded that the combined technique is better than LIBS alone in sensitivity and selectivity.

Nguyen *et al.* (1996) invented a combination of Raman-Rayleigh scattering and LIF to measure temperature and the concentration of NO in a methane-air premixed flame under three different operating conditions. Two frequency-doubled Nd:YAG-pumped dye laser systems were employed for NO LIF. Then, the quenching was corrected with information from Raman-Rayleigh scattering experiment. They observed that NO concentration reduced as the equivalence ratio increased.

As another common technique, *in situ* Raman spectroscopy has been employed for species identification and quantification. Maslar *et al.* (2000) observed various forms of

iron oxide while investigating corrosion on the surface of an electrolytic iron coupon in air saturated water at a pressure of 25.1 MPa and temperatures from 21 to 537 °C using *in situ* Raman spectroscopy. The excitation source radiation was a 647.1 nm krypton ion laser. The *in situ* Raman spectra were compared with the *ex situ* spectra using the micro-Raman system having the excitation source of 785 nm. In this study, they realized that *ex situ* spectra were similar to the *in situ* spectra taken during cooling but different from those taken during heating.

1.5 Objectives of Present Research

Although the use of fuel additives as soot suppressants has been known for over 40 years and widely studied, the mechanism of action of additives is poorly understood and still a subject of controversy. The primary objective of this project is to quantitatively explore a role of the additive for soot suppression in the flame using the elastic light scattering technique along with thermophoretic sampling followed by transmission electron microscopy (TEM) and *in situ* spectroscopy. In addition, Laser-induced fluorescence spectroscopy (LIF) and *in situ* Raman spectroscopy are used to identify the chemical state of the iron additive in the flame. Finally, numerical simulation is performed to provide additional information on iron species in the flame. As another prevalent scheme, Laser-induced incandescence (LII) is a well-researched technique for analyzing and characterizing sooting flames and combustion processes. LII occurs when a very intense laser beam encounters particulate matter like soot. A soot particle can absorb energy from the beam, which leads an increase in the particle's temperatures of 4000-4500 K. If the energy absorption rate is sufficiently high, the temperature will rise to levels where significant incandescence (essentially blackbody radiation) and vaporization can occur. LII technique was employed as a different approach for

analyzing soot particle in other part of the same research project; however, a detailed treatment of the characterization of soot particles in the context of LII technique is beyond the scope of the present study, thereby, will not be examined in this work.

A laminar prevaporized isooctane/oxygen diffusion flame was invented employing a laboratory scale diffusion burner, and iron pentacarbonyl, $\text{Fe}(\text{CO})_5$ was used as an additive for all researches. Information retrieved from this research will then be used in future application of soot reduction using practical combustion system like a real turbine engine and contribute ultimately to developing a solution to minimize health and environmental problems resulting from soot emission. Below are specific objectives.

1. To determine the differential scattering coefficient using *in situ* techniques of the light scattering and transmission measurements.
2. To evaluate scattering parameters such as the size, number density, and volume fraction of soot particles using Rayleigh-Debye-Gans scattering theory in combination with thermophoretic sampling of soot followed by TEM.
3. To provide some insights into the role of additives by analyzing scattering parameters in the unseeded and seeded flames.
4. To implement *in situ* spectroscopic methods such as LIF and Raman scattering technique to probe the chemical state of iron additives species throughout the flame.

CHAPTER 2 FUNDAMENTAL SCIENCE AND BACKGROUND THEORY

This chapter introduces fundamental theories and background knowledge of the elastic light scattering technique, spontaneous Raman, Laser Induced Fluorescence (LIF) spectroscopy, and electron microscopic schemes. The former techniques are the remarkable diagnostic methods that are nonintrusive and allow analysis of soot formation process in the diffusion flame without intervening in the chemical and physical processes. In addition, the application of each spectroscopic scheme to data analysis is discussed along with any limitations of those theories.

2.1 Elastic Light Scattering Theory

Electromagnetic radiation can interact with a particle in several ways. That is, radiation can be reflected, scattered, absorbed or emitted. These interactions are dependent on the nature of the heterogeneity: the shape of the particle, the material of the particle (i.e., refractive index), its relative size and the clearance between particles. Therefore, a certain particular system can be characterized using the way that electromagnetic radiation interacts with the particles in the system. Information such as size and number density of the particles can be inferred from the scattering response. In this study, elastic laser light scattering was employed to determine the differential scattering coefficients of soot particles in the unseeded and iron seeded flames. The determined parameter will be used to calculate the number density and total volume fraction, in combination with the size of the soot particles obtained from TEM analysis.

Elastic light scattering takes place in the case that an electromagnetic (EM) wave, the incident light, encounters a scattering particle. At the moment the EM waves collide with discrete particle, electrons oscillate within the particle at the same frequency as the incident wave. The oscillation, called an induced dipole moment, is regarded as a source of light scattering. The energy of the incident light is either discharged by light radiation or extinguished by absorption within the particle. When the frequency of the incident light is equal to that of scattered light considered, the process is called elastic scattering. In contrast, Raman scattering is considered an inelastic scattering process. More detailed explanation on Raman scattering will be given later. Figure 2-1 shows the light scattering response to an incident electromagnetic light.

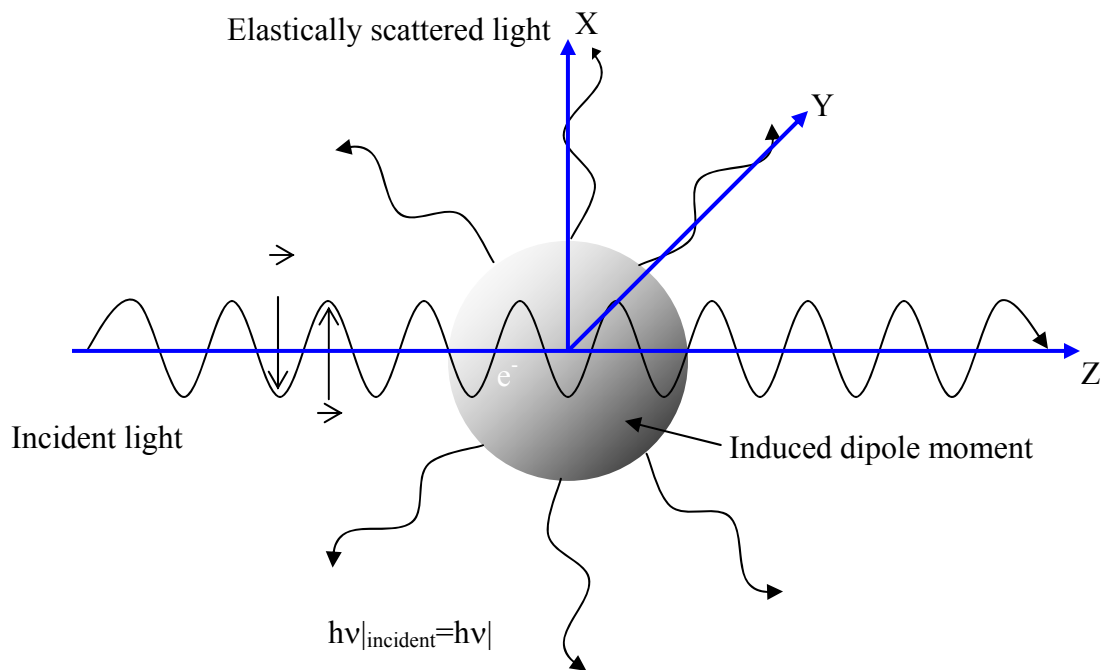


Figure 2-1. Light scattering response to an incident light.

There are two kinds of categories in the elastic light scattering. One is Rayleigh scattering theory that is applied to a system with small, dielectric (non-absorbing) and spherical particles. The other is Mie scattering theory that is used for general spherical

solution without a particular size limit; hence, it can be used for describing most spherical scattering particles, including Rayleigh scattering particles. However, Rayleigh scattering theory is usually used as long as it is applicable due to complexity of Mie scattering solution.

2.1.1 Rayleigh Scattering Theory

A valid scattering solution using Rayleigh theory for a spherical particle may be obtained under the following conditions:

1. The external electric field seen by the particle is uniform
2. The electric field penetrates faster than one period of incident electromagnetic radiation.

These two conditions are satisfied for the case of $\alpha \ll 1$ and $|\bar{m}| \alpha \ll 1$ respectively,

where α is the dimensionless size parameter given by

$$\alpha = \frac{2\pi a}{\lambda}, \quad (2-1)$$

where a indicates the particle radius, and λ is the relative wavelength defined as

$$\lambda = \frac{\lambda_o}{m_o}, \quad (2-2)$$

where λ_o means the incident wavelength in vacuum and m_o represents the refractive index of the surrounding medium. The refractive index, the property of the material is defined as

$$m = n + i\kappa. \quad (2-3)$$

In this Equation, n indicates the common refraction of light while the complex term relates to absorption. The value of κ is not exactly zero for any material, but materials with the value approaching to zero are termed dielectrics. The relative refractive index is defined as

$$\bar{m} = \frac{m}{m_o} . \quad (2-4)$$

The magnitude of the relative refractive index, $|\bar{m}|$ is

$$|\bar{m}| = \frac{(n^2 + \kappa^2)^{1/2}}{m_o} . \quad (2-5)$$

In the Rayleigh regime, the vertical-vertical differential scattering cross section (cm^2/sr) indicated in Equation 2-6 means that both the incident light and the scattered light after the interaction are vertically polarized with respect to the same scattering plane (xy-plane), see Figure 2-1.

$$\sigma'_{VV} = \frac{\lambda^2}{4\pi^2} \alpha^6 \left| \frac{\bar{m}^2 - 1}{\bar{m}^2 + 2} \right|^2 . \quad (2-6)$$

Simply, the horizontal-horizontal differential scattering cross section shown in Equation 2-7 means that both the incident light and the scattered light are polarized parallel to the scattering plane

$$\sigma'_{HH} = \sigma'_{VV} \cos^2 \theta . \quad (2-7)$$

In Equations 2-6 and 2-7, the first subscript means the incident light, and the second subscript means the scattered light. Also, subscripted V and H, respectively, refer to the vertical and horizontal polarization with respect to the scattering plane. Note that the vertical-vertical differential scattering cross section is independent of the observation angle θ , while the horizontal-horizontal differential scattering cross section has a minimum at 90 degrees. The total scattering cross section (cm^2) and absorption cross section (cm^2) are defined as

$$\sigma_{sca} = \frac{2\lambda^2}{3\pi} \alpha^6 \left| \frac{m^2 - 1}{m^2 + 2} \right|^2 \quad (2-8)$$

$$\sigma_{abs} = \frac{-\lambda^2}{\pi} \alpha^3 \operatorname{Im} \left\{ \frac{m^2 - 1}{m^2 + 2} \right\}. \quad (2-9)$$

Finally, the total extinction cross section (cm^2) is defined as a sum of the scattering and absorption cross section, namely,

$$\sigma_{ext} = \sigma_{sca} + \sigma_{abs}. \quad (2-10)$$

As represented in Equations 2-8 and 2-9, the total scattering cross section scales with α^6 whereas the absorption cross section is proportional to α^3 . Compared to σ_{abs} in the Rayleigh regime, σ_{sca} is small enough to ignore the contribution of σ_{sca} to σ_{ext} ; hence, it can be assumed that $\sigma_{ext} = \sigma_{abs}$, for an absorbing particle.

2.1.2 Systems of Particles

The light scattering theory is specifically applied in radiative analyses under the significant assumptions regarding the scattering particle. That is, the particle is assumed to be a single and spherical shape in the system. However, to extend the assumption on the scattering of single particle to a system of particles premises three criteria as elucidated below (Jones, 1979):

1. The particles are spaced far enough to have no electrical interactions between particles.
2. The light does not undergo multiple scattering.
3. There is no optical interference between the scattered waves.

The first criterion is fulfilled if individual particles are placed in a distance of 2 to 3 diameters from one another. The second criterion is met if the optical mean free

pathlength is greater than the optical length of the system. The last criterion is satisfied if a large number of particles are randomly placed in the system. In this case, the total intensity of scattered light can be determined by directly adding the intensities of scattered light from each particle.

There are two types of system of particles: monodisperse and polydisperse. A system containing uniformly sized particles is termed monodisperse. For such a system, the overall scattering and extinction of light from particles can be described by the differential scattering coefficient ($\text{cm}^{-1}\text{sr}^{-1}$) and extinction coefficient (cm^{-1}), which are expressed respectively as

$$K'_{VV} = N\sigma'_{VV} \quad (2-11)$$

$$K_{ext} = N\sigma_{ext} \quad (2-12)$$

where N is the number density of particles (particles per volume).

The transmission is defined as the intensity of the transmitted light through a system of particles per that of the incident light for a particular wavelength, namely,

$$\tau = \frac{I_{transmitted}}{I_o} \quad (2-13)$$

A τ of unity results from 100% transmission of the incident light through a system of particles, whereas a τ of zero results from the entire incident light absorbed and/or scattered by the particles. The relationship between the transmission and the extinction coefficient can be correlated by the Beer-Lambert law, namely,

$$\tau = \exp(-K_{ext}L), \quad (2-14)$$

where L is the optical length. The product $K_{ext}L$ is known as the turbidity, a measure of the ability of the system to extinguish incident light.

The volume fraction f_v is also an important parameter for characterizing the particles in a system. The volume fraction is defined as the volume of particles per unit volume, hence, it is dimensionless. For a monodisperse system, the volume fraction is given by

$$f_v = \frac{\pi}{6} d^3 N, \quad (2-15)$$

where d is the diameter of the scattering particle.

A polydisperse system is characterized by non-uniformly sized particles. A flame is a good example of the system, as the sizes of soot particles can vary throughout the sample region. The primary particle size must be determined to evaluate the scattering and extinction properties of a polydisperse system. This will be discussed in the next section.

2.1.3 Rayleigh-Debye-Gans (RDG) Scattering Theory

As discussed in Chapter 1, the morphological characteristics of soot are to evolve into a fractal structured aggregate. Using either Rayleigh scattering theory or Mie scattering theory itself is not a reliable application here for the large sized and open structured aggregates. Therefore, a new theory is necessary to exam the size and the fractal dimension of soot aggregates. Rayleigh-Debye-Gans (RDG) scattering theory has been found to be a suitable approximation for studying physical properties of soot aggregates.

2.1.3.1 Rayleigh-Debye-Gans (RDG) scattering approximation

RDG theory has been used to interpret light scattering data to determine cluster parameters. Aggregates produced in the later stage of soot formation vary considerably in size and shape while they grow. Physical features of soot aggregate can be defined

using Rayleigh-Debye-Gans (RDG) scattering theory. Regarding physical properties of soot aggregates, this theory has the major assumptions described below:

- The size parameter of primary particles is sufficiently small such that individual primary soot particles satisfy the Rayleigh scattering theory.
- Soot aggregates are composed of mono-disperse nonoverlapping spherical primary soot particles.
- Primary soot particles just touch one another.
- The number of primary particles per aggregate satisfies a lognormal probability distribution function.
- Soot aggregates are mass fractal-like objects with mass fractal dimension of less than 2.

The fractal-like objects can be defined using the following power law relationship, namely,

$$N_{par} = k_f \left(R_g / d_{par} \right)^{D_f}, \quad (2-16)$$

where N_{par} is the number of primary particles per aggregate, k_f is the fractal prefactor, R_g is the radius of gyration of an aggregate, d_{par} is the primary particle diameter, and D_f is the mass fractal dimension implying the openness of the soot aggregate. First of all, evaluation of the fractal properties requires determining optical properties. Not only N but also d_{par} can be directly determined using transmission electron microscopy (TEM) analysis of post thermophoretic sampling of soot aggregates. The radius of gyration then can be calculated using either of two correlations (Köylü *et al.*, 1995a). The first approach is to use only the maximum projected length of the aggregate, L . Alternatively, the radius of gyration can be evaluated using the geometric mean of

maximum length, and the maximum projected width normal to L , W . Two correlations are mentioned below respectively,

$$L/(2R_g) = 1.49, \quad (2-17)$$

$$(LW)^{1/2}/(2R_g) = 1.17. \quad (2-18)$$

With these parameters known, the fractal properties are obtained using a linear regression method with a least squares approach. In other words, when N is plotted as function of R_g/d_{par} in logarithmic scale for a set of aggregates, the fractal dimension describes the “slope”, the fractal prefactor determines the “magnitude” of the least-squares straight line fit to the data.

Determination of the radius of gyration requires more attention because it directly affects scattering properties. The value of R_g based on Equation 2-17 may be somewhat greater than that evaluated in Equation 2-18 unless the aggregate is equilateral shape. As a result, the smaller values of D_f are obtained when Equation 2-17 is used rather than Equation 2-18. To avoid such a conflict, some researchers adopted 1.78 or 1.67 instead of taking 1.49 in Equation 2-17. Even though specific aggregate properties differ for the various flame systems, all the flames yield the same relationship between the number of primary particles in an aggregate and its radius of gyration. Therefore, the fractal properties of aggregates are independent of various positions and flame conditions.

2.1.3.2 Evaluation of the extinction coefficient

The next phase of the present evaluation of RDG theory is to consider absorption and total scattering cross sections. Up to this point, the scattering and extinction coefficients have been assumed spatially constant for a given system. However, in the case of a flame, these parameters may be highly spatially dependent on the system. For

instance, the concentration of soot varies very much based on the location in the system. In particular, determination of the extinction coefficient is required to pay more attention because the transmission data cannot be collected only at representative points to determine it. To better characterize this type of system, the deconvolution techniques have been used if a given system is sufficiently large so that the system can be divided into several concentric regions. These techniques construct information on the radial parameters based upon information in neighboring sections. However, the technique may not be feasible in case a system area is too narrow to be separated into a few sections. In such cases, the extinction coefficient for such cases can be determined using Rayleigh-Debye-Gans scattering theory.

The differential scattering cross section (cm^2/sr) of an aggregate is defined as

$$\sigma'_{agg} = N_{par}^2 \sigma'_{par} S(q), \quad (2-19)$$

while the differential scattering cross section of the primary soot particle in an aggregate σ'_{par} is determined using Equation 2-6 presented above, namely Rayleigh theory.

Subscripts of “agg” and “par” mean an aggregate and the primary particle, respectively.

A new parameter, $S(q)$ shown in Equation 2-19 is called either the structure factor or the angular scattering form factor given differently based on the scattering angle variety.

$$S(q) = 1, \quad qR_g \ll 1 \quad (2-20a)$$

$$S(q) = 1 - q^2 R_g^2 / 3, \quad qR_g \leq 1 \quad (2-20b)$$

$$S(q) = C(qR_g)^{-D_f}, \quad qR_g > 1. \quad (2-20c)$$

Under RDG scattering approximation, the structure factor is nearly unity in the small-angle scattering regime, the so-called Guinier regime. Consequently, scattering mainly

depends upon the number of primary particles in the aggregates. Conversely, the structure factor depends strongly on the values of R_g and D_f in the large-angle scattering regime, the so-called power-law scattering regime. Herein q is the modulus of scattering vector (cm^{-1}) defined as

$$q = \frac{4\pi}{\lambda} \sin(\theta/2). \quad (2-21)$$

The constant C refers to the cutoff of the density at the perimeter of the aggregate, and is approximately unity defined empirically. The total scattering cross section (cm^2) for a fractal aggregate is also expressed as

$$\sigma_{agg}^{sca} = N_{par}^2 \sigma_{par}^{sca} G(kR_g), \quad (2-22)$$

where

$$G(kR_g) = \left(1 + \frac{4}{3D_f} k^2 R_g^2\right)^{-D_f/2}, \quad (2-23)$$

and the total scattering cross section of a single primary particle is simply given by Equation 2-8. Meanwhile, the absorption cross section of an aggregate is defined as

$$\sigma_{agg}^{abs} = N_{par} \sigma_{par}^{abs}, \quad (2-24)$$

where it is assumed that absorption is not affected by aggregation, while the absorption cross section for a primary soot particle is determined by Equation 2-9. Finally, the total extinction cross section for an aggregate is the sum of the total absorption of an aggregate and total scattering cross section of an aggregate by Equation 2-10.

Note that the scattering volume is absolutely greater than that of a typical soot aggregate; thus, a number of soot aggregates are involved in interactions with incident light. The number density of aggregate, N_{agg} in the scattering volume can be calculated

using the differential scattering coefficient, $K'_{VV,agg}$ obtained from the light scattering experiment. That is, the number density of aggregate in the scattering volume is readily determined as

$$N_{agg} = K'_{VV,agg} / \sigma'_{agg} . \quad (2-25)$$

Therefore, the total number density (particles/cm³) in the overall scattering volume is defined as

$$N_{Total} = N_{agg} N_{par} , \quad (2-26)$$

and the extinction coefficient for the overall aggregates in the volume is finally determined using the following Equation,

$$K_{agg}^{ext} = N_{agg} \sigma_{agg}^{ext} . \quad (2-27)$$

2.1.4 Sampling and Analyzing Soot Aggregate

Prior to describing all parameters characterizing morphology of soot aggregate using RDG theory, thermophoretic sampling and analysis by TEM must be implemented. The principle of thermophoretic sampling and instrumentation of TEM will be reviewed in brief.

2.1.4.1 Thermophoretic sampling

Thermophoretic sampling is employed by means of collecting particles with a thin film. As particles move across the temperature gradient existing between the hot flame and the cold mesh, a process known as thermophoretic force causes them to move from the higher temperature of the flame to the lower temperature of the mesh. This temperature gradient is readily established by introducing a mesh initially being at room temperature into the hot flame, and it drives the particles to the surface of the mesh where they are deposited. Recently, thermophoretic deposition has provided a quantitative

understanding of the drift of particles to the surface that is at a lower temperature than the surrounding gases.

2.1.4.2 Transmission electron microscopy

Information about soot aggregates obtained with thermophoretic sampling can be extracted using a high-resolution transmission electron microscope (TEM) equipped with photographic and data recording capabilities. The TEM is an evacuated metal cylinder (the column) about 2 meters high consisting of an electron gun, the illumination system, specimen, and the imaging system. A Ray diagram for TEM is schematized in Figure 2-2. As a virtual source, the electron gun at the top of the microscope emits a stream of monochromatic electrons that travel through vacuum in the column of the microscope. The electron gun has a V-shaped tungsten heating filament that is the cathode emitting electrons. When the cathode is heated, the accelerating voltage of between 40,000 to 100,000 volts is passed between the cathode and the anode placed just below the cathode. By using the high voltage, these negatively charged electrons in the cathode are accelerated to an anode positively charged. The acceleration of electrons depends on the amount of high voltage. Some of electrons passing through a tiny hole in the anode form an electron beam which travels down the column. Electrons are high energy particles so that they could easily have an influence on the interaction with any matter. The interaction causes the emission of all the lower forms of energy such as x-rays, secondary electrons, ultraviolet, and heat energy. As a result, the microscope must be kept in a high vacuum of the order of 133×10^{-8} Pa.

This electron stream is focused to a small, thin, coherent beam by the use of

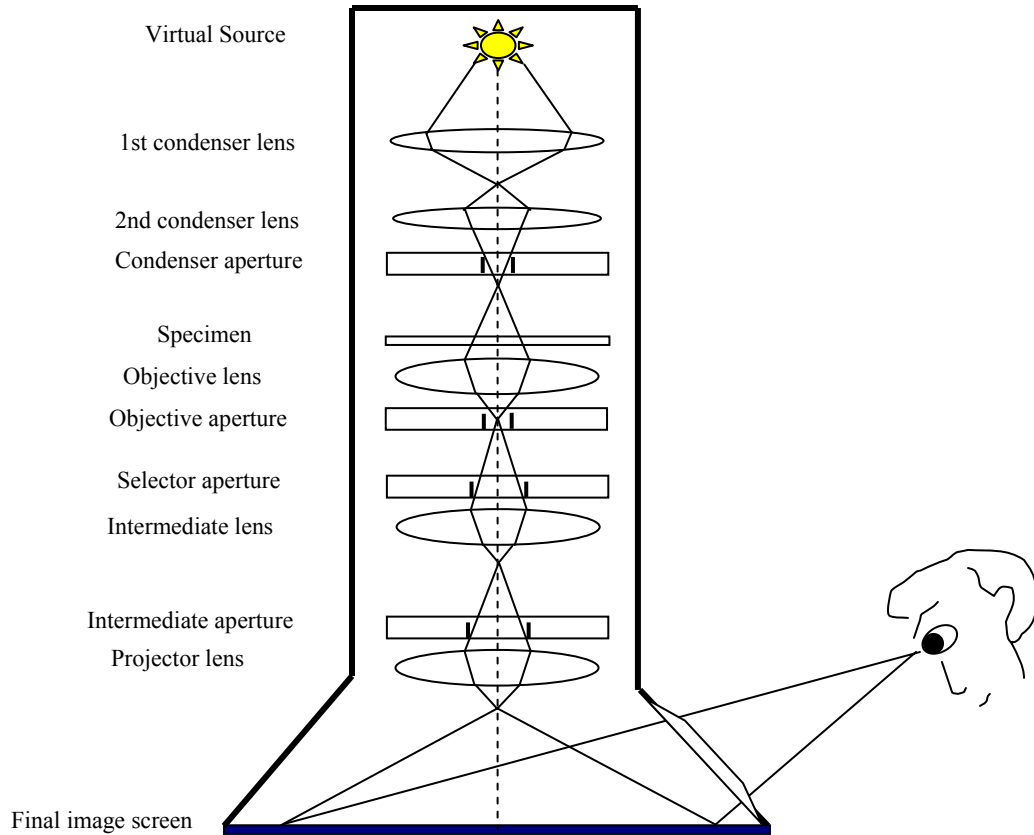


Figure 2-2. Schematic of TEM

condenser lenses. The first lens largely determines the spot size, and the second lens changes the size of the spot on the sample. The beam is restricted by the condenser aperture, blocking out electrons far from the optic axis.

Specimens in the TEM are examined by passing the electron beam through them. Therefore the mass thickness of the specimens must be thin enough (50~100 nm) to allow electrons to pass through them. When the electrons strike the specimen, they are either transmitted or scattered depending on the density of the atoms in the specimen. While some electrons are scattered, others are transmitted and hit a phosphorescent screen placed in the bottom of the microscope. It results in a contrast of the specimens that relies on both diffraction of electrons and the number of the atoms in the specimen. The

higher the atomic number of the specimen, the more electrons are scattered and the greater the contrast.

The electrons transmitted through the specimen are focused by the objective lens onto a phosphorescent screen to form an image. The quality of the objective lens plays a major role in determining the resolving power of the apparatus. Objective and selector apertures being right below the lens in a row are used to restrict the electron beam. The objective aperture blocks the unfocused electrons, resulting in an enhancement of the image contrast. The periodic diffraction of electrons is examined using selector aperture.

The transmitted electrons are passed down the column through the intermediate and projector lenses. The intermediate lens can magnify the first intermediate image, and the projector lens can form a real image on the fluorescent screen at the bottom of the microscope column. When the image strikes the phosphor image screen, light is generated, which enables the image to be observed. The image can be analyzed directly by the operator or photographed with a camera.

2.1.4.3 Energy dispersive x-ray spectroscopy (EDS)

The elemental composition of Iron seeded soot particle can be identified using energy dispersive X-ray spectroscopy (EDX or EDS) that is a method used to determine the energy spectrum of X-ray radiation. The technique employs X-rays emitted from the atoms comprising the sample's surface when the atoms are struck by electrons. In other words, when an electron from a higher shell fills in an electron vacancy, an X-ray is emitted to balance the energy difference between the two electrons. Qualitative and quantitative determinations of the elements present in the sampled volume can be evaluated using the number of emitted X-rays versus their energy. It can be measured by an EDS X-ray detector that is a solid state device discriminating X-ray energies. The

energy of the X-ray is characteristic of the element from which the X-ray was emitted. The detector is a semiconductor, usually silicon doped with lithium, and is polarized with a high voltage. When an X-ray photon hits the detector, it creates electron-hole pairs that drift due to the high voltage. The electric charge is collected and a condensator is charged. Increase in the voltage of the condensator is proportional to the energy of the photon so that the energy spectrum can be determined. The condensator voltage is reset regularly to avoid saturation. The detector is cooled to reduce the electronic noise using liquid nitrogen.

2.2 Spontaneous Raman Scattering Theory

As discussed previously, elastically scattered radiation shows the same frequency resulting in the same photon energy as the incident radiation. In contrast, inelastically scattered light governed by Raman scattering theory has certain shifts in frequency from the incident light. The incident radiation coupled into the induced dipole moment can create a quantum shift in the vibrational modes of the molecule. If the shift occurs to a lower photon frequency resulting in the lower photon energy, it is termed a Stokes shift. Conversely, a shift to a higher photon frequency resulting in the higher photon energy is referred to as an anti-Stokes shift. This shift can occur when a molecule excited via scattering interaction relaxes to a lower vibrational energy state than initial state prior to excitation. In this case, energy from a molecule is added to the photon. These inelastic shifts of the incident wavelength are determined from Equations 2-28 and 2-29 respectively,

$$\bar{\nu}_{Stokes} = \left(\frac{1}{\lambda_o} - \frac{1}{\lambda_{scat}} \right), \quad (2-28)$$

$$\bar{\nu}_{Anti-Stokes} = \left(\frac{1}{\lambda_o} + \frac{1}{\lambda_{scat}} \right), \quad (2-29)$$

where λ_o is the incident wavelength, λ_{scat} is the wavelength of the scattered light, $\bar{\nu}_{Stokes}$ and $\bar{\nu}_{Anti-Stokes}$ are Stokes and anti-Stokes shifts, respectively. The Raman shift is usually quantified by wave number expressed in dimensions of cm^{-1} . The shift in frequency of the scattered photons is species dependent, which enables Raman spectroscopy to be a powerful tool for species identification. Figure 2-3 presents elastic and inelastic scattering effect qualitatively in terms of molecular energy levels.

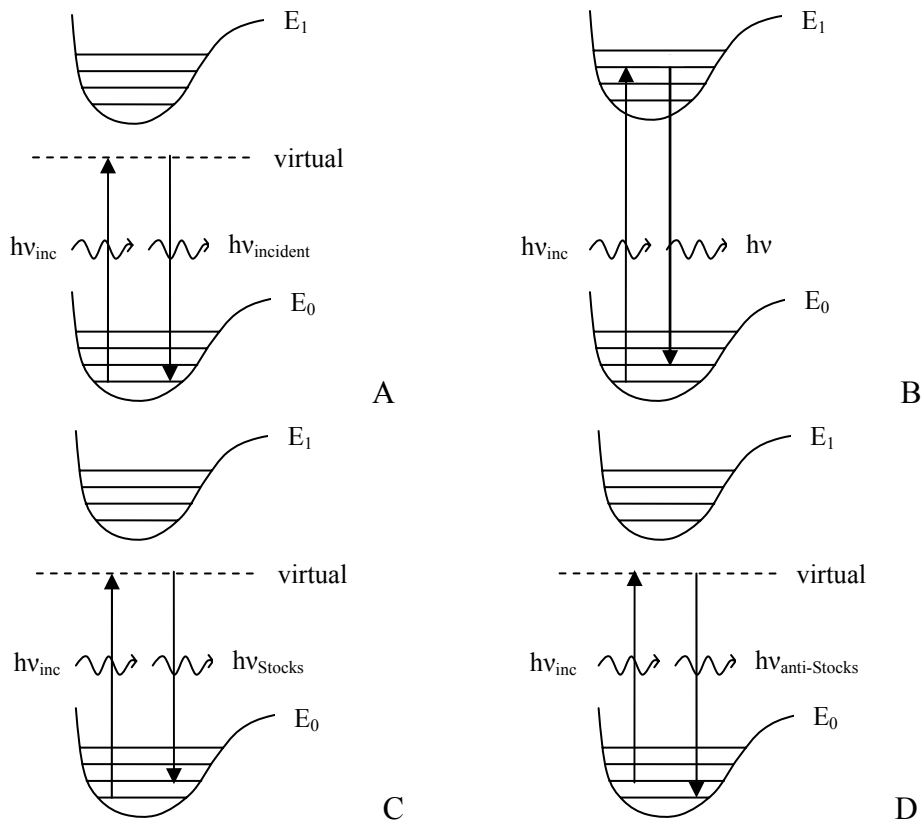


Figure 2-3. Energy level diagrams representing elastic scattering transitions and several inelastic Raman scattering transitions. A) Elastic scattering. B) Resonance Raman scattering. C) Stokes Raman scattering. D) Anti-Stokes Raman scattering.

As shown in Figure 2-3, the molecule absorbs the incident photon and is excited to a “virtual” electronic state. The case of elastic scattering transitions is that the molecule relaxes to the original vibrational level of the ground electronic state. In the case of inelastic scattering transitions, however, the molecule does not come back to its original vibrational level, so that the shifts are created. As presented in the case B in Figure 2-3, the molecule can reach stable electronic state past the virtual state when the incident photon energy exceeds an electronic transition energy. This process is called Resonance Raman scattering being closely related to fluorescence emission which will also be discussed later. Due to the similarity, fluorescence emission is a major source of noise in resonance Raman scattering technique. Compared to the fluorescence emission process, the resonance Raman process is nearly instantaneous so that the Raman signal can be discriminated from the fluorescence. Considering such a condition, the resonance Raman effect is enhanced 10^2 to 10^4 times compared with spontaneous Raman effect. Figure 2-4 elucidates the relationship of the frequency and intensity between Raman and Rayleigh spectrum. Several things are noteworthy in Figure 2-4. First, two Raman lines are symmetric with respect to Rayleigh line because the energy gain and lose are the same amount for the Stokes line and anti-Stokes line. Second, the Stokes line is apparently more intense than the anti-Stokes line. The intensity of the Stokes line is typically 100 to 1000 times higher than that of the anti-Stoke line. This is attributed to the fact that molecules are highly populated in the ground vibrational state at room temperature; hence, the chance that the incident photons encounter molecules is much more probable in the ground vibrational state than in the excited vibrational states, which is governed by the Boltzman distribution. For this reason, Stokes line is often adopted

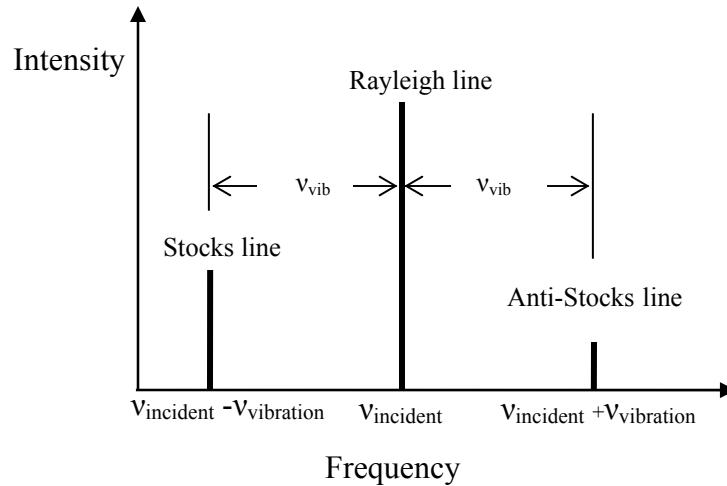


Figure 2-4. Relationship between Rayleigh and Raman scattered lines in a scattering spectrum. Source: Ingle and Crouch 1998.

for signal detection in Raman spectroscopy. In case of elevated temperature, the intensity of the anti-Stokes Raman signal is enhanced. Considering the Rayleigh scattering intensity, it is usually thousands times more intense than Raman scattering intensity.

The intensity of Raman scattered radiation is expressed as

$$I_R = \sigma' E_0 N g_{\nu_i} \frac{e^{-\varepsilon_i/kT}}{Q_\nu}, \quad (2-30)$$

where σ' is the differential Raman scattering cross section, E_0 is the source irradiance,

N is the number of gas molecules, g_{ν_i} is the vibrational degeneracy, Q_ν is the

vibrational partition function, ε_i is energy level of a molecule in the initial vibrational

state ν_i , k is the Boltzmann constant, and T is the temperature. Raman intensity is

directly proportional to several parameters shown in Equation 2-30. The most significant

parameter is the differential Raman scattering cross section that depends on the fourth

power of $\bar{\nu}_0 \pm \bar{\nu}_{vib}$; hence, higher photon energy increases the Raman scattering cross

section. Therefore, Raman scattering intensity can be significantly increased by

decreasing wavelength of the excitation light source. Higher photon energy is preferred for excitation, but gives rise to another concern about spatial resolution of detection for some species like Fe_2O_3 . Some Fe_2O_3 Raman lines are very close to the Rayleigh line resulting in a difficulty of peak discrimination. Thus, highly efficient long pass filters are essential component to prevent elastically scattered stray light from being detected in such an experiment. In addition, increase in the concentration of the active molecules in the excited volume and the intensity of the excitation source is helpful to obtain significant gains in Raman scattering intensity.

As stated before, Raman scattering takes place when molecules are excited and de-excited between rotational states as well as vibrational states. Since the polarizability of single atoms does not change with vibration or rotation, Raman scattering technique cannot be used for atomic identification. If the polarizability of a molecule does change during vibrational or rotational modes, the molecule is considered Raman-active. Each type of Raman-active molecule results in a particular shift in Raman spectrum allowing Raman spectroscopy to be useful for species identification. Raman shifts and the emission wavelengths corresponding with the excitation wavelengths of 355 nm and 532 nm for common species are summarized in Table 2-1.

Qualitative and quantitative information can be obtained using the wave numbers of the Raman shifts observed in molecules and the radiant power of Raman scattering. In addition, structural information of molecules can be provided by the depolarization ratio, ρ , defined as

$$\rho = \frac{I_{VH}}{I_{VV}}, \quad (2-31)$$

Table 2-1. Raman shifts and the emission wavelengths of common species.

Species	Shift (cm-1)	Emission 1* (nm)	Emission 2* (nm)
H ₂	4156	416.0	683.0
O ₂	1555	357.4	580.0
N ₂	2331	386.7	607.3
CO	2143	383.9	600.5
CO ₂	1285	371.6	571.0
CO ₂	1388	373.1	574.4
CH ₄	2917	395.6	629.7
CH ₃ OH	2955	396.2	631.2
H ₂ O	3650	407.5	660.2

Emission 1 and 2 are the emission wavelengths corresponding with the excitation wavelengths of 355 nm and 532 nm respectively.

where I_{VH} and I_{VV} denote the Raman radiant powers that are vertically and horizontally polarized scattered radiation with respect to the incident radiation polarization. Non-spherical shaped molecule can cause the scattered light to be depolarized when struck by polarized light. If the vibrational mode is symmetric, the depolarization ratio would be almost zero. However, if the vibrational mode is non-symmetric, depolarization of the scattered radiation can occur. In such a case, the depolarization ratio is predicted as 0.75.

The Raman scattering cross section has angular dependency on horizontally polarized incident radiation whereas it is independent of vertically polarized incident radiation over all scattering angles; hence, a vertically polarized light is often used to avoid any angular dependence on the scattered radiation.

2.3 Laser Induced Fluorescence Theory

Laser-induced fluorescence (LIF) is spontaneous emission from atoms or molecules that have been excited to higher levels by absorption of laser radiation. The fluorescence process for an atom or molecule is depicted in Figure 2-5.

When atoms or molecules are resonantly stimulated by the laser source, they absorb photon energy and are subsequently excited to higher electronic energy states.

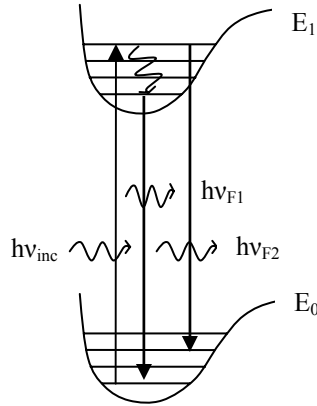


Figure 2-5. Energy level diagram of the fluorescence process for atoms or molecules. Spontaneously excited atoms or molecules decay in the ground state emitting photon energy which is lower than the incident photon energy. In general, the intensity of the fluorescence is proportional to the species concentration, the gas temperature, and pressure. Compared to spontaneous Raman spectroscopy, a great sensitivity is achievable for LIF due to the higher signal to noise ratio. In addition, selectivity of a particular excitation source for a given species is capable of avoiding interferences with other species, which is another advantage of LIF spectroscopy. However, the difficulty rises when the elastic light scattering interferes with the fluorescence signal as commonly presented in Raman scattering technique. Using high pass filters can eliminate the elastic light source from the fluorescence signal. The Stokes shift is important to eliminate such effects.

The fluorescence signal can be used in quantitative measurements of species concentration, temperature, velocity and pressure as well as qualitative analysis such as species identification. The concentration measurement is the most common one among these applications. The fluorescence signal (photons/s) is defined as

$$S_F = \eta_{\text{exp}} \cdot K_A \cdot N_0 \cdot \Phi_F, \quad (2-32)$$

where η_{exp} is an experimental constant, K_A is a rate constant for stimulated absorption, N_0 is number density of species, and Φ_F is fluorescence quantum efficiency. η_{exp} includes the incident laser intensity, a focal volume, and a solid angle which can be determined through calibration with known source. K_A is known from Einstein coefficient for stimulated absorption and Boltzmann distribution. In order to determine N_0 , Φ_F remains the only unknown given by

$$\Phi_F = \frac{K_F}{K_F + K_{IC} + K_{ISC} + K_{ec}}, \quad (2-33)$$

where K_F is fluorescence rate constant, K_{IC} is the internal conversion rate constant, K_{ISC} is intersystem crossover rate constant, and K_{ec} is the external conversion rate constant defined as

$$K_{ec} = K_q \cdot [Q]. \quad (2-34)$$

By introducing new parameter in Equation 2-33,

$$\Phi_F^0 = \frac{K_F}{K_F + K_{IC} + K_{ISC}}, \quad (2-35)$$

the number of unknowns can be reduced to Φ_F^0 and K_q , which are determined from

Stern-Volmer plot. Finally, N_0 can be evaluated with all parameters determined.

However, quantitative measurements are difficult as long as quenching is present. The variation in collisional quenching is the most common cause for uncertainty of

fluorescence measurement. Accounting for the collisional quenching is the very hard problem while the fluorescence signal is related to the absorbing species concentration.

Among several approaches to account for quenching in fluorescence measurement, the saturated fluorescence technique is prevalent. Independent condition of quenching can be

achieved by increasing the incident laser energy until absorption and fluorescence dominate quenching. This technique will not be examined here in detail.

CHAPTER 3 EXPERIMENTAL APPARATUS AND METHODS

Light scattering techniques and transmission electron microscopy (TEM) analysis following thermophoretic sampling were employed to characterize the concentration and morphology of soot in this study. In addition, two spectroscopic techniques were utilized for *in situ* species detection and identification, namely, laser induced fluorescence spectroscopy (LIF) and spontaneous Raman spectroscopy. The aim of this chapter is to describe and explain each experimental apparatus utilized, including the associated procedures and analysis methodologies employed. The experimental results are analyzed in Chapter 4.

3.1 Burner System

A concentric diffusion burner composed of stainless steel tubing was employed for all experimentations. Figures 3-1 and 3-2 represent respectively a schematic and a picture of the burner shown from side and top views. The burner dimensions are also shown in Figure 3-1. Gaseous Isooctane and nitrogen are supplied through the inner tube (0.15 cm ID) of the burner. A solid annular disk was press fit between the inner and outer tubes to maintain concentricity. The disk was perforated with 9, 0.03 cm-diameter holes, as shown. The oxygen flow was fed through the annular disk and out the nine ports at the burner outlet. Using a stainless steel mesh flame holder does promote improvement of the flame stability, as shown in a previous study (Masiello, 2004). However, in the present study the oxidation regime must remain undisturbed so that the

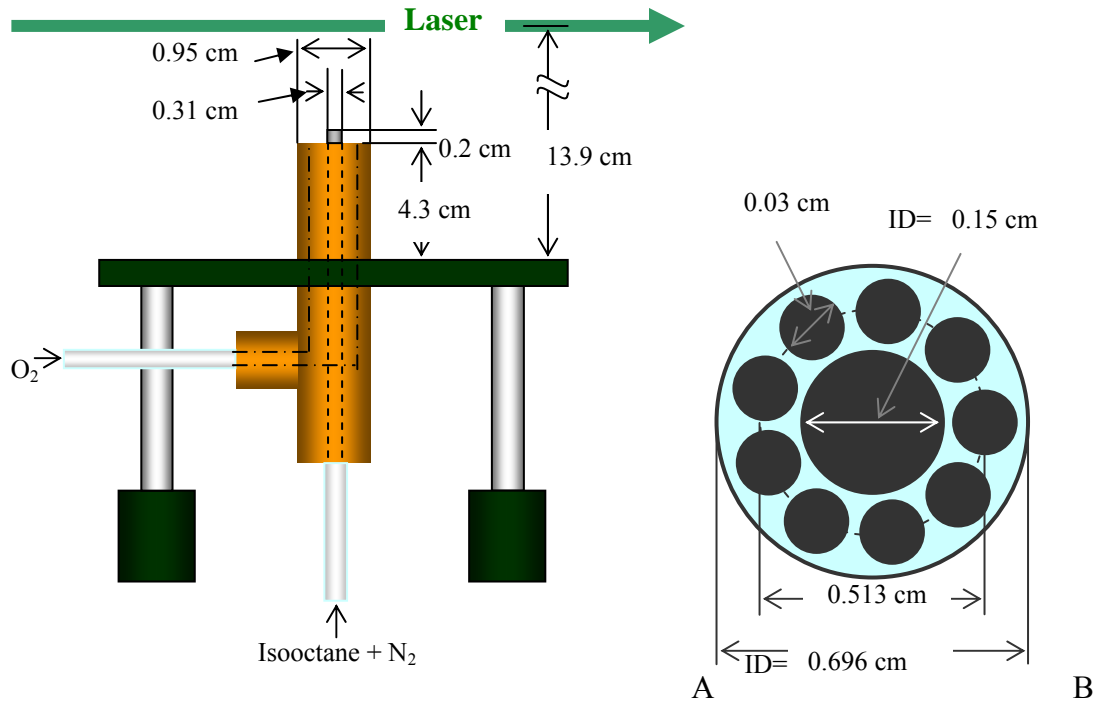


Figure 3-1. Concentric diffusion burner schematic. A) Side view. B) Top view. Oxygen goes into the system through the annular array of ports whereas isooctane and nitrogen flow through the tube in the center.

soot characteristics can be extracted purely from the flame; hence, no stabilizer was used. As recommended in the previous study, the exit area of burner was reduced to increase the flow velocity at the burner exit. As a result, a diffusion jet turbulent flame was created, and fluctuations of the flame were decreased to an acceptable level. In addition, a shroud was placed around the burner to block ambient air currents as well as prevent stray light from infiltrating into the scattering detection optics. The shroud was made of semi-transparent Plexiglas, with dimensions of 25.4×26.7cm.

In order to investigate the soot characteristics at various positions along the vertical axis of the flame, the burner was controlled with a vertical translation stage which allows the burner to move up and down. Twenty-five heights were selected and

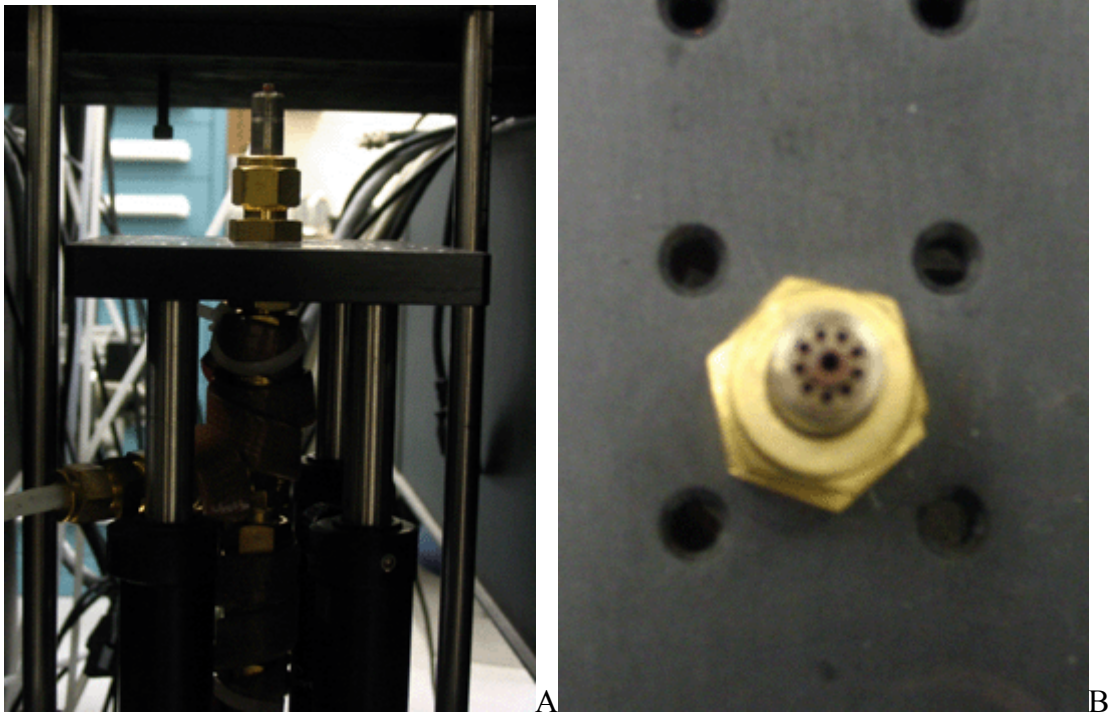


Figure 3-2. Concentric diffusion burner. A) Side view. B) Top view.

designated with the number 1 through 25, noting that the distance between heights was not necessarily constant. These heights were consistently reproducible, and corresponded to a number of specific rotations of the vertical stage knob. That is, one revolution corresponded to non-linear vertical motion. A first height designated “1” was located in 9.4 cm above the burner tip as shown in Figure 3-1A. All measurements were made along the centerline at 25 different heights from bottom to top of the flame. The summary of these heights are tabulated in Table 3-1, and Figure 3-3 represents the relative positions of these heights in the flame.

3.2 Fuel Vaporization and Delivery System

A fuel vaporization and delivery system was used for all experiments in this study. It was necessary to vaporize the liquid isooctane fuel before the fuel could be delivered to the burner in order to produce a stable, diffusion flame, in the absence of liquid droplet,

Table 3-1. Data collection heights.

Position label	Height above burner tip (cm)	Distance between two heights (cm)
1	9.40	-
2	9.75	0.35
3	10.10	0.35
4	10.50	0.40
5	10.90	0.40
6	11.30	0.40
7	11.70	0.40
8	12.20	0.50
9	12.70	0.50
10	13.20	0.50
11	13.70	0.50
12	14.30	0.60
13	14.90	0.60
14	15.50	0.60
15	16.20	0.70
16	16.95	0.75
17	17.75	0.80
18	18.60	0.85
19	19.60	1.00
20	20.65	1.05
21	21.85	1.20
22	22.80	0.95
23	23.50	0.70
24	24.20	0.70
25	25.25	1.05

for the fuel to be burned more efficiently. By heating liquid isooctane to temperatures around 100°C, vaporization was achieved when the liquid isooctane passed through a vaporization system that consists of three main sections: the preheat zone, the vaporization zone, and the delivery line. The boiling point of isooctane is about 99°C at atmospheric pressure. A schematic diagram and a picture of the fuel vaporization and delivery system are shown in Figures 3-4 and 3.5 respectively.

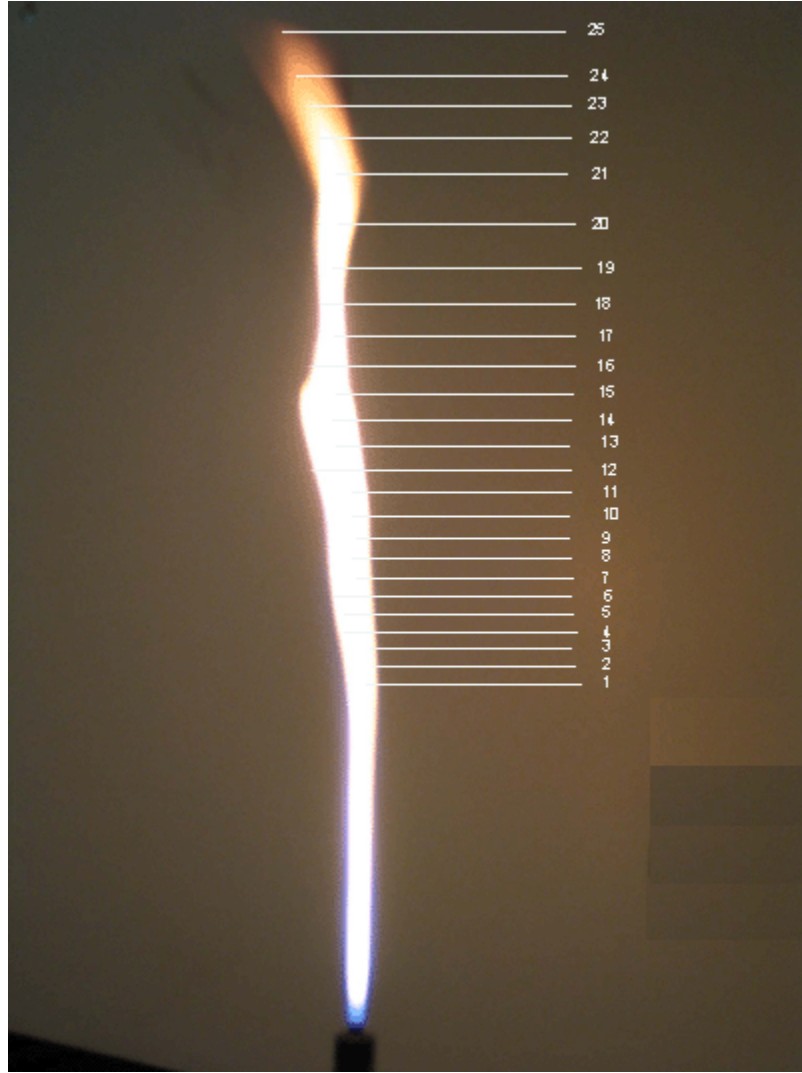


Figure 3-3. Data measurement heights.

All three sections of the vaporization system were wrapped with Omega heater tape and fiberglass insulating tape. The heaters were controlled with two PID controllers set at a temperature of 100°C , which was above the boiling point for the liquid isooctane. As shown in Figure 3-4, a nitrogen gas with a flow rate of 0.8 liter per minute was introduced into the vaporization system at the head of the preheat zone composed of a 0.625 inch diameter, 36 inch long 304 stainless steel tube packed with brass balls to promote heat transfer by increasing the surface area. The nitrogen gas was heated in

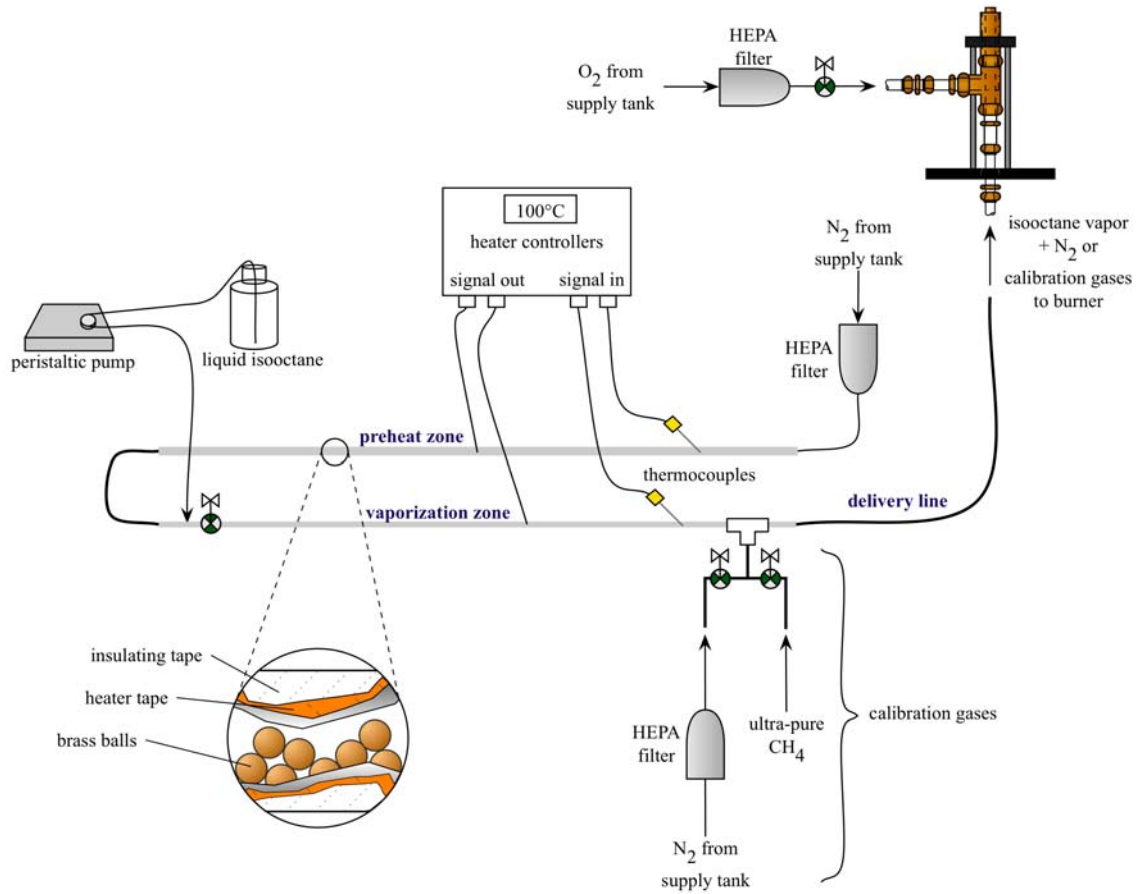


Figure 3-4. Fuel vaporization system schematic.



Figure 3-5. Fuel vaporization system.

this region, and then it traveled into the vaporization zone consisted of a 0.25 inch diameter, 36 inch long 304 stainless steel tube. The liquid isooctane was supplied into this region via a variable flow Fisher Scientific peristaltic pump at a flow rate of 0.0015 liter per minute and vaporized by the heated nitrogen gas as well as the direct heat from the hot surface of the tubing. By the nitrogen gas, the vaporized isooctane was carried to the burner passing through a delivery line composed of roughly 50 inches of 0.25 inch diameter braided PTFE hose. This zone was also heated to eliminate the fuel condensation on the way to the burner. For warming the vaporization system up, the heaters were turned on and the nitrogen coflow at a flow rate of 0.4 liter per minute about one half an hour prior to any experimentation. This ensured that the vaporization system was adequately heated before the liquid fuel was introduced into the system. The oxygen stream with a flow rate of 2.6 liter per minute and the isooctane/nitrogen stream exited the burner to produce the diffusion flame. The gas flow rates were regulated by Alicat Scientific digital flow controllers whose accuracy was 1% of full-scale. The maximum flow rates of the flow meters employed were 1 liter per minute for the nitrogen and 10 liter per minute for the oxygen, respectively. These digital flow meters are shown in Figure 3-6.

Table 3-2 summarizes the overall description of the fuel vaporization and delivery system, and Table 3-3 tabulates the description of the gases and fuel.

3.3 Flame

As discussed above, a roughly 30 cm long flame was created by the burner used in this study corresponding to the prevaporized isooctane/oxygen diffusion jet flame. The main fuel was isooctane, C_8H_{18} , which is characterized by a relatively low boiling point, promoting a stable fuel delivery system, and is compatible with a previous study

(Masiello, 2004) that probed the soot inception and growth regimes. Figure 3-7 elucidates the chemical structure of isooctane.



Figure 3-6. Alicat Scientific digital flow meters employed for regulating the flow rates of nitrogen coflow and oxygen.

Table 3-2. Summary of equipment for fuel vaporization and delivery system.

Device	Manufacturer	Model	Description
Peristaltic pump	Fisher Scientific	13-876-4	Variable flow peristaltic pump
Heater tape-preheat zone	Omega	SRT101-060	313 W
Heater tape-vaporization and delivery line	Omega	SRT051-060	156 W
Braided PTFE hose	Swagelok	SS-4BHT	PTFE-lined stainless steel flexible hose
Thermocouple	Omega	Type K	Thermocouple
Heater controller	Omega	CN9000A	2 PID controllers
HEPA filter	Gelman Laboratory	12144	2 HEPA filters
Digital flow meter-N ₂ coflow	Alicat Scientific		0-1 SLPM, accurate to 1% of full-scale
Digital flow meter-O ₂ coflow			0-10 SLPM, accurate to 1% of full-scale
Magnetic stirrers	Fisher Isotemp	11-601-16S	60~1200 rpm, 120V, 50/60 Hz

Table 3-3. Summary of gases and fuel used in the study.

O ₂	Praxair	UN 1072	>99% pure
N ₂	Praxair	UN 1066	>99% pure
Isooctane	Fisher Scientific	O296-4	HPLC-grade
CH ₄ (used for calibration)	Praxair	UN 1971	Ultrahigh purity, 99.97% pure

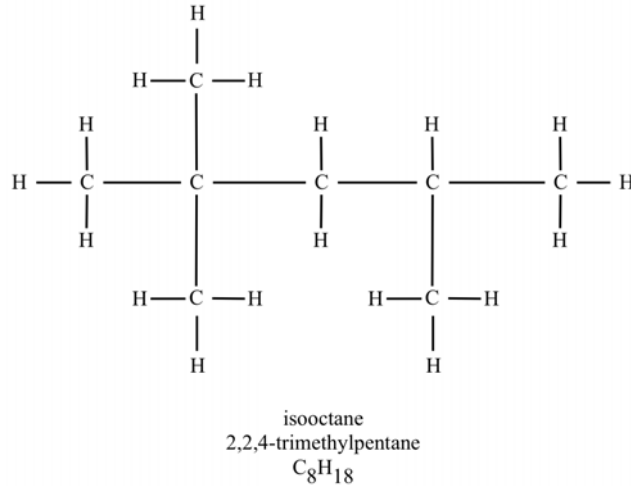


Figure 3-7. Chemical structure of isooctane.

In order to characterize the flame, Froude number and Reynolds number were calculated for the flame. The detailed calculations are attached in Appendix A. First, the Froude number was 11.8, which indicates that the flame was momentum-controlled rather than buoyancy-controlled, which was by design. Second, the Reynolds number was approximately 761.3, which denotes that the flame was laminar flow, as it was smaller than the critical value of 2300. Furthermore, the fuel equivalence ratio was calculated as 1.08 based on the oxygen and isooctane flow rates. While this value corresponds to fuel rich, significant additional oxygen is expected to diffuse into the flame. To better understand the stoichiometry, a study was made to evaluate the smoke point for the unseeded flame. Oxygen flow rates were adjusted to obtain the fuel-rich flame that operated under the smoke point. Further discussion will be presented in

Chapter 4 in detail. Visible smoke was emitted above the flame tip when the oxygen flow rate was below 4.24 L/min. The oxygen flow rate of 2.6 L/min was selected for all experiments, based on the need for a reasonable smoke load to explore soot suppression. Both the unseeded and iron seeded flames were tested under the same conditions, except for the presence of the iron pentacarbonyl. For the seeded flames, the iron pentacarbonyl was added to the liquid isooctane supply in 4000 ppm quantities by mass (~0.11% Fe per mass of fuel) and was delivered to the burner through the fuel stream. The selection of this value is discussed below. In all experimental stages, a magnetic stirrer was used to prevent the iron pentacarbonyl from setting during experiments. The flame operating conditions are summarized in Table 3-4 below.

Table 3-4. Description of the flame operating conditions.

Stream	Flow rate
C ₈ H ₁₈ (liquid)	1.5 mL/min
N ₂	0.8 L/min
O ₂	2.6 L/min
Fe(CO) ₅ (seeded flame only)	4000 ppm

3.4 Optical Systems and Diagnostics

3.4.1 Light Scattering System

Laser light scattering techniques were used to determine the scattering properties of soot particles in the unseeded and seeded flames. The optical setup for this scattering system is sketched in Figure 3-7, and the optical components are summarized in Table 3-5.

For the laser light scattering experiments, a frequency doubled Q-switched 532 nm Nd:YAG pulse laser (Continuum, Minilite ML-II) was used as a light source. The laser was operated at 10 Hz with a pulse energy of 0.3 mJ/pulse. The laser was first turned 45°

with 532 nm dichroic mirror. The laser beam then passed through an aperture to cut out the Gaussian “edge” of the laser intensity profile before it was directed through a focusing lens. Finally, the focused beam passed through the center of the flame at desired vertical position above the burner lip, and was terminated at a beam dump. The cross sectional area of the beam was 0.0033 cm^2 at the center of the flame. The scattered light from the soot particles was collected by a photomultiplier tube (PMT) at 90 degree angle from the incident beam. The scattered light first passed through neutral density (ND) filters in the collection optics line. The ND filters were required to attenuate scattered beam intensity for maintaining signal linearity. After several ND filters, the

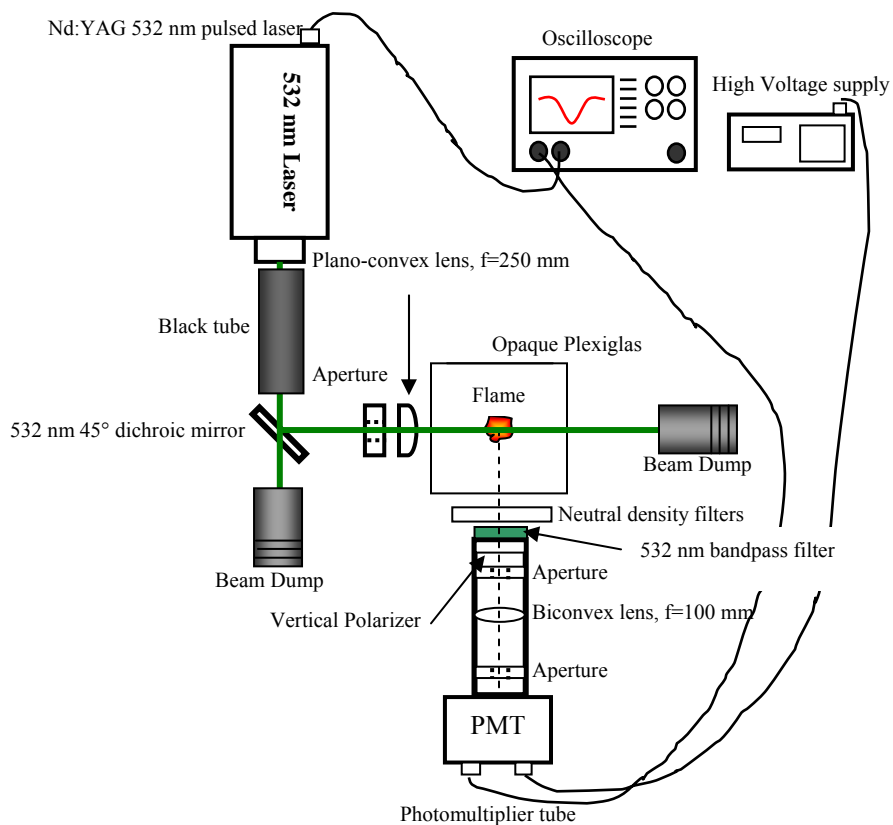


Figure 3-7. Top view of the light scattering system setup.

Table 3-5. Components of scattering system apparatus.

Device	Manufacturer	Model	Description
Equipment			
532 nm frequency doubled Nd:YAG Laser	Continuum	Minilite ML-11	Q-switched, 5 Hz, 2.4 mJ/pulse FWHM=5 ns, 20 mJ max
Beam dump	Kentek	ABD-2	Beam dump
Photomultiplier tube	Hamamatsu	R2949	Photomultiplier tube
Photomultiplier tube housing	Products for Research, Inc.	PR1402CE	Photomultiplier tube housing
Oscilloscope	LeCroy	LT 372, WaveRunner	500 Hz, 4 GS/s digital oscilloscope with 50 Ω termination
Precision high voltage supply	Stanford Research Instruments	PS325	Digital high voltage power supply
Double shielded BNC cable	Pasternack Enterprises	RG-223/U	Double shielded coaxial cable to reduce line noise
Translational stage	Mitutoyo		Micrometer-adjusted translational stages
Optics			
532 nm dichroic mirror	CVI Laser		45 degree, 532 nm dichroic mirror
Aperture	Newport	ID-1.0	2 apertures
Plano-convex lens	Newport	KBX079AR.14	BBAR coated, 430-700 nm, 25.4 mm diameter, 250 mm focal length
Neutral density filters	Optics for Research	FDU-2.0	$10^{2.0}$ attenuation
		FDU-1.0	$10^{1.0}$ attenuation
		FDU-0.3	$10^{0.3}$ attenuation (nominal values)
Polarizer	Newport		
532 nm line filter	Newport	10LF10-532	T > 50%, 25.4 mm diameter
Aperture		ID-0.5	2 apertures in collection optics
Biconvex lens			UV coating, 100 mm focal length, 25.4 mm diameter

scattered light was passed through a 532 nm band pass filter, a vertical polarizer, a first aperture, biconvex lens, and a second aperture in the collecting tube. The 532 nm band pass filter effectively removed all wavelengths except 532 nm. The vertical polarizer ensured that the scattered radiation observed was only vertically polarized, which matched the vertically polarized incident beam. The polarizer contributes to reduction of depolarized stray light, but it can also block the scattered light because the arbitrary shape of the soot agglomerates can cause the scattered light to be depolarized. It is noted that RDG scattering theory as formulated relies on only vertically polarized scattering light. Two apertures reduced background noise (i.e., stray light) and ensured that the scattered light was collected only from the small scattering volume defined in the flame. The biconvex lens of 100 mm in focal length defined a solid collection angle of about 0.05 sr. The scattered light was finally incident on a PMT and the scattered intensity was recorded on a digital oscilloscope. A precision high voltage supply set to -650 V drove the photomultiplier tube.

The photomultiplier tube (PMT) is a high gain detector so that it is very useful for low light level detection. Photons are converted into an electric signal with a small load resistor (less than 100 Ω in common) by a phenomenon, namely the photoelectric effect. The photomultiplier tube contains a photosensitive cathode and a collection anode that are separated by several electrodes, called dynodes, providing electron multiplication or gain. When the photocathode is exposed to the electromagnetic radiation, a number of photoelectrons are ejected by the photocathode and hit the first dynode. These electrons strike the next dynode, which results in releasing additional electrons. This

multiplication process continues until electrons arrive at the anode. A typical PMT is shown in Figure 3-8.

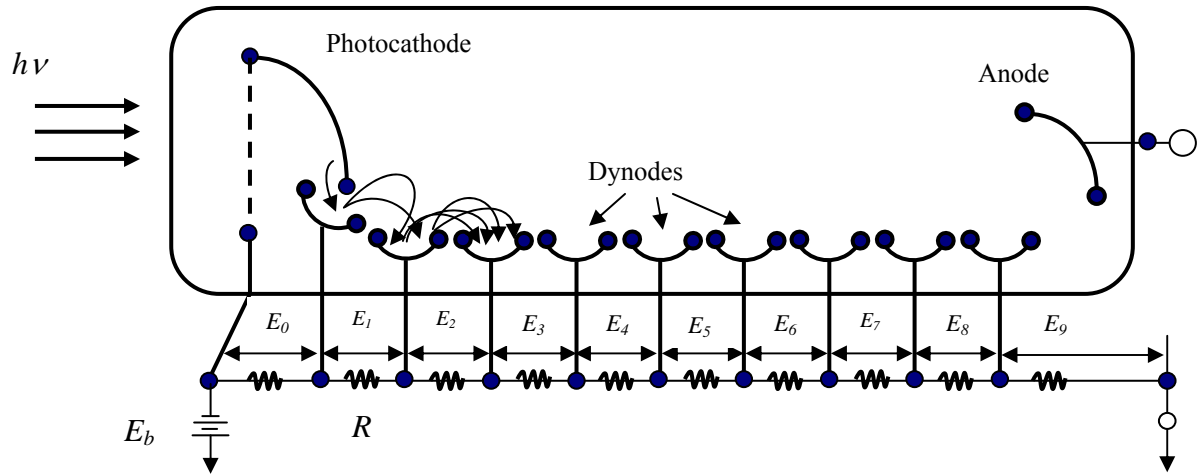


Figure 3-8. Photomultiplier tube. A series of dynodes between cathode and anode provide internal gain.

PMTs are generally able to output a linear response to a continuous signal source over several decades. However, a pulsed nanosecond-scale laser can easily invoke a non-linear response in the PMT due to the sudden flux of incident photons. Commonly, a PMT is limited to only about one decade of linearity in such a system, therefore signal linearity must be carefully considered. When the strength of a scattered signal to a PMT exceeds the linear limits, the signal must be attenuated to bring the output of the PMT back into the linear response regime using neutral density (ND) filters. A ND filter is characterized by a broad and steady transmission profile over a wide range of wavelengths. An x ND filter attenuates by a factor of 10^x . For examples, a 0.3 filter should attenuate the signal by a factor of $10^{0.3}$, or approximately 2; thus, the output signal was expected to drop by about one half if the PMT response was linear. The optical densities of the ND filters used were calibrated previously and are summarized in Table 3-6.

Table 3-6. Real optical densities for various ND filters

Filter	Optical density at 532 nm
0.3A	0.284
0.3B	0.299
1.0A	0.808
1.0B	0.806
2.0A	1.728
2.0B	1.717

As shown in Table 3-6, a total of 6 ND filters were available in a variety of attenuating strengths; thus, maintaining the PMT in its linear regime was simply a matter of adding and removing filters from the PMT incident path. Linearity was checked with nitrogen gas prior to every experiment by placing a 0.3 neutral density filter in front of the collection optics and ensuring a factor of 2 intensity reduction. The ND filters for individual height are tabulated in Table 3-7, which were used to maintain a comparable and linear signal over all heights.

As discussed in Chapter 2, the differential scattering coefficient is a key parameter for determining number densities of the scattering particles in the flame. The scattering signal obtained by the PMT is defined as

$$S_{VV} = I_o \eta (\Delta V \Delta \Omega) N \overline{\sigma'_{VV}}, \quad (3-1)$$

where I_o is the incident laser intensity, η is the efficiency of the collection optics and the PMT detector, ΔV is the scattering volume, and $\Delta \Omega$ is the solid angle of observation. N and $\overline{\sigma'_{VV}}$ are number density and the differential scattering cross section as discussed previously. The parameters η , ΔV , and $\Delta \Omega$ may be measured although it is hard to determine them individually with the utmost precision. By taking the ratio of a reference scatterer signal to the signal from the scatterer of interest, the direct evaluation

Table 3-7. The usage of the ND filters for individual height.

Position	Height	N.D. Filter
Calibration	0.80	0.3B
1	9.40	2AB+1AB+0.3A
3	10.10	2AB+1AB+0.3A
5	10.90	2AB+1AB+0.3A
7	11.70	2AB+1AB+0.3A
9	12.70	2AB+1AB+0.3A
11	13.70	2AB+1AB+0.3A
13	14.90	2AB+1AB+0.3A
15	16.20	2AB+1AB+0.3A
16	16.95	2AB+1AB+0.3A
17	17.75	2AB+1AB+0.3A
18	18.60	2AB+1AB+0.3A
19	19.60	2AB+1AB+0.3A
20	20.65	2AB+1AB
21	21.85	2AB+1AB
22	22.80	2AB+1AB
23	23.50	2AB+1AB
24	24.20	2AB+1AB
25	25.25	2AB+1AB

of the common terms $\eta(\Delta V \Delta \Omega)$ can be avoided. With this approach, $N \cdot \bar{\sigma}'_{VV} \Big|_{Soot}$ can be calculated using the following equation,

$$(N \cdot \bar{\sigma}'_{VV})_{Soot} = (N \cdot \bar{\sigma}'_{VV})_{CH_4} \left(\frac{S_{vv,Soot}}{S_{vv,CH_4,measured} - SL} \right) \left(\frac{1}{\tau} \right). \quad (3-2)$$

Recall $N \cdot \bar{\sigma}'_{VV}$ is the differential scattering coefficient. In this equation, τ is the transmission through the flame which will be determined in a later section, SL is stray light obtained by a calibration, and the subscript CH_4 refers to the methane calibration gas whose signal and the cross-section will be reported in the next section.

3.4.2 Light Scattering Calibration

A calibration is necessary for determining and illustrating the amount of stray light presented in the system. Stray light, such as any ambient light and laser light reflected from surfaces, which enters through the scattering collection optics, can distort the experimental results considerably. The magnitude of stray light can be as large as the scattered signal, thus it is very crucial to reduce errors caused by stray light.

As mentioned briefly in the foregoing section, several efforts were already used to minimize stray light entering at the PMT. First, using apertures and lenses in the collection optics, a very small scattering volume was defined in the experiment. These apertures also played a role to block any stray light from outside the scattering volume. Highly reflective surfaces of optical mounts were either painted in black or covered in black felt to minimize reflections of laser light from surfaces. In addition, by allowing the beam to pass through a black painted tube placed in the beam path, as well as the barrier with surrounding opaque Plexiglas covered in black felt, any stray light from outside the scattering volume was largely blocked from introducing into the PMT. In spite of such efforts, it is impossible to completely get rid of stray light from the system. Therefore, the stray light calibration was necessary to compensate for stray light.

The calibration was performed using methane (CH_4) and nitrogen whose differential scattering cross sections were already known as summarized in Table 3-8. The calibration gases shared the delivery line of the vaporization chamber, as depicted in Figure 3-4, thus the fuel gas was expelled from the burner for calibration measurements. A series of brass plug valves were used to shut off the flow from the vaporization chamber during calibration, and vice versa during flame operation. The supplier's specifications of methane were listed in Table 3-3 before. The calibration gases were

injected into the measuring area 8 mm far from the burner lip. Both gases flowed at a rate of approximately 10 L/min, which was controlled by a rotameter (GE700 Gilmont) flow tube. The scattering measurement for the calibration was carried using the identical configuration as used for the soot scattering study. A type K thermocouple was used to measure the temperature of gases exiting from the burner through the heated fuel delivery line. Over 24 sets of the experiment, the temperatures were on average 346 K, with the standard deviation of 1.68 K for methane, and 340 K with the standard deviation of 1.37 for nitrogen, respectively. The number density N , differential scattering cross section, σ'_{VV} (cm^2/sr) and differential scattering coefficient, K' ($\text{cm}^{-1}\text{sr}^{-1}$) for each gas were determined using temperatures measured each time. Number densities were calculated using isobaric density data tabulated by the National Institute of Standards and Technology (Lemmon *et al.*, 2003). As for the differential scattering cross sections for each of these gases, they were previously reported to be $4.56\text{E-}28 \text{ cm}^2\text{sr}^{-1}$, and $2.12\text{E-}28 \text{ cm}^2\text{sr}^{-1}$, respectively (Rudder and Bach, 1968) at an incident wavelength of $\lambda = 694.3 \text{ nm}$. With those values, σ'_{VV} at an incident wavelength of $\lambda = 532 \text{ nm}$ was calculated using the equation below,

$$\sigma'_{VV}|_{\lambda_2} = \sigma'_{VV}|_{\lambda_1} \left(\frac{\lambda_1}{\lambda_2} \right)^4 \left(\frac{n_{\lambda_2} - 1}{n_{\lambda_1} - 1} \right)^2, \quad (3-3)$$

where n_λ is the wavelength-dependent refractive index (Landolt-Bornstein and Funktion, 1962). The number density, the differential scattering cross section and coefficients for calibration gases at the wavelength of 532 nm are summarized in Table 3-8.

Table 3-8. Average of the number densities, differential scattering cross sections, and scattering coefficient sets for methane and nitrogen calibration gases at 1 atm with standard deviation for 24 experimental.

		T (K)	N (cm ⁻³)	σ'_{VV} (cm ² /sr)	K'_{VV} (cm ⁻¹ sr ⁻¹)
Methane	Average	346.29	2.12E+19	1.35E-27	2.87E-08
	S.D.*	1.68	1.03E+17	-	1.40E-10
Nitrogen	Average	340.04	2.16E+19	6.25E-28	1.35E-08
	S.D.	1.37	8.32E+16	-	5.20E-11

S.D.* : Standard deviation

The reference calibration ratio R_{ref} for methane to nitrogen can be determined by the ratio of their differential scattering coefficients as expressed below,

$$R_{ref} = \left[\frac{K'_{VV}|_{CH_4}}{K'_{VV}|_{N_2}} \right]_{reference} \quad (3-4)$$

The reference ratio, R_{ref} , can then be related to the measured signals and the corresponding stray light through the relationship,

$$R_{ref} = \frac{(S_{vv,CH_4,measured}) - SL}{(S_{vv,N_2,measured}) - SL} \quad (3-5)$$

This value was used to determine the stray light contained in the measured scattering signals from the calibration gases. In the equation, $S_{vv,CH_4,measured}$ and $S_{vv,N_2,measured}$ are the measured scattering signals of methane and nitrogen, respectively. With this relationship, the stray light in the system can be quantified as

$$SL = \frac{R_{ref} S_{pp,N_2} - S_{pp,CH_4}}{R_{ref} - 1} \quad (3-6)$$

In the light scattering studies, stray light calibration measurements were taken prior to every flame study to determine an experiment-specific stray light value. Over the range of experimental measurements, the average contribution of stray light was around 38.5%

of the methane calibration signal. The detailed discussion and calculation of stray light is represented in Appendix D.

3.4.3 Signal Processing

For scattering analysis, a number of signals were measured, including the dark signal (no laser) for calibrations, the calibration signals, the flame dark signals (flame only, no laser), and the flame scattering signals. The scattered signal from the calibration gases and the flame from a typical scattering experiment are represented in Figure 3-9.

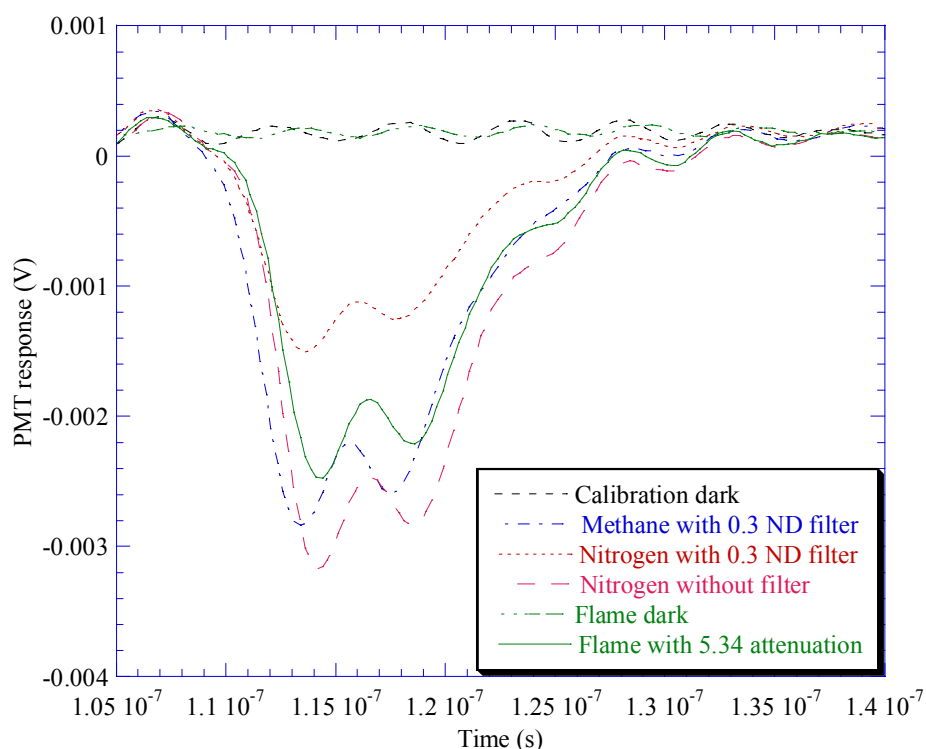


Figure 3-9. Sample scattering signals from methane, nitrogen, and flame. Calibration gases are attenuated by a factor of $10^{0.3}$ and flame signal is attenuated by a factor of $10^{5.43}$ for signal linearity.

The dark signals were recorded prior to the measurement of the scattered signals to normalize the baseline of the flame and the calibration gases. Such dark signals were integrated over a 50 ns full peak width. Since the PMT responses of the baselines to bulk signals were not consistent at all times, they were offset by subtracting the signal baseline

from the integrated scattered signal. The offset dark signals were subtracted from the offset scattered signals, which were named the calculated signal. The calculated signals then needed a correction for any attenuation factor that was used to preserve PMT linearity. For the data presented in Figure 3-9, the calculated calibration signals were attenuated by a factor of $10^{0.3}$, while the calculated flame signals was attenuated by a factor of $10^{5.34}$. Therefore, the calculated signal still including the influence of stray light was corrected by multiplying it by the overall attenuation factor. The calculated calibration signals were found to be 0.249 V-ns for methane and 0.14 V-ns for nitrogen respectively, in this example. This yielded a calibration ratio of 1.78, 16.4% deviation from the ideal reference ratio, R_{ref} , of 2.128 for this experiment, which indicates the magnitude of the stray light. Using Equation 3-5 with the calculated calibration signals and the reference ratio, the stray light was determined to be 0.043 V-ns in this case. The average results of calibration measurements over all experiments are summarized in Table 3-9 along with the standard deviation. The average calibration ratio was determined to be 1.51, with a standard deviation of 0.22, 29% deviation from R_{ref} . Overall, the stray light signal was approximately 40% of the methane gas signal for the typical experiment.

Table 3-9. Average results of calibration gas signal including stray light, a calibration ratio, stray light signal, the percentage of stray light, and the ideal reference ratio along with the standard deviation over all scattering experiments.

	Methane	Nitrogen	Ratio	Stray Light	Percent S.L.	Ideal Ratio
Average	0.30	0.21	1.51	0.13	38.48	2.126
S.D.	0.05	0.06	0.22	0.07	18.53	-

The final calibration signals were determined by subtracting the stray light from the recorded calibration signals. This yielded true calibration signals of 0.206 V-ns for

methane and 0.097 V-ns for nitrogen, respectively, for the above example. In the same manner, the calculated flame signal was determined to be 23,648 V-ns. The stray light signal may be subtracted from this signal to calculate the true flame signal; however it may be neglected without significantly altering the scattering results because it is orders of magnitude smaller than the flame signal. At any rate, the stray light signal calculated in this manner will be used to determine the differential scattering coefficient of the soot with Equation 3-2. All that remains to be determined in order to extract the differential scattering coefficient from the scattering data is the transmission of laser light through the flame, which will be discussed in a later section.

3.5 Laser Power Measurement

Accurate scattered signals may be obtained as long as modest laser pulse energies are used. However, a laser pulse can significantly heat and vaporize soot particles if the beam is focused to a small cross-sectional area. Therefore, it is important to determine suitable laser energy to eliminate any soot vaporization during the flame studies. According to Dasch (1984a and b), laser fluences greater than 0.2 J/cm^2 from a submicrosecond pulsed source can cause vaporization of soot particles, resulting in reducing the light scattering and extinction characteristics of soot by an order of magnitude. Recent work by Yoder *et al.* (2005) quantified vaporization effects, and reported vaporization of soot particles down to a fluence of 0.1 J/cm^2 . In order to ensure no vaporization effects, the laser output power was measured with a powermeter and adjusted to the appropriate energy for the spot size.

The laser power was 3.04 mW on average with standard deviation of 0.29 over 10 measurements, which yielded 0.31 mJ/pulse for the laser pulse rate of 10 Hz. These correspond to a laser fluence of 0.092 J/cm^2 based on a focal spot of 0.0033 cm^2 , where

the term fluence refers to the laser energy per the beam area. The lowest laser energy was attained by simply reducing the laser pump energy. The beam area was found by ablating ink off a slide, at increased pulse energy, and measuring the area in which the ink was removed. The beam spot was quite a perfect circle having a diameter of 0.65 mm. A summary of the laser beam power properties is given in Table 3-10.

Table 3-10. Summary of laser beam power properties for light scattering measurements.

	mW	mJ	Fluence(J/cm ²)
Average	3.04	0.304	0.0916
S.D.	0.29	-	-

3.6 Transmission

In order to complete the calculation of the differential scattering coefficient using Equation 3-2, the transmission is required to be measured at each of the flame heights investigated. Figure 3-10 shows the experimental setup for the transmission system.

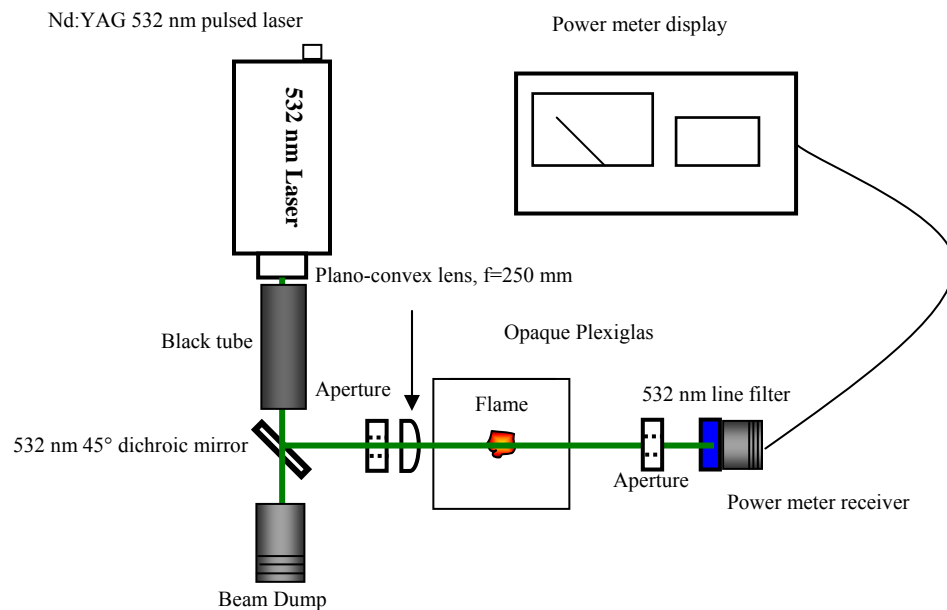


Figure 3-10. Top view of the transmission system setup.

This setup is identical to the scattering system except that the laser does not terminate at a beam dump but encounters the power meter receiver. Moreover, a narrow aperture and a 532 nm line filter were placed in front of the power meter receiver. The aperture played a role to prevent the forward scattered light from entering the power meter. The influence of the forward scattered light could be limited by distancing the power meter receiver from the flame as well. These efforts resulted in only a small solid angle of observation. In addition, the 532 nm line filter blocked all light except the 532 nm that was detected by the power meter. The transmission instrumentation is described in Table 3-11 in detail.

Table 3-11. Description of transmission apparatus.

Device	Manufacturer	Model	Description
Equipment			
532 nm frequency doubled Nd:YAG Laser	Continuum	Minilite ML-11	Q-switched, 5 Hz, 2.4 mJ/pulse FWHM=5 ns, 20 mJ max
Power meter	Molelectron	PM5200	Power meter
		PM3	Power meter head
Optics			
532 nm Dichroic mirror	CVI Laser		45 degree, 532 nm dichroic mirror
Aperture	Newport	ID-1.0	Aperture
Plano-convex lens	Newport	KBX079AR.14	BBAR coated, 430-700 nm, 25.4 mm diameter, 250 mm focal length
532 nm line filter	Newport	10LF10-532	T>50%, 25.4 mm diameter

The measured power of the laser through the flame was ratioed with the power measured at a position outside of the flame to obtain the transmission through the flame. From the Beer-Lambert law, the transmission is generally defined as

$$\tau = \frac{I_{trans}}{I_0} = \exp(-K_{ext}L), \quad (3-7)$$

where I_0 is the incident intensity of the laser, as measured at a position outside of flame, I_{trans} is the transmitted intensity measured through the flame, L is the optical pathlength through the flame, and K_{ext} is the extinction coefficient. With the transmission data determined in this manner, the extinction coefficients could be simply obtained only if the optical pathlengths are known. The optical pathlengths corresponding to 12 heights were determined statistically by taking 25 pictures of the unseeded and seeded flames each and analyzing them.

The extinction coefficients evaluated in Equation 3-7 reflect an average value through the flame, which is correct as used to correct the scattering coefficient using Equation 3-7. However, if spatially resolved extinction data is desired, deconvolution techniques are often employed. In this study, the width of the flame used was not sufficient to apply these techniques; as a consequence, no deconvolution (e.g. Abel inversion) was used.

3.7 Thermophoretic Sampling and Transmission Electron Microscopy

The conventional light scattering technique is a non-intrusive diagnostic tool that can effectively infer optical properties from a system of particulates *in situ*; however, it has been limited to point measurements, and cannot extract fractal properties of aggregates such as the radius of gyration and fractal dimension. Therefore, it is required to use a complementary technique that can measure the size and shape of soot agglomerates. Such information can be obtained utilizing *ex situ* transmission electron microscopy (TEM) following thermophoretic sampling.

3.7.1 Thermophoretic Sampling

The soot aggregates were extracted from the flame using thermophoretic sampling for the transmission electron microscope image analysis of size and morphology of aggregates. Soot samples were collected directly on formvar-carbon coated 150-mesh copper TEM grids (Electron Microscopy Sciences, Hatfield, PA, Part No. FCF150-CU50). A schematic of this device is shown in Figure 3-11.

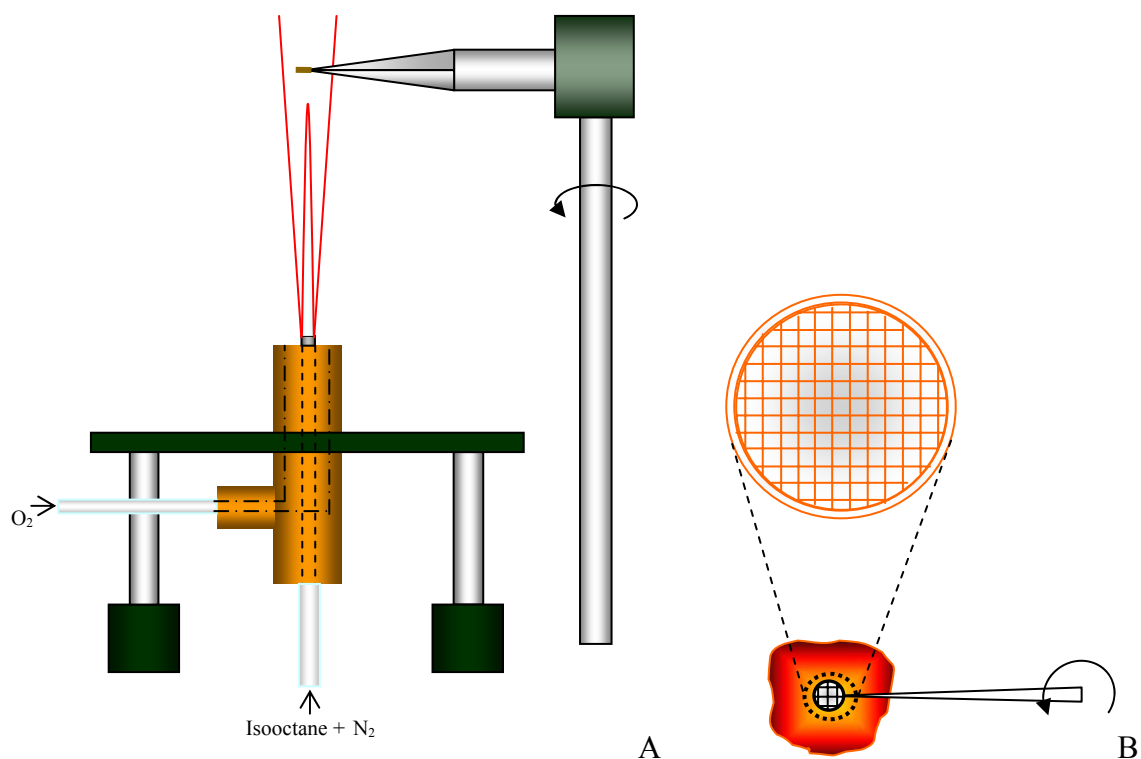


Figure 3-11. A setup of thermophoretic sampling and grid. A) Side view. B) Formvar carbon-supported 150 mesh copper grid.

Each film was held by a tweezer attached to a holder. The sampling surface faced toward the flow direction. A film was installed outside the flame and swept through the flame allowing soot aggregates to deposit directly on the grid. Samples were collected at 12 different heights along the vertical axis of both the unseeded and seeded flames.

It is significant that the exposure time of the film should be long enough to capture a reliable amount of sample, but short enough to avoid melting the grid or oversampling the aggregates. The sampling times were not controlled automatically (by e.g. using a double acting pneumatic cylinder, solenoid valves and timers) but manually in the present study. As a result, each sample had a slightly different residence time in the flame, but care was taken such that all exposure times of the films were about 1 s. In spite of the absence of an automatic controlling device, it was concluded that the samples obtained in the present study were sufficient for TEM analysis. Representative micrographs are presented in Chapter 4.

Another issue of thermophoretic sampling is to obtain samples at a desired position in the flame. To do this, a shield is used for preventing the particles from depositing on the grid while the sampling probe was out of a desired sampling location. Alternatively, the shorter transition time is used while the film was traveling out of the desired region. The flame employed in the present study was so thin that undesired sampling region was relatively narrow enough to ignore the quantity of undesired samples. After exposed to the flame producing soot aggregates, the grid was examined to observe the particle size and morphology with a TEM.

3.7.2 Transmission Electron Microscope

The soot samples collected by thermophoretic sampling were observed using a JEOL 2010F analytical electron microscope system with a point resolution of 0.19 nm. Figure 3-12 shows a photograph of the TEM system.

The diffraction grating was used to calibrate the TEM. Magnifications used for the present measurements ranged from 50,000 to 330,000, corresponding to 500 nm and 50 nm sized scale bars, respectively. For analysis, each soot aggregate was randomly picked

at low magnification, and then analyzed at the optimum magnification. Each micrograph has a scale bar indicating length, and particle diameters can be simply measured from the pictures, which will be discussed in more details in Chapter 4. TEM micrographs of soot aggregates extracted from the center region of the diffusion flame were examined as a function of increasing height. In addition to TEM analysis, the Energy Dispersive X-ray Spectroscopy (EDS) was performed for precise detection of chemical components in samples, including iron species, using an Oxford INCA Energy TEM System.



Figure 3-12. Photograph of the TEM system.

3.8 Spectroscopic Techniques

Up to this point, all studies have focused on the quantitative viewpoint such as size and concentration of soot in the flame. Next, qualitative aspects will be examined such as the identification of species in the flame. The particular species present in the flame provide information on the mechanisms of chemical reactions. Moreover,

preliminary testing for eliminating the external environment interferences and variations was performed with a CO flame. These were summarized below.

3.8.1 Preliminary CO Flame Study

CO flame was employed to pretest an availability of spectroscopic techniques such as LIF and *in situ* Raman spectroscopy before such techniques are applied to the isooctane flame study. It is well documented that the iron pentacarbonyl gas in a CO and O₂ flame is thermally decomposed and believed to form Fe₂O₃ chain agglomerates (Cheng *et al.* 1991). Further, it has an advantage that the soot particles do not interfere with a particular species to be detected because carbon dioxide is the only product from the CO flame. Figure 3-13 depicts iron pentacarbonyl vaporization system and a burner used for the CO flame study.

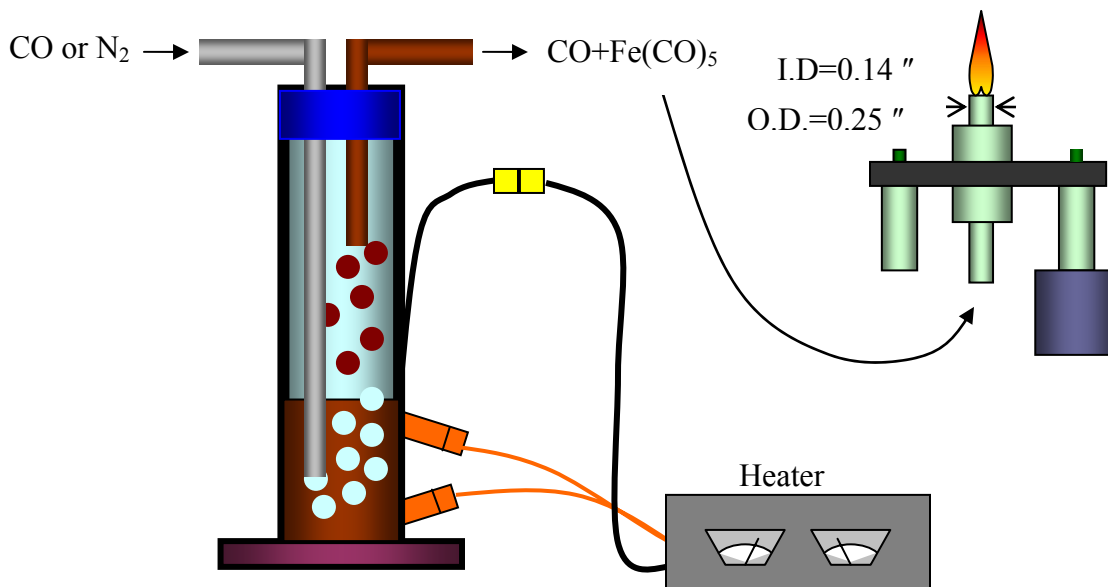


Figure 3-13. Vaporization system of iron pentacarbonyl and a CO flame burner.

The carbon monoxide gas at a flow rate of 0.45 liter per minute regulated by an Alicat Scientific digital flow controller was introduced into the fuel additive vaporization vessel through a tube. The fuel additive vaporization system was designed to seed the

CO gas with iron pentacarbonyl. To increase the concentration of the additive in the CO gas, the outside of the vaporization vessel was heated by Omega heater tape and its temperature was measured with a stainless steel type K thermocouple. A heater was used to maintain the constant temperature of the vessel at 60 °C. Figure 3-14 shows a photograph of the iron pentacarbonyl vaporization vessel and the heater.



Figure 3-14. A photograph of the iron pentacarbonyl vaporization vessel and the heater.

The CO gas was passed through the $\text{Fe}(\text{CO})_5$ liquid and combined with $\text{Fe}(\text{CO})_5$ gas before being delivered to the burner. The delivery line is also necessary to be heated to prevent the condensation of $\text{Fe}(\text{CO})_5$. Otherwise, the condensed $\text{Fe}(\text{CO})_5$ blocks the gas flow which results in the flame jumping up and down. The CO flame was approximately 6 cm tall reacted with air. The addition of iron pentacarbonyl visibly

changed the flame from the blue CO flame to the bright orange flame. This results from the blackbody radiation of the iron oxide particles present in the flame. The unseeded and seeded CO flames are shown in Figure 3-15.

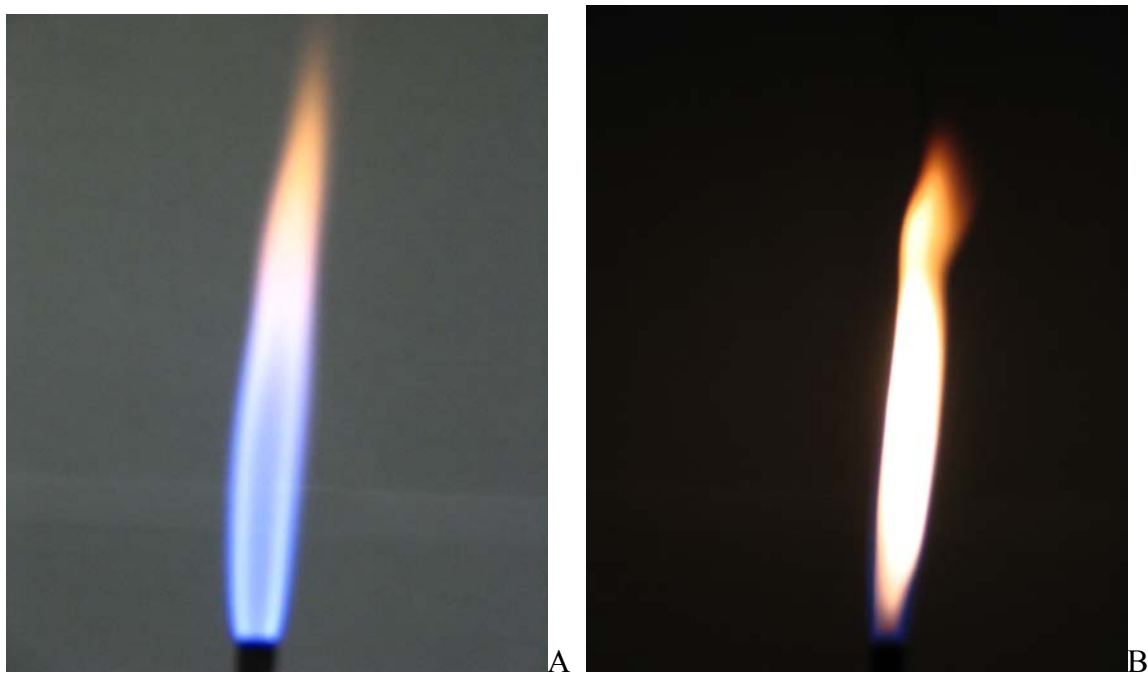


Figure 3-15. Photographs of CO flame. A) unseeded flame, B) iron seeded flame.

After all experiments were over, the nitrogen gas was filled in the vessel to prevent the dissociation of $\text{Fe}(\text{CO})_5$.

3.8.2 Experimental Apparatus of Laser Induced Fluorescence Spectroscopy

Laser-induced fluorescence spectroscopy (LIF) was employed to trace Fe atomic fluorescence emission in the seeded flame. The experimental apparatus for LIF is illustrated in Figure 3-16.

A frequency tripled Q-switched 355 nm Nd:YAG laser was used as a pump laser source. The laser was operated at a 10 Hz repetition rate with around 200 mJ/pulse energy. For the Fe excitation, the frequency-tripled laser output was tuned to the several Fe resonant transitions band using Optical Parametric Oscillator (OPO). An OPO

converts photon energy of a pump laser into lower energy by means of nonlinear optical interaction; thus, the higher photon energy of a pump laser is very essential. In addition, since the gain depends on pump power, sufficient pump power is necessary to support oscillation. In other words, the oscillation occurs only when the pump power reaches a particular threshold level. Above threshold, the gain is also dependent on the amplitude of the resonated wave. With pump wavelength of 355 nm, typical OPO yields the output wavelength ranging from 400 nm and 1000 nm. The OPO consists of not only an optical resonator and a nonlinear optical crystal, but also doubling crystal so that the output range can be broadened from 200 nm to 1000 nm. In this study, the Fe excitation wavelength was 296.69 nm that was created by frequency-doubling of 578 nm produced by means of nonlinear optical interaction. In spite of high pump power of the laser (~200 mJ/pulse), the output power passed all the way through optics in OPO drops around 2

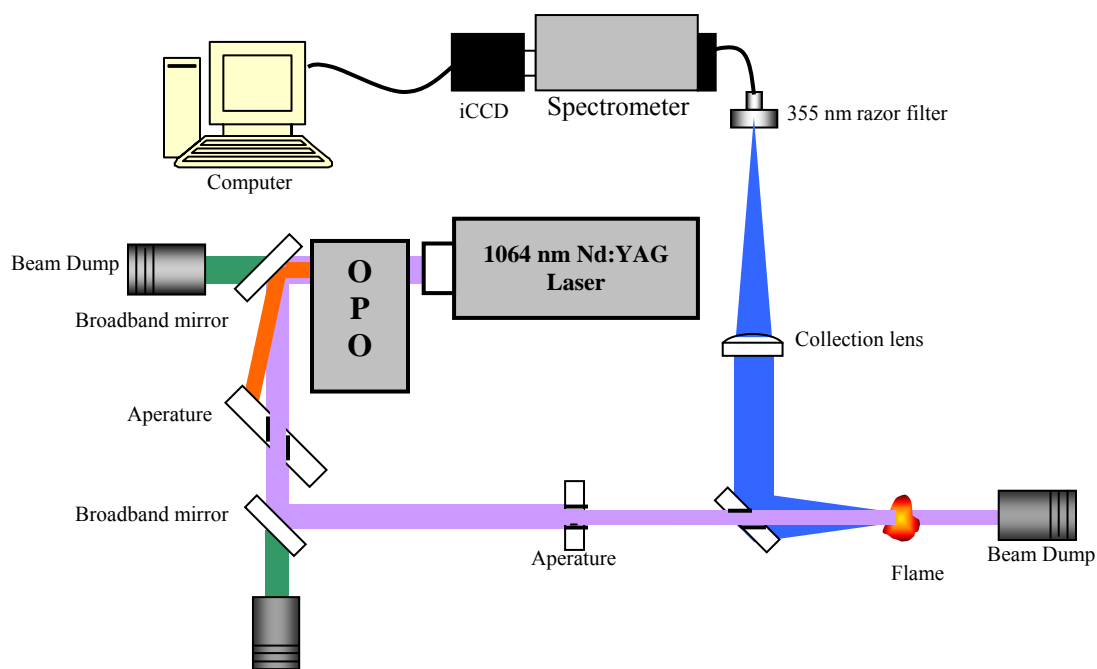


Figure 3-16. The optical setup for laser-induced fluorescence spectroscopy.

mJ/pulse. Upon exiting the OPO, the laser beam was turned by a 45° broadband mirror (200 ~ 400 nm). The output laser beam contains 3 sources of light having different wavelengths: one is tuned wavelength of 296.69 nm, another is residual of 355 nm, and the third is resonant source of 578 nm. These are dispersed by a prism. To block the unwanted beams, a 4"×4" square aperture was placed in the beam path so that only tuned beam could pass through it and strike to the sample.

3.8.3 Experimental Apparatus of *In Situ* Raman Spectroscopy

In situ Raman spectroscopy was employed to find the molecular state of iron oxide in the flame. A schematic of optical apparatus is depicted in Figure 3-17.

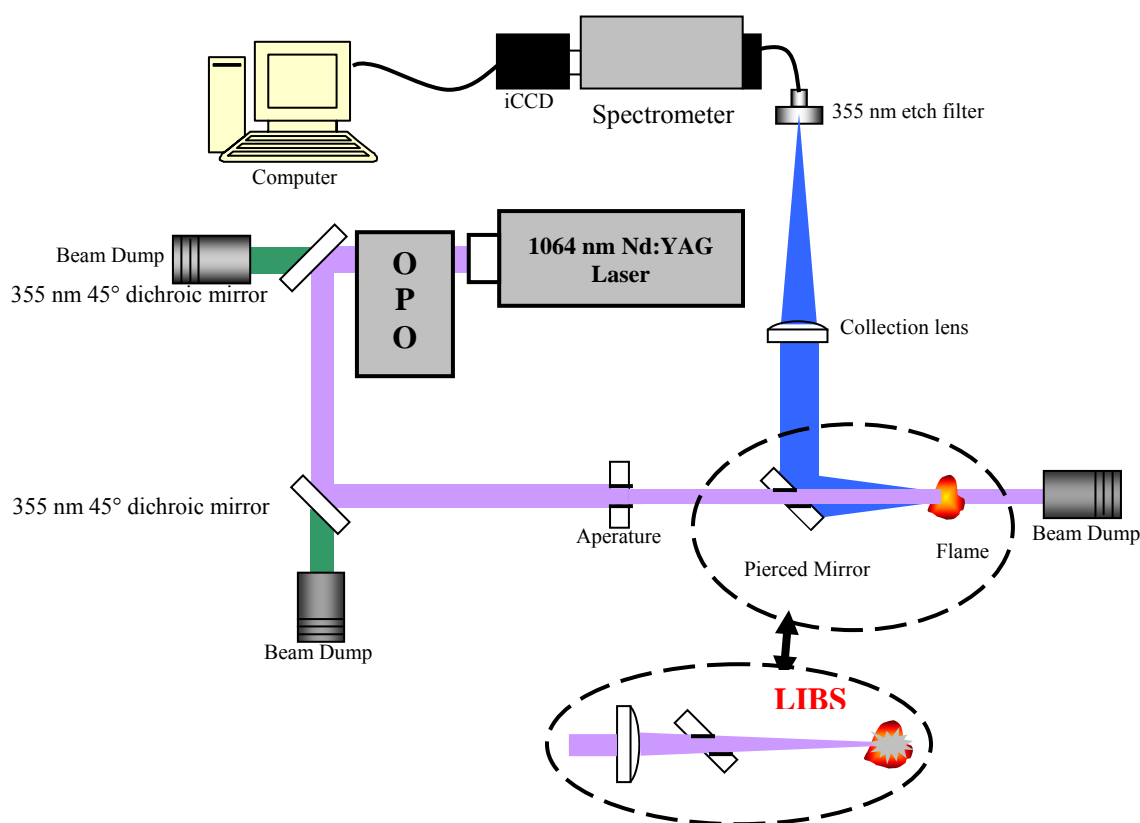


Figure 3-17. The optical set-up for *in situ* Raman spectroscopy.

Basically, the experimental setup was very similar with the LIFs set-up except several things. First, a frequency tripled Q-switched 355 nm Nd:YAG laser was used as a laser source. Two broadband mirrors were replaced in two 355 nm dichroic mirror.

Instead of using non-linear optical crystal in OPO, a 355 nm dichroic mirror was put into the line path making 4 more dichroic mirrors be available. Since the output source of 355nm was created through double and triple crystals with original source of 1064 nm, the output laser still includes 1064 nm and 532 nm residual light. A dichroic mirror reflects certain wavelengths while transmitting others; hence, the dichroic mirror is essential component to get rid of all residual wavelengths except 355 nm. Total eight dichroic mirrors were used to eliminate those unwanted lights efficiently. A dichroic mirror allows almost 99% of 355 nm light and only less one percent of others to be reflected on the surface; thus, using 8 dichroic mirrors (i.e. two in the laser, four in the OPO, two outside) can achieve that negligible amount of residual light reaches the flame. The optical set-up inside OPO is shown in Figure 3-18.

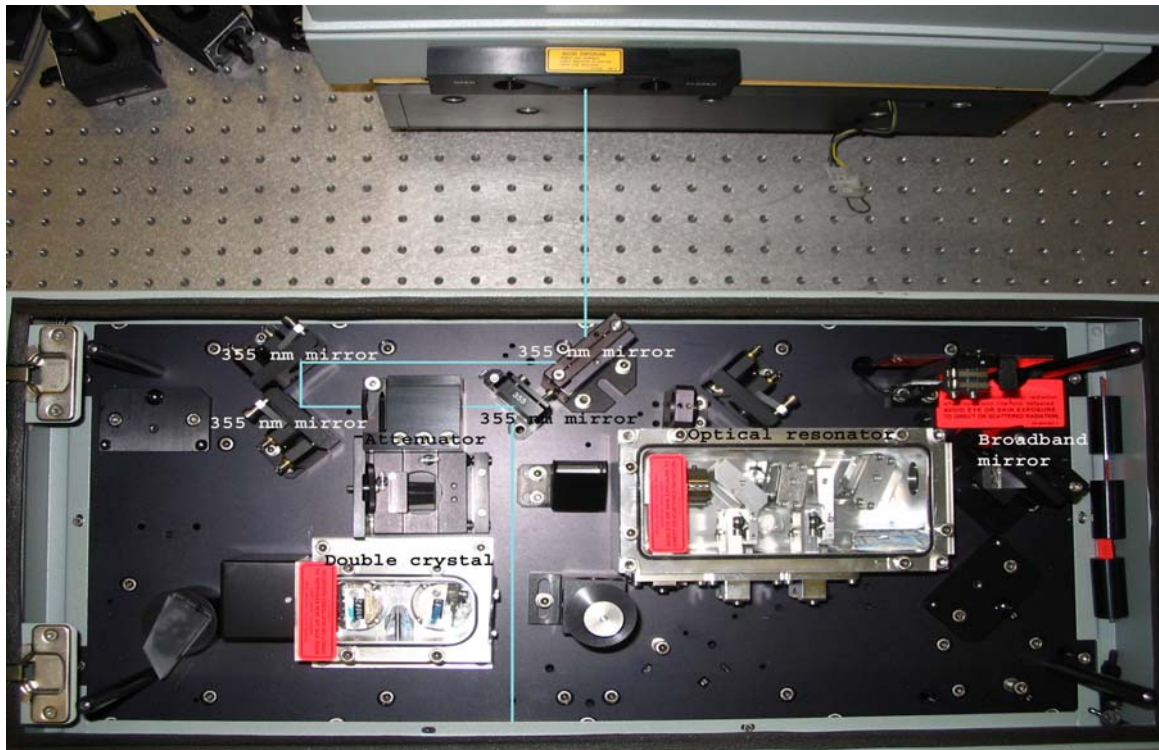


Figure 3-18. A photograph of an optical set-up inside OPO.

Since photofragmentation of species resulting from high laser power can be a serious issue in Raman spectroscopy, the laser power was attenuated using an attenuator between two 355 nm dichoric mirrors inside OPO, such that moderate laser power could be obtained in this study. In addition, a lens was placed in the beam path in order to check laser induced breakdown spectrum from iron compounds, while the layout of other optical components was maintained as illustrated in Figure 3-17.

For LIF spectroscopy, a 355 nm dichoric mirror at the right side of the attenuator was taken out, and consequently the light passed through the optical resonator and non-linear crystal such that tuned source of light could be generated.

Considering the detection of either the fluorescence or Raman scattered signal, the light was collected at an angle 0° with respect to the axis of the excitation light using a 4"×4" square center-pierced mirror and then focused to a fiber optic using 4" diameter plano convex lens. The light passed through a 355-nm razor edge long-pass filter before entering the fiber optic. Since the saturation of the detector is a significant issue in spectroscopic techniques, blocking elastically scattered stray light with the filter can efficiently prevent iCCD from being saturated by the elastic light. Using the sharp-edge filter is critical in cases where the Raman spectrum is very close to the excitation wavelength. In addition to the usage of the filter, the saturation of iCCD can be avoided by setting the grating window such that the excitation wavelength is not on the detector.

The detected light transfers through the fiber optic into a 0.275-m grating spectrometer and is recorded with an intensified charge coupled device (iCCD) array detector. Regarding a setting for the detection of Raman scattered signal as well as the LIF signal, the iCCD gate width and the delay were 200 ns and 100 ns respectively,

which centered them temporally on the laser wavelength. The spectral window for LIF signal was centered on 373 nm while that for Raman scattered signal was centered on 371.1 nm. Visualization and recording of emission spectra was achieved using an Labview program.

3.8.4 Isooctane Flame Study

Experimental setups used for isooctane flame study were basically the same as that discussed previously. The optical components and specification for the spectroscopic system apparatus are listed in Table 3-12. A concentric diffusion burner shown in Figures 3-1 and 3-2 was employed for all experimentations. Fuel was the isooctane seeded with the iron pentacarbonyl of 4000 ppm by mass of the isooctane. For LIF, twenty three heights were newly selected and designated with the number 1 through 23. Some positions of the flame overlapped with previous positions for the light scattering experiments, but mostly new positions in the soot inception regime were selected for spectroscopy. The first height designated “1” was located in 0.1 cm above the burner lip. All measurements were made along the centerline, at 23 different heights from the bottom to top of the flame. The summary of these heights are listed in Table 3-13. The results of all experimentation will be presented in the next chapter.

In addition to LIF, absorption spectroscopy was performed using a hollow cathode lamp to verify any possible LIF quenching phenomenon throughout the seeded isooctane flame. A schematic of apparatus for absorption spectroscopy is depicted in Figure 3-19. Fe atomic emission from the hollow cathode lamp was focused through the flame using a focal lens. Then, the transmitted light was collected using a collection lens and transferred through the fiber optic into the spectrometer. Finally, the signal was

Table 3-12. Components of spectroscopic system apparatus.

Device	Manufacturer	Model	Description
Equipment			
1064 nm frequency doubled/tripled Nd:YAG Laser	Continuum	PRII 8000	532/355 nm, 10Hz repetition rate, pulse energy varied
Optical Parametric Oscillator	Continuum	Panther Ex HEO	Energy: $\leq 50\%$ pump source Wavelength: 195 nm~2800 nm
Spectrometer	Action Research Corporation	SpectraPro-275, S/n 275995S	0.275 Meter Triple Grating Spectrometer
iCCD	Princeton Instruments	Model: 1024MLDS-E/1, N119302	Intensified CCD, 200 row chip
Software	Labview		Metal Emissions Program
Fiber Optic			6 foot, high optical grade, 17 fiber bundle, 1.5 mm diameter ACTON
Optics			
Beam dump	Kentek	ABD-2	Beam dump
355 nm dichroic mirror	CVI Laser corporation	Y3-2037-45-UNP	45 degree, 355 nm dichroic mirror, 2" diameter
Aperture	Newport	ID-1.0	aperture
Square Pierced Mirror	Rolyn Optics	60.2475	100 mm \times 100 mm \times 1 mm, center pierced-0.5 inch \pm 0.2" diameter
Collection Lens	Comar	160-PG-100	4" Plano-convex
355 nm Razor edge filter	Semrock	LP01-355RU-25	355 nm 99% cutoff
Focusing Lens	CVI Laser Coporation	PLCX-50.8-130.8-UV-355-532	Plano-convex, 250 mm focal length, 2" diameter
Broadband Mirror	Newport	10D20RM.2	Flat mirror, pyrex 25.4 mm diameter 300~400

recorded with an iCCD. The optical components and specification for spectroscopic system apparatus are tabulated in Table 3-14.

Table 3-13. Data collection heights for spectroscopy.

Positon label	Height Above Burner tip (cm)	Distance between two heights (cm)
1	0.10	-
2	0.60	0.50
3	1.20	0.60
4	1.80	0.60
5	2.40	0.60
6	3.00	0.60
7	3.70	0.70
8	4.50	0.80
9	5.25	0.75
10	6.10	0.85
11	7.10	1.00
12	8.30	1.20
13	9.40	1.10
14	10.60	1.20
15	11.60	1.00
16	12.60	1.00
17	13.80	1.20
18	15.10	1.30
19	16.65	1.55
20	18.50	1.85
21	20.55	2.05
22	22.20	1.65
23	23.95	1.75

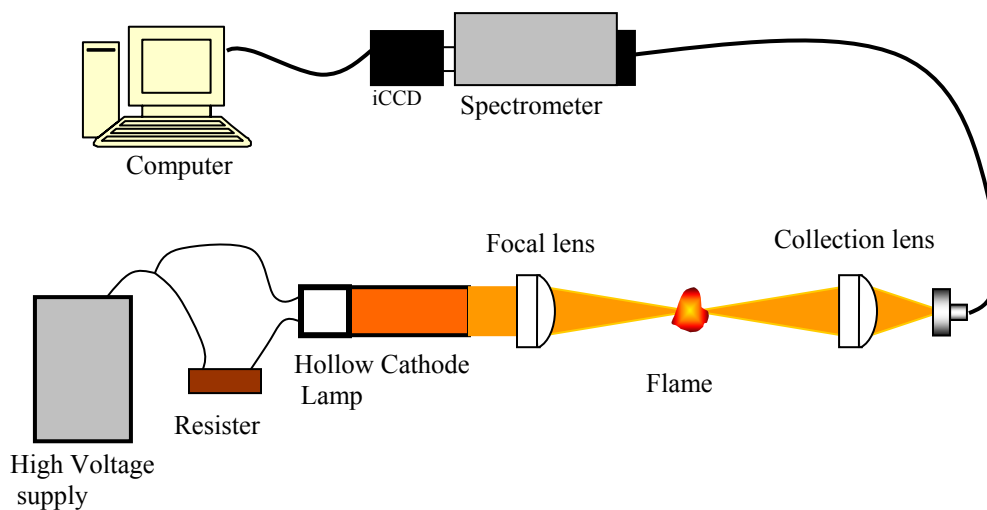


Figure 3-19. The optical set-up for absorption spectroscopy.

Table 3-14. Components of the system apparatus for absorption spectroscopy.

Device	Manufacturer	Model	Description
Equipment			
Hollow Cathode Lamp	Perkin-Elmer intensitron lamp	1380	Operation 7 mA Element: Fe
Precision high voltage supply	Stanford Research Instruments	PS325	Digital high voltage power supply
Spectrometer	Action Research Corporation	SpectraPro-275, S/n 275995S	0.275 Meter Triple Grating Spectrometer
iCCD	Princeton Instruments	Model: 1024MLDS-E/1, N119302	Intensified CCD, 200 row chip
Software	Labview		Metal Emissions Program
Fiber Optic			6 foot, high optical grade, 17 fiber bundle, 1.5 mm diameter ACTON
Optics			
Focusing Lens	CVI Laser Coporation	PLCX-50.8-51.5-UV	Plano-convex, 100 mm focal length, 2" diameter
Collection Lens	CVI Laser Coporation	PLCX-50.8-51.5-UV-355	Plano-convex, 100 mm focal length, 2" diameter

CHAPTER 4 INTEGRATED RESULTS AND DATA ANALYSIS

All data and results of the experiments obtained from smoke point study, the elastic light scattering measurement, transmission, and transmission electron microscopy with thermophoretic sampling are presented and analyzed in this chapter. Characteristic size, number density, and volume fraction data for soot particles in the unseeded and seeded flames will be extracted using all experimental data. In addition, the results invoked from Laser-induced fluorescence and *in situ* Raman spectroscopy are discussed in this chapter.

4.1 Smoke Point Study

The quantity of stoichiometric oxidizer is a measure of an amount of oxidizer needed to completely burn a quantity of fuel. If the oxidizer supplied is more than the stoichiometric quantity, the flame is called a fuel lean flame, while supplying less than the stoichiometric oxidizer in the flame leads to a fuel-rich flame. The primary purpose of this project is to investigate the effect of the metal additives on soot suppression in the flame. This can be accomplished in part through comparing soot profiles of the unseeded and seeded flame. This process may be optimized by working within a stoichiometric regime with a noticeable additive effect. To accomplish this, the smoke point of the unseeded flame was investigated. The smoke point is defined as the point in which the soot plume in the flame tip (i.e. visible smoke) visually disappeared as the oxygen flow was increased. It was noted that the smoke point kept changing during the early period of the experiment, due presumably to the expansion of rubber pumping tube leading to an increase in fuel supply, and possibly to burner heating. This also resulted in a noticeable

change in the flame height. To avoid this issue, it was first essential to find the period that the smoke point and the flame height were consistent. Oxygen flow rate at the observed smoke point with respect to time is shown in Figure 4-1.

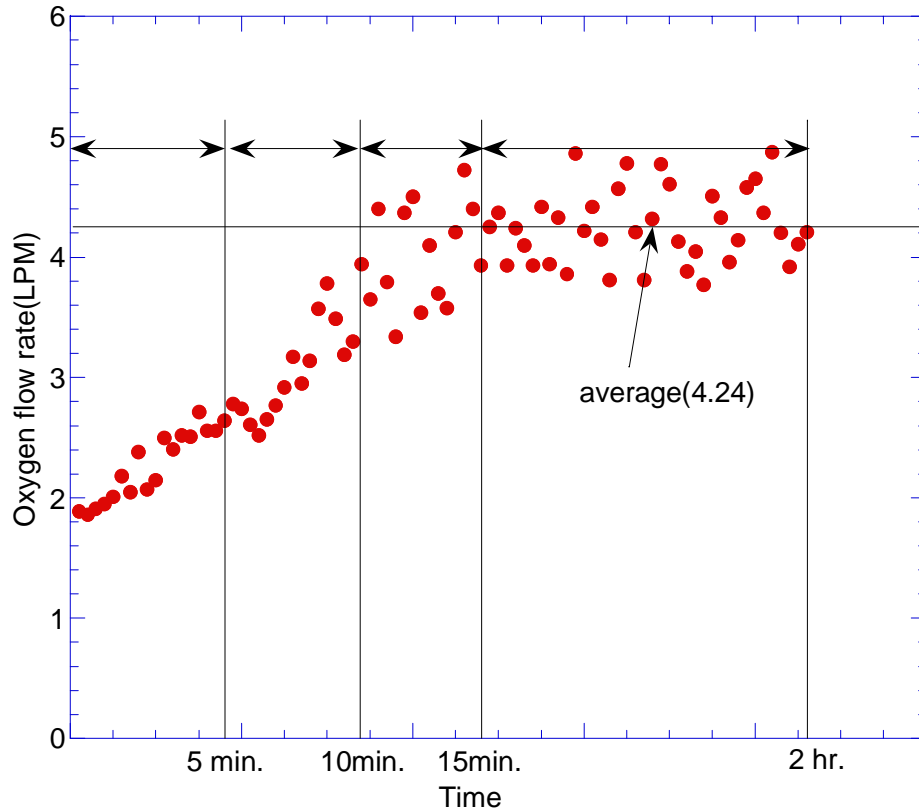


Figure 4-1. Plot of oxygen flow rate at the smoke point as function of time.

Initially, oxygen flow rate increases and it converges after about 15 minutes. After that point, the oxygen flow rate was stable at a flow rate of 4.24 LPM corresponding to the smoke point. This measurement shows that at least 15 minutes warming up is required to reach the steady flame condition after ignition. To explore soot suppressing effects, it is then desirable to run the flame at or above the smoke point, as running significantly below the smoke point (i.e. excess oxygen) diminishes the sooting behavior.

A study of an influence on the smoke point by the concentration of the metal additive was then investigated to arrive at an optimal additive concentration. Due to the

complexity of the experimental measurements, a simple parametric study was avoided. Rather, it was determined to select a single best condition for in depth study. The concentration of iron additive and the resulting smoke point was evaluated using fuels doped to 10 different concentration of $\text{Fe}(\text{CO})_5$. The smoke point of each additive concentration was found in the same manner explained above, and four experimental data sets over a number of days were collected for all different concentrations. A summary of the oxygen flow rate, the equivalence ratio, and oxygen to fuel ratio at the smoke point with respect to 10 different concentration of $\text{Fe}(\text{CO})_5$ is tabulated in Table 4-1 and plotted in Figure 4-2.

Table 4-1. Average of 4 oxygen flow rates with their standard deviation and relative standard deviation, the equivalence ratio, and oxygen to fuel ratio for 10 different concentrations.

Concentration of $\text{Fe}(\text{CO})_5$ (ppm)	Average of O_2 flow rate (LPM)	Standard deviation	RSD (%)	ϕ	A/F ratio
0	4.23	0.08	1.79	0.66	18.90
500	3.74	0.17	4.48	0.75	16.71
750	3.35	0.07	2.06	0.83	14.97
1000	3.23	0.39	12.19	0.87	14.44
2000	3.16	0.17	5.51	0.89	14.12
4000	3.05	0.05	1.65	0.92	13.63
6000	3.07	0.1	3.15	0.91	13.72
8000	3.1	0.16	5.03	0.90	13.85
15000	2.96	0.18	5.94	0.94	13.23
20000	2.96	0.17	5.7	0.94	13.23

As shown in Figure 4-2, the oxygen to fuel ratio decreases rapidly at lower concentrations, and is flattened out after reaching the minimum at the concentration of 4000 ppm. Since reduced oxygen to fuel ratio corresponds to a reduced propensity to smoke, 4000 ppm was determined to be the best value. At the zero concentration, the

oxygen flow rate is determined to be 4.23, which is identical to the stoichiometric quantity of oxygen flow rate obtained in the foregoing smoke point study, as it should be.

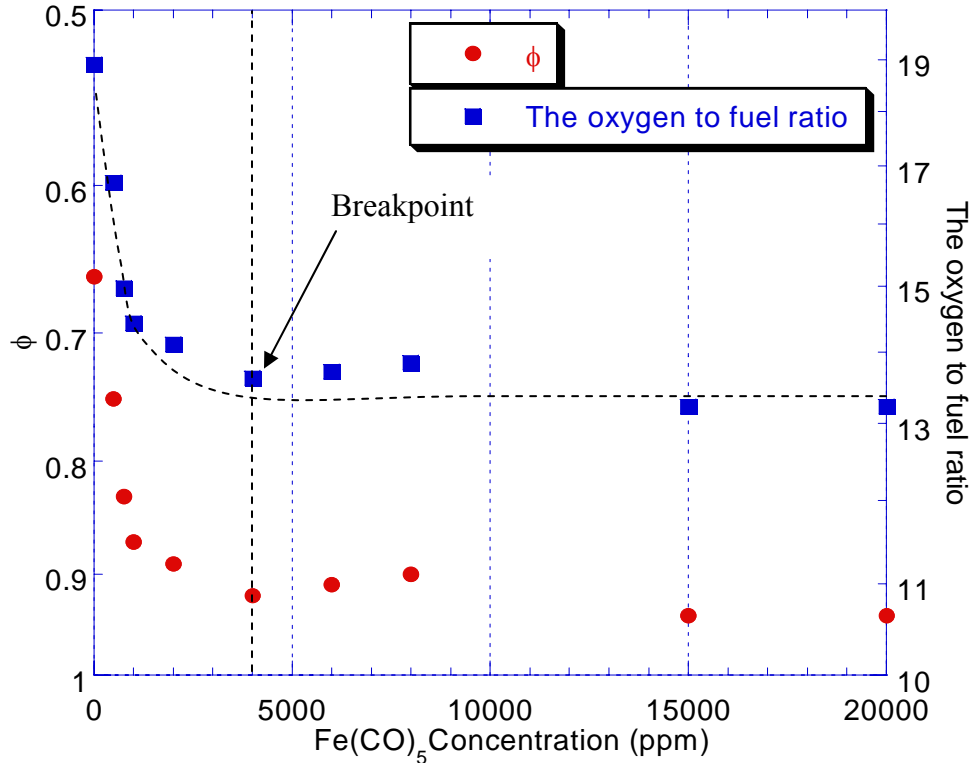


Figure 4-2. Smoke point, as measured by the corresponding oxygen to fuel ratio and the equivalence ratio, as a function of iron pentacarbonyl concentration. Note that the equivalence ratio increases due to a reduction of the necessary oxygen quantity.

4.2 Elastic Light Scattering Results

The light emitted from the laser cavity was vertically polarized, and only vertically polarized scattered light was captured by a polarizer at the head of the scattering collection optics. Therefore, the vertical-vertical differential scattering coefficient, K'_{VV} was the scattering parameter of interest. This parameter was extracted from the PMT raw signal output accurately using two calibrations. One is a stray light calibration using methane and nitrogen to eliminate the extraneous signal induced by the reflection of laser

light from various surfaces (i.e. stray light). The other is a methane calibration to relate K'_{VV} to the signal S_{VV} . The same methane signal was used for both calibration operations. Figure 4-3 shows a typical PMT response signal for the calibration gases and the flame signals.

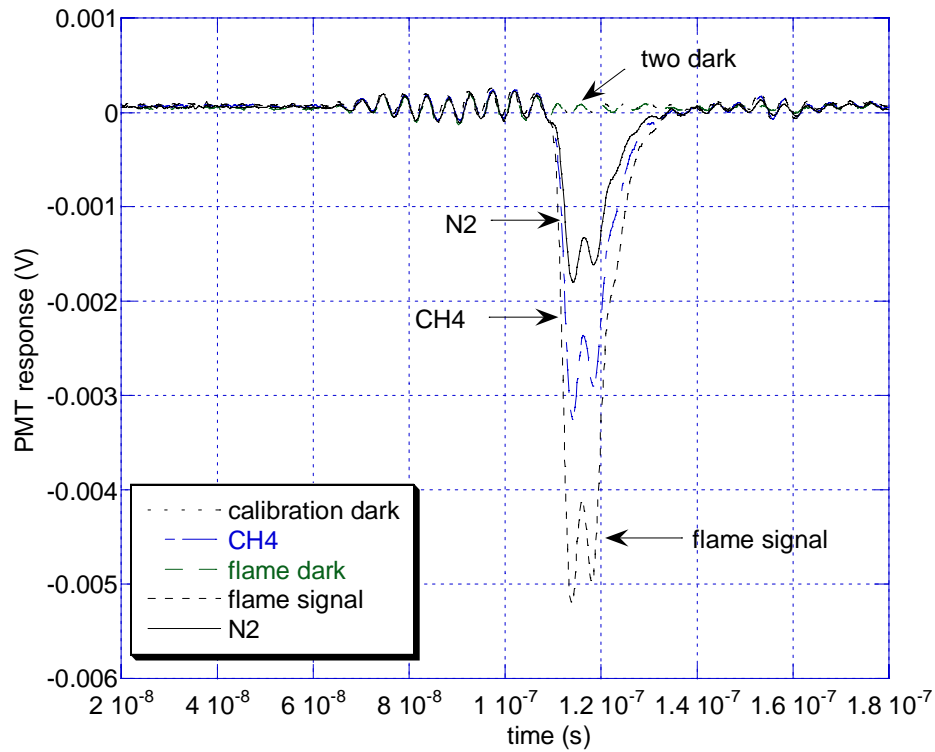


Figure 4-3. Typical scattered signal response from photomultiplier tube measuring calibration gases and flames. Calibration gas signals are attenuated by a factor of $10^{0.3}$, and flame signals are attenuated by a factor of 10^5 to preserve signal linearity.

In Figure 4-3, calibration gas and flame signals have been attenuated by a factor of $10^{0.3}$ and 10^5 , respectively, to preserve linearity in the PMT response. The baseline of each signal contains a repeatable noise signal attributed to electrical noise stemming from the laser Q-switch discharge. The repeatable noise signal can be removed using dark signals taken for both the calibration gas and the flame signal shown in Figure 4-3. These dark signals were taken prior to each measurement of both the calibration gases and the flame signals, with the laser blocked from the detector.

Ten experimental raw data sets (N=10) over a number of days were collected for the conditions of both the unseeded and iron seeded flames respectively. With the PMT raw signals, the differential scattering coefficient was calculated by the following procedures. First, intensities of the scattered and dark signals were integrated over the signal width of 50 ns. The integrated value of the dark signal was then subtracted from that of the scattered signal. The final step of the calculation was to consider the attenuation factors of the neutral density filters and correct the final value for stray light. The average values of the differential scattering coefficient in the unseeded and seeded flames for each height are summarized in Table 4-2 along with the standard deviations.

Table 4-2. Average (N=10) K'_{VV} results of the unseeded and seeded flame and standard deviations. Flame heights are measured from the burner lip.

Height (cm)	Unseeded K'_{VV} ($\text{cm}^{-1}\text{sr}^{-1}$)		Seeded K'_{VV} ($\text{cm}^{-1}\text{sr}^{-1}$)	
	Average	Standard deviation	Average	Standard deviation
1	3.70E-03	8.59E-04	3.98E-03	7.31E-04
3	3.87E-03	4.71E-04	2.91E-03	9.92E-04
5	3.26E-03	1.11E-03	2.67E-03	8.99E-04
7	2.97E-03	1.11E-03	3.05E-03	1.08E-03
9	3.60E-03	1.15E-03	2.68E-03	5.83E-04
11	4.10E-03	6.99E-04	3.77E-03	8.65E-04
13	3.78E-03	4.21E-04	3.13E-03	1.23E-03
15	2.76E-03	3.54E-04	2.28E-03	8.58E-04
17	1.74E-03	4.36E-04	1.40E-03	3.25E-04
19	1.04E-03	2.04E-04	1.01E-03	2.62E-04
21	5.44E-04	1.06E-04	3.95E-04	1.20E-04
25	2.44E-04	4.27E-05	6.35E-05	4.07E-05

In spite of the consistent experimental conditions, the raw (i.e. absolute) scattered light signals at each data point had a large standard deviation (32% RSD on average) due to laser fluctuations and changes in the quantity of the stray light from day to day. As discussed in Chapter 2, this problem was eliminated in the procedure of the differential scattering coefficient calculation using the relative scattered intensities between the

calibration scatterer (i.e. methane) and the scattered signal from the soot particles. The absolute signal intensities vary day in, day out, but still remain in relative agreement with respect to the methane calibration signal. As shown in Table 4-2, the standard deviation for the differential scattering coefficient is much less than that in the daily absolute scattering signals. Consequently, the scattering data were characterized as remaining relatively consistent and repeatable over all experiments, with an average relative standard deviation of 27%.

The differential scattering coefficients for the unseeded and seeded flames are plotted at each height in Figure 4-4, noting the logarithmic scale.

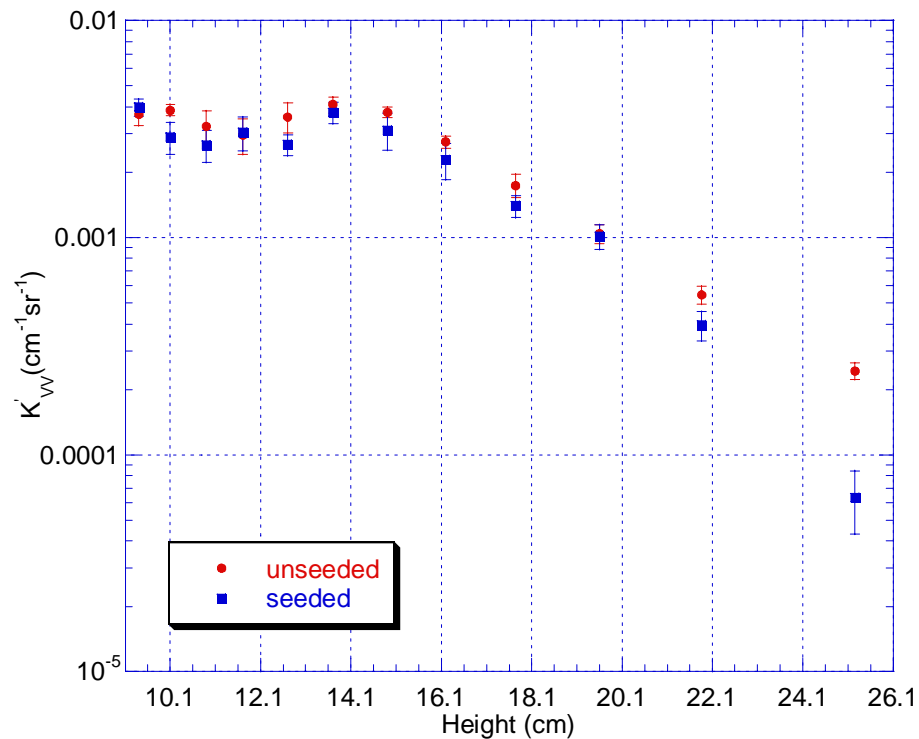


Figure 4-4. Unseeded and seeded differential scattering coefficients in logarithmic scale. Error bars represent one standard deviation.

The scattering coefficients tend to peak in both cases near about 14 cm above the surface, and then steadily decrease with additional height (i.e. increasing residence time).

This behavior indicates that the soot profile has transitioned from the growth regime to the oxidation regime, which is characteristic of diffusion flames. Regarding the comparison of the unseeded and the iron-seeded flames in the growth regime, the coefficients are almost identical to both flames at these early heights. Meanwhile, the prominent deviation between two flames in scattering coefficient is shown in the soot oxidation zone. It is concluded that the additive does not have any noticeable influence on soot growth characteristics in the soot growth regime but does in the soot oxidation regime. This is consistent with the observations of Masiello (2004), following detailed investigation of the growth regime.

It is also significant to note that intensities of both the incident and scattered light were attenuated due to soot particles existing out of the scattering volume during radial passage of light in the flame. Therefore, the values of the scattering coefficient are required to be corrected by the transmission data presented in the following section. The absolute values of the coefficient were calculated by dividing the original values by the transmission. Only the corrected coefficients for both flames were presented in Figure 4-4, the uncorrected values will be found in Appendix B.

4.3 Transmission Results

Six transmission measurements ($N=6$) for the unseeded and seeded flames were carried out at the flame heights corresponding to the positions in the scattering experiments. As discussed in Chapter 3, the transmission through the flame is described by the ratio of the laser pulse power transmitted through the flame to a reference power measured from a position outside of the flame. The summary of the transmission results for the unseeded and seeded flames is tabulated in Table 4-3. In addition, the transmission for the unseeded and seeded flames are plotted at each height in Figure 4-5.

Table 4-3. Average (N=6) transmission results of the unseeded and seeded flames and standard deviations. Flame heights are measured from the burner lip.

Height (cm)	Unseeded		Seeded	
	average	Standard deviation	average	Standard deviation
9.4	0.78	0.02	0.77	0.03
10.1	0.75	0.02	0.77	0.03
10.9	0.75	0.04	0.75	0.03
11.7	0.72	0.02	0.73	0.03
12.7	0.73	0.04	0.75	0.06
13.7	0.73	0.04	0.70	0.03
14.9	0.74	0.03	0.76	0.04
16.2	0.75	0.05	0.79	0.04
17.75	0.84	0.07	0.88	0.01
19.6	0.88	0.05	0.94	0.02
21.85	0.93	0.04	0.96	0.02
25.25	0.94	0.02	0.97	0.02

Transmission for both unseeded and seeded flames are greater at the higher heights, which further corroborates the soot burnout regime due to oxidation of soot as discussed above. Furthermore, while the transmission between the unseeded and seeded flame shows little deviation at the lower heights, the transmission of the seeded flame is larger than that of the unseeded flames at the higher heights. This is evidence that soot in the seeded flame was additionally reduced within the oxidation zone.

In general, the transmission provides an overall extinction coefficient for the line of sight through the flame using the Beer-Lambert law if the optical pathlengths of the flame are known. However, this is not the proper way to determine the extinction coefficient if the path is not homogeneous. It can correctly be determined using deconvolution techniques (e.g. Abel inversion) in case the flame width is sufficiently large, but such techniques were not used in this study.

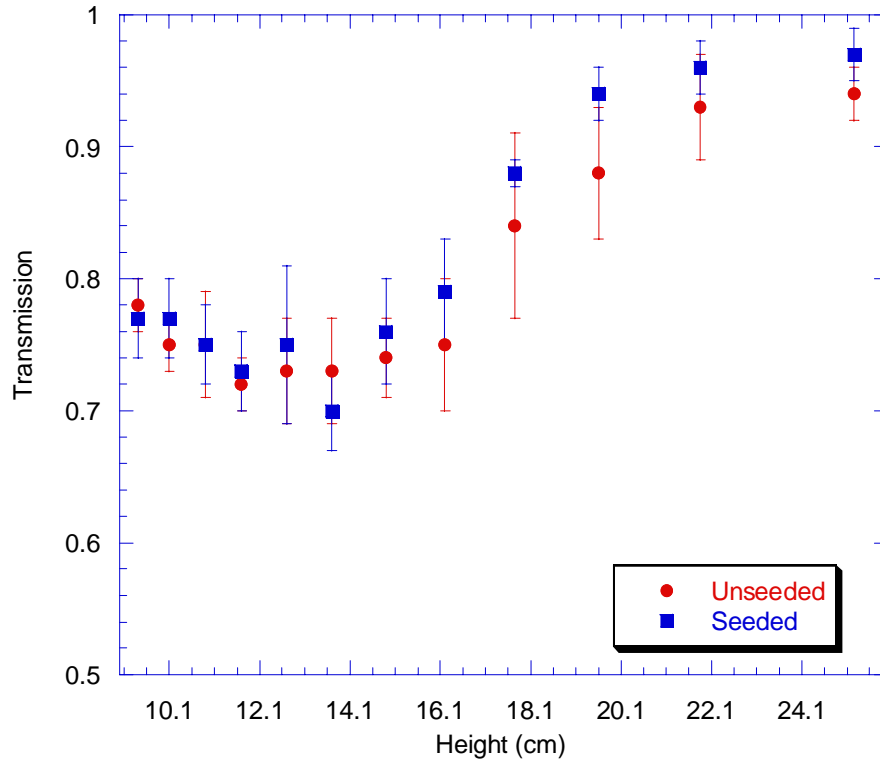


Figure 4-5. Transmission through the unseeded and seeded flames.

4.4 Soot Characteristics Determined from RDG Theory

4.4.1 Transmission Electron Microscopy

Soot aggregates were deposited on electron microscopy grids by thermophoretic sampling at 12 various heights in the unseeded and seeded flame. By means of a transmission electron microscope (TEM), 25 digital photographs of soot samples on each grid were taken so that measurements could be made to determine the fractal morphology of soot aggregates, and characterize scattering parameters of primary soot particle such as size, number density and volume fraction using Rayleigh-Debye-Gans (RDG) scattering theory. TEM images of typical soot aggregate at different heights in the unseeded and seeded flames are represented in Figure 4-6.

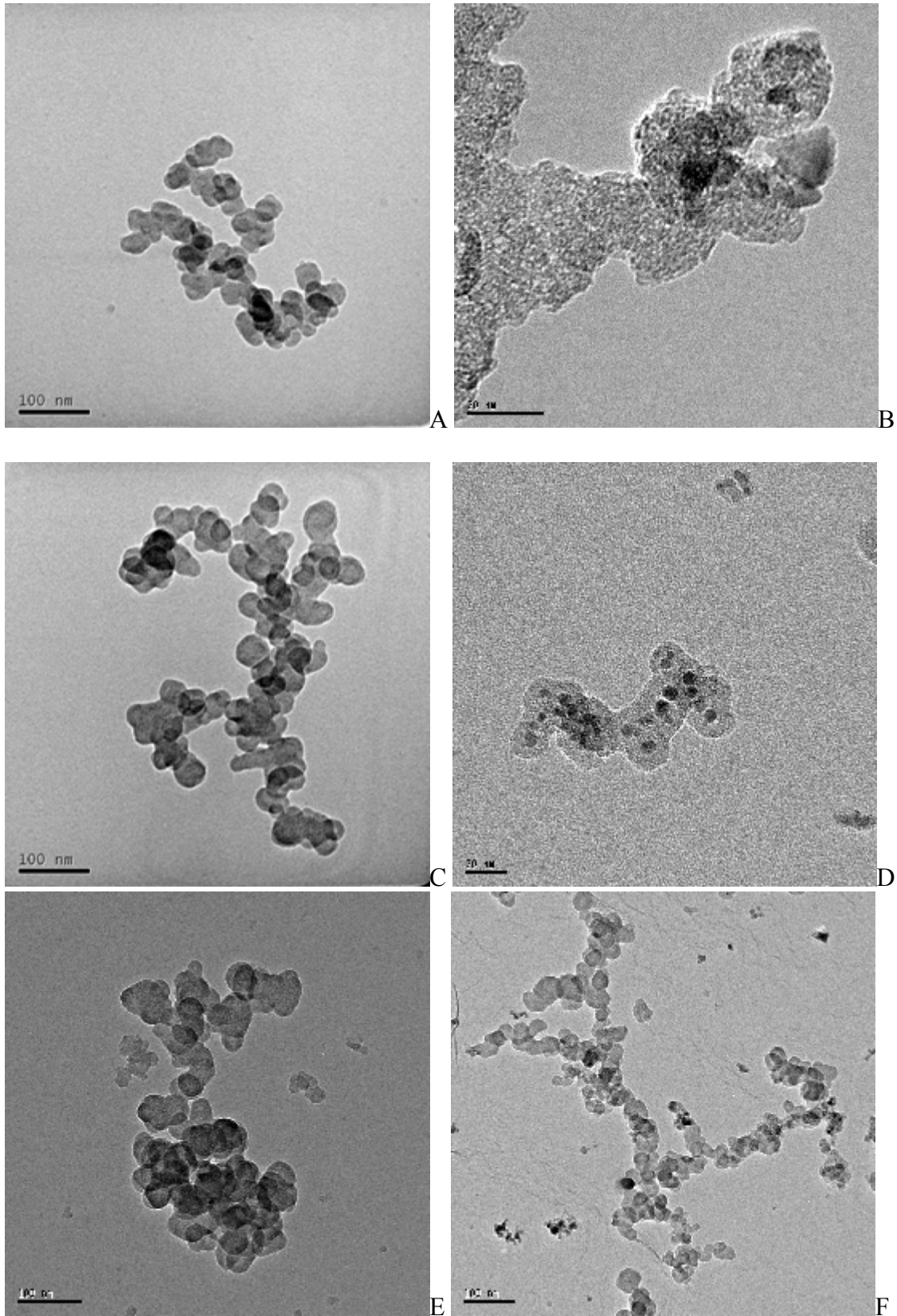


Figure 4-6. Transmission electron micrographs of soot particles at different axial positions.

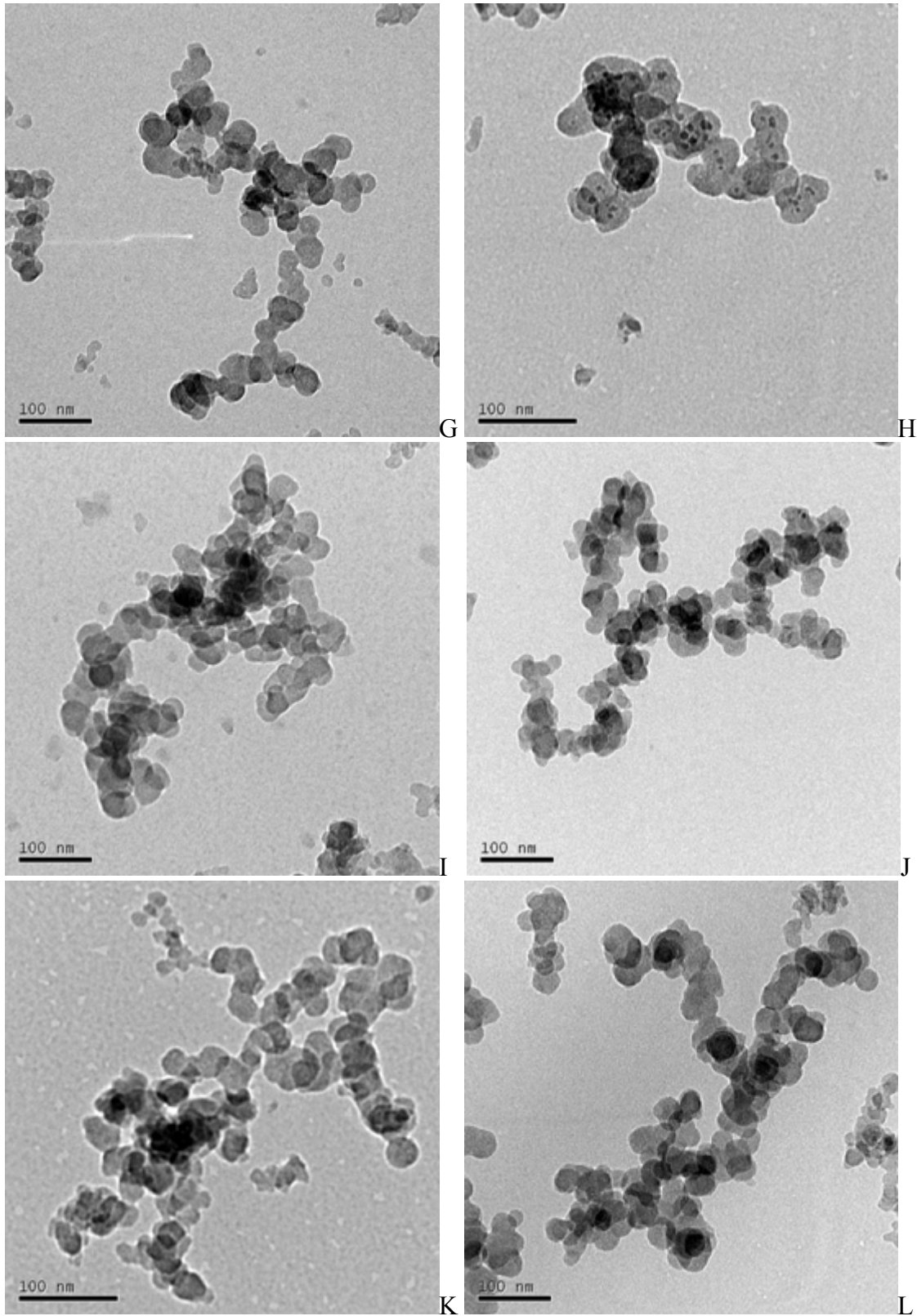


Figure 4-6. Continued

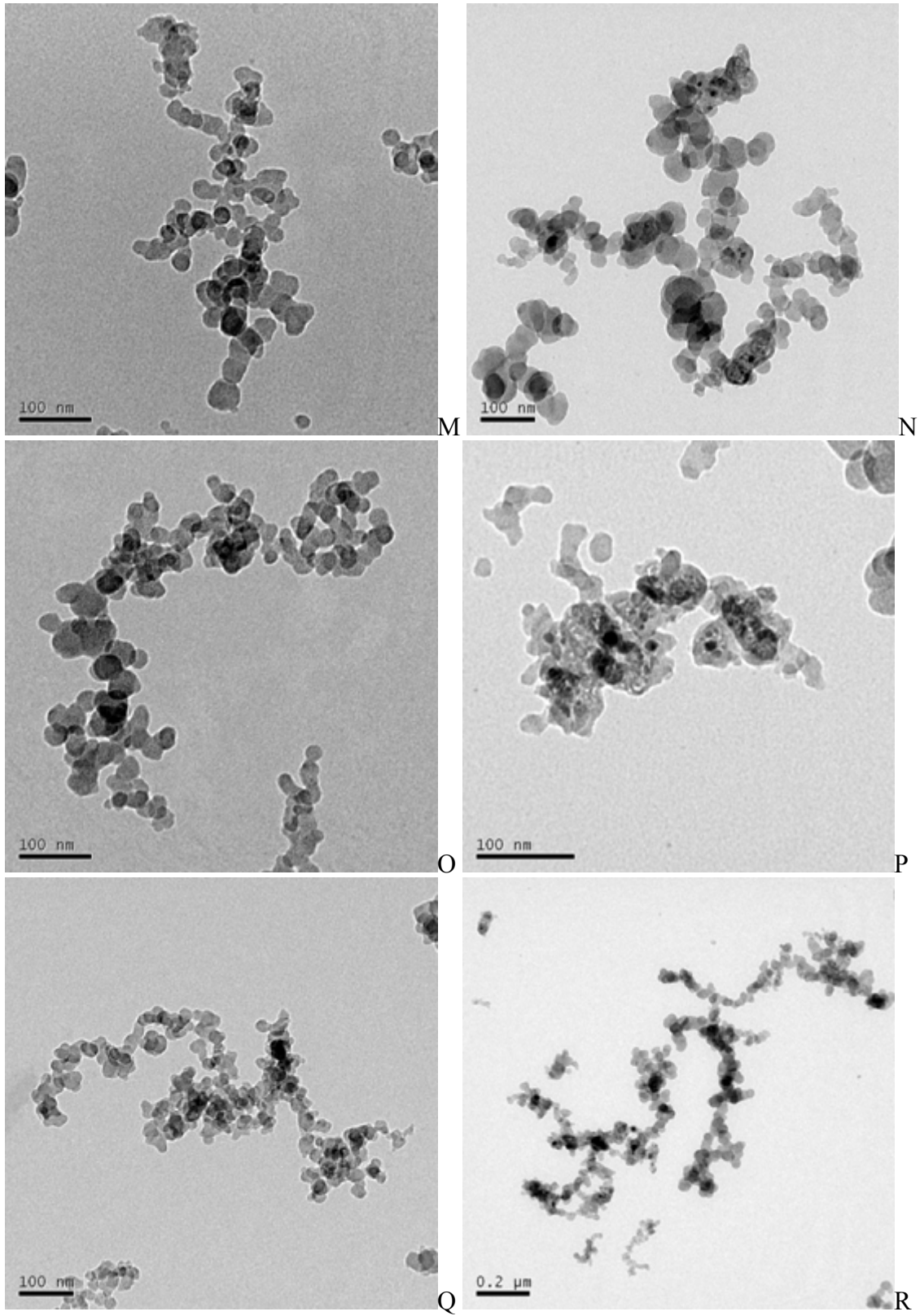


Figure 4-6. Continued

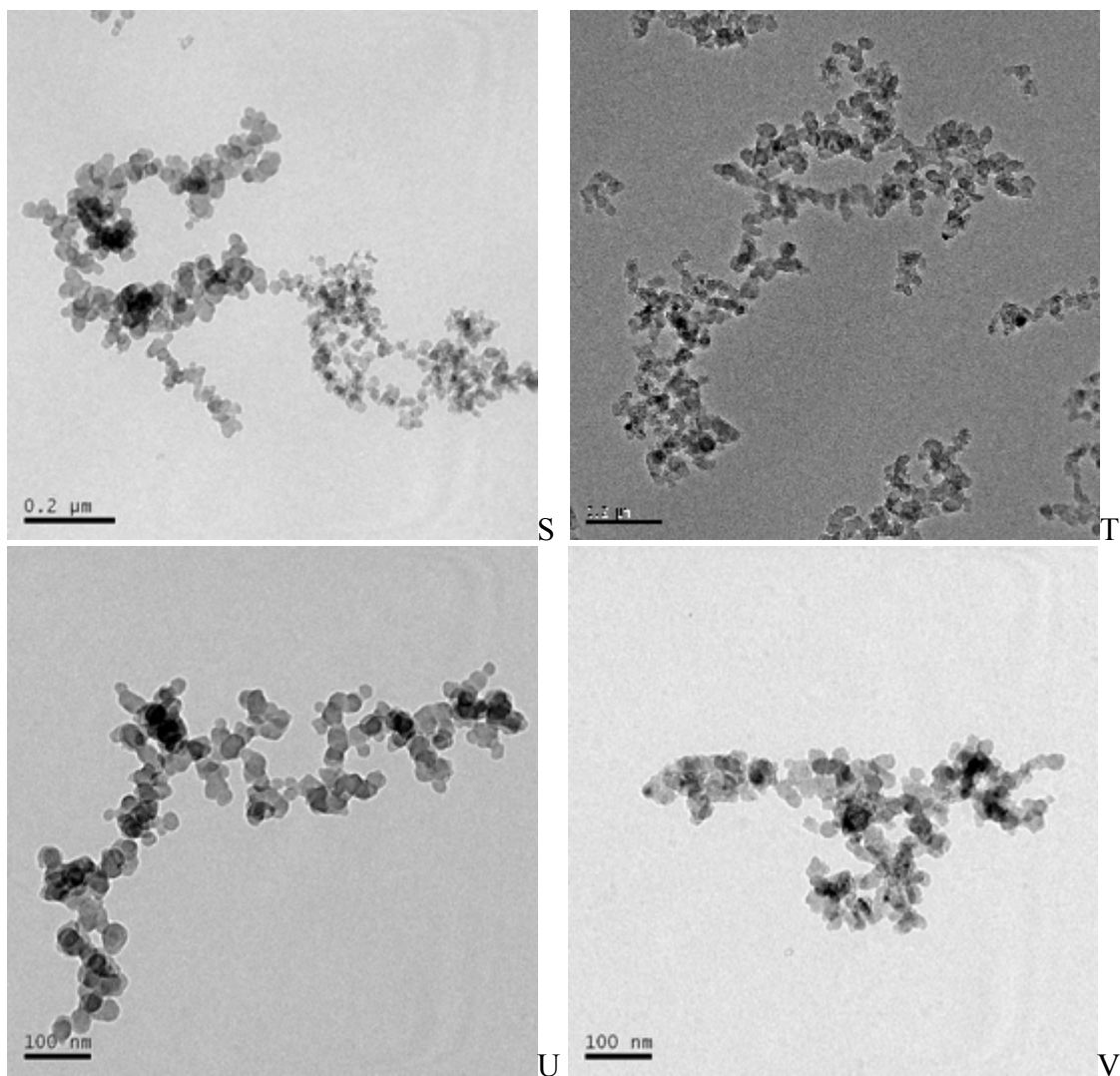


Figure 4-6. Continued. A) H=9.4 cm, unseeded flame. B) H=9.4 cm, seeded flame. C) H=10.1 cm, unseeded flame. D) H=10.1 cm, seeded flame. E) H=10.9 cm, unseeded flame. F) H=10.9 cm, seeded flame. G) H=11.7 cm, unseeded flame. H) H=11.7 cm, seeded flame. I) H=12.7 cm, unseeded flame. J) H=12.7 cm, seeded flame. K) H=13.7 cm, unseeded flame. L) H=13.7 cm, seeded flame. M) H=16.2 cm, unseeded flame. N) H=14.9 cm, seeded flame. O) H=17.75 cm, unseeded flame. P) H=16.2 cm, seeded flame. Q) H=19.6 cm, unseeded flame. R) H=19.6 cm, seeded flame. S) H=21.85 cm, unseeded flame. T) H=21.85 cm, seeded flame. U) H=25.25 cm, unseeded flame. V) H=25.25 cm, seeded flame.

Based on TEM analysis, the soot aggregates have a primary particle diameter ranging from 13.7 to 48.3 nm, and contain primary particles ranging between about 10 and nearly

1000 per aggregate. It is noteworthy that the primary particle diameters are generally less than 35 nm (see Figure 4-9), which yields the dimensionless size parameter no greater than 0.21 for the wavelength of 532 nm. It indicates that assuming individual primary particles as Rayleigh scattering particles is reasonable. In addition, soot aggregates shown in Figure 4-6 are approximately composed of spherical primary particles, consistent with flame-generated soot.

More agglomerated soot clusters were often observed at a higher position; thus, the number density of primary soot particle per aggregate was greater while the size of individual particles was smaller, attributed to soot oxidation. Overall, TEM analysis has an advantage in observing the aggregate directly; however, there are difficulties in characterizing the size and morphology of three-dimensional aggregates from a projected image. It is a drawback of TEM analysis.

It is also observed that the iron is concentrated in the cores of the soot particles in TEM images for iron-seeded flame. Evidence presented here demonstrates that iron pentacarbonyl seeded flames yield particulates that are soot/iron composites. Such effects were carefully investigated. It is noted that when soot particles overlap one another, the transmission is reduced, resulting in dark regions that might be mistaken for iron-rich clusters. Therefore, using EDS avoids such confusion between overlapping of particles and the inclusion of iron-rich species within the particle. Additional comments will be offered later relating to Figure 4-6 images as it relates to iron-cluster analysis.

4.4.2 Fractal Properties of Soot Aggregates

The morphological fractal features of soot aggregate can be characterized by a power law relationship between the number of primary particles in an aggregate and its projected area on TEM image, as described in Equation 2-16,

$$N_{par} = k_f \left(R_g / d_{par} \right)^{D_f}, \quad (2-16)$$

where the key parameters to fully characterize aggregates are the fractal dimension, D_f and the fractal prefactor, k_f . In a TEM image, the number of primary particles per aggregate, N_{par} was manually counted one by one, and the primary particle diameter, d_{par} was measured using Measure tool in Photoshop computer software. The number of pixels of both the particle diameter and the length of the absolute scale bar on the image were taken, and the pixel value of each particle diameter was then converted to absolute scale value. In the same manner, the maximum length of the aggregate and the normal width of it were measured to calculate the radius of gyration of the aggregate, R_g , using Equation 2-18,

$$(LW)^{1/2} / (2R_g) = 1.17. \quad (2-18)$$

The remaining parameters were determined using a linear regression method with a least squares approach with 25 known values of N_{par} , d_{par} , and R_g . Two representative log-log plots of N_{par} versus R_g / d_{par} for determining these parameters are shown in Figures 4-7 and 4-8. The power law correlation is seen to provide an excellent fit of the data in Figure 4-8. Based on the correlated equation of a least square linear fit in Figure 4-8, the fractal dimension and the fractal prefactor are determined to be 1.82 and 4.3 respectively. It is noted that these parameters are dimensionless quantities. Because the fractal dimension directly affects determining scattering parameters, more attention was paid to it rather than the fractal prefactor in this study. In the same manner, the fractal dimension was determined at all heights in the unseeded and seeded flames. This was summarized in Table 4-4.

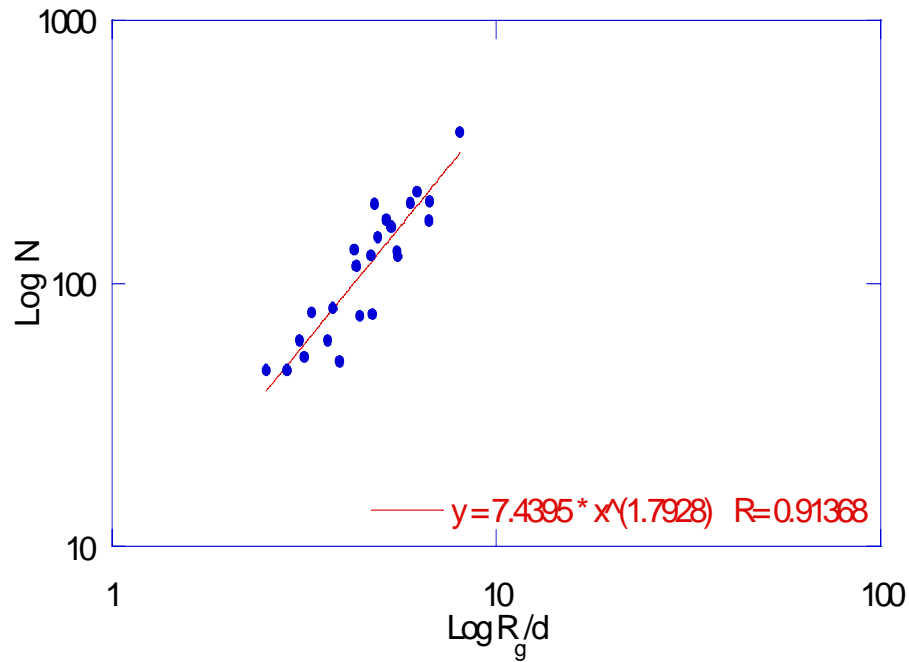


Figure 4-7. A log-log plots of N versus R_g/d_p 25 soot aggregates were sampled at the height 7 in the unseeded flame.

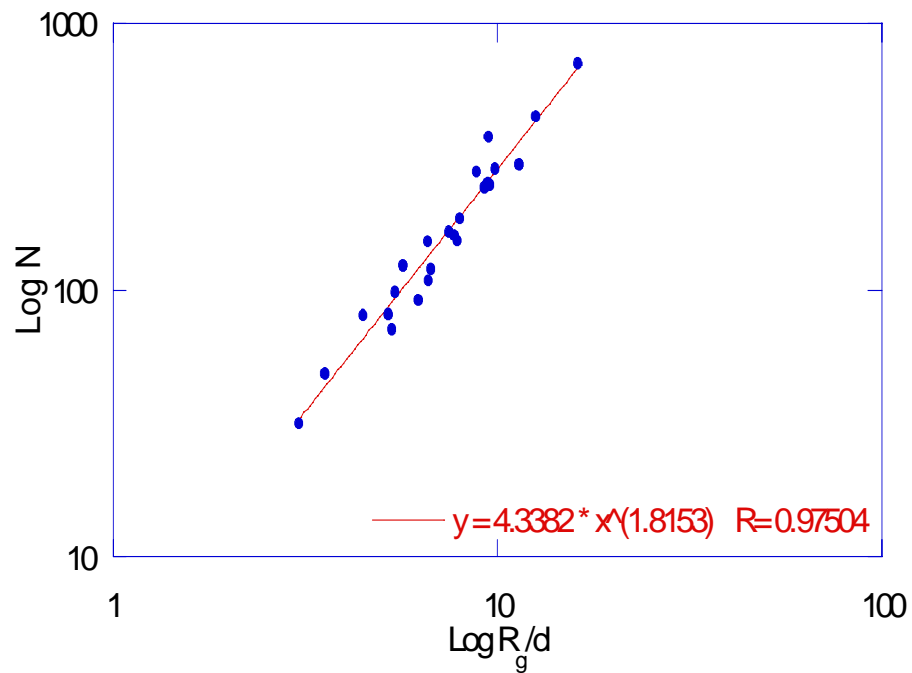


Figure 4-8. A log-log plots of N versus R_g/d_p 25 soot aggregates were sampled at the height 7 in the seeded flame.

Table 4-4. The summary of the fractal dimension at all heights in the unseeded and seeded flames.

Height (cm)	Unseeded	Seeded
1	1.93	1.96
3	1.82	1.75
5	1.78	1.63
7	1.79	1.82
9	1.72	1.90
11	1.93	1.64
13	-*	1.60
15	1.85	1.87
17	1.82	-*
19	1.84	1.72
21	1.73	1.99
25	1.99	1.89

*Analysis was skipped for the unseeded flame at height 13, and the seeded flame at height 17 due to the poor condition of the resulting soot samples.

25 soot aggregate samples were used to determine the fractal dimension for each height. The values fluctuate slightly because of the highly variant nature of soot agglomerates and limited sample size. While it is useful to explore the changes vs. height, the fractal dimension is essentially independent of the various positions; thus, it is appropriate to examine an ensemble of a total of 550 aggregates on average. The statistical average of all was 1.82 along with the standard deviation of 0.11, which would be considered a more accurate value of the fractal dimension of the two flames. The fractal dimension of 1.82 agrees well with those obtained in other conventional studies. The value averaged over all heights for the unseeded and seeded flames were 1.84 ± 0.08 and 1.80 ± 0.14 , respectively, which are not statistically different.

4.4.2 Primary Soot Particle Size

For each investigating position, samples of 375 soot primary particles randomly selected from 25 aggregates were used to find the mean value of the soot primary

particles size within experimental uncertainty. From this measurement, the statistical averages of the primary soot particle diameter at each height for the unseeded and seeded flames were calculated along with the standard deviation. The results are presented below in Table 4-5. In addition, Figure 4-9 represents the unseeded and seeded soot particle diameters graphically at all heights.

Table 4-5. Diameters of primary soot particle at each height in the unseeded and seeded flames.

Height (cm)	Unseeded		Seeded	
	Average (nm)	S.D. (nm)	Average (nm)	S.D. (nm)
9.40	34.1	9.3	27.1	5.4
10.10	29.7	8.2	25.9	6.2
10.90	32.4	5.7	29.4	5.7
11.70	28.8	4.8	28.9	6.1
12.70	31.4	5.9	28.9	3.5
13.70	32.1	5.0	32.2	2.9
14.90	31.7	4.5	31.4	5.7
16.20	31.2	4.0	29.9	3.6
17.75	30.4	4.7	28.4	5.0
19.60	26.6	4.2	26.8	6.3
21.85	24.9	5.2	24.8	4.5
25.25	23.5	5.7	20.1	4.9

*S.D. is standard deviation.

Figure 4-9 shows that the primary particle size data fluctuate somewhat, especially at the lower height of flames. Such a trend is expected to result primarily from the experimental error, due to the nature of discrete agglomerate analysis. To avoid propagation of these experimental variations, a smoothing routine was used. A polynomial curve fit was used to extract more accurate and consistent particle diameters from the experimental results. The curve fit had the effect of averaging over a greater number of agglomerates. Corrected data from the curve fit will be used for the calculation of volume fraction.

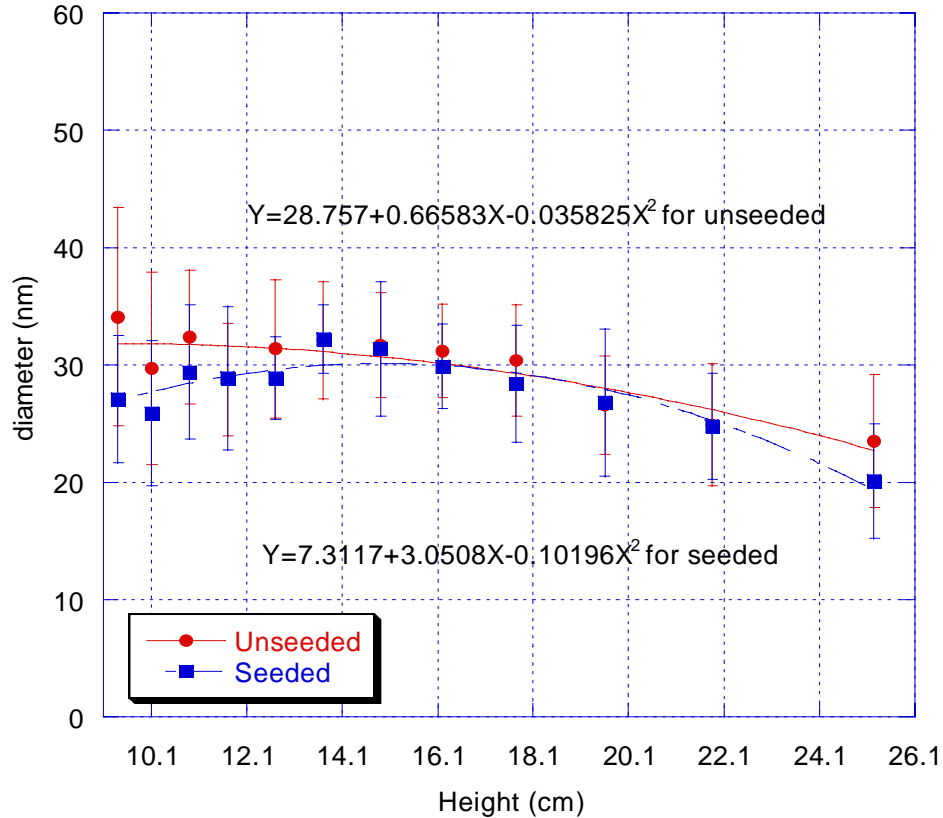


Figure 4-9. Diameters of the primary soot particle as a function of the flame height in the unseeded and seeded flames. A polynomial curve fit was used for extracting more accurate values of d_{par} .

4.4.3 Number Density of Particles

The number density of total primary soot particles in the scattering volume was determined based on the calculating procedure discussed in Chapter 2. Note that this should not be confused with the number of particles per aggregate, N_{par} , determined above. Using the primary soot particle parameters in combination with RDG theory enables the average aggregate differential scattering cross-section to be calculated. The ratio of the measured differential scattering coefficient and the calculated differential scattering cross-section yields the soot aggregate number density, N_{agg} . Finally, the number density of primary soot particles is simply calculated by multiplying the number

of particles per aggregate by the number density of aggregates in the scattering volume.

The summary of number densities is represented in Table 4-6.

Table 4-6. The summary of number densities for the unseeded and iron-seeded flames.

Height (cm)	Unseeded				Seeded			
	N_{pri}^*	Fit N_{pri}	N_{agg}^*	N_{total}^*	N_{pri}	Fit N_{pri}	$N_{agg} (cm^{-3})$	$N_{total} (cm^{-3})$
9.4	77	103	1.61E+09	1.65E+11	64	99	2.60E+09	2.57E+11
10.1	108	115	1.34E+09	1.53E+11	60	113	1.02E+09	1.16E+11
10.9	135	128	1.46E+09	1.86E+11	116	128	1.74E+09	2.23E+11
11.7	133	139	8.12E+08	1.13E+11	203	143	3.22E+09	4.59E+11
12.7	203	153	1.57E+09	2.40E+11	211	159	1.70E+09	2.70E+11
13.7	164	166	1.08E+09	1.80E+11	244	174	2.87E+09	4.99E+11
14.9	171	180	1.05E+09	1.89E+11	286	191	1.69E+09	3.23E+11
16.2	178	194	8.06E+08	1.57E+11	212	208	7.83E+08	1.63E+11
17.75	231	210	8.08E+08	1.69E+11	256	226	6.10E+08	1.38E+11
19.6	346	226	5.95E+08	1.35E+11	301	246	5.99E+08	1.47E+11
21.85	254	245	3.23E+08	7.91E+10	223	268	2.25E+08	6.02E+10
25.25	247	269	2.14E+08	5.75E+10	170	297	1.10E+08	3.26E+10

* N_{par} : the number of particles per aggregate; * $N_{agg}(cm^{-3})$: the number density of aggregates in the scattering volume; * $N_{total}(cm^{-3})$: the number density of total particles in the scattering volume.

In a manner similar to what was done in determining the primary particle diameter, a logarithmic curve fit was used for extracting more accurate values of N_{par} . Instead of using raw N_{par} , new values from curve fitting were used to determine N_{total} . It is illustrated in Figure 4-10. Moreover, Figure 4-11 graphically represents N_{total} as a function of flame height for the unseeded and iron-seeded flames.

4.4.4 Volume Fraction of Soot Particle

With the primary soot particle diameter and number density of total particle determined above, the overall soot volume fraction is calculated from Equation 4-1,

$$f_v = V_{agg} \cdot N_{agg}, \quad (4-1)$$

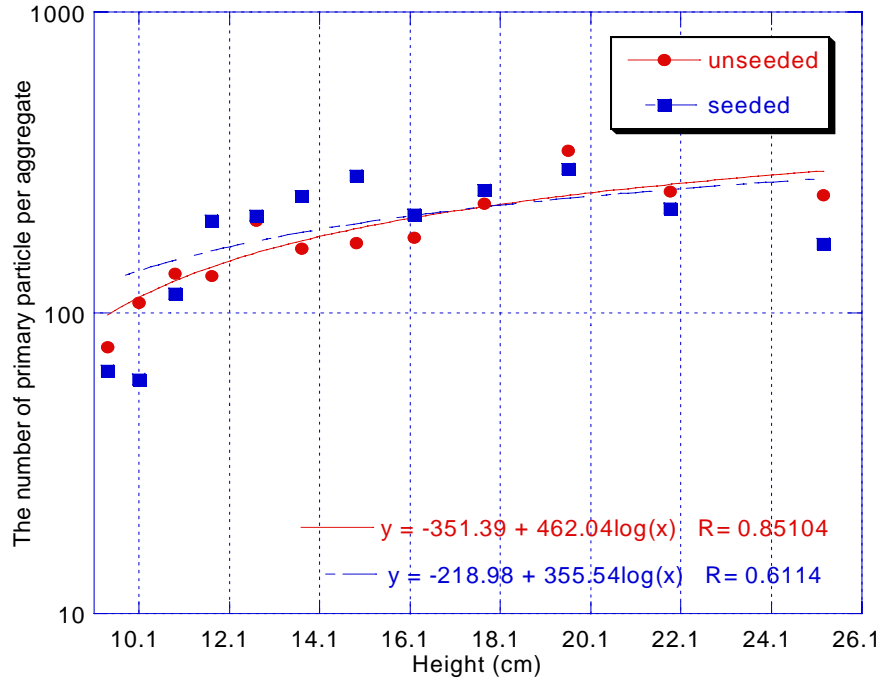


Figure 4-10. The number of primary soot particle as a function of the flame height in the unseeded and iron-seeded flames. A logarithmic curve fit was used for extracting more accurate values of N_{par} .

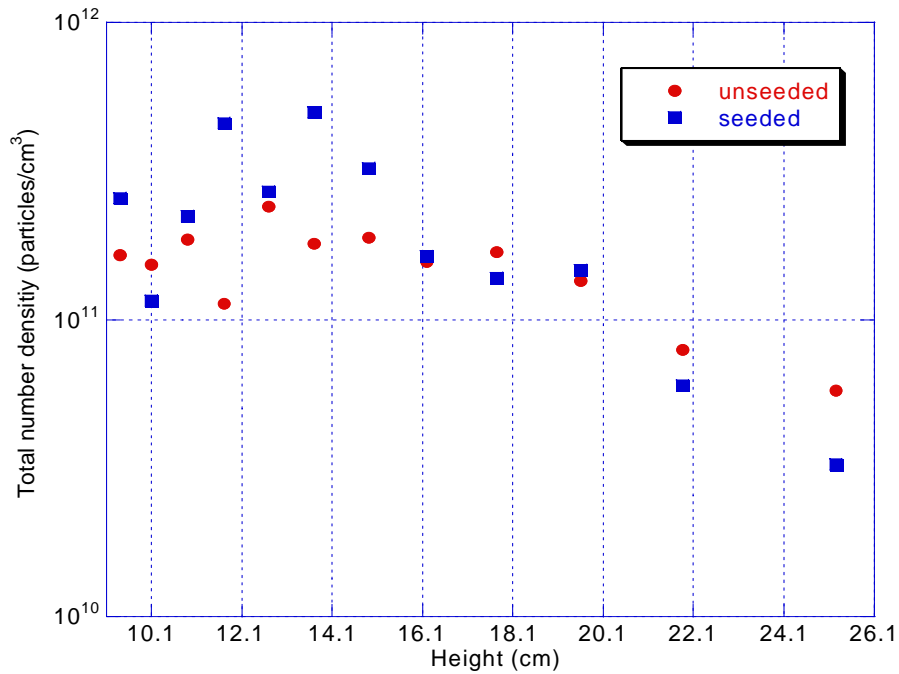


Figure 4-11. Number density of the total soot particle for the unseeded and iron-seeded flames.

where the volume of an aggregate, V_{agg} is given by

$$V_{agg} = \frac{\pi}{6} d_p^3 N_{par}. \quad (4-2)$$

Finally, the volume fraction which is representative of the total soot loading, as a function of flame position is compiled in Table 4-7 with errors determined through uncertainty analysis and graphically presented in Figure 4-12 for the unseeded and iron-seeded flames. The detailed results and discussion of the analysis will be found in Appendix C.

Table 4-7. The volume fraction as a function of flame height for the unseeded and iron-seeded flames.

Height (cm)	Unseeded (cm ³ soot/cm ³)	S.D.* (cm ³ soot/cm ³)	Seeded (cm ³ soot/cm ³)	S.D. (cm ³ soot/cm ³)	% Reduction
9.4	2.78E-06	3.75E-06	2.64E-06	3.53E-06	5.0
10.1	2.58E-06	3.43E-06	1.29E-06	1.82E-06	50.0
10.9	3.11E-06	4.24E-06	2.70E-06	3.68E-06	13.2
11.7	1.87E-06	2.65E-06	5.91E-06	8.14E-06	-216.0
12.7	3.89E-06	5.42E-06	3.69E-06	4.97E-06	5.1
13.7	2.85E-06	3.85E-06	7.06E-06	9.79E-06	-147.7
14.9	2.87E-06	3.45E-06	4.64E-06	6.75E-06	-61.7
16.2	2.24E-06	3.06E-06	2.30E-06	3.16E-06	-2.7
17.75	2.23E-06	3.01E-06	1.83E-06	2.74E-06	17.9
19.6	1.55E-06	2.16E-06	1.69E-06	2.32E-06	-9.0
21.85	7.43E-07	1.00E-06	5.08E-07	6.92E-07	31.6
25.25	3.52E-07	4.78E-07	1.22E-07	1.82E-07	65.3

S.D.: Standard deviation

4.4.5 The Extinction Coefficient of Soot Particle

In addition to the scattering analysis, the extinction coefficient was determined from

$$K_{ext} = N\sigma_{ext}. \quad (2-12)$$

The extinction coefficient as a function of flame height is summarized in Table 4-8 and graphically presented in Figure 4-13 for the unseeded and iron-seeded flames.

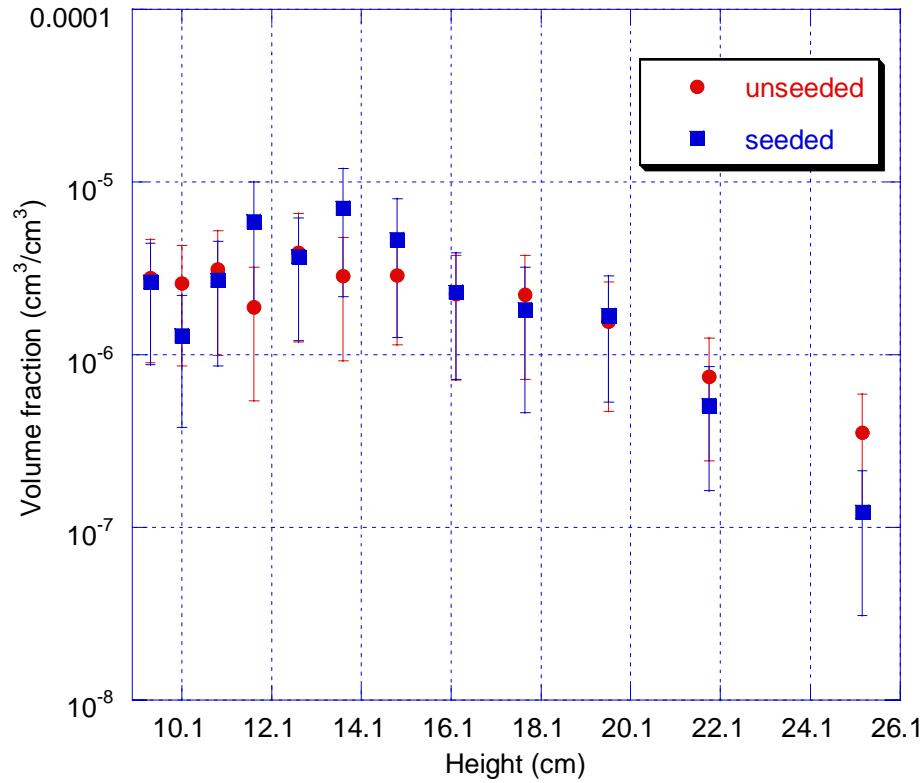


Figure 4-12. The volume fraction as a function of flame height for the unseeded and iron-seeded flames. The error bar represents one standard deviation.

Table 4-8. The extinction coefficient of soot particle as function of flame height for the unseeded and iron seeded flames.

Height (cm)	Unseeded (cm ⁻¹)	Seeded (cm ⁻¹)
9.4	1.36E-01	1.29E-01
10.1	1.29E-01	6.72E-02
10.9	1.48E-01	1.26E-01
11.7	9.47E-02	2.61E-01
12.7	1.82E-01	1.68E-01
13.7	1.42E-01	3.13E-01
14.9	1.41E-01	2.10E-01
16.2	1.09E-01	1.09E-01
17.75	1.02E-01	8.39E-02
19.6	7.03E-02	7.56E-02
21.85	3.39E-02	2.33E-02
25.25	1.59E-02	5.37E-03

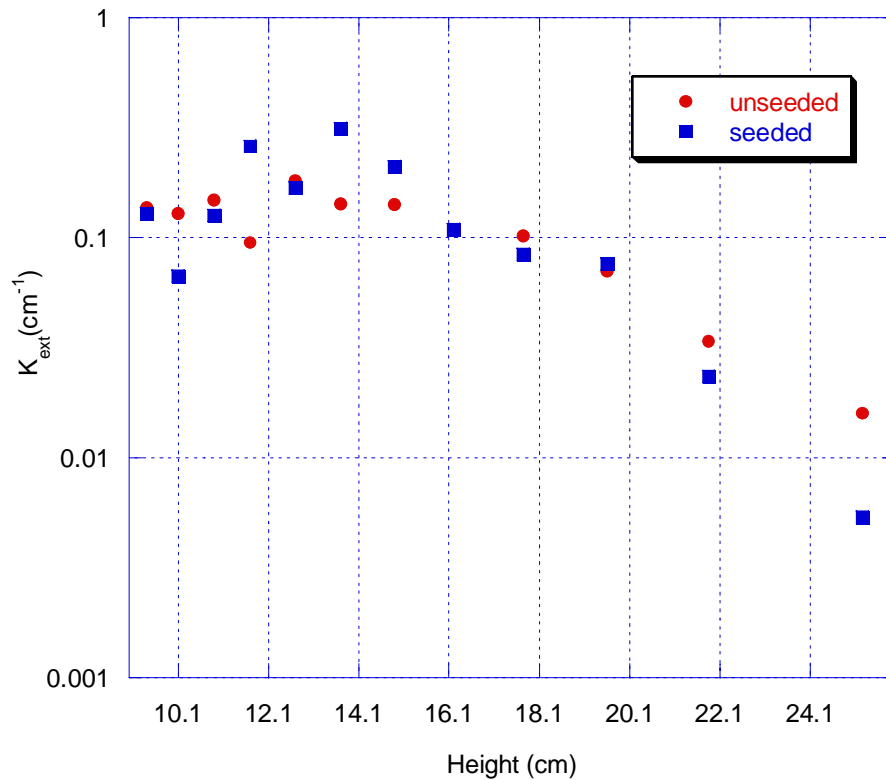


Figure 4-13. The extinction coefficient of soot particle as a function of flame height for the unseeded and iron-seeded flames.

4.4.6 Discussion of Results

In comparing all results for diameter, number density, volume fraction, and extinction coefficient shown in Figures from 4-9 to 4-13, it is seen that all data have the same trend, within experimental uncertainty, and the data at the final position are always found to be greater in the unseeded flame than in the iron seeded flame.

Data can be specified in terms of two regimes regarding the comparison of the unseeded and iron-seeded flames, namely, the growth regime ($\leq \sim 14$ cm) and the oxidation regime ($\geq \sim 14$ cm). No distinct trends between the two flames were observed in the lower growth regime, below about 14 cm. This indicates that the iron additive has little effect on suppression of soot growth in this regime. As noted above, this is consistent with the work of Masiello (2004), in which detailed measurements within the

inception and growth led to the conclusion that iron particulates are quickly incorporated within soot agglomerates, giving way to “typical” soot growth. The inconsistent perturbation of the number density in this region, especially for the seeded flame in Figure 4-11, is linked to the propagation of error, including the differential scattering coefficient data and TEM data, as shown in Figure 4-4. This perturbation directly affects volume fraction and the extinction coefficient data. The main error of measured data such as the differential scattering coefficient and transmission results from unsteady light signal caused by spatial excursions of the thin reaction zone.

On the other hand, the iron-seeded flame data present a consistent change with respect to the unseeded flames in the higher regime (i.e. oxidation regime). In particular, the maximum deviation between the two flames is shown at the last height, which is near the flame tip, where the volume fraction is reduced by nearly 66%. In Figure 4-9, the average primary soot particle diameters at the lower heights, from 9.4 to 11.7 cm above burner, were 31 and 29 nm in the unseeded and seeded flames, respectively. The relative standard deviations were about 6.5% for these data; hence, the difference is on the order of the experimental uncertainty. In contrast, at the greatest residence time investigated ($H = 25$ cm), the primary particle diameters were reduced to 24 and 20 nm in the unseeded and iron-seeded flames, respectively. Such a decrease in particle size is consistent with significant soot oxidation. Overall, the primary particle diameters and volume fraction data, as measured from the TEM micrographs and scattering signal, depict the transition from soot growth to soot oxidation along the length of the flame. To explore the overall differences between the conditions of two flames, it is useful to examine the total soot volume fractions in detail.

In Figure 4-12, the soot volume fraction is reduced from $3.52\text{E-}7$ in the unseeded flame to a value of $1.22\text{E-}7$ in the iron-seeded flame, corresponding to a 66% reduction in soot emissions. This was visually observed as well. A pronounced smoke plume escaping from the flame tip disappeared when the iron seeded fuel was supplied, which was recorded with a video camera. Figure 4-14 shows both the unseeded and seeded flames.

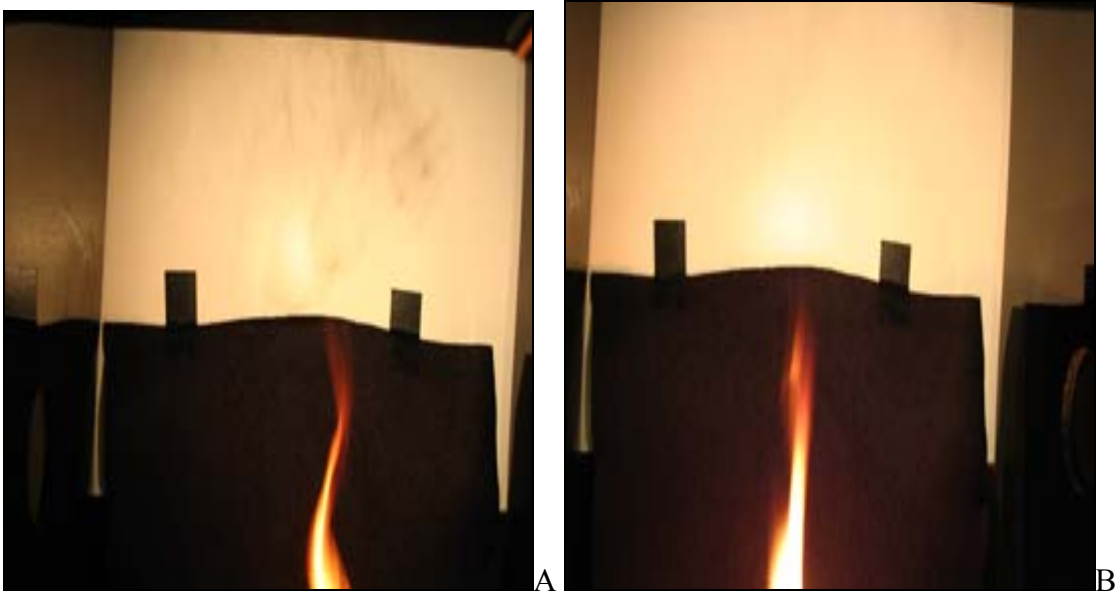


Figure 4-14. Photographs of tips of the unseeded and seeded flames. Soot plume is seen in the unseeded flame while being not seen in seeded flame. A) the unseeded flame. B) the seeded flame.

As evidenced above, it can be concluded that the iron additive has a significant role on soot reduction that takes place in the oxidation regime, as evidenced by the data in Figures 4-9 and 4-12.

With measured optical length of the flame and the transmission data determined above, the extinction coefficient for the optical length can be calculated from Beer-Lambert law. Overall, the absolute values of it were about 43% higher than the extinction coefficient presented in Figure 4-13; however, the relative trend of two results

is in good agreement. The agreement between these two values is excellent when one considers the uncertainty in the pathlength, spatial variations along the path, and uncertainties in the optical properties. The detailed results of the analysis will be found in Appendix B.

The effect of iron pentacarbonyl on the visible structure of the flame is shown in Figure 4-15. Iron pentacarbonyl addition is characterized by a decrease in the dark orange zone in the flame tip, and vague lateral outline of the flame. It may be attributed to the soot oxidation, but qualitative diagnostics are required for more precise analysis.

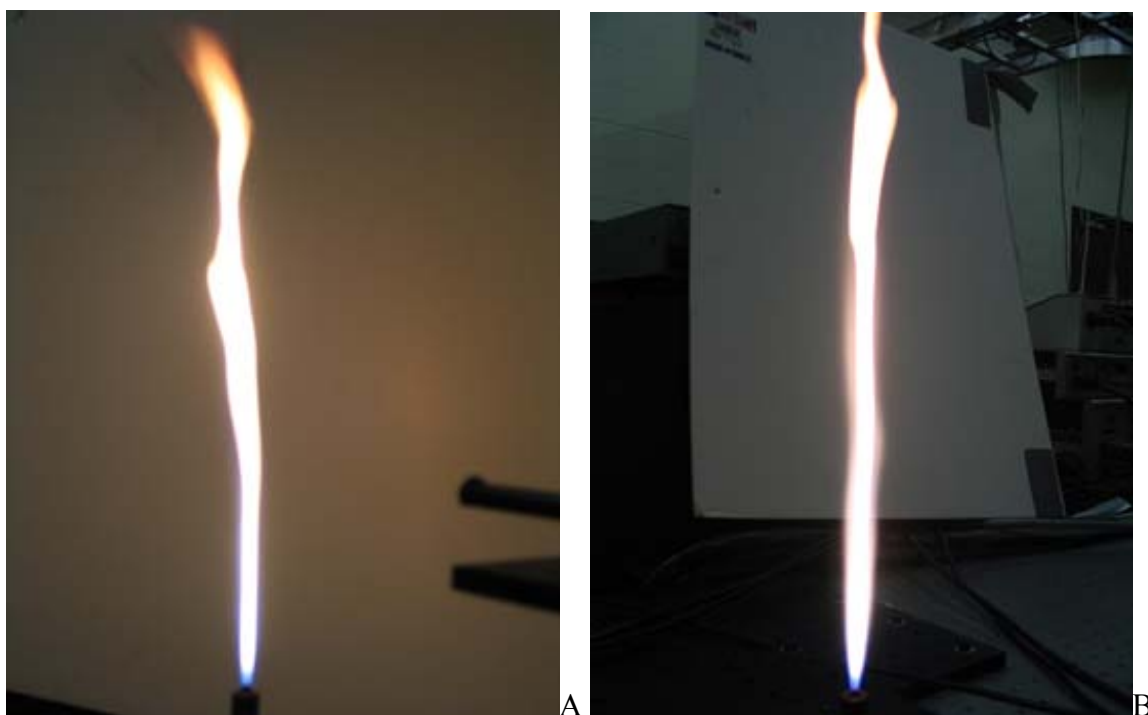


Figure 4-15. Photographs of the unseeded and seeded flames. A) the unseeded flame. B) the seeded flame.

All analysis was carried out assuming a constant value for the complex index of refraction of soot. A value of $\bar{m} = 2.0 - 0.35i$ was used for this study. Wide variations in the complex refractive index of soot have been reported in the literature, and no single

value has been generally accepted. The findings for \bar{m} from key studies are listed in Table 4-9.

Table 4-9. Complex refractive indices for soot from various sources. (2001)

Authors	Type of soot	Incident Wavelength (nm)	$\bar{m} = n - ki$	
			n	k
Chippett and Gray (1978)	acetylene	visible	1.9-2.0	0.35-0.50
Charalampopoulos and Chang (1988)	propane	457.9	1.58-1.82	0.65-0.83
		488	1.57-1.82	0.65-0.85
		514.5	1.54-1.71	0.67-0.87
	soot	540	1.77	0.63
Dalzell and Sarofim (1969)	propane	435.8	1.57	0.46
		550	1.57	0.53
		650	1.56	0.52
	Standard value	visible	1.57	0.56
	acetylene	435.8	1.56	0.46
		550	1.56	0.46
		650	1.57	0.44
Pluchino <i>et al.</i> (1980)	carbon	488	1.6-1.8	0.06-0.19
	8 um carbon sphere		1.7	0.7
Roessler and Faxvog	Mean of review	515	1.75	0.5
Lee and Tien	soot	633	1.8-2.0	0.45-0.65
Sloane	soot	633	1.7	0.8
Mullins and Williams	soot	633	1.85	0.4
Stagg and Charalampopoulos	soot	633	1.53	0.38
Köylü and Faeth	soot	515	1.54	0.48
Mulholland and Choi	soot specific mass extinction	-	1.55	0.8

The value chosen for this study is the one reported by Chippett and Gray (1978), which was based on a similar light scattering analysis with a heavily sooting fuel. According to a study by Dobbins and Megaridis (1991), a value of $\bar{m} = 1.57 - 0.56i$ is typically recommended for carbonaceous soot when the fractal dimensions are ranged between 1.7 and 1.9. The same analysis with this refractive index will be presented in Appendix B. Overall, the conclusions are identical for the alternative refractive index, although absolute values change by about 23%.

4.5 Spectroscopy

This study has focused so far on the quantitative points of view to find how much soot can be reduced by adding the additive. However, the additional information is required to elucidate how the soot can be reduced, and what mechanisms contribute to the reduction of soot. In order to determine the best configuration for species detection using spectroscopic methods, preliminary sets of experiments were conducted with the CO flame. The advantage for using the CO flame is to prevent the desired signal from interfering with soot particles. As stated previously, the intensity of Raman scattering is very weak; thus, a sensitive detection configuration is ideal. In other words, evaluating the detection ability of the desired species in the CO flame with spectroscopic techniques is the initial focus for a practical implementation in the isooctane flame.

As done previously, products in the CO flame were collected via thermophoretic sampling at three different flame heights, recorded using TEM, and analyzed with EDS. Figure 4-16 represents TEM images of samples from the CO flame. The shape of individual particle is hexagonal, which is distinguishable from soot particles.

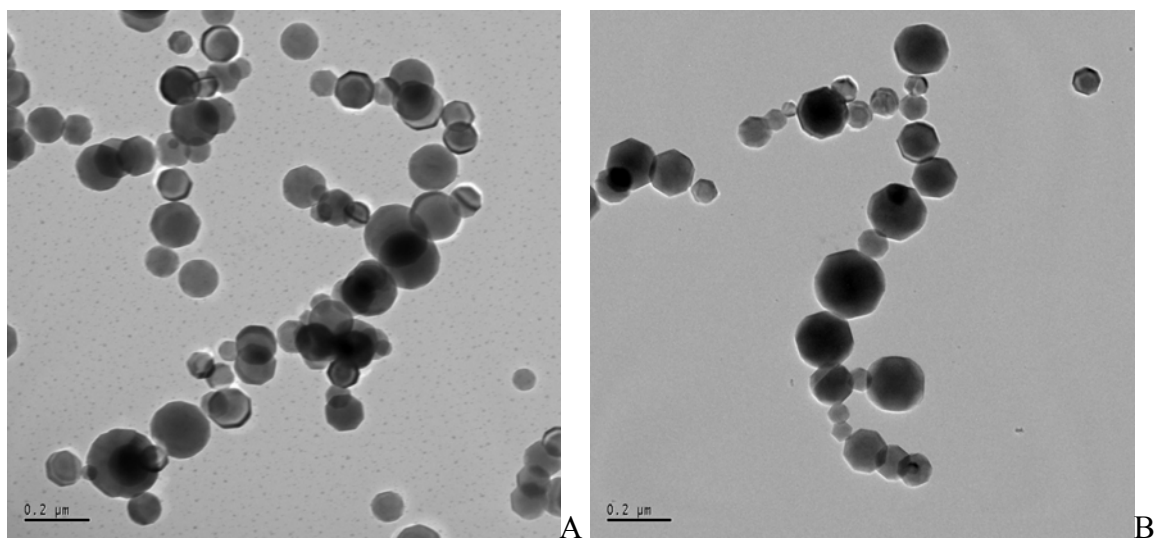


Figure 4-16. TEM images of samples collected in the Fe-seeded CO flame. A) sampled at the middle of the flame height. B) sampled at the flame tip.

It is well documented that the iron pentacarbonyl gas in a CO and O₂ flame is thermally decomposed, and presumably forms in Fe₂O₃ chain agglomerates (Cheng *et al.* 1991). EDS can be helpful for identifying these species more correctly. The typical signal window of EDS is shown in Figure 4-17.

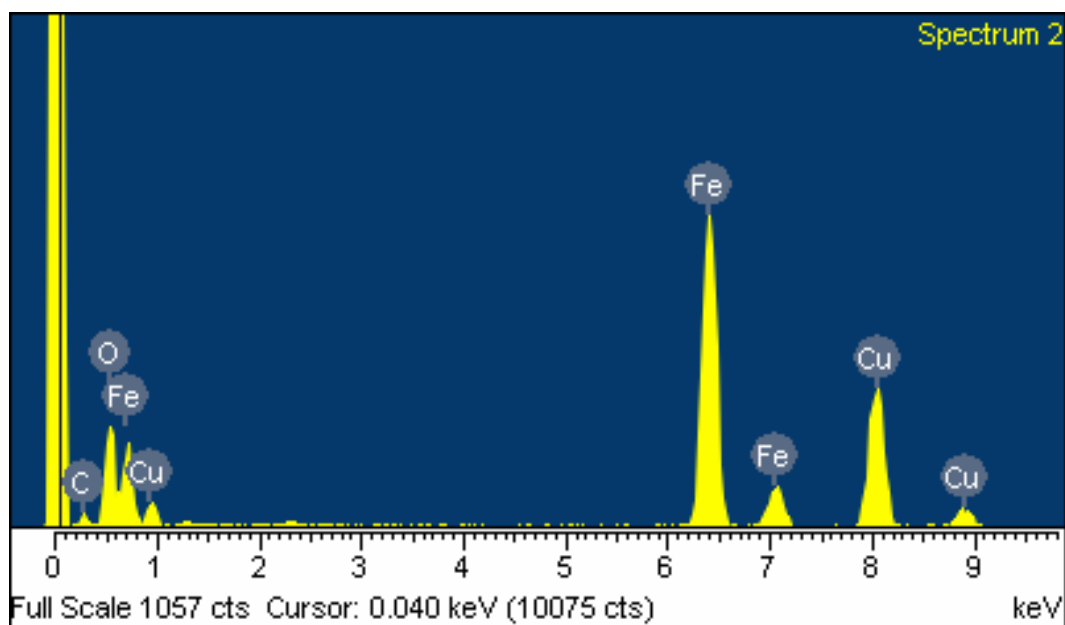


Figure 4-17. The typical signal window of EDS.

The intensity of x-ray emission from elements was represented at each energy level. It was also noted that Cu signal was attributed to the sampling grid. Table 4-10 summarizes the atomic ratio of iron and oxygen in the particles from EDS.

Table 4-10. EDS result atomic ratio of iron oxide.

Sample	Flame	Fe	O	ratio
1	Isooctane flame	24.7	54.34	1:2.20
2		4.97	20.17	1:4.06
3		4.71	7.7	1:1.63
4		5.57	0	-
5		4.38	0	-
6		10.09	16.72	1:1.66
7		4.96	2.8	1:0.56
8		0	2.14	-
9		34.27	0	-
10		22.67	0	-
11	CO flame	26.94	50.49	1:1.87
12		25	49.34	1:1.97
13		37.36	36.4	1:0.97
14		26.31	32.46	1:1.23
15		26.01	40.45	1:1.56
16		14.97	26.15	1:1.75
17		25.86	30.51	1:1.18
18		6.93	20.19	1:2.91
19		18.43	40.02	1:2.17
20		22.89	49.98	1:2.18
21		17.11	38.37	1:2.24

The ratio is quite random; therefore, it is very hard to explain that a particular formation of iron oxide (i.e. especially Fe_2O_3) is dominantly present in the CO seeded flame. As discussed later, iron oxides were likely formed after sampling was done. Since this analysis is an *ex situ* method, the sample may be affected by the oxygen post sampling process. The use of *in situ* analytical methods yields more real and accurate information on the chemical states.

4.5.1 Laser Induced Fluorescence (LIF) Spectroscopy

Laser induced fluorescence spectroscopy was used to detect the concentration of Fe along the axial direction of the seeded flame, which would give information on the role of the additive for the soot reduction. In order to find the strong resonance transition lines of Fe, the tunable laser was scanned across the particular wavelength ranging from 295 nm and 298 nm. During the scanning, laser induced fluorescence of Fe was found at three excitation wavelengths, which are listed in Table 4-11, with fluorescence lines corresponding to each excitation wavelength.

Table 4-11. Fe resonance transition wavelengths and corresponding fluorescence emission lines with their relative intensity.

	Wavelength (nm)		Relative Intensity
	Excitation	Emission	
1	295.39	372.76	0.10
		376.38	0.27
		378.79	0.05
2	296.69	373.49	1.00
3	297.31	374.95	0.60
		375.82	0.29

This can be also displayed in an energy level diagram as represented in Figure 4-18. In addition, Figure 4-19 describes the laser induced fluorescence peaks for three excitation sources, all recorded within the CO flame (two third from the burner lip).

These peaks are in agreement with the reference Fe atomic wavelength and relative peak intensity in the NIST database. The strongest fluorescence at 373.49 nm was obtained with the resonance transition of 296.69 nm, which was chosen for all further experimentation. To ensure resonant excitation, daily spectral calibration was necessary to ensure the correct output laser wavelength. Prior to all experiments, the laser was tuned into the resonance transition of 296.69 nm by stepping the laser in small increments

across the transition line until the exact resonance transition was calibrated using the spectrometer.

First, Fe fluorescence was measured as a function of the normalized CO flame heights, namely, zero, 1/2, 2/3, and 1 (i.e. flame tip). Typical LIF signals are shown in Figure 4-20. As discussed previously, the fluorescence signal is proportional to the concentration of species, temperature and pressure. Herein, the goal of LIF was to trace the Fe concentration in the flame. Since CO flame is diffusion flame, the flame temperature would increase toward downstream. In spite of increase in temperature, the intensity of Fe fluorescence also decreases toward downstream of the flame. This may

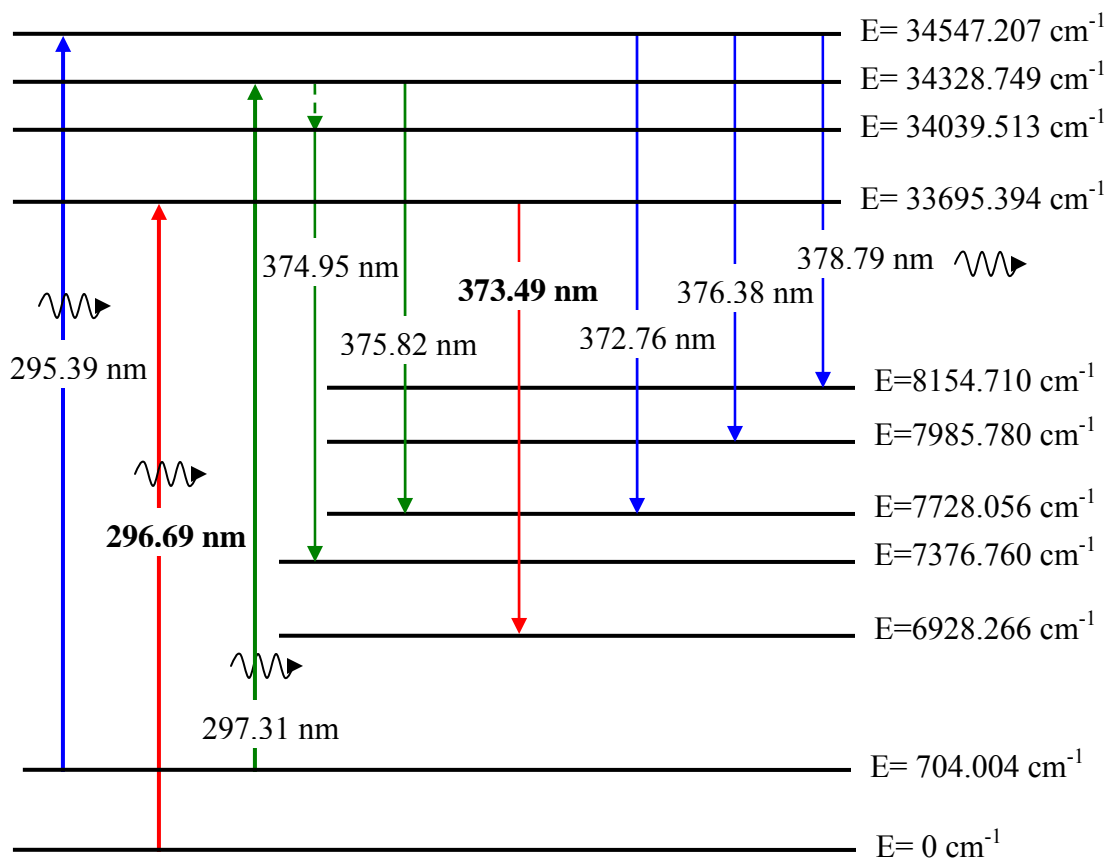


Figure 4-18. Energy level diagram of Fe atom. Bold font indicates the best combination.

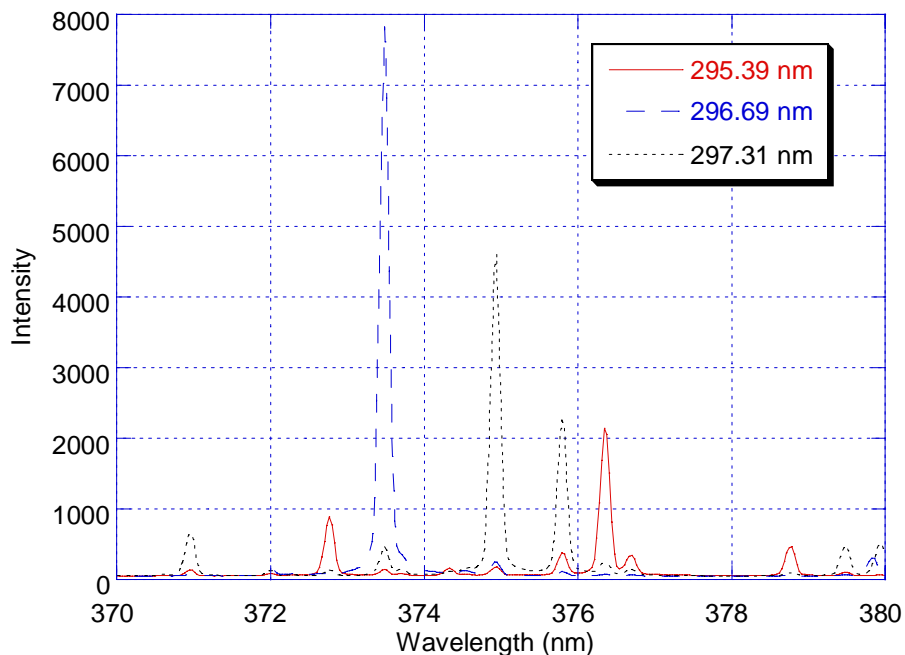


Figure 4-19. Laser induced fluorescence peak for three excitation sources at the two third of normalized CO seeded flame height. Excitation lines are shown.

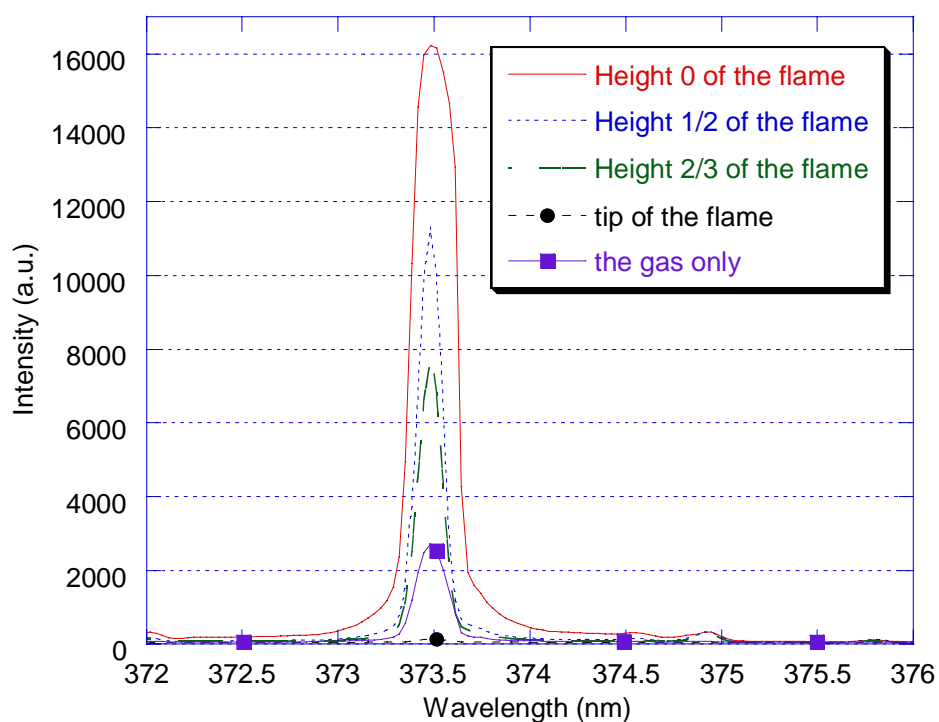


Figure 4-20. Fe fluorescence corresponding to the excitation line of 296.69 nm as a function of the CO flame normalized four heights. “The gas only” is the Fe fluorescence from the unreacted CO gas seeded with $\text{Fe}(\text{CO})_5$.

illustrate that the concentration of Fe is reduced throughout the flame due to a certain chemical reaction, namely iron oxide formation. It is noteworthy that Fe fluorescence was observed from the CO gas seeded with iron pentacarbonyl (i.e. non-reacting). Iron pentacarbonyl is very easily dissociated in even ambient temperature, so Fe atomic intensity is quite strong and even stronger than the signal obtained from the flame.

The sensitive LIF Fe probe was then used to investigate the isooctane flame seeded with iron pentacarbonyl. Six measurements were performed at 23 different flame heights, and intensities of the signals were calculated. The average values of intensities of the Fe emission line at 373.49 nm (integrated peak) for each height are presented in Figure 4-21.

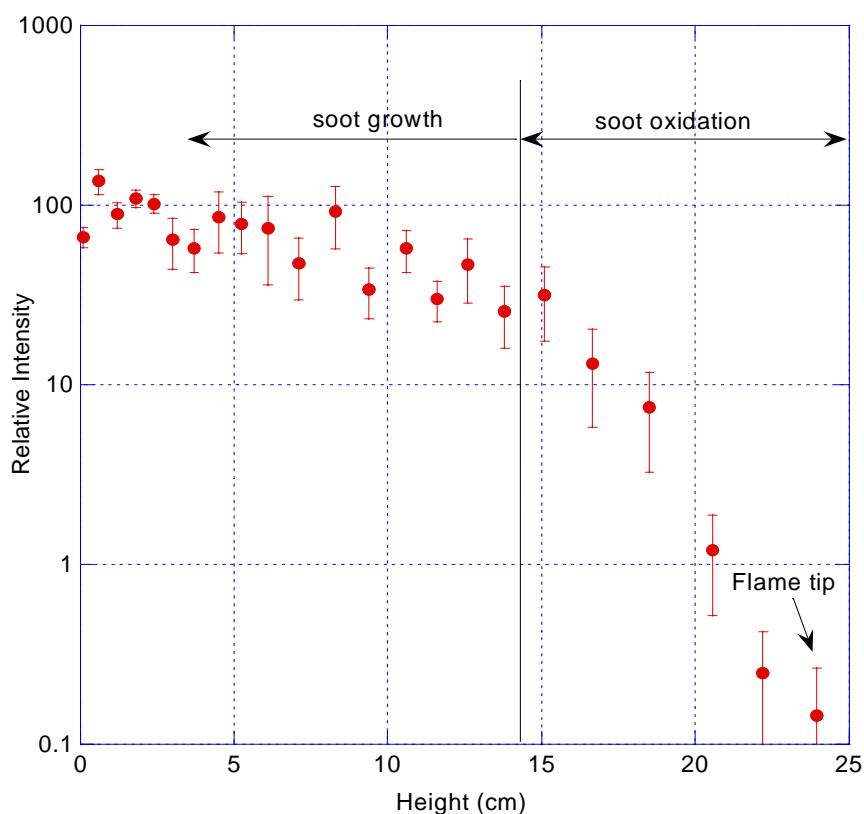


Figure 4-21. Intensity of LIF measured in isooctane seeded flame at emission line of 373.49 nm corresponding to the excitation line of 296.69 nm. Flame tip is at height of 23.95 cm. Error bars represent one standard deviation.

The LIF data were normalized by the mean value of the initial five data points in order to minimize the large standard deviation attributed to the varying OPO laser power from day to day. The LIF signal is higher near the burner lip and is observed to decrease as the height increases. However, the Fe LIF signal is observed to undergo a more rapid drop with the oxidation regime, falling by more than 2 orders of magnitude. As discussed in Ch2, quenching is a common issue in the LIF spectroscopy. Such a rapid change in quenching is unlikely to have occurred in the flame, but any possibility of quenching was explored by absorption spectroscopy using a hollow cathode lamp. While LIF is subject to quenching, the absorption spectroscopy is free from this phenomenon. The Fe atomic emission from the hollow cathode lamp passing through the Fe seeded flame was measured along the vertical axis of the flame. Then, the emission from the flame itself was subtracted from the overall emission of both the flame and the lamp. Finally, transmission was determined by dividing the lamp signal excluding the flame signal by pure lamp emission. Since the Fe atomic emission is absorbed by the elemental Fe present in the seeded flame, the transmission is low at Fe resonant transition lines. Two transmission measurements at two different heights are represented in Figure 4-22. A strong Fe transition line of 271.9 nm was chosen for this study. This transition originated from the ground state; thus, the signal was more sensitive to absorption. Peak values at the wavelength of 271.9 nm were plotted as a function of 5 different heights of the seeded flame in Figure 4-23. The amount of the elemental Fe is high in the soot growth regime; therefore, the Fe atomic photons are absorbed by the elemental Fe resulting in the low transmission of the light. However, the transmission of the light was high in the soot oxidation regime because the concentration in the elemental Fe is low.

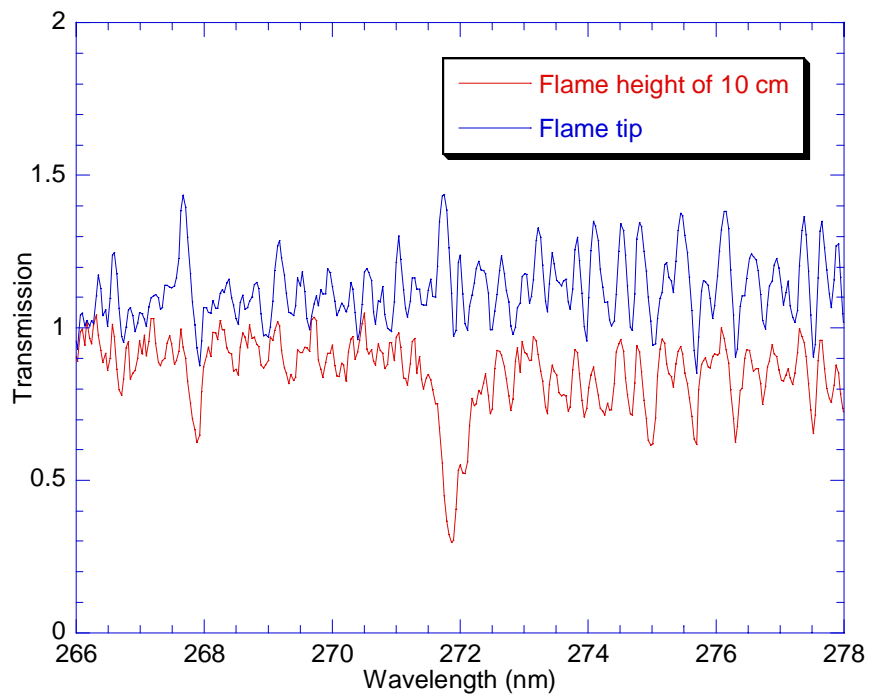


Figure 4-22. Transmission of Fe atomic light passing through the seeded flame at two different heights. Fe resonance transition line of 271.9 nm was chosen for this study. Flame tip is at the height of 23.95 cm.

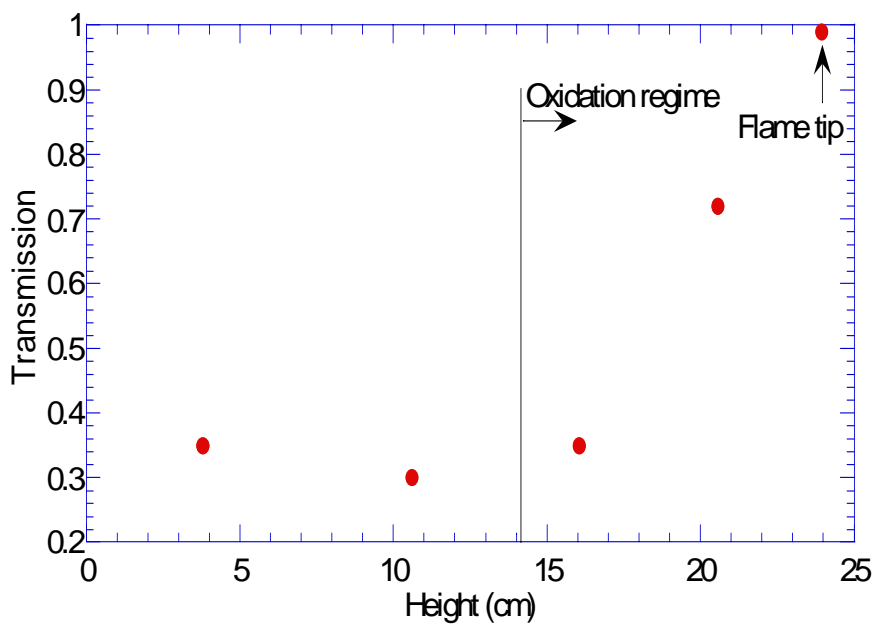


Figure 4-23. Transmission of Fe atomic light from the lamp as a function of 5 different heights of the seeded flame. Fe resonance transition line of 271.9 nm was chosen for this study. Flame tip is at the height of 23.95 cm.

The transmission data was observed to be nearly constant in the growth regime and then rapidly rise up throughout the oxidation regime. This trend is in an excellent agreement with the LIF result. Therefore, the absorption spectroscopy ensured that the quenching was not responsible for Fe LIF signal drop in the oxidation regime. The more possible explanations on the Fe LIF signal drop throughout the oxidation regime will be discussed in Chapter 6.

Since the LIF signal could be influenced by laser-induced plasma excited atomic emission as discussed below, the LIF signal must be discriminated from such a signal, especially at the near flame tip. Spectra were measured as function of the incident laser power at the flame tip using the 355 nm source in order to validate the laser-induced plasma effect on the LIF signal. This is shown in Figure 4-24.

Figure 4-24 elucidates that laser induced plasma (LIP) emission starts emerging when the laser energy is over 25 mJ/pulse. Because only 1.8 mJ/pulse was used for the LIF experiments, the laser power used for LIF was low enough not to be concerned about laser-induced plasma formation and induced iron emission.

A final test to ensure the validity of the LIF probe was made by tuning the OPO on and off the 296.69 nm transition line, while keeping the total laser energy constant. Offline measurements were taken at flame heights 7, 15, 21, and 25 with 296.19 nm to examine the presence of LIBS emission. Figure 4-25 represents the on and off resonant LIF signal induced by the excitation wavelengths of 296.69 nm and 296.19 nm.

As shown in Figure 4-25, no signal was observed when the laser wavelength was tuned to 296.19 nm. Therefore, the LIF probe was concluded to accurately measure elemental Fe without perturbing the overall flame species, including any iron species.

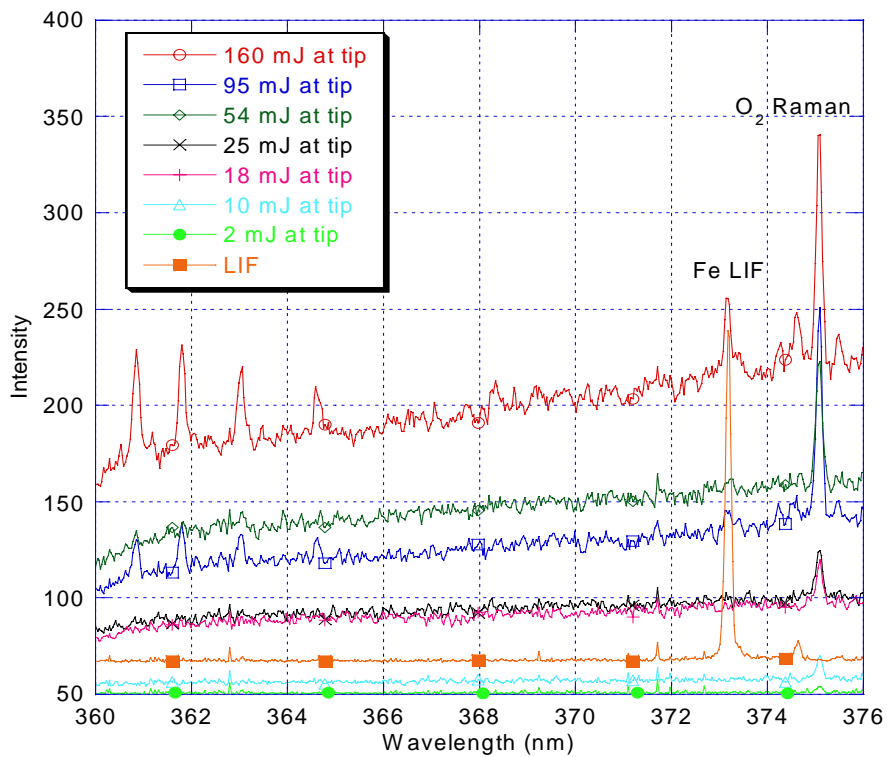


Figure 4-24. Spectra measured as function of the incident laser energy at flame tip using the 355 nm source in order to validate the LIBS effect on the LIF signal.

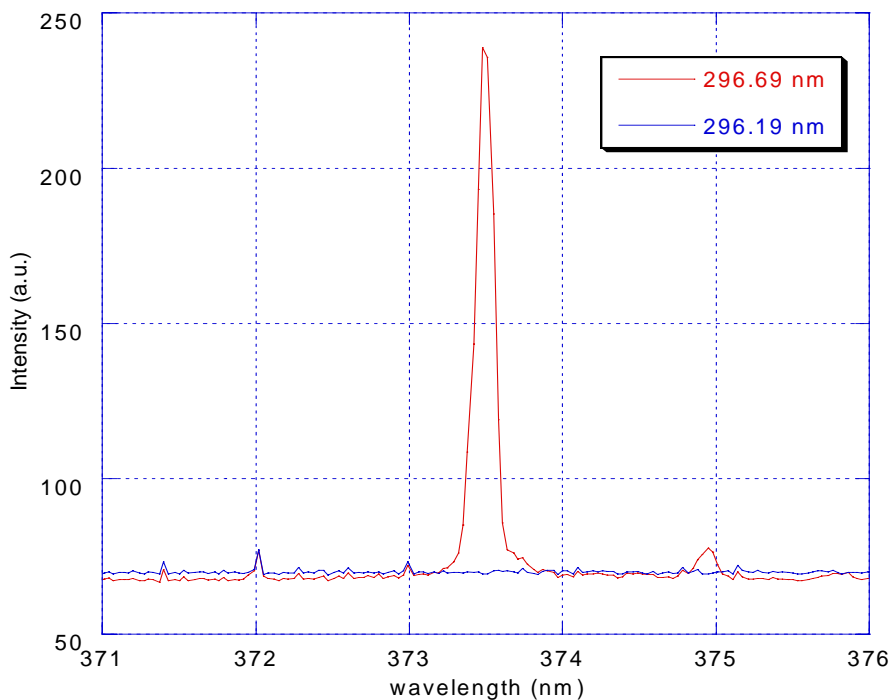


Figure 4-25. On-and-off resonant LIF signal induced by the excitation wavelength of 296.69 nm and 296.19 nm with the same pulse energy.

Finally, LIF was also used for exploring the presence of FeO in the flame. Several FeO resonant transition wavelengths (Mavrodineanu *et al.*, 1965) used in this study are diagrammed with corresponding emission wavelengths in Figure 4-26. However, no LIF of FeO was detected at transition wavelengths shown in Figure 4-26.

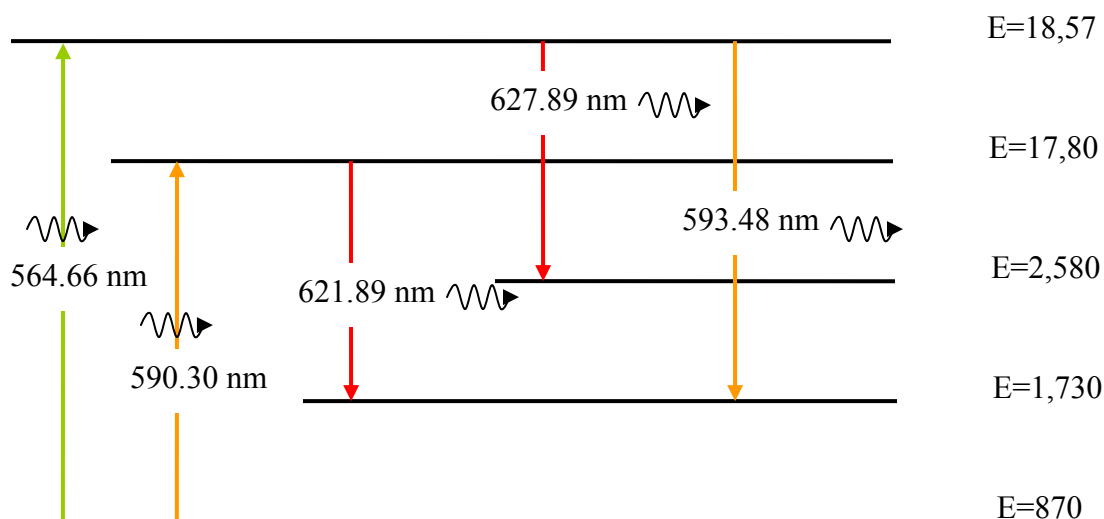


Figure 4-26. Energy level diagram of FeO molecule.

It is concluded that FeO may not be significantly present as an iron species in the flame configuration for this study. Although FeO may exist in the flame, the amount would be below the detection limit.

4.5.2 *In Situ* Raman Spectroscopy

In situ Raman spectroscopy was employed to extract the molecular information of iron oxides which may form throughout the flame. Initially, the CO flame was investigated for this purpose at 532 nm and 355 nm excitation wavelengths. According to the results from an *ex situ* study (Masiello, 2004), Fe₂O₃ was the most possible formation of iron oxide in the Fe-seeded flame. However, such data was not recorded within the flame. Literature reference to the iron oxide Raman shifts (cm⁻¹) are summarized in Table 4-12 (Faria *et al.*, 1997 and Maslar *et al.*, 2000).

Table 4-12. Reference to iron oxides Raman shift (cm⁻¹)

FeO	Fe ₂ O ₃		Fe ₃ O ₄	
Faria et al.	Maslar et al.	Faria et al.	Maslar et al.	Faria et al.
	224	225		
	243	247		
	290	293	292	300
	406	412		
	494	498	524	532
	607	613		
652*	655		665	661
	813			
	1055			
	1100			
	1310	1320		

*Bold font means the strongest line.

As discussed in Chapter 2, the Raman signal is proportional to the inverse fourth power of the excitation wavelength; however, the background fluorescence also increases with decreasing wavelength, notably in the UV, causing increases in noise level. Another issue to be considered for the use of lower wavelength as an excitation source is the separation of Raman signal from the elastic scattering signal. Although the razor edge filter can sharply cut the elastic scattering light off, it is very hard to invoke the first Fe₂O₃ Raman peak when the 355 nm excitation laser was employed. Therefore, using 532 nm and 355 nm involves a trade-off between those issues. Figure 4-27 shows a spectrum obtained from *in situ* Raman experiment of CO flame using 532 nm as an excitation source with the laser pulse energy of 11 mJ/pulse.

It is not clear that the spectrum shown in the Figure 4-25 represents the Fe₂O₃ Raman spectrum. Furthermore, neither FeO nor Fe₃O₄ Raman peaks are observed in the spectrum. Rather, the observed peaks correspond to Fe atomic emission lines, which are listed in Table 4-13.

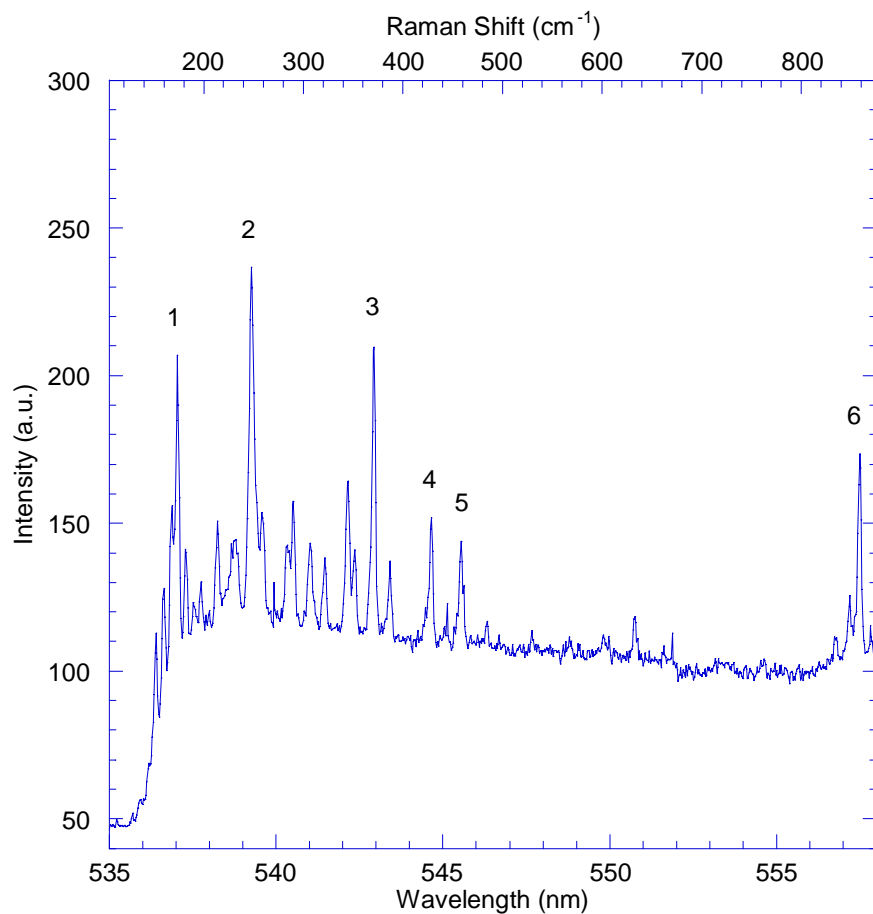


Figure 4-27. A spectrum obtained from *in situ* Raman experiment of CO flame using 532 nm as an excitation source.

Table 4-13. Fe atomic emission peaks.

Peak Label	Wavelength (nm)	Element
1	537.15	Fe I
2	539.32	Fe I
3	542.97	Fe I
4	544.69	Fe I
5	545.56	Fe I
6	557.70	Fe I

In the same manner, the more intense study was achieved using 355 nm excitation laser. Several spectra taken at four normalized CO flame heights are shown in Figure 4-28.

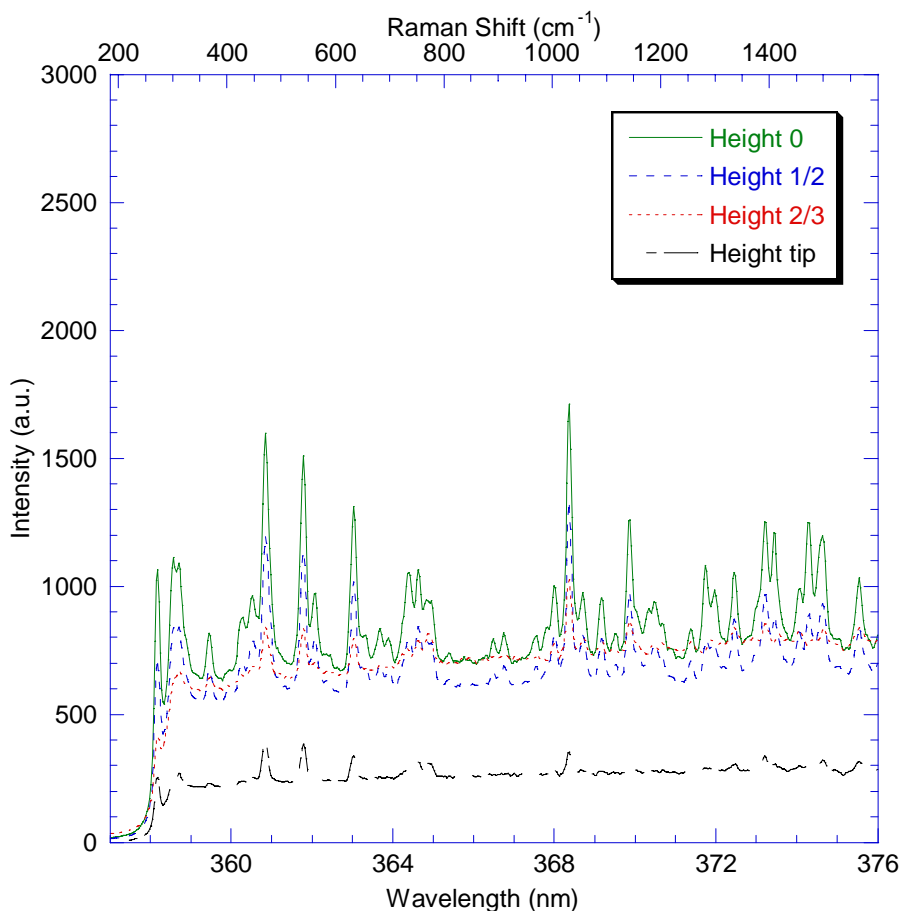


Figure 4-28. Spectra obtained from *in situ* Raman experiment of CO flame using 355 nm as an excitation source at four different heights.

Similar with the spectrum excited in 532 nm, peaks observed in Figure 4-28 may be Fe atomic emission peaks rather than possible iron oxide Raman peaks. For peak identification, a steel rod was examined using an increased laser fluence (achieved by focusing) to verify the Fe atomic emission lines produced by a laser induced plasma. Not only was the pulse energy increased, but also a focal lens was positioned in a manner to generate a breakdown on the surface of the steel rod. The same manner for data collection was used for LIBS. Figure 4-29 shows the atomic emissions from steel rod. Each peak is summarized in Table 4-14.

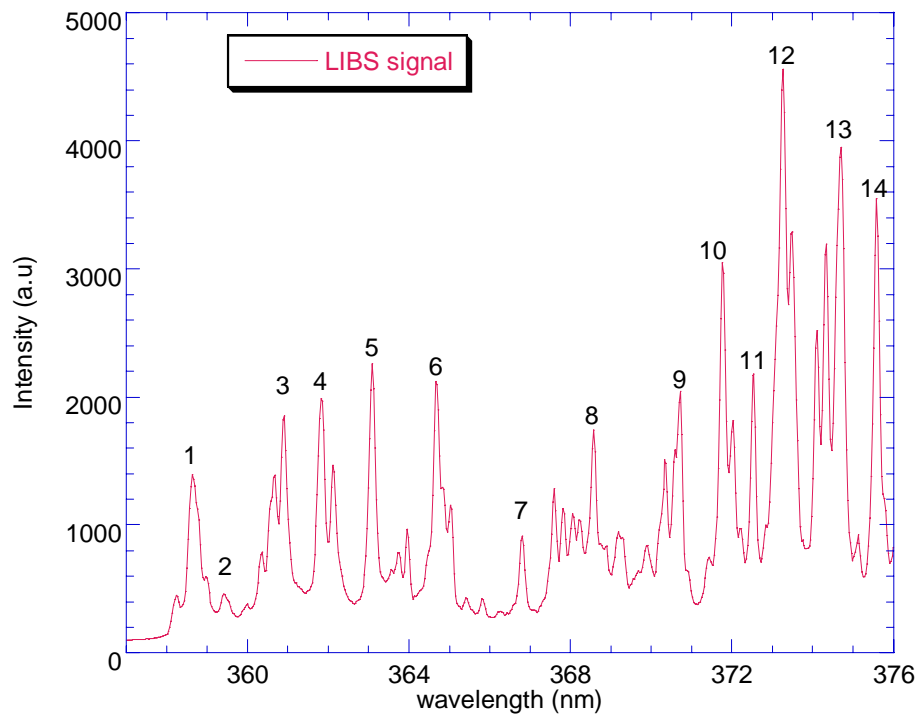


Figure 4-29. LIBS emission spectrum obtained from steel rod using 355 nm as an excitation source.

Table 4-14. LIBS emission peaks.

Peak Label	Wavelength (nm)	Element
1	358.67	-
2	359.48	-
3	360.89	Fe I
4	361.88	Fe I
5	363.15	Fe I
6	364.78	Fe I
7	366.81	-
8	368.57	-
9	370.56	Fe I
10	371.99	Fe I
11	372.55	-
12	373.49	Fe I
13	374.56	Fe I
14	375.55	Fe I

The profile of spectrum from the CO seeded flame is quite identical to that from steel rod; therefore, the spectrum obtained from *in situ* Raman spectroscopy is not iron oxide Raman signal but Fe atomic emission most likely caused by laser-induced

breakdown. However, this result may be attributed to breakdown of the iron oxides inside of the CO flame due to higher pulse energy. The effect of the sample breakdown must be very carefully considered during the Raman experiment. In order to ensure this, the laser energy was attenuated to find the optimum power sufficiently high to detect the iron oxide Raman signal, but simultaneously low to avoid breakdown of the sample. For the CO flame, no Fe signals were detected below the pulse energy of 10 mJ/pulse. Unfortunately, no Raman signals corresponding to iron oxides were noted. Additionally, it was noted in Figure 4-28 that the intensity of detected signal decreases as the flame height increases. This will be discussed later.

The same experiment was then carried out using the isooctane iron seeded flame, and the similar trend was observed. In this experiment, Fe concentration is lower than that in CO flame; thus, the higher laser pulse energy still did not provide a strong signal. As depicted in Figure 4-24, neither Fe nor iron oxides spectra were observed when the pulse energy was lower than 25 mJ/pulse. Since O₂ is present along the beam path as well as it was supplied in the flame, relatively strong Raman O₂ signal was detected at Raman shift of 1543 cm⁻¹.

In short, Fe atomic emission and pronounced Fe LIF signals were observed using *in situ* LIF in this study. This is not consistent with the results from *ex situ* studies that Fe₂O₃ was the dominant species created in iron pentacarbonyl seeded flame. However, a recent similar study accomplished by Kim *et al.* (2005) supports the result of this study. They analyzed the products from Fe(CO)₅ seeded ethylene diffusion flame using a Laser Microprobe Mass Spectrometry, and found that Fe dominated over iron oxides such as FeO and Fe₂O₃. The detailed discussion will be presented in Chapter 6.

CHAPTER 5
NUMERICAL ANALYSIS

5.1 Thermodynamic Equilibrium Calculations

Thermodynamic equilibrium calculations were carried out using STANJAN code (3.89 version, Department of Mechanical Engineering, Stanford University, Reynolds 1990) so that mass fraction of products from the isooctane flame seeded with iron pentacarbonyl could be numerically evaluated on several given conditions: flame temperatures, O₂ flow rates, and Fe(CO)₅ concentrations.

5.1.1 Flame Temperature

First of all, moles of each reactant were determined for the calculations using STANJAN code. They were calculated based on the quantities of reactants supplied in the seeded flame in the experiment. The calculations for each reactant are following below,

$$\text{N}_2: \quad 0.8 \times 10^{-3} \frac{m^3}{min} \times \frac{1 \text{ min}}{60 \text{ sec}} \times \frac{350 \text{ K}}{298 \text{ K}} \times 0.9625 \frac{Kg}{m^3} = 1.508 \times 10^{-5} \frac{Kg}{sec}, \quad (5-1)$$

$$1.508 \times 10^{-5} \frac{Kg}{sec} \times \frac{1 \text{ mol}}{28 \text{ g}} = 5.393 \times 10^{-4} \frac{mol}{sec}, \quad (5-2)$$

$$\text{O}_2: \quad 2.6 \times 10^{-3} \frac{m^3}{min} \times \frac{1 \text{ min}}{60 \text{ sec}} \times \frac{350 \text{ K}}{298 \text{ K}} \times 1.1 \frac{Kg}{m^3} = 5.6 \times 10^{-5} \frac{Kg}{sec}, \quad (5-3)$$

$$5.6 \times 10^{-5} \frac{Kg}{sec} \times \frac{1 \text{ mol}}{32 \text{ g}} = 1.75 \times 10^{-3} \frac{mol}{sec}, \quad (5-4)$$

where the densities of N₂ and O₂ are 0.9625 and 1.1 Kg/m³ respectively at the temperature of 350 K. For isooctane,

$$C_8H_{18}: 1.5 \times 10^{-6} \frac{m^3}{min} \times \frac{1 \text{ min}}{60 \text{ sec}} \times 703 \frac{Kg}{m^3} = 1.7575 \times 10^{-5} \frac{Kg}{sec}, \quad (5-5)$$

$$1.7575 \times 10^{-5} \frac{Kg}{sec} \times \frac{1 \text{ mol}}{114.23 \text{ g}} = 1.539 \times 10^{-4} \frac{mol}{sec}, \quad (5-6)$$

where the density of C_8H_{18} is $703 \text{ Kg}/m^3$ at the temperature of 298 K. The mass flow rate is always constant. Since 1 g of C_8H_{18} has $\frac{4}{1000}$ g of $Fe(CO)_5$,

$$\frac{4}{1000} \times 1.7575 \times 10^{-5} \frac{Kg}{sec} = 7.03 \times 10^{-8} \frac{Kg}{sec}, \quad (5-7)$$

$$7.03 \times 10^{-8} \frac{Kg}{sec} \times \frac{1 \text{ mol}}{195.845 \text{ g}} = 3.59 \times 10^{-7} \frac{mol}{sec}. \quad (5-8)$$

Moles of reactants used for calculation are tabulated in Table 5-1. Although the flame is diffusion flame, the air was excluded in reactants to simplify the calculation. This might be a serious limitation, but nonetheless, the current results provide a starting point for theoretical analysis.

Table 5-1. Mole of reactants used for input in the STANJAN code.

N_2	5393
O_2	17500
C_8H_{18}	1539
$Fe(CO)_5$	3.59

In the simulation, the following species considered to be equilibrium products were summarized in Table 5-2.

Table 5-2. Products from STANJAN simulation.

Reactant		Name of Species
		$C_8H_{18}, Fe(CO)_5, O_2, N_2$
Products	phase 1	$C(g^*), CH_4, CO, CO_2, C_3H_8, C_8H_{18}, Fe(CO)_5(g), Fe(OH)_2(g), Fe(g), FeO(g), H, HO, H_2, H_2O, N, NO, NO_2, N_2, O, O_2$
	phase 2	$C(s^*), Fe(CO)_5(l^*), Fe(OH)_2(s), Fe(OH)_3(s), Fe(a), Fe(l), Fe(r), FeCO_3(s), FeO(l), FeO(s), Fe_2O_3(s), Fe_3O_4(s), Fe_4N(s), H_2O(l)$

*g:gas; l:liquid; s:solid; r:radical

First, the mass fractions of all products were presented as a function of the adiabatic temperature. Figures 5-1, 5-2 and 5-3 represent the relative mass fraction of products obtained over the temperature ranging from 400 K to 2000 K at atmospheric pressure. This is in good agreement with the result obtained by Yang (2004).

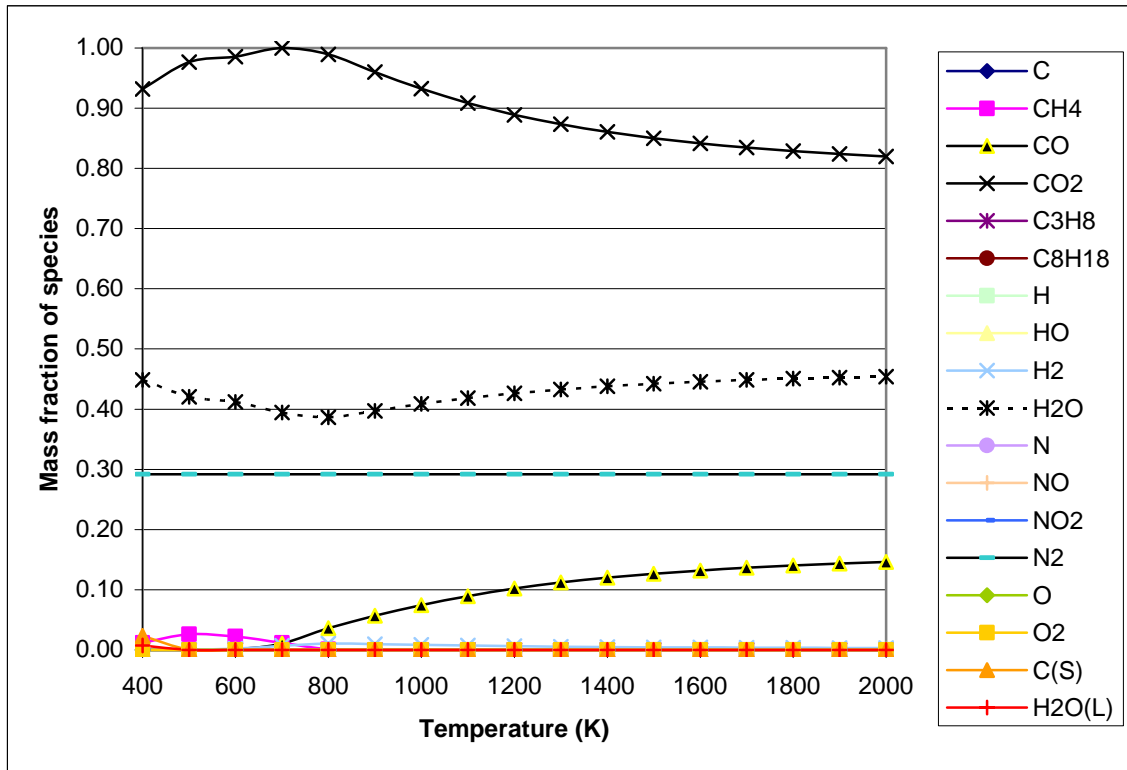


Figure 5-1. Relative mass fraction of products as a function of temperature.

For comparison, the flame temperatures were measured with a type K thermocouple along the axial direction of the flame. Due to radiation loss, the temperatures measured with the thermocouple should be corrected using the following equation,

$$h(T_f - T_{tc}) = \varepsilon\sigma(T_{tc}^4 - T_0^4) \quad (5-9)$$

where h is the convection heat transfer coefficient, ε is the emissivity of the thermocouple, σ is the Stefan-Boltzman constant, T_f is the temperature of the flame, T_{tc}

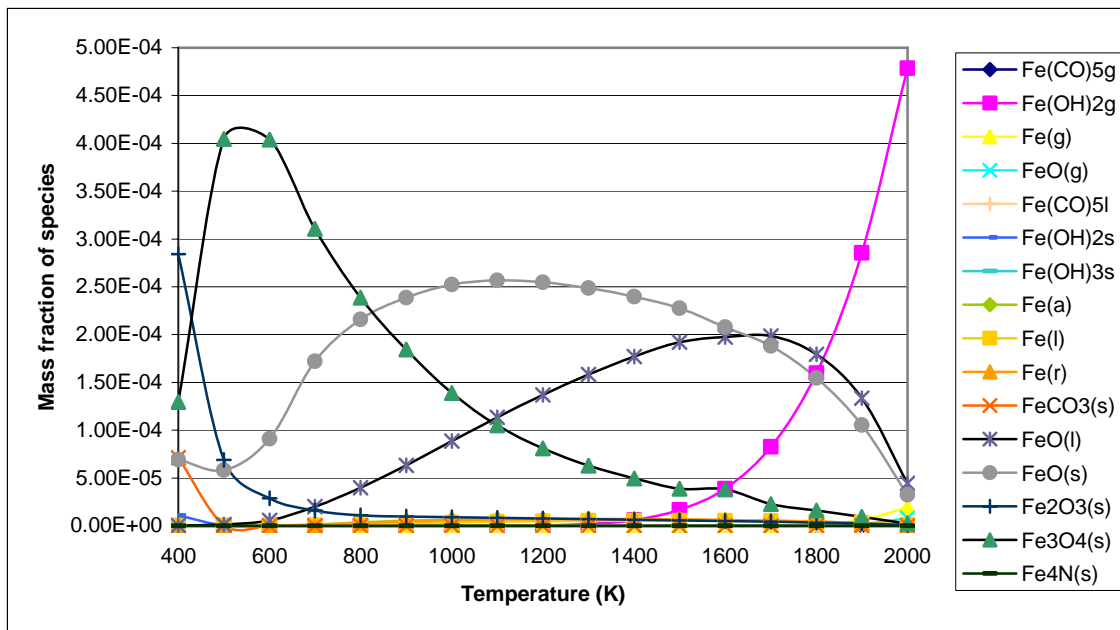


Figure 5-2. Relative mass fraction of Fe species as a function of temperature.

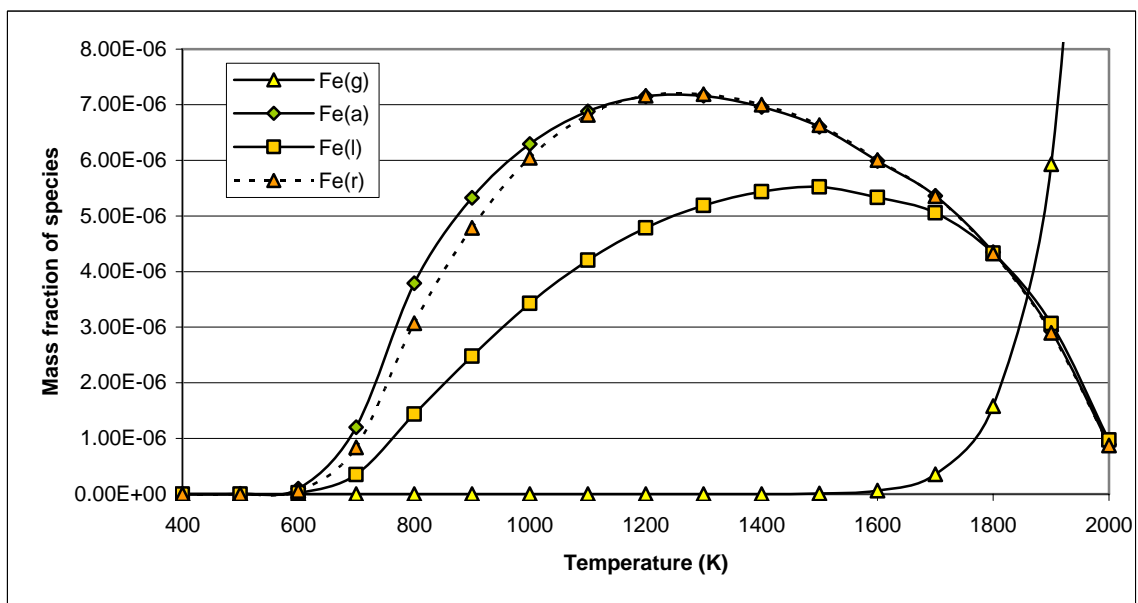


Figure 5-3. Relative mass fraction of Fe as a function of temperature.

is the temperature of the thermocouple, and T_0 is the ambient temperature. An emissivity of thermocouple was selected in 0.3 based on a report of the Greene *et al.* (2000). A

convection coefficient was calculated using an appropriate correlation given by Incropera and Dewitt (2002).

$$\frac{hD}{k} = 2 + (0.4 \cdot \text{Re}_D^{1/2} + 0.06 \cdot \text{Re}_D^{2/3}) \cdot \text{Pr}^{0.4} \left(\frac{\mu}{\mu_s} \right)^{1/4}, \quad (5-10)$$

where Re_D is the Reynolds number based on the diameter of the sphere, Pr is the Prandtl number, μ is the dynamic viscosity, μ_s is the dynamic viscosity at the surface temperature, k is thermal conductivity, and D is the characteristic length. The calculated convection coefficient was from 294 to 374 $\text{W}/\text{m}^2 \cdot \text{K}$. The flame temperature is presented in Figure 5-4.

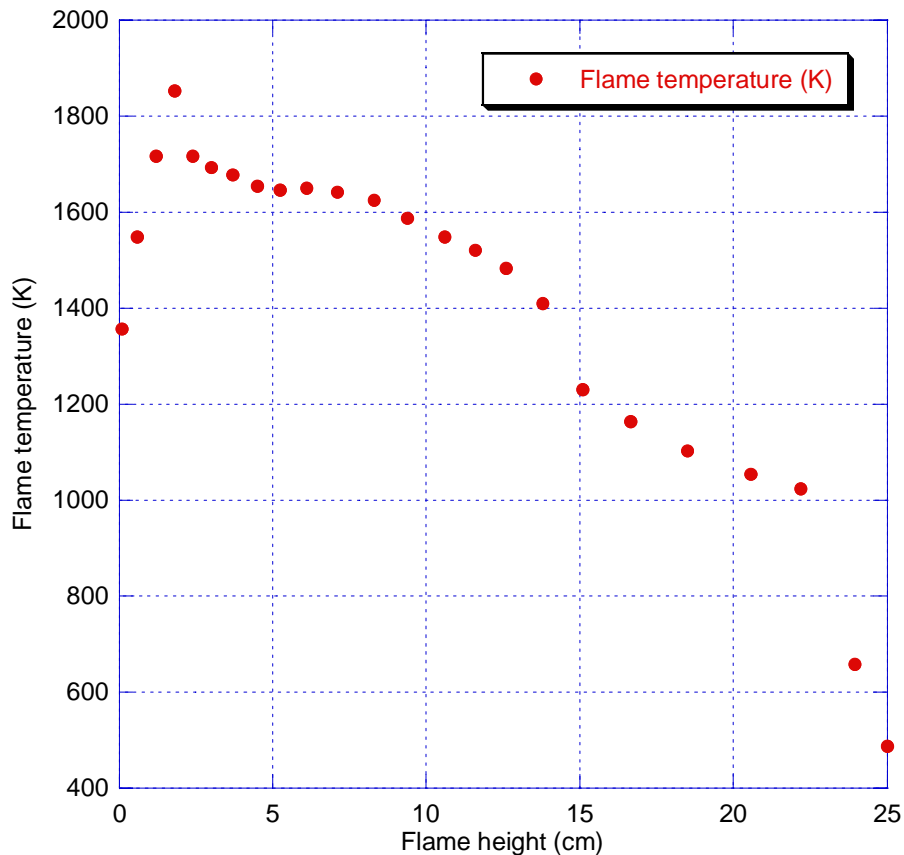


Figure 5-4. Flame temperature as a function of flame height.

Within this temperature range, the equilibrium calculation reveals that there are five major iron oxide species: $\text{Fe}(\text{OH})_2(\text{g})$, $\text{FeO}(\text{l})$, $\text{FeO}(\text{s})$, $\text{Fe}_2\text{O}_3(\text{s})$ and $\text{Fe}_3\text{O}_4(\text{s})$. Overall, $\text{FeO}(\text{s})$ is the dominant species among the iron oxides in the range from 800 to 1800 K. However, Fe_3O_4 is the dominant species over the other species at the temperature below 800 K, and Fe_2O_3 may be the dominant species at the ambient temperature.

As shown in the Figure 5-3, Fe fraction decreases as flame height increases, which was proven during the LIF experiment of both iron-seeded CO and isoctane flames. This result is in good agreement with the trend found in LIF experiments.

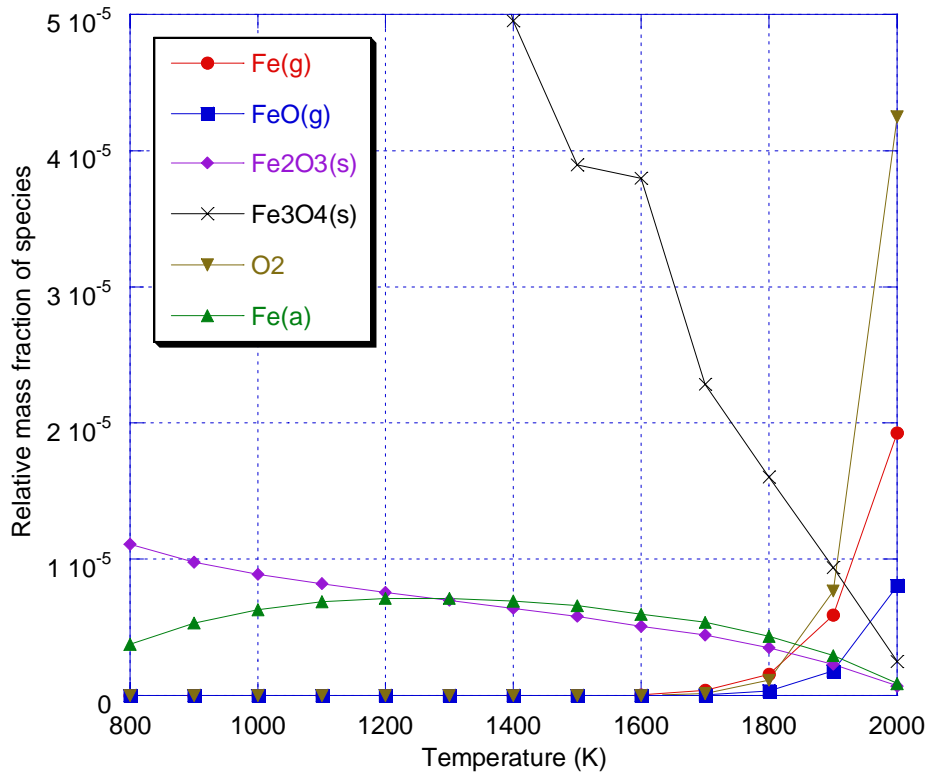


Figure 5-5. Relative mass fraction of species as a function of temperature.

With respect to FeO , gaseous phase FeO at the temperature of 2000 K is shown in Figure 5-5. McMillin *et al.* (1996) observed FeO LIF signal at the primary reaction zone in the premixed flame experimentally, and their numerical model showed the FeO was

dominant species throughout the flame (McMillin *et al.* 1996& Biswas *et al.* 1997). Since the temperature distribution of the premixed flame is normally from 2400 K to 1800 K, FeO could be formed in such an equilibrium condition. Son *et al.* (2000) also found FeO LIF signal from a iron composite mixture, but they used photolysis of Fe(CO)₅ to create FeO molecules. According to Mitchell and Hackett (1990), the reaction between Fe atoms in the ground-state and O₂ is endothermic reaction; therefore, the following reaction is unlikely to proceed in an appreciable rate at low temperature.



Gaseous FeO is not a very stable compound under equilibrium at temperatures below 1800 K so that the formation of FeO is not easy to occur under the flame configuration in this study. Therefore, the high concentration of FeO (solid and liquid phase) shown in Figure 5-2 may not be appreciable in this study.

5.1.2 O₂ Flow Rates

The change in the concentration of carbon was examined at the temperature of 1800 K as the oxygen flow rate increases. Figure 5-6 shows the relative mass fraction of carbon as a function of the oxygen flow rates.

Figure 5-6 shows the decrease in soot as a function of the oxygen flow rate. Although this is little a bit different from the smoke point of 4.25 LPM obtained from the smoke point study, this is in an excellent agreement with the oxygen flow rate of 2.6 LPM employed for all experiments. In addition, the concentration of iron oxides is plotted as a function of the oxygen flow rate in Figure 5-7.

Figure 5-7 elucidates that FeO dominates in the fuel-lean condition while Fe₂O₃ and Fe₃O₄ start dominating in the fuel-rich condition. As the oxygen flow rate increases,

the amount of Fe decreases, and Fe_2O_3 and Fe_3O_4 dominate FeO because the chance of reaction between Fe and O_2 is high. It is noted here that the role of additional oxygen diffusion is neglected.

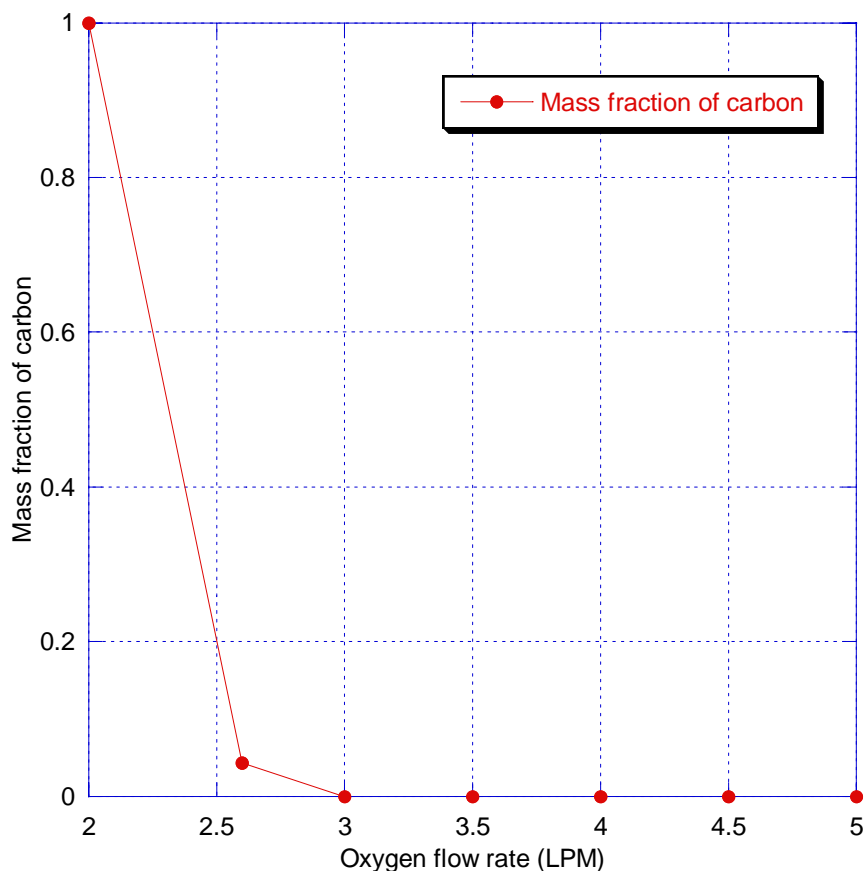


Figure 5-6. The decrease in relative mass fraction of the solid carbon as a function of the oxygen flow rate.

5.1.3 $\text{Fe}(\text{CO})_5$ Concentrations

The change in the concentration of carbon was also examined at the temperature of 1800 K as the concentration of $\text{Fe}(\text{CO})_5$ increases. Figure 5-8 represents the relative mass fraction as a function of the iron pentacarbonyl concentration.

In case of simulation on carbon mass fraction, the amount of carbon increased as the mole of $\text{Fe}(\text{CO})_5$ increased, and mass fraction of carbon increased when iron

pentacarbonyl was added to isooctane, which was not realistic. The increase in carbon appears to be attributed to increase in $(\text{CO})_5$ decomposed from iron pentacarbonyl.

Overall, the numerical simulation does not provide the distinctive transitions, but predict the relative stability and the potential mixture of each species at a given temperature. For example, Figure 5-2 does not mean that FeO decomposes around

800 K and forms Fe_3O_4 at the lower temperature. Furthermore, the significant uncertainty of this simulation was to exclude the air in the reaction. It is also important to note that all species can partially evaporate at a given temperature as long as they have appreciable vapor pressure. In addition to these uncertainties, the most significant

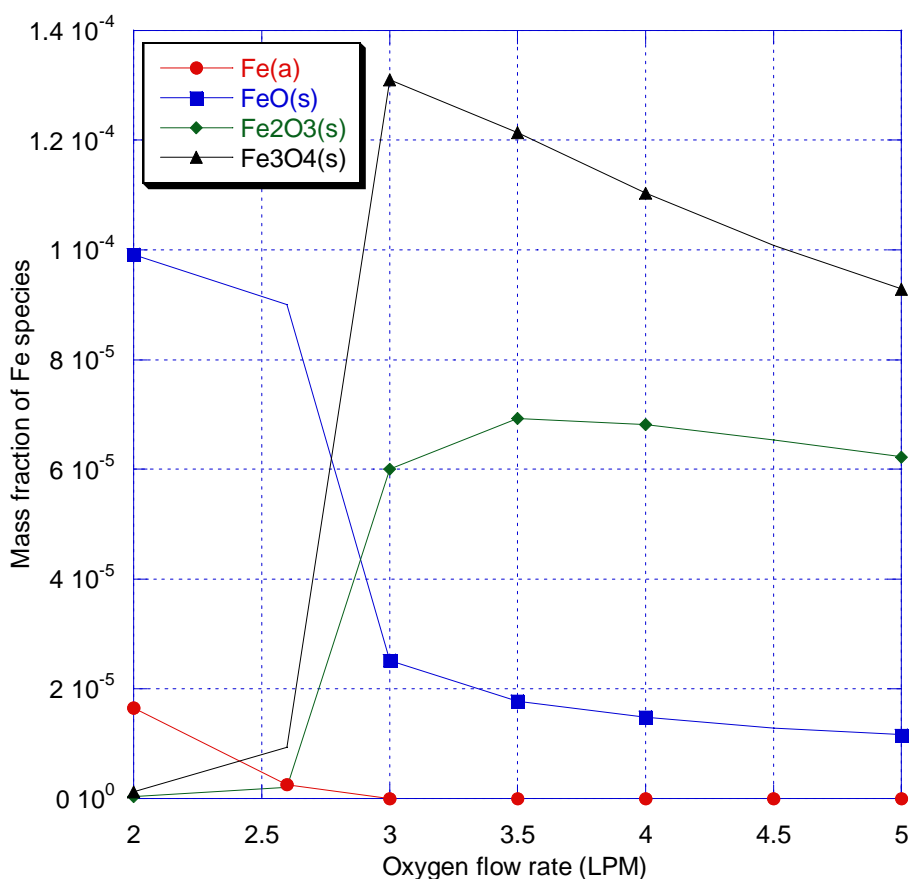


Figure 5-7. Relative mass fraction of the iron species as a function of the oxygen flow rate.

discrepancy was that it was very difficult for species to reach thermal equilibrium condition inside of the flame. The residence time of the iron species inside of the flame would be about 50 milliseconds. This means the flame temperature drops down from 1800 K to 500 K within 50 ms. In such a condition, the equilibrium iron oxide particle formation is very unlikely to occur while the additive decomposition is still very active. The detailed discussion will be achieved in Chapter 6.

Shortly, these numerical simulations can more correctly illustrate the state of species in the equilibrium condition. Therefore, this simulation results are limited of use to predict the experimental results in this study.

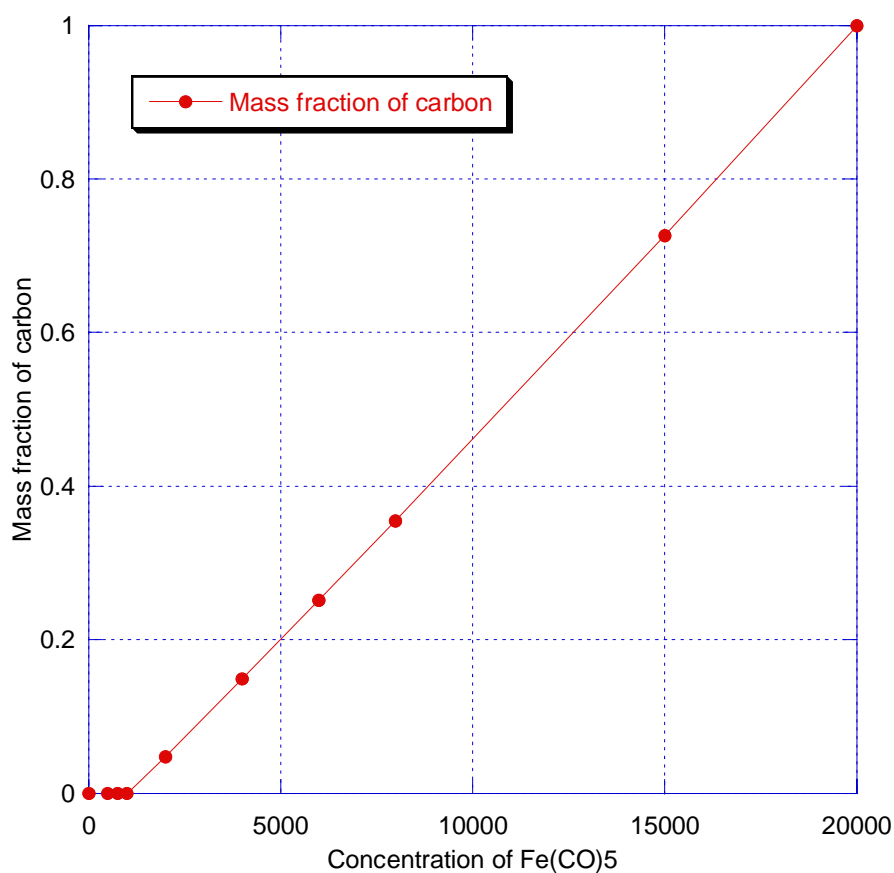


Figure 5-8. Mass fraction of carbon as a function of the Fe(CO)₅ concentration.

CHAPTER 6 CONCLUSIONS AND FUTURE WORK

6.1 Summary and Conclusions

This study was designed to explore and document the role that iron has the effect on the soot burning processes in the iron-seeded diffusion flame. Since an earlier study was achieved on the soot inception regime, the primary focus was on the latter regime of the flame, namely soot growth and oxidation regimes. Elastic light scattering and transmission data coupled with TEM analysis of soot particles sampled thermophoretically were used to extract information on size, number density, and volume fraction of soot particle in the unseeded and seeded flames. In comparison with all results, no distinct trends between the two flames were observed in the soot growth regime, which indicates that the iron additive has little effect on soot growth in this regime. This is consistent with the work of Masiello (2004), in which detailed measurements within the inception and growth regimes led to the conclusion that iron particulates are quickly incorporated within soot agglomerates, giving way to “typical” soot growth.

On the other hand, the iron-seeded flame data showed a consistent change with respect to the unseeded flames in the soot oxidation regime. In particular, the maximum deviation between the two flames was observed near the flame tip where the final soot volume fraction is reduced by nearly 66%. The average primary soot particle diameters at the lower heights (from 9.4 to 11.7 cm above burner) were 31 and 29 nm in the unseeded and seeded flames, respectively. In contrast, at the greatest residence time

investigated ($H = 25$ cm), the primary particle diameters were reduced to 24 and 20 nm in the unseeded and iron-seeded flames, respectively. Such a decrease in particle size is consistent with significant soot oxidation. Overall, the primary particle diameters and volume fraction data, as measured from the TEM micrographs and scattering signal, depict the transition from soot growth to soot oxidation along the length of the flame. The reduction in soot emission was visually observed as well. A pronounced smoke plume escaping from the flame tip disappeared when the iron seeded fuel was supplied. Based on all evidence stated above, it can be concluded that the iron additive has a significant effect of soot reduction that takes place in the oxidation regime.

The remaining questions are how this reduction occurs, and what mechanisms are involved in the process of soot reduction. In order to answer these questions, it is useful to identify the iron species present in the flame. While *ex situ* measurements of Masiello (2004) suggested that Fe_2O_3 would be the most probable state of the iron in the oxidized soot particle, a numerical calculation reveals FeO may be a dominant iron species under conditions of thermodynamic equilibrium. Indeed, the residence time of iron species inside the flame is about 50 milisecond, which may be too short to reach the equilibrium condition; hence, the formation of FeO or Fe_2O_3 is unlikely to occur on the inside of the flame. This is consistent with the recent work of Kim *et al.* (2005), which found considerable elemental Fe in a ethylene diffusion flame. Laser-induced fluorescence and *in situ* Raman spectroscopy were examined to identify the chemical state of iron additive inside the seeded flame in this study. With these techniques, any form of iron oxides was not observed in the flame. In contrast, a strong Fe LIF signal was found throughout the flame heights. As discussed before, the primary conclusion is that the iron species do not

reach thermodynamic equilibrium conditions, so that Fe atoms are significant, notably in the growth regimes. However, the rapid loss of elemental Fe within the oxidation regime may suggest some oxide formation, which is presumably below the current detection limits. Based on the spectroscopic evidence, the conclusion is that the soot is primarily reduced by a direct Fe catalytic effect.

Theoretically, both iron oxides and atoms can contribute to the reduction of soot. They may lead to direct oxidation of the soot particle, which can be expressed in chemical reaction below,



McMillin *et al.* (1996) found that some Fe atoms were combined with oxygen radical in the inner cone of the premixed flame. In this case, the mechanism of soot reduction could be explained with Equation 6-1. On the other hand, they may help to oxidize the soot particles as catalysts. The chemical reactions 6-3 and 6-4 illustrate the catalytic soot oxidation processes,



There are two types of catalysts, namely homogeneous catalyst and heterogeneous catalyst. Homogeneous catalyst promotes the reaction via dissolving into the gas phase or solution, while heterogeneous catalyst enhances the reaction by increasing probability of the reaction on the surface of the catalyst. Transition metals (i.e. Fe) are typical heterogeneous catalysts. Figure 6-1 illustrated heterogeneous catalytic mechanism of soot oxidation.

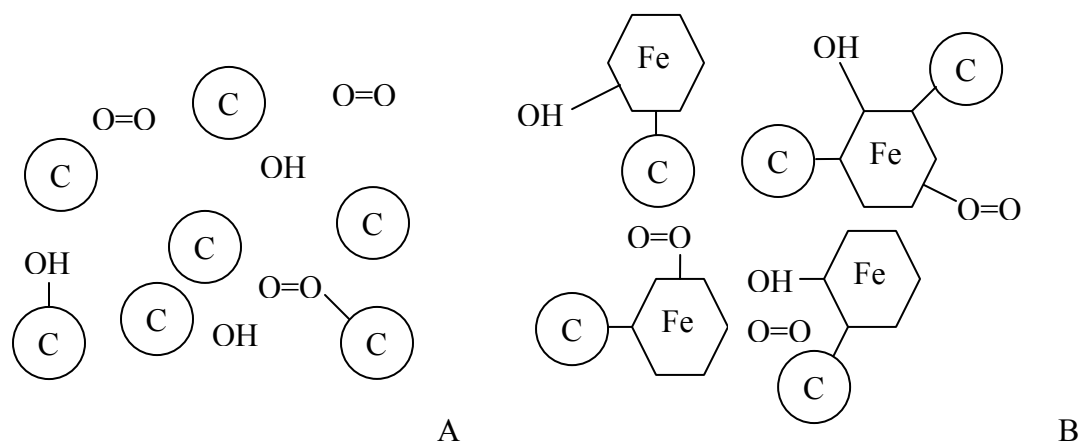


Figure 6-1. Schematic of soot oxidation mechanism. A) Soot oxidation without Fe. B) Soot oxidation with Fe.

Soot particles can be oxidized by three major oxidizers such as O atoms, OH radicals, and O₂. However, the concentration of O in sooting flame is very low compared with other oxidizers; hence, the primary oxidation of soot is considered to be due to OH and O₂. In particular, the role of OH as an oxidizer may be significant in the combustion of hydrocarbon fuel. Surface reactions are responsible for the creation of OH. The first step of this mechanism is the dissociative adsorption of oxygen molecules on the surface of the elemental Fe expressed in Equation 6-5,



These adsorbed O atoms collide with adsorbed H atoms, forming OH in surface reactions.



In these equations, Fe (s) denotes free surface sites, and (s) behind O and H atoms indicate surface species. Finally, OH radicals are desorbed from the surface of Fe and attack the solid carbon as shown in Equation 6-4. It is noted that no H is consumed

overall in the mechanism. The surface reaction mechanism of hydrogen oxidation was delineated in Figure 6-2. Experimental validation of the presence of OH inside of the flame will be achieved in the future research work.

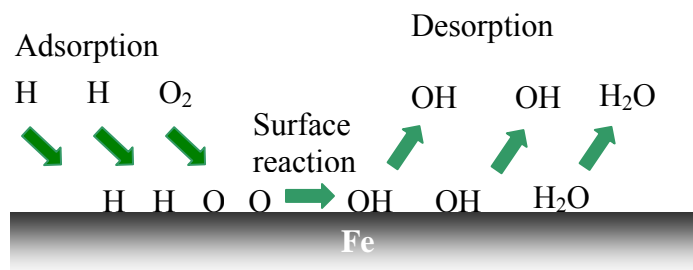


Figure 6-2. Schematic of surface reaction mechanism of hydrogen oxidation. Three steps of the mechanism are adsorption, surface reaction, and desorption.

The mechanism of surface reaction produces H₂O as well. Both iron and iron oxide are well known catalyst for rapid conversion of CO to CO₂, so called water-gas shift reaction,



Lowered CO concentrations in the gas phase may favor the reaction of solid carbon and oxygen.

Finally, a simple analysis was performed to support the conclusion that the catalysis effect of Fe is the primary reason on soot reduction. One mole of iron is able to oxidize at most 4 moles of carbon to satisfy the direct oxidation mechanism. However, approximately 500 moles of carbon are oxidized per 1 mole of iron exist, as based on the realized soot reduction; hence, the iron additive must play a role of the catalyst to enhance the chemical reaction between soot and oxidizers rather than directly oxidize the soot in the flame, which is consistent with the conclusion from the experiments.

Regarding Fe LIF signal drop, there are some possibilities to explain it. Although the overall concentration of Fe atom may be conserved, the density of Fe in the scattering volume is lower in downstream of the flame due to the diffusion of Fe atoms. However, the most likely reason is the Fe atom loss due to oxidation,



Equilibrium may be delayed at lower heights due to several reasons. First, the flame residence time is limited, as noted. In addition, the iron is encapsulated within the soot, which protects it from oxidation. Finally, oxygen is limited due to the competition with hydrocarbon oxidation. However, at longer residence times, the oxidation of carbon exposes the iron to additional oxygen, oxygen concentrations are increased by diffusion, and time-scales are longer allowing the approach to equilibrium. Once iron transitions occur, additional catalytic pathways may emerge, such as



that involved additional iron oxide species.

In addition, the Fe LIF signal drop can be explained in terms of Fe vapor pressure. As shown in TEM images, iron species are concentrated in the core of soot particles. In the soot growth regime, the same elemental iron exists in gas phase due to high temperature, so that they can diffuse through the soot particle and into the gas. Such elemental Fe can be detected by LIF probe. However, the flame temperature is significantly dropped throughout the oxidation regime, which results in the reduction of Fe vapor pressure. As a result of this, the concentration of gas phase elemental Fe is also reduced. Even though Fe that remained in the core would be somewhat exposed due to

the loss of soot, the oxidation by an enhanced amount of the oxygen would keep the concentration of Fe still low.

Overall, the exact flame configuration, combustor residence times, and combustor stoichiometry are all expected to play key roles in the soot suppressing effects realized with iron-based additives.

6.2 Future Work

The current study has yielded quantitative and qualitative insights into the mechanisms of soot suppression with iron-based fuel additives. With further understanding of the iron mechanisms gained via this study, the next phase of the investigation is to examine such effects using the practical combustion engines.

Future works should include:

1. Perform additional *in situ* probes for iron oxides (e.g. photofragmentation).
2. Perform OH LIF probe for validating the presence of OH radical in the flame.
3. Perform extractive sampling probe with on-line mass spectrometry.
4. Assess the role of iron addition in a laboratory-scale gas turbine engine applying all techniques used for lab studies.

APPENDIX A
ANALYSIS OF THE FLAME

In order to evaluate Froude number, Reynolds number and equivalence ratio, a complete calculation was performed for the flame and presented here.

With respect to Froude Number, it physically represents the ratio of the initial jet momentum flow to the buoyant force experienced by the flame as given by

$$Fr_f \equiv \frac{v_e^2}{L_c \cdot g}, \quad (\text{A-1})$$

where the flame length(L_c) is around 0.31 m which was measured rather than calculated considering the flame temperature. Moreover, the gravity is 9.81 m/sec^2 , and v_e is the exit velocity given by

$$\begin{aligned} v_e &= v_{center} + v_{annular} \\ &= \frac{\dot{m}_{mix}}{\rho_{mix} \pi d_c^2 / 4} + \frac{\dot{m}_{O_2}}{\rho_{O_2} \pi (d_a^2 - d_c^2) / 4} . \\ &= 5.99 \text{ m/sec} \end{aligned} \quad (\text{A-2})$$

In this equation, the volume flow rate was measured that $\dot{V}_{fuel} = 0.0015 \text{ LPM}$, and the density of isooctane was 0.688 g/mL at 25°C . Therefore, the mass flow rate is calculated below,

$$\dot{m}_{fuel} = 1.72 \times 10^{-5} \text{ Kg/sec}, \quad (\text{A-3})$$

$$\begin{aligned} \dot{m}_{N_2} &= \frac{0.8 \times 10^{-3} \text{ m}^3}{60 \text{ sec}} \times 1.123 \frac{\text{Kg}}{\text{m}^3} . \\ &= 1.5 \times 10^{-5} \text{ Kg/sec} \end{aligned} \quad (\text{A-4})$$

The density (ρ_{N_2}) of nitrogen is 1.123 Kg/m³ and the density (ρ_{O_2}) of oxygen is 1.284 Kg/m³ at the temperature of 300 K. The molecular weight (fuel + nitrogen) is defined as

$$MW_{mix} = MW_{fuel} + MW_{N_2} = 114.23 + 28 = 142.23, \quad (A-5)$$

$$\rho_{mix} = \frac{P}{(R_u/MW_{mix})T} = \frac{101325}{(8315/142.23)350} = 4.95 \text{ Kg/m}^3, \quad (A-6)$$

$$\begin{aligned} \dot{m}_{O_2} &= \frac{2.6 \times 10^{-3} \text{ m}^3}{60 \text{ sec}} \times 1.284 \frac{\text{Kg}}{\text{m}^3} \\ &= 5.6 \times 10^{-5} \text{ Kg/sec} \end{aligned} \quad (A-7)$$

The diameter of the center hole of the burner (d_{center}) was 1.5×10^{-3} m, and that of the nine annular holes of the burner was 3×10^{-4} m. It is noteworthy that the annular holes were assumed as one concentric circle having the outer diameter of 5.13×10^{-3} m. See Figure 3-1.

$$\dot{m}_{mix} = \dot{m}_{fuel} + \dot{m}_{N_2} = 1.72 \times 10^{-5} + 1.5 \times 10^{-5} = 3.22 \times 10^{-5} \text{ Kg/sec}. \quad (A-8)$$

Finally, the Froude number was determined to be 11.8.

As for Reynolds number,

$$Re = \frac{\rho_e \cdot v_e \cdot d}{\mu}, \quad (A-9)$$

$$\rho_{mix} = \frac{P}{(R_u/MW_{mix})T} = \frac{101325}{(8315/174.23)350} = 6.07 \text{ Kg/m}^3, \quad (A-10)$$

$$d = d_{center} + d_{annular} = 5.13 \times 10^{-3} \text{ m}. \quad (A-11)$$

With respect to viscosity (μ), $\mu_{C_8H_{18}}$ is 4.7×10^{-4} Kg/m·s and μ_{air} is 2×10^{-5} Kg/m·s. μ_{mix} is assumed around 2.45×10^{-5} Kg/m·s. Therefore, the Reynolds number was 761.3.

In addition, the equivalence ratio, ϕ was evaluated. The governing combustion stoichiometric reaction for this experiment is given by



In the experimental case, the volumetric flow rates of fuel and oxidizer were 4.38 cc per second and 50.9 cc per second, respectively (see Appendix E). For an ideal gas, the volumetric ratio is equal to the molar ratio defined as the ratio of the actual air to fuel ratio to the stoichiometric air to fuel ratio. The equivalence ratio is greater than unity representing fuel lean combustion while being less than unity indicating fuel rich combustion. The equivalence ratio, ϕ was calculated as

$$\phi = \frac{A/F_{stoichiometric}}{A/F_{experimental}} = \frac{25/2}{50.9/4.38} = 1.08. \quad (A-13)$$

In conclusion, first, the flame was not buoyancy-controlled because the Froude number was greater than unity. Second, it was laminar flow because the Reynolds number was less than ~ 2300 . Third, the diffusion flame employed in the experiment was run on the fuel rich side of stoichiometry.

APPENDIX B
RESULTS OF RDG CALCULATIONS

In order to determine scattering parameters, Rayleigh Debye Gans scattering theory was employed. The detailed results are presented here. In addition, new calculation was carried out based on a complex refractive index of $\bar{m} = 1.57-0.56i$. Table B-1 shows the radius of the primary soot particle determined by TEM analysis. Curve fit data were used in the following calculation.

Table B-1. Measured radius of the primary soot particle.

Height (cm)	Unseeded		Seeded	
	Radius (cm)	Fit radius (cm)	Radius (cm)	Fit radius (cm)
9.4	1.71E-06	1.59E-06	1.36E-06	1.35E-06
10.1	1.48E-06	1.59E-06	1.29E-06	1.39E-06
10.9	1.62E-06	1.59E-06	1.47E-06	1.42E-06
11.7	1.44E-06	1.58E-06	1.45E-06	1.45E-06
12.7	1.57E-06	1.57E-06	1.45E-06	1.48E-06
13.7	1.60E-06	1.56E-06	1.61E-06	1.50E-06
14.9	1.58E-06	1.54E-06	1.57E-06	1.51E-06
16.2	1.56E-06	1.51E-06	1.50E-06	1.50E-06
17.75	1.52E-06	1.46E-06	1.42E-06	1.47E-06
19.6	1.33E-06	1.40E-06	1.34E-06	1.40E-06
21.85	1.25E-06	1.31E-06	1.24E-06	1.26E-06
25.25	1.17E-06	1.13E-06	1.00E-06	9.62E-07

The first step in determining the characteristics of the soot particles was to calculate the differential scattering cross section using the equation,

$$\sigma'_{VV} = \frac{\lambda^2}{4\pi^2} \alpha^6 \left| \frac{m^{-2} - 1}{m^{-2} + 2} \right|^2 \quad (B-1)$$

The result is listed in Table B-2.

Table B-2. The differential scattering cross section (cm²/sr).

Height (cm)	Unseeded		Seeded	
	m=2.0-0.35i	m=1.57-0.56i	m=2.0-0.35i	m=1.57-0.56i
9.4	8.82E-16	6.83E-16	3.29E-16	2.55E-16
10.1	8.79E-16	6.81E-16	3.88E-16	3.00E-16
10.9	8.69E-16	6.73E-16	4.54E-16	3.52E-16
11.7	8.51E-16	6.59E-16	5.15E-16	3.99E-16
12.7	8.19E-16	6.34E-16	5.79E-16	4.48E-16
13.7	7.77E-16	6.02E-16	6.23E-16	4.83E-16
14.9	7.15E-16	5.54E-16	6.44E-16	4.99E-16
16.2	6.38E-16	4.94E-16	6.24E-16	4.83E-16
17.75	5.37E-16	4.16E-16	5.48E-16	4.24E-16
19.6	4.14E-16	3.21E-16	4.07E-16	3.15E-16
21.85	2.75E-16	2.13E-16	2.22E-16	1.72E-16
25.25	1.16E-16	9.02E-17	4.32E-17	3.35E-17

The radius of gyration and the structure factor then can be calculated using the equations,

$$(LW)^{1/2}/(2R_g) = 1.17, \quad (\text{B-2})$$

$$S(q) = C(qR_g)^{-D_f}, \quad qR_g > 1. \quad (\text{B-3})$$

where the constant C is approximately one. In order to determine the total scattering cross section for a fractal aggregate, $G(kR_g)$ is also calculated by

$$G(kR_g) = \left(1 + \frac{4}{3D_f} k^2 R_g^2\right)^{-D_f/2}, \quad (\text{B-4})$$

where the fractal dimension was 1.82 for all conditions. The results are summarized in Tables B-3 and B-4. In addition, the number density of primary particles in an aggregate and curve fit values are shown in Tables. The differential scattering coefficients obtained from the light scattering experiments and corrected values by considering transmission are shown in Table B-5.

Table B-3. Summary of calculated results for the unseeded flame.

Height (cm)	Unseeded					
	Rg	Npri	Fit Npri	qRg	S(q)	G(kRg)
9.4	1.29E-05	77	103	2.16	0.25	0.18
10.1	1.28E-05	108	115	2.14	0.25	0.18
10.9	1.65E-05	135	128	2.76	0.16	0.12
11.7	1.37E-05	133	139	2.29	0.22	0.16
12.7	1.93E-05	203	153	3.22	0.12	0.09
13.7	1.56E-05	164	166	2.6	0.18	0.13
14.9	-	171	180	-	-	-
16.2	1.75E-05	178	194	2.93	0.14	0.11
17.75	2.24E-05	231	210	3.73	0.09	0.07
19.6	2.37E-05	346	226	3.95	0.08	0.07
21.85	2.10E-05	254	245	3.51	0.10	0.08
25.25	1.80E-05	247	269	3.00	0.14	0.11

Table B-4. Summary of calculated results for the seeded flame.

Height (cm)	Seeded					
	Rg	Npri	Fit Npri	qRg	S(q)	G(kRg)
9.4	8.98E-06	64	99	1.50	0.48	0.30
10.1	8.12E-06	60	113	1.36	0.57	0.34
10.9	1.43E-05	116	128	2.39	0.21	0.15
11.7	2.24E-05	203	143	3.75	0.09	0.07
12.7	2.04E-05	211	159	3.41	0.11	0.09
13.7	2.59E-05	244	174	4.33	0.07	0.06
14.9	2.42E-05	286	191	4.04	0.08	0.06
16.2	2.03E-05	212	208	3.4	0.11	0.09
17.75	-	256	226	-	-	-
19.6	2.62E-05	301	246	4.38	0.07	0.06
21.85	2.01E-05	223	268	3.36	0.11	0.09
25.25	1.69E-05	170	297	2.82	0.15	0.12

The differential scattering cross section of an aggregate is defined as

$$\sigma'_{agg} = N_{par}^2 \sigma'_{par} S(q), \quad (\text{B-5})$$

The results are shown in Table B-6.

Table B-5. Uncorrected and corrected differential scattering coefficients ($\text{cm}^{-1}\text{sr}^{-1}$).

Height (cm)	Unseeded		Seeded	
	$K'_{vv, \text{uncorrected}}$	$K'_{vv, \text{corrected}}$	$K'_{vv, \text{uncorrected}}$	$K'_{vv, \text{corrected}}$
9.4	2.87E-03	3.70E-03	3.08E-03	3.98E-03
10.1	2.90E-03	3.87E-03	2.24E-03	2.91E-03
10.9	2.43E-03	3.26E-03	1.99E-03	2.67E-03
11.7	2.16E-03	2.97E-03	2.24E-03	3.05E-03
12.7	2.63E-03	3.60E-03	2.02E-03	2.68E-03
13.7	2.98E-03	4.10E-03	2.65E-03	3.77E-03
14.9	2.81E-03	3.78E-03	2.38E-03	3.13E-03
16.2	2.07E-03	2.76E-03	1.80E-03	2.28E-03
17.75	1.47E-03	1.74E-03	1.24E-03	1.40E-03
19.6	9.17E-04	1.04E-03	9.44E-04	1.01E-03
21.85	5.04E-04	5.44E-04	3.78E-04	3.95E-04
25.25	2.29E-04	2.44E-04	6.16E-05	6.35E-05

Table B-6. Differential scattering cross section for a fractal aggregate (cm^2/sr).

Height (cm)	Unseeded		Seeded	
	m=2.0-0.35i	m=1.57-0.56i	m=2.0-0.35i	m=1.57-0.56i
9.4	2.30E-12	1.78E-12	1.53E-12	1.18E-12
10.1	2.89E-12	2.24E-12	2.84E-12	2.20E-12
10.9	2.24E-12	1.73E-12	1.54E-12	1.19E-12
11.7	3.66E-12	2.84E-12	9.48E-13	7.35E-13
12.7	2.30E-12	1.78E-12	1.58E-12	1.22E-12
13.7	3.78E-12	2.93E-12	1.32E-12	1.02E-12
14.9	3.60E-12	2.79E-12	1.86E-12	1.44E-12
16.2	3.42E-12	2.65E-12	2.92E-12	2.26E-12
17.75	2.16E-12	1.67E-12	2.30E-12	1.78E-12
19.6	1.75E-12	1.35E-12	1.68E-12	1.30E-12
21.85	1.68E-12	1.31E-12	1.76E-12	1.36E-12
25.25	1.14E-12	8.85E-13	5.77E-13	4.47E-13

The number density of aggregate, N_{agg} in the scattering volume can be calculated using the equation,

$$N_{agg} = K'_{vv,agg} / \sigma'_{agg} \quad (\text{B-6})$$

The results are presented in Table B-7.

Table B-7. Number density of soot aggregates in the scattering volume (particles/cm³).

Height (cm)	Unseeded		Seeded	
	m=2.0-0.35i	m=1.57-0.56i	m=2.0-0.35i	m=1.57-0.56i
9.4	1.61E+09	2.08E+09	2.60E+09	3.36E+09
10.1	1.34E+09	1.73E+09	1.02E+09	1.32E+09
10.9	1.46E+09	1.88E+09	1.74E+09	2.24E+09
11.7	8.12E+08	1.05E+09	3.22E+09	4.16E+09
12.7	1.57E+09	2.02E+09	1.70E+09	2.19E+09
13.7	1.08E+09	1.40E+09	2.87E+09	3.70E+09
14.9	1.05E+09	1.35E+09	1.69E+09	2.18E+09
16.2	8.06E+08	1.04E+09	7.83E+08	1.01E+09
17.75	8.08E+08	1.04E+09	6.10E+08	7.87E+08
19.6	5.95E+08	7.67E+08	5.99E+08	7.74E+08
21.85	3.23E+08	4.17E+08	2.25E+08	2.90E+08
25.25	2.14E+08	2.76E+08	1.10E+08	1.42E+08

The total scattering cross sections for a primary particle and an aggregate are,

respectively, calculated by

$$\sigma_{sca} = \frac{2\lambda^2}{3\pi} \alpha^6 \left| \frac{m^2 - 1}{m^2 + 2} \right|^2, \quad (\text{B-7})$$

$$\sigma_{agg}^{sca} = N_{par}^2 \sigma_{par}^{sca} G(kR_g). \quad (\text{B-8})$$

The results are tabulated in Tables B-8 and B-9 respectively. The absorption cross

sections for a primary particle and an aggregate are, respectively, calculated by

$$\sigma_{abs} = \frac{-\lambda^2}{\pi} \alpha^3 \text{Im} \left\{ \frac{m^2 - 1}{m^2 + 2} \right\}, \quad (\text{B-9})$$

$$\sigma_{agg}^{abs} = N_{par} \sigma_{par}^{abs}. \quad (\text{B-10})$$

The results are listed in Tables B-10 and B-11.

Table B-8. Total scattering cross section for a primary soot particle (cm²).

Height (cm)	Unseeded		Seeded	
	m=2.0-0.35i	m=1.57-0.56i	m=2.0-0.35i	m=1.57-0.56i
9.4	7.39E-15	5.72E-15	2.75E-15	2.13E-15
10.1	7.36E-15	5.71E-15	3.25E-15	2.52E-15
10.9	7.28E-15	5.64E-15	3.80E-15	2.95E-15
11.7	7.13E-15	5.52E-15	4.31E-15	3.34E-15
12.7	6.86E-15	5.31E-15	4.85E-15	3.76E-15
13.7	6.51E-15	5.04E-15	5.22E-15	4.04E-15
14.9	5.99E-15	4.64E-15	5.39E-15	4.18E-15
16.2	5.34E-15	4.14E-15	5.22E-15	4.05E-15
17.75	4.50E-15	3.49E-15	4.59E-15	3.55E-15
19.6	3.47E-15	2.69E-15	3.41E-15	2.64E-15
21.85	2.30E-15	1.78E-15	1.86E-15	1.44E-15
25.25	9.76E-16	7.56E-16	3.62E-16	2.80E-16

Table B-9. Total scattering cross section of an aggregate (cm²).

Height (cm)	Unseeded		Seeded	
	m=2.0-0.35i	m=1.57-0.56i	m=2.0-0.35i	m=1.57-0.56i
9.4	1.39E-11	1.08E-11	8.10E-12	6.28E-12
10.1	1.75E-11	1.36E-11	1.43E-11	1.11E-11
10.9	1.43E-11	1.11E-11	9.56E-12	7.41E-12
11.7	2.26E-11	1.75E-11	6.34E-12	4.91E-12
12.7	1.51E-11	1.17E-11	1.04E-11	8.08E-12
13.7	2.39E-11	1.85E-11	8.91E-12	6.91E-12
14.9	2.30E-11	1.79E-11	1.25E-11	9.68E-12
16.2	2.21E-11	1.72E-11	1.93E-11	1.50E-11
17.75	1.44E-11	1.12E-11	1.53E-11	1.19E-11
19.6	1.17E-11	9.09E-12	1.14E-11	8.83E-12
21.85	1.12E-11	8.66E-12	1.16E-11	8.99E-12
25.25	7.43E-12	5.76E-12	3.72E-12	2.88E-12

The total extinction cross section is defined as a sum of the scattering and absorption cross section, namely,

$$\sigma_{ext} = \sigma_{sca} + \sigma_{abs} \quad (B-11)$$

The calculated results are presented in Table B-12.

Table B-10. Absorption cross section of a primary particle (cm²).

Height (cm)	Unseeded		Seeded	
	m=2.0-0.35i	m=1.57-0.56i	m=2.0-0.35i	m=1.57-0.56i
9.4	6.86E-13	1.55E-12	4.19E-13	9.45E-13
10.1	6.85E-13	1.55E-12	4.55E-13	1.03E-12
10.9	6.81E-13	1.54E-12	4.92E-13	1.11E-12
11.7	6.74E-13	1.52E-12	5.25E-13	1.18E-12
12.7	6.61E-13	1.49E-12	5.56E-13	1.25E-12
13.7	6.44E-13	1.45E-12	5.77E-13	1.30E-12
14.9	6.18E-13	1.39E-12	5.86E-13	1.32E-12
16.2	5.84E-13	1.32E-12	5.77E-13	1.30E-12
17.75	5.36E-13	1.21E-12	5.41E-13	1.22E-12
19.6	4.70E-13	1.06E-12	4.66E-13	1.05E-12
21.85	3.83E-13	8.64E-13	3.44E-13	7.77E-13
25.25	2.49E-13	5.63E-13	1.52E-13	3.43E-13

Table B-11. Absorption cross section of an aggregate (cm²).

Height (cm)	Unseeded		Seeded	
	m=2.0-0.35i	m=1.57-0.56i	m=2.0-0.35i	m=1.57-0.56i
9.4	7.04E-11	1.59E-10	4.13E-11	9.32E-11
10.1	7.86E-11	1.77E-10	5.14E-11	1.16E-10
10.9	8.69E-11	1.96E-10	6.32E-11	1.43E-10
11.7	9.40E-11	2.12E-10	7.47E-11	1.69E-10
12.7	1.01E-10	2.29E-10	8.84E-11	1.99E-10
13.7	1.07E-10	2.41E-10	1.00E-10	2.27E-10
14.9	1.11E-10	2.51E-10	1.12E-10	2.53E-10
16.2	1.13E-10	2.56E-10	1.20E-10	2.71E-10
17.75	1.12E-10	2.53E-10	1.22E-10	2.76E-10
19.6	1.06E-10	2.40E-10	1.15E-10	2.59E-10
21.85	9.38E-11	2.12E-10	9.23E-11	2.08E-10
25.25	6.71E-11	1.51E-10	4.51E-11	1.02E-10

The extinction coefficient for the overall aggregates in the volume is finally determined using the following equation,

$$K_{ext}^{agg} = N_{agg} \sigma_{ext}^{agg} . \quad (B-12)$$

The calculated results are summarized in Table B-13.

Table B-12. The extinction cross section of an aggregate (cm^2).

Height (cm)	Unseeded		Seeded	
	m=2.0-0.35i	m=1.57-0.56i	m=2.0-0.35i	m=1.57-0.56i
9.4	8.43E-11	1.70E-10	4.94E-11	9.95E-11
10.1	9.61E-11	1.91E-10	6.57E-11	1.27E-10
10.9	1.01E-10	2.07E-10	7.27E-11	1.50E-10
11.7	1.17E-10	2.30E-10	8.11E-11	1.74E-10
12.7	1.16E-10	2.40E-10	9.88E-11	2.07E-10
13.7	1.31E-10	2.60E-10	1.09E-10	2.34E-10
14.9	1.34E-10	2.69E-10	1.24E-10	2.62E-10
16.2	1.36E-10	2.73E-10	1.39E-10	2.86E-10
17.75	1.27E-10	2.65E-10	1.38E-10	2.88E-10
19.6	1.18E-10	2.49E-10	1.26E-10	2.68E-10
21.85	1.05E-10	2.20E-10	1.04E-10	2.17E-10
25.25	7.45E-11	1.57E-10	4.88E-11	1.05E-10

Table B-13. The extinction coefficient (cm^{-1}).

Height	Unseeded			Seeded		
	m=2.0-0.35i	m=1.57-0.56i	B-L Law*	m=2.0-0.35i	m=1.57-0.56i	B-L Law
9.4	1.36E-01	3.53E-01	3.03E-01	1.29E-01	3.34E-01	2.45E-01
10.1	1.29E-01	3.29E-01	3.18E-01	6.72E-02	1.68E-01	2.43E-01
10.9	1.48E-01	3.90E-01	2.98E-01	1.26E-01	3.37E-01	2.65E-01
11.7	9.47E-02	2.41E-01	3.07E-01	2.61E-01	7.22E-01	2.77E-01
12.7	1.82E-01	4.86E-01	2.80E-01	1.68E-01	4.55E-01	2.48E-01
13.7	1.42E-01	3.64E-01	2.70E-01	3.13E-01	8.64E-01	3.02E-01
14.9	1.41E-01	3.64E-01	2.42E-01	2.10E-01	5.72E-01	2.33E-01
16.2	1.09E-01	2.84E-01	2.26E-01	1.09E-01	2.88E-01	1.99E-01
17.75	1.02E-01	2.76E-01	1.33E-01	8.39E-02	2.26E-01	1.07E-01
19.6	7.03E-02	1.91E-01	9.87E-02	7.56E-02	2.07E-01	5.68E-02
21.85	3.39E-02	9.18E-02	6.50E-02	2.33E-02	6.29E-02	4.11E-02
25.25	1.59E-02	4.33E-02	7.05E-02	5.37E-03	1.48E-02	3.30E-02

*B-L Law is Beer-Lambert law.

The extinction coefficients for the optical length determined using Beer-Lambert law and transmission data are listed in Table B-13 as well. The optical lengths were obtained from 25 digital photographs of the unseeded and seeded flames. In the same

manner discussed for analyzing soot particles in TEM images, the flame widths corresponding to 12 heights were measured using Measure tool in Photoshop computer software. Alternatively, it can be determined by using either the scattered signal or transmission data taken along the radial positions of the flame. Figure B-1 represents the differential scattering coefficients measured along the radial positions at three different heights.

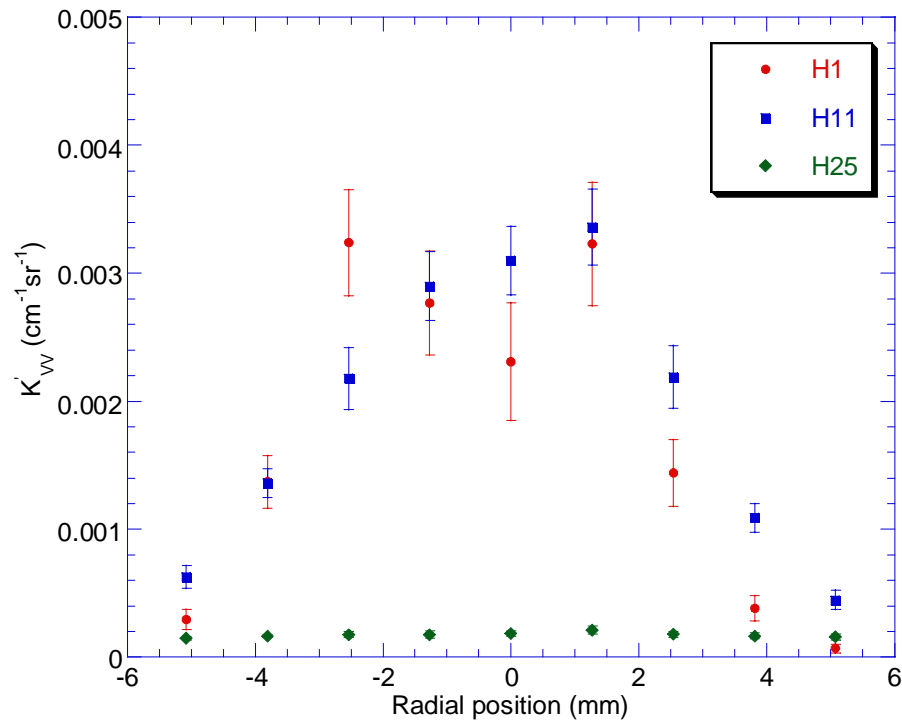


Figure B-1. The differential scattering coefficients measured along the radial positions at three different heights. Error bars represent one standard deviation.

This is the common way to determine the optical pathlength; however, not only was the flame employed in this study very thin but also somewhat severe fluctuation of the flame made it hard to obtain reasonable data. Therefore, this data was not use for determining the extinction coefficient using Beer-Lamberts law in this study.

Overall, the deviations of the absolute values of it were about 43% for the extinction coefficients determined with both the former and the latter refractive indices.

The extinction coefficients are presented in Figures B-2 and B-3.

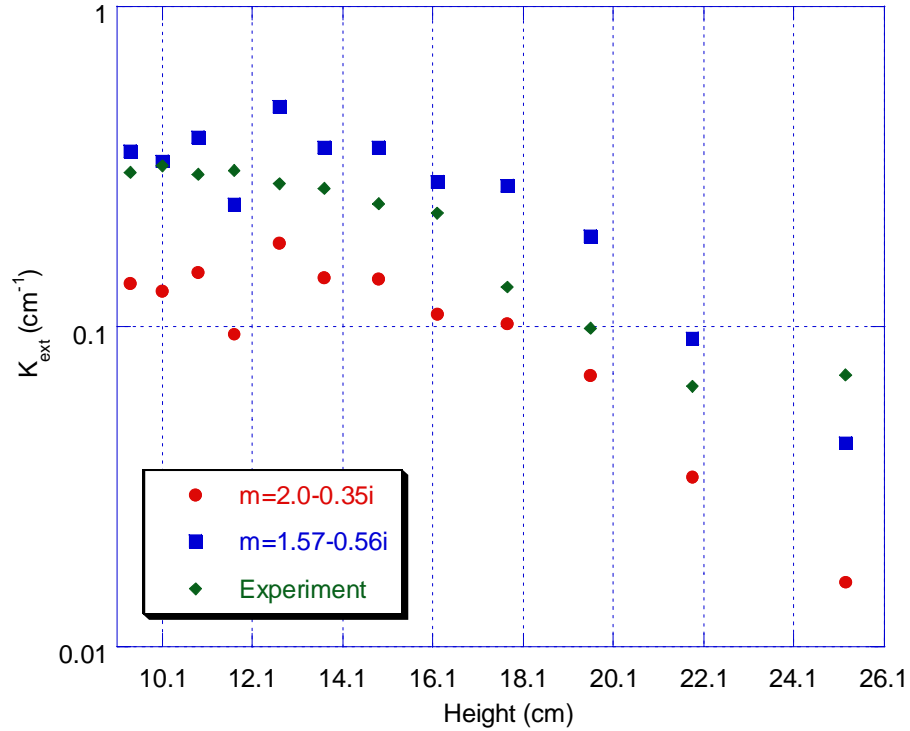


Figure B-2. The extinction coefficients as a function of the unseeded flame height. The extinction coefficients determined using RDG scattering theory for two different refractive index were compared with that from transmission experiments.

Finally, the total number density in the overall scattering volume is defined as

$$N_{Total} = N_{agg} N_{par} . \quad (B-13)$$

The volume of an aggregate is given by

$$V_{agg} = \frac{\pi}{6} d_{par}^3 N_{par} , \quad (B-14)$$

and the volume fraction f_v is calculated by Equation B-15,

$$f_v = V_{agg} \cdot N_{agg} . \quad (B-15)$$

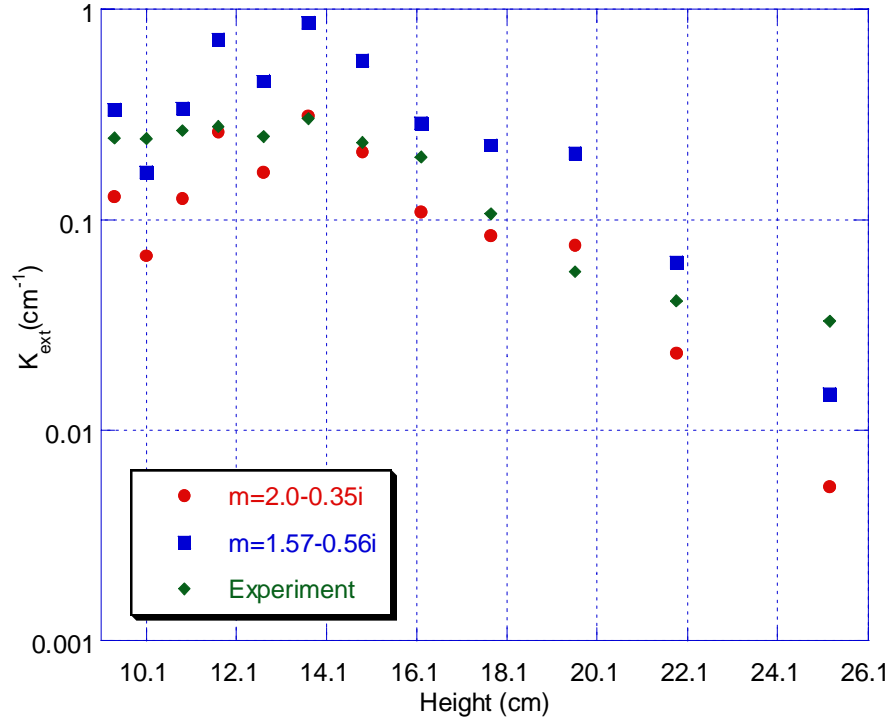


Figure B-3. The extinction coefficients as a function of the seeded flame height. The extinction coefficients determined using RDG scattering theory for two different refractive index were compared with that from transmission experiments.

The results are tabulated in Tables B-14 and B-15 respectively.

The refractive index of $m=1.57-0.56i$ yielded about 23% greater results for the all scattering parameters and 56% greater results for absorption cross sections of both a primary particle and an aggregate, which resulted in 63% of deviation for the extinction coefficient. However, the trend and the relative ratios of the unseeded to seeded flame results were identical for the alternative refractive indices.

Table B-14. Number density of soot particles in the scattering volume (particles/cm³).

Height (cm)	Unseeded		Seeded	
	m=2.0-0.35i	m=1.57-0.56i	m=2.0-0.35i	m=1.57-0.56i
9.4	1.65E+11	2.13E+11	2.57E+11	3.31E+11
10.1	1.53E+11	1.98E+11	1.16E+11	1.49E+11
10.9	1.86E+11	2.40E+11	2.23E+11	2.88E+11
11.7	1.13E+11	1.46E+11	4.59E+11	5.93E+11
12.7	2.40E+11	3.10E+11	2.70E+11	3.49E+11
13.7	1.80E+11	2.32E+11	4.99E+11	6.44E+11
14.9	1.89E+11	2.44E+11	3.23E+11	4.16E+11
16.2	1.57E+11	2.02E+11	1.63E+11	2.10E+11
17.75	1.69E+11	2.19E+11	1.38E+11	1.78E+11
19.6	1.35E+11	1.74E+11	1.47E+11	1.90E+11
21.85	7.91E+10	1.02E+11	6.01E+10	7.76E+10
25.25	5.75E+10	7.42E+10	3.26E+10	4.21E+10

Table B-15. The volume fraction of soot particles in the scattering volume (cm³ soot/cm³).

Height (cm)	Unseeded		Seeded	
	m=2.0-0.35i	m=1.57-0.56i	m=2.0-0.35i	m=1.57-0.56i
9.4	2.78E-06	3.59E-06	2.64E-06	3.41E-06
10.1	2.58E-06	3.33E-06	1.29E-06	1.67E-06
10.9	3.11E-06	4.01E-06	2.70E-06	3.48E-06
11.7	1.87E-06	2.42E-06	5.91E-06	7.63E-06
12.7	3.89E-06	5.02E-06	3.69E-06	4.76E-06
13.7	2.85E-06	3.67E-06	7.06E-06	9.11E-06
14.9	2.87E-06	3.70E-06	4.64E-06	5.99E-06
16.2	2.24E-06	2.89E-06	2.30E-06	2.97E-06
17.75	2.23E-06	2.87E-06	1.83E-06	2.36E-06
19.6	1.55E-06	2.00E-06	1.69E-06	2.18E-06
21.85	7.43E-07	9.59E-07	5.08E-07	6.56E-07
25.25	3.52E-07	4.54E-07	1.22E-07	1.57E-07

APPENDIX C
ERROR ANALYSIS

An error analysis was carried out for the volume fraction at each height. In general, for a function $x = f(a, b, \dots, y, z)$, the standard deviation in x and σ_x is determined from the propagation of the errors of a through z . Namely,

$$\sigma_x = \sqrt{\left(\frac{\partial x}{\partial a}\right)^2 \cdot \sigma_a^2 + \left(\frac{\partial x}{\partial b}\right)^2 \cdot \sigma_b^2 + \dots + \left(\frac{\partial x}{\partial y}\right)^2 \cdot \sigma_y^2 + \left(\frac{\partial x}{\partial z}\right)^2 \cdot \sigma_z^2} \quad (\text{C-1})$$

The volume fraction is defined as

$$\begin{aligned} f_V &= \left(\frac{\pi}{6} d_{par}^3\right) \cdot (N_{par}) \cdot \left(\frac{K'_{VV,agg}}{\sigma'_{VV,agg}}\right) \\ &= \frac{2}{3} \cdot \frac{\lambda^4}{\pi^3} \cdot \left|\frac{\bar{m}^2 + 2}{\bar{m}^2 - 1}\right| \cdot \frac{K'_{VV,agg}}{N_{par}} \cdot \frac{1}{S(q)} \cdot \frac{1}{d_{par}^3} \end{aligned} \quad (\text{C-2})$$

where the differential scattering cross section for an aggregate and primary particle is given by

$$\sigma'_{agg} = N_{par}^2 \sigma'_{par} S(q), \quad (\text{C-3})$$

$$\sigma'_{par} = \frac{\lambda^2}{4\pi^2} \alpha^6 \left|\frac{\bar{m}^2 - 1}{\bar{m}^2 + 2}\right|^2 = \left(\frac{2\pi}{\lambda}\right)^4 \left(\frac{d_p}{2}\right)^6 \left|\frac{\bar{m}^2 - 1}{\bar{m}^2 + 2}\right|^2. \quad (\text{C-4})$$

Therefore, for the volume fraction, $f_V = f(K'_{VV,agg}, N_{par}, S(q), d_{par})$, the standard deviation is determined from

$$\sigma_{f_V} = \sqrt{\left(\frac{\partial f_V}{\partial K'_{VV,agg}}\right)^2 \cdot \sigma_{K'_{VV,agg}}^2 + \left(\frac{\partial f_V}{\partial N_{par}}\right)^2 \cdot \sigma_{N_{par}}^2 + \left(\frac{\partial f_V}{\partial S(q)}\right)^2 \cdot \sigma_{S(q)}^2 + \left(\frac{\partial f_V}{\partial d_{par}}\right)^2 \cdot \sigma_{d_{par}}^2}, \quad (\text{C-5})$$

where,

$$\frac{\partial f_V}{\partial K'_{VV,agg}} = \frac{A}{N_{par} \cdot S(q) \cdot d_{par}^3}, \quad (C-6)$$

$$\frac{\partial f_V}{\partial N_{par}} = -\frac{A \cdot K'_{VV,agg}}{S(q) \cdot d_{par}^3} \cdot \frac{1}{N_{par}^2}, \quad (C-7)$$

$$\frac{\partial f_V}{\partial S(q)} = -\frac{A \cdot K'_{VV,agg}}{N_{par} \cdot d_{par}^3} \cdot \frac{1}{S(q)^2}, \quad (C-8)$$

$$\frac{\partial f_V}{\partial d_{par}} = -\frac{3A \cdot K'_{VV,agg}}{N_{par} \cdot S(q)} \cdot \frac{1}{d_{par}^4}. \quad (C-9)$$

In these equations, A is determined from

$$A = \frac{2}{3} \cdot \frac{\lambda^4}{\pi^3} \cdot \left| \frac{\bar{m}^2 + 2}{\bar{m}^2 - 1} \right| = 6.14 \times 10^{-19}. \quad (C-10)$$

The parameters calculated using these equations at each height were summarized in

Tables C-1 and 2 for the unseeded and seeded flames respectively.

Table C-1. Summary of the calculated parameters with Equations C-6 through C-9 for the unseeded flame.

Height (cm)	$\partial f_V / \partial K'_{VV,agg}$	$\partial f_V / \partial N_{par}$	$\partial f_V / \partial S(q)$	$\partial f_V / \partial d_{par}$
9.4	7.52E-04	-2.71E-08	-1.12E-05	-2.63E+00
10.1	6.67E-04	-2.25E-08	-1.03E-05	-2.43E+00
10.9	9.53E-04	-2.44E-08	-1.96E-05	-2.94E+00
11.7	6.30E-04	-1.34E-08	-8.46E-06	-1.78E+00
12.7	1.08E-03	-2.54E-08	-3.26E-05	-3.72E+00
13.7	6.95E-04	-1.71E-08	-1.61E-05	-2.74E+00
14.9	7.59E-04	-	-	-
16.2	8.13E-04	-1.15E-08	-1.58E-05	-2.23E+00
17.75	1.28E-03	-1.06E-08	-2.44E-05	-2.28E+00
19.6	1.50E-03	-6.86E-09	-1.89E-05	-1.66E+00
21.85	1.37E-03	-3.04E-09	-7.26E-06	-8.51E-01
25.25	1.44E-03	-1.31E-09	-2.60E-06	-4.65E-01

Table C-2. Summary of the calculated parameters with Equations C-6 through C-9 for the seeded flame.

Height (cm)	$\partial f_V / \partial K'_{VV,agg}$	$\partial f_V / \partial N_{par}$	$\partial f_V / \partial S(q)$	$\partial f_V / \partial d_{par}$
9.4	6.63E-04	-2.68E-08	-5.51E-06	-2.94E+00
10.1	4.44E-04	-1.14E-08	-2.25E-06	-1.40E+00
10.9	1.01E-03	-2.10E-08	-1.31E-05	-2.84E+00
11.7	1.93E-03	-4.15E-08	-6.52E-05	-6.10E+00
12.7	1.37E-03	-2.32E-08	-3.42E-05	-3.73E+00
13.7	1.87E-03	-4.05E-08	-1.01E-04	-7.06E+00
14.9	1.48E-03	-2.43E-08	-5.87E-05	-4.61E+00
16.2	1.01E-03	-1.11E-08	-2.12E-05	-2.30E+00
17.75	1.30E-03	-	-	-
19.6	1.67E-03	-6.85E-09	-2.47E-05	-1.81E+00
21.85	1.29E-03	-1.90E-09	-4.61E-06	-6.03E-01
25.25	1.92E-03	-4.10E-10	-8.02E-07	-1.90E-01

The differential scattering coefficient corrected for transmission was determined from the relationship, namely,

$$K'_{VV,corr} = \frac{K'_{VV,raw}}{\tau} \quad (C-11)$$

The error in this calculation was determined from

$$\begin{aligned} \sigma_{K'_{VV,agg}} &= \sqrt{\left(\frac{\partial K'_{VV,corr}}{\partial K'_{VV,raw}}\right)^2 \cdot \sigma_{K'_{VV,raw}}^2 + \left(\frac{\partial K'_{VV,corr}}{\partial \tau}\right)^2 \cdot \sigma_{\tau}^2} \\ &= \sqrt{\left(\frac{1}{\tau}\right)^2 \cdot \sigma_{K'_{VV,raw}}^2 + \left(-\frac{K'_{VV,raw}}{\tau^2}\right)^2 \cdot \sigma_{\tau}^2} \end{aligned} \quad (C-12)$$

where, $\sigma_{K'_{VV,raw}}$ and σ_{τ} are standard deviations of $K'_{VV,raw}$ and τ , which were obtained from experimental data. Tables C-3 and C-4 tabulate the experimental data and calculated parameters at each height for the unseeded and seeded flame respectively.

Table C-3. Results of the calculation using Equation C-12 for the unseeded flame.

Height (cm)	$\partial K'_{VV,corr} / \partial K'_{VV,raw}$	$\sigma_{K'_{VV,raw}}$	$\partial K'_{VV,corr} / \partial \tau$	σ_{τ}	$\sigma_{K'_{VV,agg}}$
9.4	1.29E+00	6.67E-04	-4.77E-03	1.72E-02	8.63E-04
10.1	1.34E+00	3.53E-04	-5.16E-03	2.03E-02	4.82E-04
10.9	1.34E+00	8.30E-04	-4.37E-03	3.91E-02	1.12E-03
11.7	1.38E+00	8.03E-04	-4.10E-03	2.32E-02	1.11E-03
12.7	1.37E+00	8.38E-04	-4.92E-03	4.40E-02	1.17E-03
13.7	1.37E+00	5.09E-04	-5.62E-03	3.78E-02	7.31E-04
14.9	1.35E+00	3.13E-04	-5.08E-03	3.43E-02	4.56E-04
16.2	1.33E+00	2.66E-04	-3.67E-03	4.77E-02	3.95E-04
17.75	1.19E+00	3.68E-04	-2.07E-03	6.64E-02	4.57E-04
19.6	1.13E+00	1.80E-04	-1.18E-03	5.50E-02	2.14E-04
21.85	1.08E+00	9.78E-05	-5.87E-04	3.71E-02	1.08E-04
25.25	1.07E+00	4.01E-05	-2.60E-04	2.46E-02	4.32E-05

Table C-4. Results of the calculation using Equation C-12 for the seeded flame.

Height (cm)	$\partial K'_{VV,corr} / \partial K'_{VV,raw}$	$\sigma_{K'_{VV,raw}}$	$\partial K'_{VV,corr} / \partial \tau$	σ_{τ}	$\sigma_{K'_{VV,agg}}$
9.4	1.29E+00	5.66E-04	-5.15E-03	2.83E-02	7.46E-04
10.1	1.30E+00	7.64E-04	-3.78E-03	2.63E-02	9.97E-04
10.9	1.34E+00	6.71E-04	-3.58E-03	2.58E-02	9.04E-04
11.7	1.37E+00	7.91E-04	-4.17E-03	3.31E-02	1.09E-03
12.7	1.33E+00	4.38E-04	-3.57E-03	6.01E-02	6.21E-04
13.7	1.42E+00	6.09E-04	-5.36E-03	3.21E-02	8.82E-04
14.9	1.32E+00	9.37E-04	-4.12E-03	3.74E-02	1.24E-03
16.2	1.27E+00	6.78E-04	-2.89E-03	3.69E-02	8.65E-04
17.75	1.13E+00	2.86E-04	-1.59E-03	1.30E-02	3.25E-04
19.6	1.07E+00	2.45E-04	-1.08E-03	1.51E-02	2.62E-04
21.85	1.05E+00	1.15E-04	-4.13E-04	2.05E-02	1.20E-04
25.25	1.03E+00	3.95E-05	-6.55E-05	1.87E-02	4.08E-05

With respect to $\sigma_{N_{par}}$, standard deviations for 25 samples at each height are errors of propagation from large distribution of them rather than true experimental errors. Thus, $\sigma_{N_{par}}$ was estimated using deviation between experimental values and corrected values from curve fit, namely,

$$\Sigma_{N_{par}} = \frac{\left| (N_{par})_{exp} - (N_{par})_{corr} \right|}{(N_{par})_{corr}}, \quad (C-13)$$

$$\sigma_{N_{par}} = (N_{par})_{corr} \times average \left[\left(\overline{\Sigma_{N_{par}}} \right)_{unseeded}, \left(\overline{\Sigma_{N_{par}}} \right)_{seeded} \right]. \quad (C-14)$$

Similar to the number density calculation, $\sigma_{d_{par}}$ was estimated. The average values of

$\overline{\Sigma_{N_{par}}}$ and $\overline{\Sigma_{d_{par}}}$ were 0.216 and 0.038 respectively. Table C-5 shows the calculated

errors for the particle size and number density.

Table C-5. Summary of calculated errors at each height for the particle size and number density.

True Height (cm)	$\sigma_{d_{par}}$		$\sigma_{N_{par}}$	
	unseeded	seeded	unseeded	seeded
9.4	1.20E-07	1.02E-07	2.21E+01	2.13E+01
10.1	1.20E-07	1.05E-07	2.47E+01	2.44E+01
10.9	1.20E-07	1.08E-07	2.75E+01	2.77E+01
11.7	1.19E-07	1.10E-07	3.01E+01	3.07E+01
12.7	1.19E-07	1.12E-07	3.31E+01	3.43E+01
13.7	1.18E-07	1.13E-07	3.58E+01	3.76E+01
14.9	1.16E-07	1.14E-07	3.89E+01	4.12E+01
16.2	1.14E-07	1.13E-07	4.19E+01	4.48E+01
17.75	1.11E-07	1.11E-07	4.52E+01	4.88E+01
19.6	1.06E-07	1.06E-07	4.88E+01	5.31E+01
21.85	9.90E-08	9.55E-08	5.28E+01	5.78E+01
25.25	8.58E-08	7.27E-08	5.80E+01	6.40E+01

Lastly, the structure factor of an aggregate was given by the relationship, namely,

$$S(q) = C(qR_g)^{-D_f}. \quad (C-15)$$

The error, $\sigma_{s(q)}$, was determined from

$$\sigma_{s(q)} = \sqrt{\left(\frac{\partial S(q)}{\partial C} \right)^2 \cdot \cancel{\sigma_C} + \left(\frac{\partial S(q)}{\partial q} \right)^2 \cdot \cancel{\sigma_q} + \left(\frac{\partial S(q)}{\partial R_g} \right)^2 \cdot \sigma_{R_g}^2 + \left(\frac{\partial S(q)}{\partial D_f} \right)^2 \cdot \sigma_{D_f}^2}. \quad (C-16)$$

In this equation,

$$\frac{\partial S(q)}{\partial R_g} = -D_f \cdot q^{-D_f} \cdot R_g^{-D_f-1}. \quad (\text{C-17})$$

As for σ_{R_g} , the radius of the gyration is determined from

$$(LW)^{1/2} / (2R_g) = 1.17. \quad (\text{C-18})$$

The error in this calculation was given by

$$\sigma_{R_g} = \sqrt{\left(\frac{\partial R_g}{\partial L}\right)^2 \cdot \sigma_L^2 + \left(\frac{\partial R_g}{\partial W}\right)^2 \cdot \sigma_W^2}, \quad (\text{C-19})$$

where

$$\frac{\partial R_g}{\partial L} = \frac{1}{4 \times 1.17} \cdot W^{1/2} \cdot L^{-1/2}, \quad (\text{C-20})$$

$$\frac{\partial R_g}{\partial W} = \frac{1}{4 \times 1.17} \cdot W^{-1/2} \cdot L^{1/2}. \quad (\text{C-21})$$

σ_L and σ_W were obtained from experimental data.

Meanwhile,

$$\frac{\partial S(q)}{\partial D_f} = -q \cdot R_g^{-D_f} \cdot \ln(qR_g), \quad (\text{C-22})$$

where σ_{D_f} was obtained from experimental data. The calculated parameters were

summarized in Tables C-6 and C-7 for the unseeded and seeded flame. σ_C and σ_q are

zero because C and q are the constants; thus, $\frac{\partial S(q)}{\partial C}$ and $\frac{\partial S(q)}{\partial q}$ were not necessary to be

determined.

Table C-6. Summary of calculated parameters at each height for the unseeded flame.

True Height (cm)	$\frac{\partial S(q)}{\partial R_g}$	σ_{R_g}	$\frac{\partial S(q)}{\partial D_f}$	σ_{D_f}	$\sigma_{S(q)}$
9.4	-3.48E+04	9.26E-06	-1.90E-01	1.10E-01	3.23E-01
10.1	-3.53E+04	9.18E-06	-1.90E-01	1.10E-01	3.25E-01
10.9	-1.74E+04	1.18E-05	-1.60E-01	1.10E-01	2.05E-01
11.7	-2.93E+04	1.01E-05	-1.83E-01	1.10E-01	2.98E-01
12.7	-1.12E+04	1.41E-05	-1.39E-01	1.10E-01	1.59E-01
13.7	-2.06E+04	1.13E-05	-1.68E-01	1.10E-01	2.32E-01
14.9	-	-	-	1.10E-01	-
16.2	-1.47E+04	1.28E-05	-1.52E-01	1.10E-01	1.90E-01
17.75	-7.40E+03	1.60E-05	-1.20E-01	1.10E-01	1.19E-01
19.6	-6.30E+03	1.76E-05	-1.13E-01	1.10E-01	1.12E-01
21.85	-8.84E+03	1.51E-05	-1.28E-01	1.10E-01	1.34E-01
25.25	-1.37E+04	1.31E-05	-1.49E-01	1.10E-01	1.80E-01

Table C-7. Summary of calculated parameters at each height for the seeded flame.

True Height (cm)	$\frac{\partial S(q)}{\partial R_g}$	σ_{R_g}	$\frac{\partial S(q)}{\partial D_f}$	σ_{D_f}	$\sigma_{S(q)}$
9.4	-9.69E+04	6.44E-06	-1.94E-01	1.10E-01	6.24E-01
10.1	-1.29E+05	6.00E-06	-1.75E-01	1.10E-01	7.71E-01
10.9	-2.61E+04	1.02E-05	-1.78E-01	1.10E-01	2.67E-01
11.7	-7.32E+03	1.61E-05	-1.19E-01	1.10E-01	1.19E-01
12.7	-9.58E+03	1.46E-05	-1.32E-01	1.10E-01	1.41E-01
13.7	-4.87E+03	1.91E-05	-1.02E-01	1.10E-01	9.37E-02
14.9	-5.92E+03	1.83E-05	-1.10E-01	1.10E-01	1.09E-01
16.2	-9.66E+03	1.45E-05	-1.32E-01	1.10E-01	1.41E-01
17.75	-	-	-	1.10E-01	-
19.6	-4.72E+03	1.91E-05	-1.00E-01	1.10E-01	9.06E-02
21.85	-9.93E+03	1.44E-05	-1.33E-01	1.10E-01	1.44E-01
25.25	-1.63E+04	1.23E-05	-1.57E-01	1.10E-01	2.01E-01

APPENDIX D STRAY LIGHT CONSIDERATION

Stray light consideration is very crucial in the light scattering experiment because stray light is able to dominate the scattering signal resulting in skewing experimental data significantly; therefore, errors attributed to stray light must be reduced by calibration and minimization of stray light in the various ways discussed in Chapter 3. In addition, vertical polarizer contributes to blocking non-vertically polarized stray light from introducing into PMT. The influence of stray light was discussed here through determining theoretical photon arrival rates that photons of stray light could be incident on the PMT.

The major sources of the stray light are laser light reflected from surfaces of optical mounts and scattered light from dust particles in the beam pathway, which was illustrated in Figure D-1.

First, the number of photon, $N_{\text{photon},0}$ of experimental laser flunces is calculated as

$$N_{\text{photon},0} = \frac{E_0}{h\nu} = \frac{0.304 \times 10^{-3} \text{ J}}{3.74 \times 10^{-19} \text{ J/photon}} = 8.13 \times 10^{14} \text{ photon} \quad (\text{D-1})$$

where E_0 is the laser pulse energy measured to be 0.304 mJ/pulse, h is Plank's constant determined to be 6.6261×10^{-34} [Js], ν is frequency given by

$$\nu = \frac{C}{\lambda} = \frac{3 \times 10^8 \text{ [m/s]}}{532 \times 10^{-9} \text{ [m]}} = 5.64 \times 10^{14} \text{ s}^{-1}. \quad (\text{D-2})$$

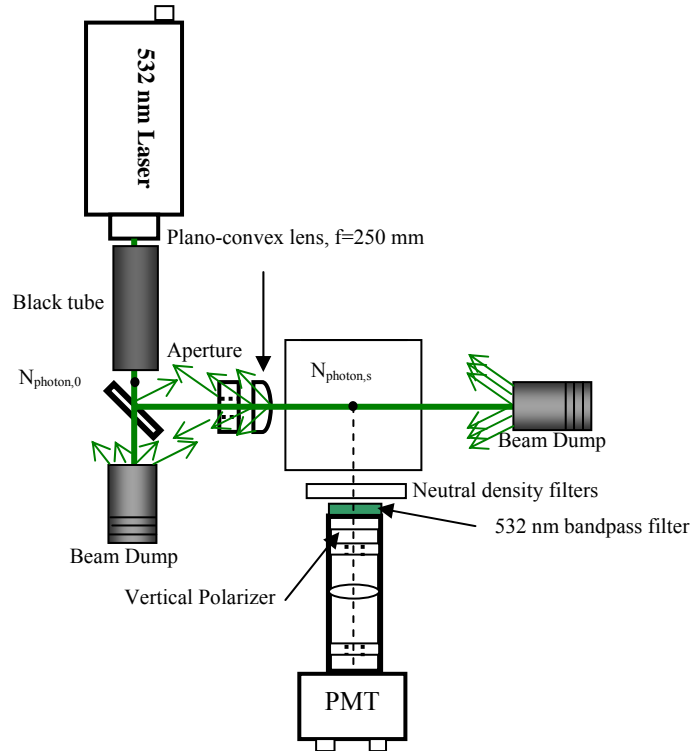


Figure D-1. Source of stray light in the light scattering optical setup.

For the focusing lens, around 4% of light is reflected from both front and rear surfaces of focal lens. As an approximation 1% of light are reflected from beam dumps, aperture, and dichroic mirror. That is, 12% of the number of photon, $N_{\text{photon},0}$ of experimental flunces may play a role as stray light. Compared to this, the contribution of scattered light from dust particles in the beam path is negligibly small. The influence of any ambient light was corrected by considering dark signal. Therefore, a total of 9.77×10^{13} photons have the potential to travel around the room and to be incident on the PMT after undergoing interactions in several ways such as reflection, scattering, and absorption. Some photons can be directly incident on the PMT along the collection optic line while others can enter into the photon counting system from arbitrary angles.

On the other hand, the number of photon in the scattering volume is calculated as

$$\begin{aligned}
N_{\text{photon},s} &= I_0 \cdot \Delta\Omega \cdot \Delta V \cdot N \cdot \sigma'_{VV} \cdot \frac{1}{h\nu} \cdot \eta \\
&= \frac{0.0916 \left[\frac{J}{\text{cm}^2} \right] \cdot 8.11 \times 10^{-3} [\text{sr}] \cdot 1.44 \times 10^{-4} [\text{cm}^3] \cdot 2.86 \times 10^{-8} [\text{cm}^{-1} \text{sr}^{-1}] \cdot 0.88}{3.74 \times 10^{-19} \left[\frac{J}{\text{photon}} \right]}, \quad (\text{D-3}) \\
&= 7.2 \times 10^3 \text{ photon}
\end{aligned}$$

where I_0 is the fluences of the laser in the scattering volume measured to be 0.0916 J/cm^2 , $\Delta\Omega$ is the solid angle, ΔV is the scattering volume, η is the efficiency of the system optics, and $(N \cdot \sigma'_{VV})$ is defined as the differential scattering coefficient of methane calibration gas which was determined to be $2.86 \times 10^{-8} \text{ cm}^{-1} \text{sr}^{-1}$. The calculations for individual parameters are following below.

$$\Delta\Omega = \frac{\pi r^2}{S^2} = 8.11 \times 10^{-3} \text{ sr}, \quad (\text{D-4})$$

where the focal length is 25 cm, and the diameter of the focal lens is 2.54 cm.

$$\Delta V = \frac{\pi D^3}{6} = 1.44 \times 10^{-4} \text{ cm}^3, \quad (\text{D-5})$$

where the diameter of the cross section of the beam is 0.065 cm.

The efficiency of the system optics is given by

$$\eta = 0.99^4 \cdot 0.92 = 0.88. \quad (\text{D-6})$$

Since the average contribution of the stray light is around 40% of the calibration methane signal, which is the photon number of 2880, the probability that the stray light are incident on the PMT is around 2.95×10^{-11} ($2880/9.77 \times 10^{13}$). Such a dramatic reduction of stray light was achieved through all efforts for stray light minimization. Careless examination or lack of these efforts will tremendously increase this probability.

APPENDIX E
SOOT REDUCTION MECHANISM

There are two possible mechanisms of soot suppression. The first process is direct oxidation of soot. The other process is catalytic effect that iron species enhance the reaction between soot and oxidizer. More possible mechanism can be experimentally found by investigating chemical state of iron species. In addition, it can be proved by determining the molar ratio of Fe to C in the flame tip. Calculations were accomplished in two different approaches here.

In the first approach, the molar ratio of Fe to C was calculated by estimating the mass flow rates of soot and iron. Volume flow rates were 0.8, 2.6, and 1.5×10^{-3} liter per minute at the temperature of 298 K for N_2 , O_2 , and C_8H_{18} respectively. At the burner lip where the temperature was assumed to be 350 K, volume flow rates became 15.7, 50.9, and 4.38 cc per second for N_2 , O_2 , and C_8H_{18} respectively as calculated below.

$$0.8 \left[\frac{l}{min} \right] \times \frac{350 \left[\frac{K}{K} \right]}{298 \left[\frac{K}{K} \right]} \times \frac{1 \left[\frac{min}{sec} \right]}{60 \left[\frac{min}{sec} \right]} = 15.7 \left[\frac{cc}{sec} \right], \quad (E-1)$$

$$2.6 \left[\frac{l}{min} \right] \times \frac{350 \left[\frac{K}{K} \right]}{298 \left[\frac{K}{K} \right]} \times \frac{1 \left[\frac{min}{sec} \right]}{60 \left[\frac{min}{sec} \right]} = 50.9 \left[\frac{cc}{sec} \right], \quad (E-2)$$

$$1.5 \left[\frac{ml}{min} \right] \times \frac{0.7 \left[\frac{g/cc}{g/cc} \right]}{0.004 \left[\frac{g/cc}{g/cc} \right]} \times \frac{1 \left[\frac{min}{sec} \right]}{60 \left[\frac{min}{sec} \right]} = 4.38 \left[\frac{cc}{sec} \right], \quad (E-3)$$

where the density of isooctane at the temperature of 350 K was estimated from the ideal state equation,

$$\frac{101325}{(8315/114) \times 350} = 0.004 \left[\frac{g}{cc} \right]. \quad (E-4)$$

Therefore, total volume flow rate of gases at the burner lip was 70.98 cc per second.

To determine the volume flow rate at the flame tip, the temperature of the flame tip was assumed to be 1800 K, and it was assumed that air was added from outside of flame by 10 times greater volume flow rate than that of gases at the burner lip.

$$781.22 \left[\frac{\text{cc}}{\text{sec}} \right] \times \frac{1800 \left[\frac{\text{K}}{\text{K}} \right]}{350 \left[\frac{\text{K}}{\text{K}} \right]} = 4017.7 \left[\frac{\text{cc}}{\text{sec}} \right]. \quad (\text{E-5})$$

Volume fraction of soot at the flame tip for the unseeded flame was 3.52×10^{-7} , and the density of soot is approximately 2 gram per cc. Therefore, the mass flow rate of soot at the flame tip was calculated as

$$4017.7 \left[\frac{\text{cc}}{\text{sec}} \right] \times 3.52 \times 10^{-7} \left[\frac{\text{cm}^3 \text{ soot}}{\text{cm}^3 \text{ gas}} \right] \times 2 \left[\frac{\text{g}}{\text{cc}} \right] = 2.83 \times 10^{-3} \left[\frac{\text{g}}{\text{sec}} \right]. \quad (\text{E-6})$$

Since 66% reduction of soot was observed, 1.56×10^{-4} mole of carbon was oxidized per second as calculated below.

$$2.83 \times 10^{-3} \left[\frac{\text{g}}{\text{sec}} \right] \times 0.66 \times \frac{1}{12} \left[\frac{\text{mol}}{\text{g}} \right] = 1.56 \times 10^{-4} \left[\frac{\text{mol}}{\text{sec}} \right]. \quad (\text{E-7})$$

Meanwhile, Fe was supplied into the flame in 4000 ppm quantities by mass (~0.11% Fe per mass of fuel). Therefore, 3.4×10^{-7} mole of iron was supplied into the flame per second as calculated below.

$$1 \left[\frac{\text{g fuel}}{\text{min}} \right] \times \frac{4000}{10^6} \times \frac{55.845 \left[\frac{\text{mol/g}}{\text{mol/g}} \right]}{195.845} \times \frac{1}{60} \left[\frac{\text{min}}{\text{sec}} \right] = 1.9 \times 10^{-5} \left[\frac{\text{g}}{\text{sec}} \right], \quad (\text{E-8})$$

$$1.9 \times 10^{-5} \left[\frac{\text{g}}{\text{sec}} \right] \times \frac{1}{55.845} \left[\frac{\text{mol}}{\text{g}} \right] = 3.4 \times 10^{-7} \left[\frac{\text{mol}}{\text{sec}} \right]. \quad (\text{E-9})$$

The molar ratio of Fe to C was 1 to 459.

Alternatively, the molar ratio of Fe to C could be directly estimated by calculating moles of carbon and iron.

1 g of C_8H_{18} has 8.75×10^{-3} mole as calculated below.

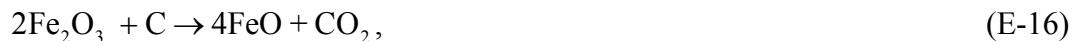
$$1[g] \times \frac{1}{114.23} \left[\frac{mol}{g} \right] = 8.75 \times 10^{-3} [mol]. \quad (E-10)$$

Since 1 g of C_8H_{18} has $\frac{4}{1000}$ g of $Fe(CO)_5$,

$$\frac{4}{1000} [g] \times \frac{1}{195.845} \left[\frac{mol}{g} \right] = 2.04 \times 10^{-5} [mol] \text{ for } Fe(CO)_5. \quad (E-11)$$

Therefore, the total mole of carbon was 0.07 moles ($8 \times 8.75 \times 10^{-3}$). Since around 25% of carbon converts to soot at smoke point, 0.0175 moles of soot were in the flame. 0.0116 moles of soot were destroyed, considering 66% soot reduction. The molar ratio of Fe to C was 1 to 569.

For direct oxidation mechanism, several possible stoichiometric chemical reactions are given by





According to these chemical reactions, one mole of iron can oxidize no more than 4 moles of carbon. Since around 500 moles of carbon are oxidized per 1 mole of iron exist in the flame, based on calculations above, the iron additive in soot suppression plays a role of the catalyst to enhance the chemical reaction between soot and oxidizers rather than directly oxidize the soot in the flame.

APPENDIX F
PROPERTIES OF IRON PENTACARBONYL

The properties of iron pentacarbonyl are presented here after the data of Alfa Products (1980).

A. Physical Data

- Molecular formula: $\text{Fe}(\text{CO})_5$
- Boiling point: 103°C
- Freezing/Melting point: -25°C
- Vapor pressure: see Figure F-1
- Solubility in water: insoluble
- Evaporation rate (butyl acetate = 1): greater than 1
- Vapor density (air = 1): 6.75
- Appearance: yellow to dark red liquid
- Odor: nearly odorless

B. Safety Data

- Flammability: flammable
- Toxicity: Toxic. Iron pentacarbonyl may cause skin and eye irritation. Inhalation and/or ingestion may cause shock, loss of consciousness, and headaches occasionally accompanied by fever, cyanosis and cough due to pulmonary edema.

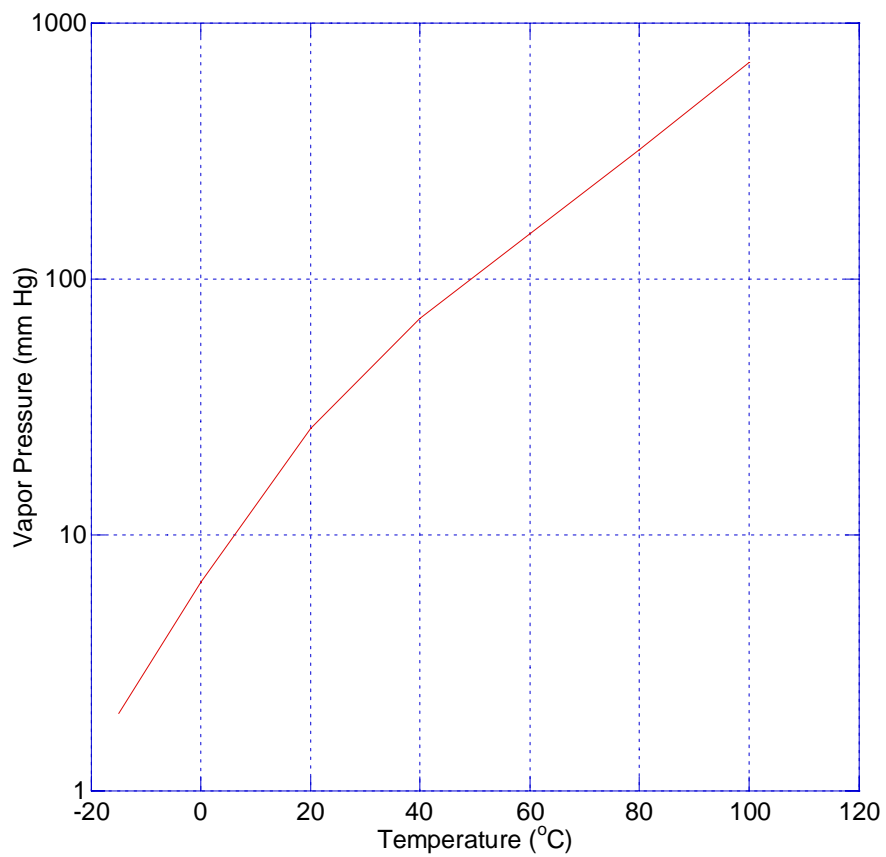


Figure F-1. Fe(CO)₅ vapor pressure as a function of temperature (Gilbert and Sulzmann 1974, Trautz and Badstubner, 1929).

Table F-1. Fe vapor pressure in Torr (mm Hg) as a function of the flame height.

	Flame Height (cm)	Flame temperature (°C)	Vapor pressure (mm Hg)
1	0.1	1084	5.5E-06
2	0.6	1275	3.0E-04
3	1.2	1444	5.0E-03
4	1.8	1579	4.0E-02
5	2.4	1444	5.0E-03
6	3	1420	4.0E-03
7	3.7	1404	3.5E-03
8	4.5	1381	3.0E-03
9	5.25	1373	2.6E-03
10	6.1	1376	2.7E-03
11	7.1	1368	2.5E-03
12	8.3	1352	2.3E-03
13	9.4	1314	6.0E-04
14	10.6	1275	3.0E-04
15	11.6	1247	2.7E-04
16	12.6	1210	8.0E-05
17	13.8	1137	1.8E-05
18	15.1	957	1.0E-07
19	16.65	891	_*
20	18.5	829	-
21	20.55	780	-
22	22.2	750	-
23	23.95	385	-

*Vapor pressure is negligible

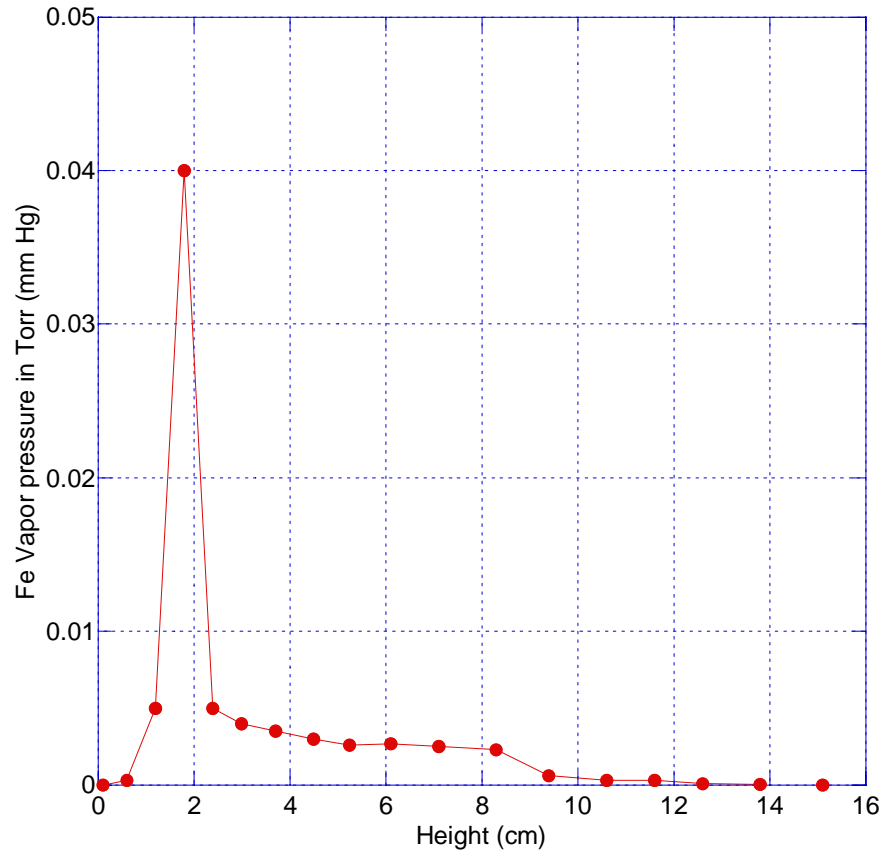


Figure F-2. Fe vapor pressure as a function of the flame height. Over the flame height of 15 cm which is the oxidation regime, the vapor pressure is negligibly small.

LIST OF REFERENCES

- Agency for Toxic Substances and Disease Registry (ATSDR). *Toxicology Profile for Jet Fuels JP-4 and JP-7*. U. S. Department of Health and Human Services, Public Health Service, Atlanta, GA (1995).
- Agency for Toxic Substances and Disease Registry (ATSDR). *Toxicology Profile for Jet Fuels JP-5 and JP-8*. U. S. Department of Health and Human Services, Public Health Service, Atlanta, GA (1998).
- Baranska H., Labudzinska A., and Termpinski J. *Laser Raman Spectrometry: Analytical Applications*. Ellis Horwood Limited. Chichester, England (1987).
- Biswas P., Wu, C. Y., Zachariah, M. R., and McMillin B. "Characterization of iron oxide-silica nanocomposites in flames: Part II. Comparison of discrete-sectional model predictions to experimental data," *Journal of Materials Research*. 12:714-723 (1997).
- Bittner J. D., and Howard J. B. "Composition Profiles and Reaction Mechanisms in a Near-Sooting Premixed Benzene/Oxygen/Argon Flame," *18th Symp. (Int.) Combust.* 18:1105-1116, The Combustion Institute, Pittsburgh (1981).
- Bockhorn H. (ed.). *Soot Formation in Combustion: Mechanisms and Models*. Springer-Verlag, Berlin (1994).
- Bonczyk P. A. "Effect of Ferrocene on Soot in a Pre vaporized Iso-Octane/Air Diffusion Flame," *Combust. Flame*. 87:233-244 (1991).
- Bulewicz E. M., Evans D. G., and Padley P. J. "Effect of Metallic Additives on Soot Formation Processes in Flames," *15th Symp. (Int.) Combust.* 1461-1470, The Combustion Institute, Pittsburgh (1974).
- Charalampopoulos T. T., and Chang H. "In Situ Properties of Soot Particles in the Wavelength Range from 340 nm to 600 nm," *Combust. Sci. Tech.* 59:401-421 (1988).
- Cheng M. T., Xie G. W., Yang. M., and Shaw D. T. "Experimental Characterization of Chain-Aggregate Aerosol by Electrooptic Scattering," *Aerosol Science and Technology*. 14:74-81(1991).
- Chippett S., and Gray W. A. "The Size and Optical Properties of Soot Particles," *Combust. Flame*. 31:149-159 (1978).

- Choi M., Cho J., Lee J., and Kim H. W. "Measurement of silica aggregate particle growth using light scattering and thermophoretic sampling in a coflow diffusion flame," *Journal of Nanoparticle Research*. 1:169-183 (1999).
- Cotton D. H., Friswell N. J., and Jenkins D. R. "Suppression of Soot Emission From Flames by Metal Additives," *Combust. Flame*. 17(1):87-98 (1971).
- Dalzell W. H., and Sarofim A. F. "Optical Constants of Soot and Their Application to Heat-Flux Calculations," *J. Heat Transfer*. 91:100-104 (1969).
- Dasch C. J. "Continuous-Wave Probe Laser Investigation of Laser Vaporization of Small Soot Particles in a Flame," *Combust. Flame*. 23(13):2209-2215 (1984a).
- Dasch C. J. "New Soot Diagnostics in Flames Based on Laser Vaporization of Soot," *20th Symp. (Int.) Combust.* 1231-1237, The Combustion Institute, Pittsburgh, (1984b).
- Dasch C. J. "The Decay of Soot Surface Growth Reactivity and Its Importance in Total Soot Formation," *Combust. Flame*. 61(3):219-225 (1985).
- Dasch C. J. "One-Dimensional Tomography A Comparison of Abel, Onion-Peeling, and Filtered Backprojection Methods," *Combust. Flame*. 31(8):1146-1152 (1992).
- de Faria D. L. A., Venâncio Silvia S., and de Oliveira M. T. "Raman Microspectroscopy of Some Iron Oxides and Oxyhydroxides," *J. Raman Spec.* 28(11):873-878 (1997).
- Dobbines R. A., and Megaridis C. M. "Absorption and Scattering of Light by Polydisperse Aggregates," *Applied Optics*. 30(33):4747-4754 (1991).
- Espensheid W. F., Kerker M., and Matijevic E. "Logarithmic Distribution Functions for Colloidal Particles," *J. Phys. Chem.* 68:3093-3097 (1964).
- Farias T. L., Carvalho M. G., Köylü Ü. Ö., and Faeth G. M. "Computational Evaluation of Approximate Rayleigh-Debye-Gans/Fractal-Aggregate Theory for the Absorption and Scattering Properties of Soot," *J. Heat Transfer*. 117:152-159 (1995).
- Farmer P. B., Singh R., Kaur B., Sram R. J., Binkova B., Kalina I., Popov T. A., Garte S., Taioli E., Gabelova A., and Cebulska-Wasilewska A. "Molecular Epidemiology Studies of Carcinogenic Environmental Pollutants – Effects of Polycyclic Aromatic Hydrocarbons (PAHs) in Environmental Pollution on Exogenous and Oxidative DNA Damage," *Mutation Research – Reviews in Mutation Research*. 544(2-3):397-402 (2003).
- Feitelberg A.S., Longwell J.P., and Sarofim A.F. "Metal Enhanced Soot and PAH Formation," *Combust. Flame*. 92(3):241-253 (1993).

- Frenklach M. "Reaction Mechanism of Soot Formation in Flames," *Phys. Chem.* 4:2028-2037 (2002).
- Frenklach M., Yuan T., and Ramachandra M. K. "Soot Formation in Binary Hydrocarbon Mixtures," *Energy Fuels.* 2(4):462-480 (1988).
- Gilbert A. G., and Sulzmann K. G. P. "The Vapor Pressure of Iron Pentacarbonyl," *J. Electrochem. Soc.* 121, 832-834. (1974).
- Goldstein J. I. *Scanning Electron Microscopy and X-ray Microanalysis.* Plenum Press, New York (1992).
- Greene G. A., Finfrock, C.C. and Irvine, T. F. "Total hemispherical emissivity of oxidized Inconel 718 in the temperature range 300-1000°C," *Experimental Thermal and Fluid Science.* 22:145-153 (2000).
- Hahn D. W. *Soot Suppressing Mechanisms of Iron in Premixed Hydrocarbon Flames.* Ph.D. dissertation. Department of Mechanical Engineering, Louisiana State University, Baton Rouge (1992).
- Harris S. J., and Weiner A. M. "Surface Growth of Soot Particles in Premixed Ethylene/Air Flame," *Combust. Sci. Tech.* 31:155-167 (1983).
- Harris S. J., and Weiner A. M. "Determination of the Rate Constant for Soot Surface Growth," *Combust. Sci. Tech.* 32:267-275 (1983).
- Hayhurst A. N., and Jones H. R. N. "The Effect of Metallic Additives on Ionization and Soot Formation in Oxy-Acetylene Flames," *Combust. Flame.* 78:339-356 (1989).
- Haynes B. S., Jander H., and Wagner H. G. "The Effect of Metal Additives on the Formation of Soot in Premixed Flames," *17th Symp. (Int.) Combust.* 1365-1373, The Combustion Institute, Pittsburgh (1979).
- Haynes B. S., Jander H., and Wagner H. G. "Optical Studies of Soot-Formation Processes in Premixed Flames," *Ber. Bunsen. Phys. Chem.* 84(6):585-592 (1980).
- Haynes B. S., and Wagner H. G. "Soot Formation," *Prog. Energy Combust. Sci.* 7(4):229-273 (1981).
- Incropera F. P., and Dewitt D. P. *Fundamentals of Heat and Mass Transfer.* John Wiley & Sons, New York (2002).
- Ingle J. D., and Crouch S. R. *Spectrochemical Analysis.* Prentice-Hall, New Jersey (1988).
- Jones A. R. "Scattering of Electromagnetic Radiation in Particulate Laden Fluids," *J. Prog. En. Comb. Sci.* 5:73-96 (1979).

- Kasper M., Sattler K., Siegmann K., Matter U., and Siegmann H. C. "The Influence of Fuel Additives on The Formation of Carbon During Combustion," *J. Aerosol Sci.* 30 (2):217-225 (1999).
- Katsouyanni K., and Pershagen G. "Ambient Air Pollution Exposure and Cancer," *Cancer Causes and Control.* 8:289-291 (1997).
- Kerker M. *The Scattering of Light and Other Electromagnetic Radiation.* Academic Press, New York (1969).
- Kim H. W., and Choi M. "In situ Line Measurement of Mean Aggregate Size and Fractal Dimension along the Flame Axis by Planar Laser Light Scattering," *Aerosol Science.* 34:1633-1645 (2003).
- Kim S. H., Fletcher R. A., and Zachariah M. R. "Understanding the Difference in Oxidative Properties between Flame and Diesel Soot Nanoparticles: The Role of Metals," *Environ. Sci. and Technol.* 39(11):4021-4026 (2005).
- Köylü Ü. Ö., and Faeth G. M. "Optical Properties of Overfire Soot in Buoyant Turbulent Diffusion Flames at Long Residence Times," *J. Heat Transfer,* 116:152-159 (1994).
- Köylü Ü. Ö., Faeth G. M., Farias T. L., and Carvalho M. G. "Fractal and Projected Structure Properties of Soot Aggregates," *Combust. Flame,* 100:621-633 (1995).
- Köylü Ü. Ö., Xing Y., and Rosner D. E. "Fractal Morphology Analysis of Combustion-Generated Aggregates Using Angular Light Scattering and Electron Microscope Images," *Langmuir,* 11:4848-4854 (1995)
- Krishnan S. S., Lin K. C., and Faeth G. M. "Optical Properties in the Visible of Overfire Soot in large Buoyant Turbulent Diffusion Flames," *J. Heat Transfer,* 122:517-524 (2000).
- Krishnan S. S., Lin K. C., and Faeth G. M. "Extinction and Scattering Properties of Soot Emitted from Buoyant Turbulent Diffusion Flames," *J. Heat Transfer.,* 123:331-339 (2001).
- Landolt-Bornstein Zahlenwerte und Funktionen aus Physik, Chemie, Astronomie, Goephysik und Technik. 11.8, 6-884 (1962).
- Lemmon E.W., McLinden M.O., and Friend D.G. Thermophysical Properties of Fluid Systems, *NIST Chemistry WebBook, NIST Standard Reference Database No. 69,* (Linstrom, P. J., and Mallard, W.G. (eds.)). National Institute of Standards and Technology, Gaithersburg MD (March 2003). <http://webbook.nist.gov>
- Linteris G. T., Knyazev V. D., and Babushok V. I. "Inhibition of Premixed Methane Flames by Manganese and Tin Compounds," *Combust. Flame.* 129:221-238 (2002).

- Masiello A. K. *Study of Soot Formation in an Iron-Seeded Isooctane Diffusion Flame Using In Situ Light Scattering*. Master Thesis. Department of Mechanical and Aerospace Engineering, University of Florida, Gainesville (2004).
- Maslar J. E., Hurst W. S., Hendricks J. H., and Aquino M. I. "In situ Raman spectroscopic investigation of aqueous iron corrosion at elevated temperatures and pressures," *Journal of The Electrochemical Society*. 147:2532-2542 (2000).
- Mavrodineanu R., and Boiteux H. *Flame Spectroscopy*. John Wiley & Sons, New York (1965).
- McMillin B. K., Biswas P., and Zachariah M. R. "In situ characterization of vapor phase growth of iron oxide-silica nanocomposites: Part I. 2-D planar laser-induced fluorescence and Mie imaging," *Journal of Materials Research*, 11:1552-1561 (1996).
- McNesby K. L., Daniel R. G., Morris J. B., and Miziolek A. W. "Tomographic Analysis of CO Absorption in a Low-Pressure Flame," *Appl. Opt.* 34(18):3318-3324 (1995).
- Mie G. "Beitrage zur Optik Truber Medien, Speziell Kolloidaler Metallosungen," *Ann. Physik*. 25:377-445 (1908).
- Miller J. A., and Melius C. F. "Kinetic and Thermodynamic Issues in the Formation of Aromatic-Compounds in Flames of Aliphatic Fuels," *Combust. Flame*. 91(1):21-39 (1992).
- Mitchell S. A., and Hackett P. A. "Chemical reactivity of iron atoms near room temperature," *Chem. Phys.* 93:7822-7829 (1990).
- Mountain R. D., and Mulholland G. W. "Light Scattering from Simulated Smoke Agglomerates," *Langmuir*. 4:1321-1326 (1988)
- National Academy of Sciences, December 2003, "Soot Worse for Global Warming than Thought," Proceedings of the National Academy of Sciences, New Scientist.com News Service, <http://www.newscientist.com/article.ns?id=dn4508>, last accessed June 15, 2005.
- Nguyen, Q. V., Dibble, R. W., Carter, C. D., Fiechtner, G. J., and Barlow, R. S. "Raman-LIF measurements of temperature, major species, OH, and NO in a Methane-air Bunsen flame," *Combustion and flame*. 105:499-510 (1996).
- Palmer H. B., and Cullis H. F. *The Formation of Carbon from Gases*. Chemistry and Physics of Carbon, Vol. 1, p. 265, Marcel Dekker, New York (1965).
- Pluchino A. B., Goldberg S. S., Dowling J. M., and Randall C. M. "Refractive-Index Measurements of Single Micron-Sized Carbon Particles," *Appl. Optics*. 19(19):3370-3372 (1980).

- Pope C. A., Burnett R. T., Thurston G. D., Thun M. J., Calle E. F., Krewski D., and Godleski J. J. "Cardiovascular mortality and long-term exposure to particulate air pollution - Epidemiological evidence of general pathophysiological pathways of disease," *Circulation* 109 (1):71-77 (2004).
- Prado G., and Lahaye J. *Physical Aspects of Nucleation and Growth of Soot Particles*. Particulate Carbon (Siegla, D. C., and Smith, G. W. (eds.)). Plenum Press, New York, 143 (1981).
- Rayleigh Lord. "On the Light From the Sky, Its Polarization and Colour," *Philos. Mag.*, 41:107-120,274-279 (reprinted in *Scientific Papers by Lord Rayleigh*, Vol. I, No. 8, Dover, New York, 1964).
- Ritrievi K. E., Longwell J. P., and Sarofim A. F. "The Effects of Ferrocene Addition on Soot Particle Inception and Growth in Premixed Ethylene Flames," *Combust. Flame*. 70(1):17-31 (1987).
- Rudder R. R., and Bach D. R. "Rayleigh Scattering of Ruby-Laser Light by Neutral Gases," *J. Opt. Soc. Amer.* 58(9):1260-1266 (1968).
- Samson R. J., Mulholland G. W., and Gentry J. W. "Structural Analysis of Soot Agglomerates," *Langmuir*. 3:272-281 (1987)
- Son H. S., Lee K., Shin S. K., and Ku, J. K. "Radiative lifetimes of the FeO orange system," *Chemical Physics Letter*. 320:658-664 (2000).
- Sorensen C. M., Lu N., and Cai J. "Fractal Cluster Size Distribution Measurement Using Static Light Scattering," *Colloid Interface Sci.* 174:456-460(1995).
- Sorensen C.M. "Light Scattering by Fractal Aggregates: A Review," *Aerosol Science and Technology*. 35:648-687 (2001).
- Telle H. H., Beddows D. C. S., Morris G. W., and Samek O. "Sensitive and selective spectrochemical analysis of metallic samples: the combination of laser-induced breakdown spectroscopy and laser-induced fluorescence spectroscopy," *Spectrochimica Acta Part B*. 56:947-960 (2001).
- Trautz V. M. and Badstubner W. "Die Dampfdrucke und Verdampfungswarmen des Eisenpentacarbonyls $\text{Fe}(\text{CO})_5$," *Z. Elektrochemie*. 35, 799-802. (1929).
- Turns, S. R. *An Introduction to Combustion, 2nd ed.* McGraw Hill, Boston (2000).
- U. S. Environmental Protection Agency, May 2003, "EPA PM 2.5 Weighing Laboratory – PM 2.5 Objectives and History," Region 4 Science & Ecosystem Support Division, East Coast Weighing Laboratory, <http://www.epa.gov/region4/sesd/pm25/p2.htm>, last accessed June 15, 2005.

- U. S. Environmental Protection Agency, September 2003, "PM – How Particulate Matter Affects the Way We Live and Breathe," Office of Air Quality Planning and Standards, original publication November 2000, <http://www.epa.gov/air/urbanair/pm/index.html>, last accessed June 15, 2005.
- U. S. Environmental Protection Agency, August 2003, *2002 Air Quality Trends Summary Report*, EPA 454/K-03-001, Office of Air Quality Planning and Standards, Research Triangle Park, NC.
- Wang G., and Sorensen C. M. "Experimental Test of the Rayleigh-Debye-Gans Theory for Light Scattering by Fractal Aggregates," *Applied Optics*. 41(22):4645-4651 (2002)
- Warnatz J., Mass U., and Dibble R. W. *Combustion – Physical and Chemical Fundamentals, Modeling and Simulation, Experiments, Pollutant Formation, 3rd ed.* Springer-Verlag, Berlin (2001).
- Wei Y. L., and Lee J. H. "Manganese Sulfate Effect on PAH Formation from Polystyrene Pyrolysis," *The Science of the Total Environment*. 228:59-66 (1999).
- Williams D. B., and Carter C. B. *Transmission Electron Microscopy*. Plenum Press, New York (1996).
- Wu J. S., Krishnan S. S., and Faeth G. M. "Refractive Indices at Visible Wavelengths of Soot Emitted from Buoyant Turbulent Diffusion Flames," *J. Heat Transfer*. 119:230-237 (1997)
- Yang. G. S. "Study on the effect of iron on PM10 formation and design of a particle-generating system using a concentric diffusion burner flame," *Journal of the Air & Waste Management Association*. 54:898-907 (2004).
- Yoder G. D., Diwakar P. K., and Hahn D. W. "Assessment of Soot particle Vaporization Effects during Laser-Induced Incandescence with Time-Resolved Light Scattering," *Appl. Opt.* 44(20):4211-4219 (2005).
- Zhang J., and Megaridis C. M. "Soot Suppression by Ferrocene in Laminar Ethylene/Air Nonpremixed Flames," *Combust. Flame*. 105(4):528-540 (1996).

BIOGRAPHICAL SKETCH

Kibum Kim, the elder of Yong-Hyun Kim and Pill-Young Kim's two sons, was born in Dae-Jeon, Republic of Korea, on February 4, 1975. He grew up and spent most of his early life in the city. In 2000, he was awarded a bachelor's degree in naval architecture and ocean engineering from Chung-Nam National University in the Republic of Korea. In his senior year, he built the first Korean human-powered ship with water foils. The next year, he was given the opportunity to experience American culture and study English at the University of Alabama. In August 2001, he began graduate study at the University of Florida. Kibum graduated with a Master of Science degree in mechanical engineering from the University of Florida in August 2003. He went on to earn his Ph.D. in mechanical engineering, also at the University of Florida, in August 2006.